Measuring Dark Energy with 1,345 Supernovae: Reducing Statistical Uncertainties on the Equation of State and Understanding the Dependence of Type Ia Supernovae on Their Local Environments

by

David O. Jones

A dissertation submitted to The Johns Hopkins University in conformity with the requirements for the degree of Doctor of Philosophy.

Baltimore, Maryland

June, 2017

Abstract

The acceleration of the universe at late cosmic times is one of the fundamental questions in astrophysics today. Larger and larger samples of Type Ia supernovae (SNe Ia) have been compiled to measure the expansion history of the universe and in so doing deduce the nature of the dark energy driving the expansion. The goals of this thesis are to improve SN Ia classification, better understand the relationship between SNe Ia and their host galaxy properties, and measure the dark energy equation of state parameter, w, with the largest current sample of SNe Ia. First, I present observations of a SN Ia at redshift 1.914, one of the most distant SNe Ia to be discovered. I develop new methods to classify this SN using both its light curve and spectrum, and discuss the unique challenges of determining SN types at high redshift. Second, I study the dependence of SNe Ia on the star formation environment near the progenitor. It has been suggested that this dependence is a possible source of large systematic uncertainties on w. I find no evidence of a relationship between SNe Ia and their local star formation environments. Third, I measure spectroscopic host galaxy redshifts for over 3,000 SNe discovered in the Pan-STARRS survey, $\sim$1,150 of

ABSTRACT

which can be used to measure cosmological parameters. These SNe can be used to measure cosmological parameters if precise redshifts are known. I develop a Bayesian framework to marginalize over the contaminating distribution of core-collapse (CC) SNe and find that even with significant CC SN contamination, I can measure w with a bias of just 0.004 (8% of its statistical uncertainty). Finally, I use these methods to combine 1,345 SNe from Pan-STARRS and low-redshift compilations with constraints from the cosmic microwave background, baryon acoustic oscillations, and the locally measured Hubble constant to measure w.

Primary Reader: Adam Riess

Acknowledgments

I would like to thank my parents for their support over many, many years, and Laura for keeping me grounded and always with a new adventure on the horizon.

I would also like to thank my Advisor, Adam Riess, for his guidance and a fantastic thesis plan. I really appreciate that Adam is always available for questions, loves research, and directs that research toward answering some of the biggest open questions in science. This work would also not be possible without the help of Steve Rodney, whose patience and thoughtfulness in my first few years of graduate school was invaluable. I also owe a huge debt of gratitude to Dan Scolnic for many, many long conversations about photometry, supernova simulations, systematic uncertainties, and paper writing over the last six years. Obtaining the data necessary for this thesis would not have been possible without Bob Kirshner, Edo Berger, Ryan Chornock and Ryan Foley. Finally, I would like to thank all my co-authors for their invaluable comments and suggestions.

Chapter 2 is based on "The Discovery of the Most Distant Known Type Ia Supernova at Redshift 1.914". Authors: D. O. Jones, S. A. Rodney, A. G. Riess,

ACKNOWLEDGMENTS

B. Mobasher, T. Dahlen, C. McCully, T. F. Frederiksen, S. Casertano, J. Hjorth, C. R. Keeton, A. Koekemoer, L.-G. Strolger, T. G. Wiklind, P. Challis, O. Graur, B. Hayden, B. Patel, B. J. Weiner, A. V. Filippenko, P. Garnavich, S. W. Jha, R. P. Kirshner, H. C. Ferguson, N. A. Grogin, and D. Kocevski.

Acknowledgements: We thank the anonymous referee for many helpful comments, and Masao Sako and Rick Kessler for their invaluable assistance with SNANA and PSNID. In addition, our aXe and aXeSim analysis was made possible by help from Jeremy Walsh, Harold Kuntschner, Martin Kummel, Howard Bushouse, and Nor Pirzkal. We also thank Daniel Scolnic for many useful discussions. Financial support for this work was provided by NASA through grants HST-GO-12060 and HST-GO-12099 from the Space Telescope Science Institute, which is operated by Associated Universities for Research in Astronomy, Inc., under NASA contract NAS 5-26555. Additional support for S.R. was provided by NASA through Hubble Fellowship grant HST-HF-51312. A.V.F. is also grateful for the support of National Science Foundation (NSF) grant AST-1211916, the TABASGO Foundation, and the Christopher R. Redlich Fund. The Dark Cosmology Centre is funded by the DNRF. R.P.K. was supported in part by NSF grant PHY11-25915 to the Kavli Institute for Theoretical Physics at the University of California, Santa Barbara. O.G. acknowledges support by a grant from the Israeli Science Foundation. *Facilities: HST (WFC3, ACS) VLT:Kueyen (X-shooter)*

Chapter 3 is based on "Reconsidering the Effects of Local Star Formation on

Type Ia Supernova Cosmology". Authors: D. O. Jones, A. G. Riess, D. M. Scolnic. Acknowledgements: This work would not have been possible without comments, suggestions, and other assistance from Mickael Rigault. We also thank the anonymous referee and Pat Kelly for many useful comments and suggestions.

Chapter 4 is based on "Measuring the Properties of Dark Energy with Photometrically Classified Pan-STARRS Supernovae. I. Systematic Uncertainty from Core-Collapse Supernova Contamination". Authors: D. O. Jones, D. M. Scolnic, A. G. Riess, R. Kessler, A. Rest, R. P. Kirshner, E. Berger, C. A. Ortega, R. J. Foley, R. Chornock, P. J. Challis, W. S. Burgett, K. C. Chambers, P. W. Draper, H. Flewelling, M. E. Huber, N. Kaiser, R.-P. Kudritzki, N. Metcalfe, R. J. Wainscoat, C. Waters.

Chapter 5 is based on "Measuring Dark Energy with Photometrically Classified Pan-STARRS Supernovae. I. Cosmological Parameters". Authors: D. O. Jones, D. M. Scolnic, A. G. Riess, R. Kessler, A. Rest, R. P. Kirshner, E. Berger, C. A. Ortega, R. J. Foley, R. Chornock, P. J. Challis, W. S. Burgett, K. C. Chambers, P. W. Draper, H. Flewelling, M. E. Huber, N. Kaiser, R.-P. Kudritzki, N. Metcalfe, R. J. Wainscoat, C. Waters.

Acknowledgements for Chapters 3 and 4: This manuscript is based upon work supported by the National Aeronautics and Space Administration under Contract No. NNG16PJ34C issued through the *WFIRST* Science Investigation Teams Programme. R.J.F. and D.S. were supported in part by NASA grant 14-WPS14-0048. The UCSC group is supported in part by NSF grant AST-1518052 and from fellowships from the

ACKNOWLEDGMENTS

Alfred P. Sloan Foundation and the David and Lucile Packard Foundation to R.J.F. This work was supported in part by the Kavli Institute for Cosmological Physics at the University of Chicago through grant NSF PHY-1125897 and an endowment from the Kavli Foundation and its founder Fred Kavli. D.S, gratefully acknowledges support from NASA grant 14-WPS14-0048. D.S. is supported by NASA through Hubble Fellowship grant HST-HF2-51383.001 awarded by the Space Telescope Science Institute, which is operated by the Association of Universities for Research in Astronomy, Inc., for NASA, under contract NAS 5-26555.

Many of the observations reported here were obtained at the MMT Observatory, a joint facility of the Smithsonian Institution and the University of Arizona. This paper uses data products produced by the OIR Telescope Data Center, supported by the Smithsonian Astrophysical Observatory. Additional data are thanks to the Anglo Australian Telescope, operated by the Australian Astronomical Observatory, through the National Optical Astronomy Observatory (NOAO PropID: 2014B-N0336; PI: D. Jones). We also use data from observations at Kitt Peak National Observatory, National Optical Astronomy Observatory, which is operated by the Association of Universities for Research in Astronomy (AURA) under a cooperative agreement with the National Science Foundation. Also based on observations obtained with the Apache Point Observatory 3.5-meter telescope, which is owned and operated by the Astrophysical Research Consortium.

The computations in this paper used a combination of three computing clusters.

ACKNOWLEDGMENTS

BEAMS analysis was performed using the University of Chicago Research Computing Center and the Odyssey cluster at Harvard University. We are grateful for the support of the University of Chicago Research Computing Center for assistance with the calculations carried out in this work. The Odyssey cluster is supported by the FAS Division of Science, Research Computing Group at Harvard University. Supernova light curve reprocessing would not have been possible without the Data-Scope project at the Institute for Data Intensive Engineering and Science at Johns Hopkins University.

Funding for the Sloan Digital Sky Survey IV has been provided by the Alfred P. Sloan Foundation, the U.S. Department of Energy Office of Science, and the Participating Institutions. SDSS- IV acknowledges support and resources from the Center for High-Performance Computing at the University of Utah. The SDSS web site is www.sdss.org.

SDSS-IV is managed by the Astrophysical Research Consortium for the Participating Institutions of the SDSS Collaboration including the Brazilian Participation Group, the Carnegie Institution for Science, Carnegie Mellon University, the Chilean Participation Group, the French Participation Group, Harvard-Smithsonian Center for Astrophysics, Instituto de Astrofsica de Canarias, The Johns Hopkins University, Kavli Institute for the Physics and Mathematics of the Universe (IPMU) / University of Tokyo, Lawrence Berkeley National Laboratory, Leibniz Institut fr Astrophysik Potsdam (AIP), Max-Planck-Institut fr Astronomie (MPIA Heidelberg), Max-Planck-

ACKNOWLEDGMENTS

Institut fr Astrophysik (MPA Garching), Max-Planck-Institut fr Extraterrestrische Physik (MPE), National Astronomical Observatory of China, New Mexico State University, New York University, University of Notre Dame, Observatrio Nacional / MCTI, The Ohio State University, Pennsylvania State University, Shanghai Astronomical Observatory, United Kingdom Participation Group, Universidad Nacional Autnoma de Mxico, University of Arizona, University of Colorado Boulder, University of Oxford, University of Portsmouth, University of Utah, University of Virginia, University of Washington, University of Wisconsin, Vanderbilt University, and Yale University.

This research makes use of the VIPERS-MLS database, operated at CeSAM/LAM, Marseille, France. This work is based in part on observations obtained with WIRCam, a joint project of CFHT, Taiwan, Korea, Canada and France. The CFHT is operated by the National Research Council (NRC) of Canada, the Institut National des Science de lUnivers of the Centre National de la Recherche Scientifique (CNRS) of France, and the University of Hawaii. This work is based in part on observations made with the Galaxy Evolution Explorer (GALEX). GALEX is a NASA Small Explorer, whose mission was developed in cooperation with the Centre National dEtudes Spatiales (CNES) of France and the Korean Ministry of Science and Technology. GALEX is operated for NASA by the California Institute of Technology under NASA contract NAS5-98034. This work is based in part on data products produced at TERAPIX available at the Canadian Astronomy Data Centre as part of the Canada-France-

ACKNOWLEDGMENTS

Hawaii Telescope Legacy Survey, a collaborative project of NRC and CNRS. The TERAPIX team has performed the reduction of all the WIRCAM images and the preparation of the catalogues matched with the T0007 CFHTLS data release.

Funding for the DEEP2 Galaxy Redshift Survey has been provided by NSF grants AST-95-09298, AST-0071048, AST-0507428, and AST-0507483 as well as NASA LTSA grant NNG04GC89G. This research uses data from the VIMOS VLT Deep Survey, obtained from the VVDS database operated by Cesam, Laboratoire d'Astrophysique de Marseille, France. zCosmos data are based on observations made with ESO Telescopes at the La Silla or Paranal Observatories under programme ID 175.A-0839.

Additional Acknowledgements for Chapter 3: We would like to thank the anonymous referee for many helpful suggestions.

Contents

List of Tables

List of Figures

Chapter 1

Introduction

In the decades since Edwin Hubble first discovered the expanding Universe, the mystery of its expansion has become greater than he could ever have anticipated. With the discovery that the Universe is not just expanding but accelerating, it is now known that the late time evolution of the Universe is dominated by the influence of "dark energy" (Riess et al., 1998; Perlmutter et al., 1999).

In general relativity, the expansion of a universe comprised of matter, radiation, and dark energy is governed by the Friedmann equation:

$$H(a)^2 = H_0^2(\frac{\Omega_R}{a^4} + \frac{\Omega_M}{a^3} + \frac{\Omega_k}{a^2} + \Omega_\Lambda a^{-3(1+w)}). \tag{1.1}$$

As a function of the scale factor of the Universe, a, the Friedmann equation models the expansion rate of the Universe using the Hubble parameter $H(a) = \frac{\dot{a}}{a}$. H_0 is the Hubble constant, and Ω_R, Ω_M, Ω_k and Ω_Λ are the present day energy densities of

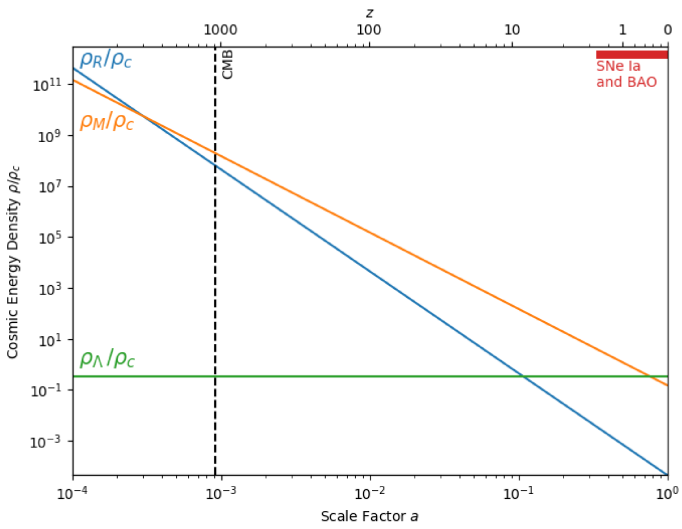

Figure 1.1: Energy density for radiation ($\rho_R \propto \frac{\Omega_R}{a^4}$), matter ($\rho_M \propto \frac{\Omega_M}{a^3}$), and dark energy ($\rho_\Lambda \propto \Omega_\Lambda$) as a function of cosmic time. SNe Ia and Baryon Acoustic Oscillations probe the dark energy-dominated phase of the Universe at $z \lesssim 0.5$.

photons, matter, curvature and dark energy as a fraction of the critical density of the Universe, $\rho_c = 3H^2/8\pi G$. w is the dark energy equation of state parameter, equal to $P/\rho c^2$. The redshift, z is equal to $1/a - 1$. Figure 1.1 shows the contributions to the cosmic energy density from radiation, matter, and dark energy as a function of cosmic scale factor and redshift.

In the case of $w = -1$, Ω_Λ is the cosmological constant from Einstein's equations of General Relativity. The cosmological constant model, if correct, implies the presence of vacuum energy, a spatially and temporally constant negative pressure. Though vacuum energy is predicted by Quantum Mechanics, its estimated size is 120 orders of magnitude greater than the cosmological constant we observe.

If dark energy is not a cosmological constant, another possible explanation is a dynamic scalar field, often referred to as "quintessence" dark energy, which would yield $w \geq -1$ depending on the nature of the field. A w less than -1 would imply so-called "phantom" dark energy, which is thought to be unphysical at the quantum level and as such would require very exotic physics (Amendola et al., 2013). Finally, if the equations of General Relativity require modification at long distances, crossing of the phantom boundary from $w > -1$ to $w < -1$ (or vice versa) could be possible as redshift changes (Bamba et al., 2011).

Insight into these models can be gained through precise measurements of the late time expansion history of the Universe using Type Ia supernovae (SNe Ia). SNe Ia are formed by the detonation of a Carbon-Oxygen white dwarf after it has accreted matter from a binary companion (Livio, 2001). The nature of this binary companion is unclear (Maoz et al., 2014), as are the physics of the explosion (Hillebrandt & Niemeyer, 2000). Even the traditionally accepted hypothesis that SN Ia detonation typically occurs just below $1.39 M_{\odot}$, the Chandrasekhar limit for the maximum mass of a white dwarf, is a subject of considerable debate (e.g. Howell, 2011). In spite of this uncertainty, the homogeneity of SNe Ia and their excellent accuracy as cosmic distance indicators is unambiguous, once two empirical relationships have been taken into account: the relation between light curve width and SN luminosity (Phillips, 1993) and the relation between light curve color and SN luminosity (Tripp, 1998; Riess et al., 1996). After correcting for these relationships, SNe Ia can be used to measure

distances with up to ∼6% accuracy and are luminous enough to be discovered at up to $z \sim 2$ with current telescopes (Jones et al., 2013; Rodney et al., 2015).

SNe Ia are the best probe of cosmic expansion during the dark-energy dominated phase of the Universe, $z \lesssim 0.5$, but measuring w precisely also requires constraints on the cosmic matter density. These constraints can be determined from the CMB temperature power spectrum, which gives constraints on Ω_M at z $\sim$ 1090 (Planck Collaboration et al., 2015). Matter-dominated cosmic epochs are largely independent of evolving or non-constant dark energy (see Figure 1.1). Baryon acoustic oscillations, the size of the acoustic wave imprint on the galaxy density correlation function, complement SN Ia distances at $z \gtrsim 0.3$. At $z \lesssim 0.3$, measurements of the acoustic peak are limited by the weak BAO signal, which requires enormous cosmic volumes for a precise measurement (Weinberg et al., 2013). The BAO feature is proportional to the Hubble parameter H(z).

In conjunction with improvements in CMB and BAO data, larger and larger samples of accurate SN Ia distances have been compiled over the last 20 years, beginning in the mid-1990s with 29 SNe Ia from Calan/Tololo (Hamuy et al., 1996) and 22 from the CfA1 survey (Riess et al., 1999). The most recent measurement of w uses a compilation of 740 SNe Ia, including those early SN samples, additional low-z SN data (Jha et al., 2006; Hicken et al., 2009c,a; Contreras et al., 2010; Folatelli et al., 2010), Sloan Digital Sky Survey (SDSS) SNe Ia (Alam et al., 2015; Kessler et al., 2009a), and SuperNova Legacy Survey (SNLS) SNe Ia out to $z \sim 1$. It also uses SNe Ia out

to $z \sim 2$ discovered by the Hubble Space Telescope (Riess et al., 2007). High-z SNe can give new insights into possible variations of the dark energy equation of state in (likely) matter-dominated epochs (Rodney et al., 2012). In Chapter 2, I present the discovery of one such SN Ia, focusing primarily on the unique challenges of classifying SNe Ia at $z > 1.5$.

Combined with the most recent BAO constraints (Anderson et al., 2014; Ross et al., 2015), CMB temperature and lensing data from Planck Collaboration et al. (2015), and SNe Ia from Betoule et al. (2014), the best current measurement of w is $w = -1.006 \pm 0.045$. Statistical and systematic uncertainties on this measurement are approximately equal. The primary goal of current efforts in SN Ia cosmology is to reduce both the statistical and systematic uncertainties on w.

Calibration of the photometric system has long been the dominant systematic uncertainty on w, but several important systematic uncertainties due to SN physics are just beginning to be studied and included in the measurement error. In particular, it has been suggested that the relationship between SN color and luminosity could evolve with redshift (Conley et al., 2011). Furthermore, our understanding of SN physics has been complicated by the discovery of a relationship between SN luminosity (after shape and color correction) and the mass of the SN host galaxy (the mass step; Kelly et al., 2010; Lampeitl et al., 2010; Sullivan et al., 2010). The underlying cause of the mass step is unclear, though hypotheses exist (e.g. Hayden et al., 2013; Childress et al., 2014). Also unclear is whether the uncertain nature of the mass step contributes

significantly to the systematic uncertainty on w. For example, it has been suggested that the size of the mass step could change with redshift due to the changing mean ages of SN progenitors (Childress et al., 2014), thereby biasing SN Ia distances, and also that perhaps the host galaxy environment within a ∼few kpc of the SN might better correlate with the SN luminosity (Rigault et al., 2013, 2015).

In this thesis, I present one aspect of SN Ia systematic uncertainties. In Chapter 3, I discuss whether the local SN environment indeed correlates with SN Ia luminosity, and whether this effect could cause suggest unforeseen systematic uncertainties in not just the dark energy equation of state but also H_0.

In addition to systematic uncertainties, statistical uncertainties will be reduced with the thousands of new SNe that were discovered by Pan-STARRS (Kaiser et al., 2010), are currently being discovered by the Dark Energy Survey (Bernstein et al., 2012), and will soon be discovered by the Large Synoptic Survey Telescope. Unfortunately, obtaining spectroscopic classifications for so many SNe − previously a prerequisite for cosmological analyses with SNe Ia − will be prohibitively expensive. Without spectroscopic classifications, core-collapse (CC) SNe will contaminate the SN Ia sample and bias measurements of cosmological parameters.

To address this complication, in Chapters 4 and 5 I present the Pan-STARRS SN Ia sample. Pan-STARRS observed 5,200 SNe over its 4 years of operation, but obtained spectroscopic classifications for just 10%. With my collaborators, I measured spectroscopic host galaxy redshifts for over 3,000 of these SNe in order to use them

to measure w.

The Pan-STARRS sample consists of ∼90% SNe Ia, which are excellent distance indicators, and ∼10% core-collapse (CC) SNe, which are not. In Chapter 4, I present a Bayesian framework for marginalizing over the CC SNe in the data and measuring accurate SN Ia distances from this contaminated sample. I test the method on simulations, finding that it can be used to give a measurement of w with negligible bias due to CC SN contamination. In Chapter 5, I use these methods to measure cosmological parameters by combining SNe, cosmic microwave background measurements, baryon acoustic oscillations, and local measurements of the Hubble constant.

Chapters 2 and 3 have been published in The Astrophysical Journal (ApJ), and Chapter 4 is currently in press for publication in ApJ. Chapter 5 is in preparation for publication and will be submitted in 2017.

Chapter 2

The Discovery of the Most Distant Known Type Ia Supernova at Redshift 1.914

2.1 Abstract

We present the discovery of a Type Ia supernova (SN) at redshift $z = 1.914$ from the CANDELS multi-cycle treasury program on the *Hubble Space Telescope (HST)*. This SN was discovered in the infrared using the Wide-Field Camera 3, and it is the highest-redshift Type Ia SN yet observed. We classify this object as a SN Ia by comparing its light curve and spectrum with those of a large sample of Type Ia and core-collapse SNe. Its apparent magnitude is consistent with that expected from the

ΛCDM concordance cosmology. We discuss the use of spectral evidence for classification of $z > 1.5$ SNe Ia using *HST* grism simulations, finding that spectral data alone can frequently rule out SNe II, but distinguishing between SNe Ia and SNe Ib/c can require prohibitively long exposures. In such cases, a quantitative analysis of the light curve may be necessary for classification. Our photometric and spectroscopic classification methods can aid the determination of SN rates and cosmological parameters from the full high-redshift CANDELS SN sample.

2.2 Introduction

Over the past decade, measurements of Type Ia supernovae (SNe) at redshift $z \gtrsim 1$ have extended the observed population to a time when the universe was matter dominated (Riess et al., 2001, 2004, 2007; Suzuki et al., 2012; Rodney et al., 2012; Rubin et al., 2012). At these lookback times of $\gtrsim 7$ Gyr, the predicted effects of dark energy are small, while the typical conditions under which SNe form are increasingly different from local environments.

These characteristics may allow observations at high redshift to constrain an evolutionary change in SN Ia brightness independent of our understanding of dark energy. This type of systematic shift in magnitude could be caused by changing metallicity or progenitor masses (e.g., Domínguez et al., 2001). Such an effect could be present at a lower level in intermediate-redshift SN samples ($0.2 \lesssim z \lesssim 1.0$), and therefore

be a source of uncertainty in the determination of the dark energy equation-of-state parameter ($w = P/(\rho c^2)$; Riess & Livio, 2006).

Observations of high-redshift SNe Ia could also place constraints on the binary companions of SN progenitors. The two most likely SN Ia progenitor models are the single-degenerate scenario, where a white dwarf accretes matter from a main-sequence or giant companion, and the double-degenerate scenario, where SNe occur through the merging of two carbon-oxygen (C-O) white dwarfs. A substantial difference between these mechanisms, however, is the typical time interval from progenitor formation to explosion; progenitors would likely take $\gtrsim 10^9$ yr to reach the Chandrasekhar limit by mass transfer from a nondegenerate companion, but would more often take less time in a system of two C-O white dwarfs (for a recent review of SN Ia progenitors, see Wang & Han, 2012). The distribution of times between formation and explosion, known as the delay-time distribution (DTD), can therefore be used to set constraints on SN progenitor models. Observations of SN rates measure the convolution of the DTD with the cosmic star-formation history, and high-redshift rates are the most sensitive to delay times (Strolger et al., 2010; Graur et al., 2011).

Due to the high sensitivity and angular resolution of the *Hubble Space Telescope (HST)*, its Advanced Camera for Surveys (ACS) has been an effective instrument for observing and monitoring SNe out to $z \approx 1.5$. To find SNe at higher redshifts in the rest-frame optical, where they are brightest and we understand them best, searching in the near-infrared (IR) with the recently installed Wide-Field Camera 3 (WFC3)

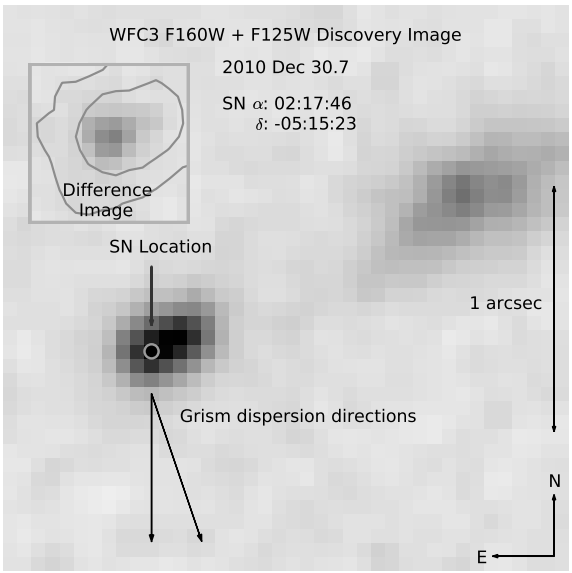

Figure 2.1: The WFC3 F160W + F125W discovery and difference images (using a late-time, SN-free template) for SN UDS10Wil. The SN is located $\sim 0''.1$ from the center of the host galaxy (2 ACS pixels). The contours plotted on the difference image of the SN (upper left) show the regions containing 68% and 95% of the host galaxy light. The center of the nearest neighboring galaxy, which causes minimal lensing of the SN (see §2.5.1), is located $\sim 1''.5$ away.

allows SN surveys to reach unprecedented depths not accessible from the ground (F160W limiting Vega magnitude ~ 25.5, equal to the peak observed brightness of a typical SN Ia at $z \approx 2.5$).

In this paper we present observations of a SN Ia at $z = 1.91$ (SN UDS10Wil), the highest-redshift SN Ia discovered to date. It was found in the Cosmic Assembly Near-infrared Deep Extragalactic Legacy Survey (CANDELS, PI: Faber & Ferguson; Grogin et al., 2011; Koekemoer et al., 2011). The full CANDELS SN sample is designed to measure SN rates and to study SN systematics at redshifts greater than

1.5. Similar to SN Primo, a $z = 1.55$ WFC3-discovered SN (Rodney et al., 2012; Frederiksen et al., 2012), UDS10Wil also has spectroscopic evidence for classification. We present the discovery of SN UDS10Wil in §2. Section 3 discusses its classification from photometry and *HST* grism spectroscopy. In §4 we estimate the brightness correction due to gravitational lensing and fit the light curve. We discuss our results and the *HST* spectral classification in §5, and our conclusions are given in §6.

2.3 Discovery

SN UDS10Wil was discovered in the second epoch of CANDELS observations of the UKIDSS Ultra-Deep Survey field (UDS; Lawrence et al., 2007; Cirasuolo et al., 2007) on 2010 December 30, after subtracting the images obtained in the first epoch (2010 November 11). It was detected at high significance in both F160W and F125W difference images, while a flux decrement was seen at the same location in the ACS filter F814W difference image (detected at $\sim 2.5\sigma$). The SN searching is performed by eye in the difference images, and in this case we could only subtract the first epoch of UDS observations (50 days before) from the second epoch, as no earlier WFC3 data were available. The F814W flux decrement suggests that pre-maximum SN light was present in the first epoch of UDS observations. Thus, the SN was brighter in the pre-maximum, shorter-wavelength ACS imaging.

The WFC3 (F125W + F160W) discovery-epoch image of SN UDS10Wil is shown

Table 2.1. Photometric Observations

UT Date	MJD	Filter	Exposure Time	Flux (counts s^{-1})	Vega Mag
2010 Nov. 08.8	55508.1	ACS/F814W	3517.0	0.143 ± 0.054	27.635 ± 0.413
2010 Nov. 11.2	55511.2	WFC3/F160W	1605.8	0.517 ± 0.074	25.221 ± 0.156
2010 Nov. 11.2	55511.2	WFC3/F125W	955.9	0.698 ± 0.096	25.535 ± 0.149
2010 Dec. 28.0*	55557.4	ACS/F814W	3817.0	−0.063 ± 0.041	...
2010 Dec. 30.7*	55560.7	WFC3/F160W	1705.9	1.22 ± 0.079	24.290 ± 0.070
2010 Dec. 30.8*	55560.8	WFC3/F125W	955.9	1.403 ± 0.102	24.776 ± 0.079
2011 Jan. 12.6	55573.6	WFC3/F160W	3617.6	0.901 ± 0.063	24.616 ± 0.076
2011 Jan. 12.8	55573.8	WFC3/F125W	3617.6	0.759 ± 0.062	25.443 ± 0.089
2011 Jan. 13.6	55574.6	ACS/F850LP	1994.0	−0.018 ± 0.035	...
2011 Jan. 23.4	55584.3	WFC3/F160W	3667.6	0.780 ± 0.061	24.774 ± 0.085
2011 Jan. 23.4	55584.4	WFC3/F125W	3867.6	0.535 ± 0.059	25.823 ± 0.118
2011 Feb. 04.2	55596.1	WFC3/F160W	3767.6	0.441 ± 0.061	25.392 ± 0.150
2011 Feb. 04.2	55596.1	WFC3/F125W	3717.6	0.437 ± 0.062	26.043 ± 0.154
2011 Feb. 16.1	55608.1	WFC3/F160W	4973.5	0.309 ± 0.058	25.779 ± 0.205
2011 Feb. 16.3	55608.2	WFC3/F125W	4973.5	0.183 ± 0.057	26.989 ± 0.337
2011 Jan. 12.7	55573.7	G141	39088.0	(grism obs)	...

*Discovery epoch.

in Figure 2.1, using a late-time (2011 December), SN-free template for the difference imaging. The J2000 SN coordinates are $\alpha = 02^{\rm h}17^{\rm m}46^{\rm s}$, $\delta = -05°15'23''$. It was $\sim 0''.1$ from the center of its host galaxy ($\sim$ 2 ACS pixels, $\sim$ 0.9 kpc in distance), making it highly probable that this galaxy was the host and unlikely that the object was an active galactic nucleus.

At the time of discovery, we determined the photometric redshift of the host galaxy to be > 1.5, although this was measured before SN-free WFC3 host-galaxy images were available. At this redshift, the SN colors (F160W $-$ F814W 3σ upper limit, and F125W $-$ F160W) were consistent with those expected for a SN Ia at $z > 1.5$ and inconsistent with a core-collapse (CC) SN, so we triggered follow-up observations with the X-shooter spectrograph on the ESO Very Large Telescope (VLT) to obtain a spectroscopic redshift of the host.[1]

Moreover, we monitored the SN with the *HST* SN Multi-Cycle Treasury follow-up program (GO-12099; PI: Riess). We imaged the SN with *HST* (20 orbits, to obtain the light curve as well as SN-free template observations) and we obtained G141 grism spectroscopy (15 orbits, for resolution $R \approx 130$).

To measure the photometry of the SN, we subtracted the late-time template images from the UDS/SN follow-up observations. We measured the flux within a fixed aperture of 3-pixel radius and estimated errors in the flux from the sky noise of the nearby background-subtracted image. Details of the *HST* observations are listed in

[1]Based on observations made with ESO telescopes at the La Silla Paranal Observatory under program IDs 086.A-0660 and 089.A-0739.

Table 2.1, and the grism spectrum is discussed along with the SN classification in §2.4.2.

2.3.1 Redshift

We remeasured the spectral energy distribution (SED) of the SN UDS10Wil host galaxy, including photometry from late-time WFC3 and ACS templates as well as Subaru, UKIRT, and IRAC data. The Balmer break is between the Subaru z band and the WFC3 J band, making the most likely redshift between 1.8 and 2.2 (see the lower-left panel of Fig. 2.3). Using the X-shooter spectrum, we narrowed this result by identifying [O 2] and [O 3] doublets in the host-galaxy spectrum, giving a precise redshift of 1.914.

The result is also consistent with the *HST* G141 grism spectrum, which contains a clear detection of [O 3] $\lambda\lambda$4959, 5007. However, the grism spectrum cannot resolve the doublet, as the spectrum is convolved with both the shape of the host galaxy and the point-spread function (PSF; combined full width at half-maximum intensity ~ 116 Å) and sampled at a resolution of only 46.5 Å pixel^{-1}. The VLT spectrum, along with an analysis of the late-type host galaxy of SN UDS10Wil, will be presented by Frederiksen et al. (in preparation).

2.4 Classification

We classified SN UDS10Wil by analyzing its light curve and spectrum, informed by the host redshift. As detailed below, we first examined the light curve, finding that it is consistent only with a SN Ia. In particular, the combination of its early-time colors with its rapid late-time decline rate does not agree with CC SN models. We then used the spectrum to independently rule out SNe II. While the spectral absorption features alone are unable to convincingly distinguish between a SN Ia and a SN Ib/c, SNe II have features that are inconsistent with the data (see Filippenko, 1997 for a review of SN spectra).

2.4.1 Photometric Classification

To classify SN UDS10Wil we compared the observed UDS10Wil light curve against Monte Carlo simulations of Type Ia and CC SNe at redshift 1.91, generated with the SuperNova ANAlysis software (SNANA[2]; Kessler et al., 2009a). We used a least-squares fit to scale the magnitude of the simulated light curves to match our data, thus allowing us to examine how our data compare to the shapes and colors of simulated SNe while removing any assumptions on cosmology or intrinsic SN luminosity. We then measured the χ^2 statistic for each simulated SN compared to our data and converted these χ^2 values into a Type Ia SN classification probability using a simple Bayesian framework, similar to Poznanski et al. (2007), Kuznetsova & Connolly

[2] `http://sdssdp62.fnal.gov/sdsssn/SNANA-PUBLIC/`.

(2007), and Sako et al. (2011). The full Bayesian formalism, along with a description of the simulations and our Bayesian priors, is presented in the Appendix.

Our procedure gives us a very high probability that SN UDS10Wil is a SN Ia. As such, varying our priors on parameters such as shape, color, A_V, R_V, or SN rates has a very minor effect on the outcome. The reliance on only 43 CC SN templates constitutes the greatest uncertainty in our procedure. However, using a classification procedure very similar to ours, Sako et al. (2011) found that classification using only 8 CC SN templates still returns SN Ia classification purities of $\gtrsim 90\%$.

We find that the probability of a SN Ia was 99.98%, with a SN Ib/c probability of 2.1×10^{-4} (ruled out at $\sim 3.7\sigma$) and a SN II probability of 1.0×10^{-7} (ruled out at $\sim 5.3\sigma$). This indicates that the Type Ia model dominates the probability calculation, and no CC SN models can adequately describe the observed photometric data.

Figure 2.2 shows the best-fit light curves, along with the flux range of simulated SN light curves encompassing 95% of the Bayesian evidence for each SN type. The best-fit light curves for Types Ia, Ib/c, and II SNe return χ^2/ν values of 18.6/11, 35.5/11, and 51.1/11, respectively. Note that these χ^2 values are only illustrative of the quality of the match for each model. They represent the best match from a large but limited number of random simulations, so one cannot use these values in χ^2 goodness-of-fit tests for model rejection. By contrast, the final classification probability relies on the weight of evidence from all realizations of each model.

Our best-fit x_1 and C values for the Type Ia model were -1.56 and -0.12, re-

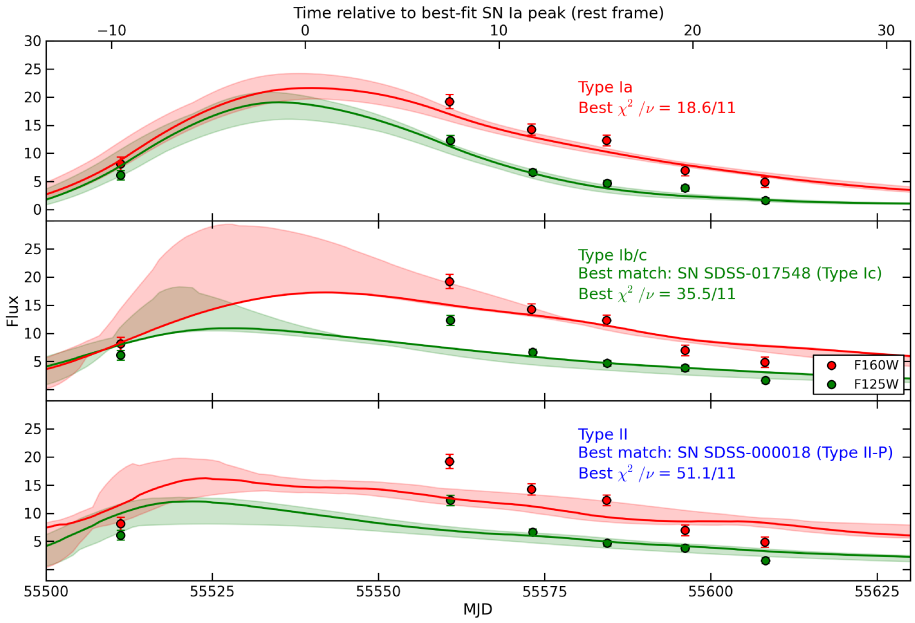

Figure 2.2: The best-fit light curves using SNANA-simulated Type Ia, Type Ib/c, and Type II SNe (top to bottom). Red and green colors indicate photometry and simulations for the F160W and F125W filters (approximately rest-frame B and V), respectively. Shaded regions include the range of SN fits that encompass 95% of the Bayesian evidence for a given SN type. Type Ib/c and Type II fits have higher χ^2 values (even including model uncertainties), due to their inability to match the combination of the colors nearest to maximum light and the rapid rate of decline. The sum of the evidence for a SN Ia model gives a nearly 100% probability that the SN is of Type Ia. We included F814W and F850LP data in the χ^2 fitting, but have omitted them in this figure for visual clarity. The fluxes shown are transformed from Vega magnitudes using a zeropoint of 27.5.

spectively. These values are fully consistent with the SALT2 parameters derived from light-curve fitting in §2.5.2 ($x_1 = -1.50 \pm 0.51$ and $C = -0.07 \pm 0.11$). We note that if we increase the errors such that the SN Ia $\chi^2/\nu \approx 1$ (accounting for the possibility that we underestimated the uncertainties), the Type Ia probability is still as high as 99.84%. Figure 2.2 shows that the nearly 100% probability of classification as a SN Ia (and the superior best-fit χ^2 value) arises because the SN Ib/c and SN II light-curve fits are unable to match the combination of SN UDS10Wil's high signal-to-noise ratio (S/N) discovery-epoch colors and its rapid light-curve decline rate.

As a verification of this light-curve classification, we used the Photometric SuperNova IDentification software (PSNID; Sako et al., 2008), finding that it also prefers a SN Ia with a slightly higher 4.1σ confidence. The difference in probability is primarily due to our conservative CC model uncertainties (see the Appendix), which reduce the χ^2 values of CC SNe. Although it only uses 8 CC SNe, the purity of PSNID classifications has been robustly tested using Sloan Digital Sky Survey (SDSS) SNe, and it obtained the highest figure of merit in the SN Photometric Classification Challenge (Kessler et al., 2010).

2.4.2 Spectrum

Spectroscopic confirmation of SNe has proven challenging at these redshifts (see the discussions in Rodney et al., 2012 and Rubin et al., 2012), due to the difficulty of obtaining high S/N observations and the paucity of defining features in the available

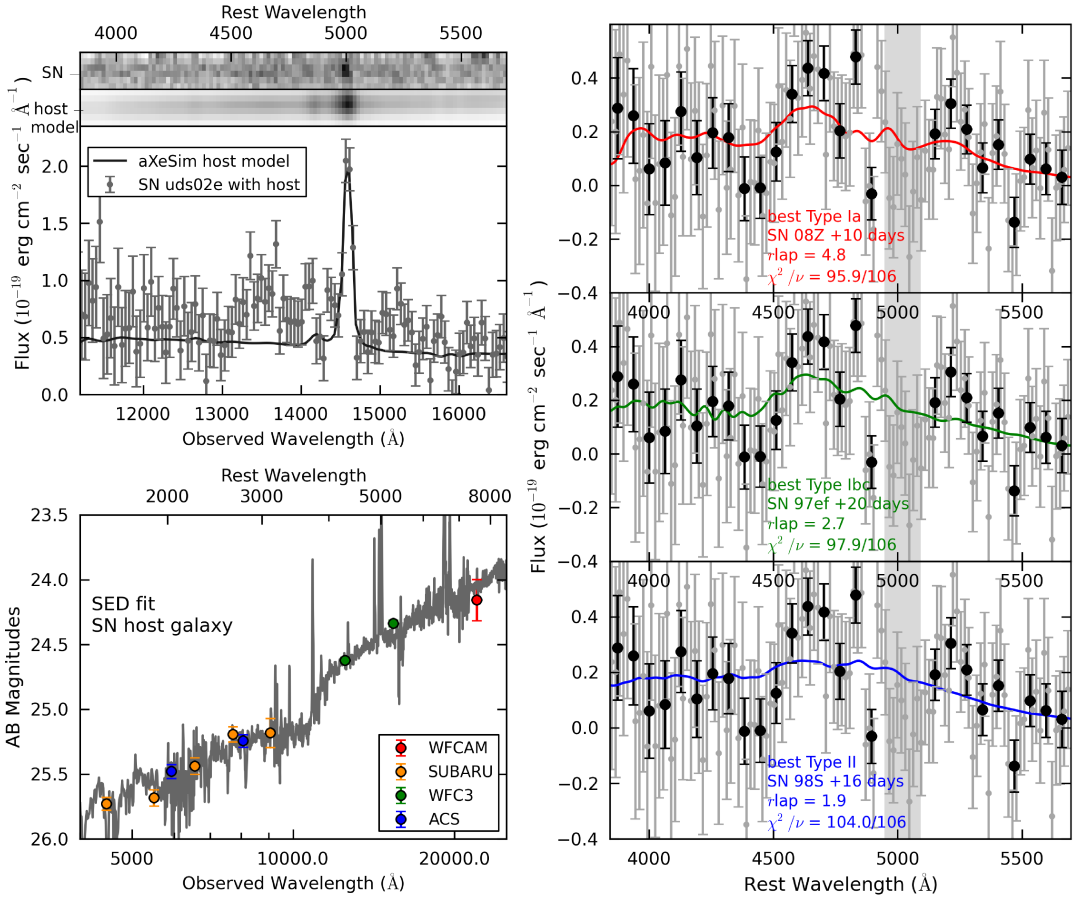

Figure 2.3: The spectrum of SN UDS10Wil, from which the host-galaxy light has been subtracted using a spectrum fit to the host's SED. The host SED and its best-fit spectral template is shown at the bottom left. The two-dimensional and one-dimensional grism spectrum along with the simulated host-galaxy spectrum (the SED convolved with the shape of the host using aXeSim) are given at the upper left. On the right we show the best-fit SN templates from SNID for Types Ia, Ib/c, and II. We illustrate median bins to visually emphasize the spectral features, but have used the unbinned data for our analysis. Although the spectrum can be fit reasonably well by both a SN Ia or a SN Ib/c, a SN II does not contain the spectral features seen at ~ 4600 and ~ 5200 Å in the rest frame. Data in the [O 3] subtraction region (the shaded region) were not used in the fit.

window (for UDS10Wil, $\sim$ 1.12–1.65 μm; rest frame $\sim$ 3840–5660 Å). In the case of SN UDS10Wil, the SN was separated from its host galaxy by only $\sim 0''.1$, contaminating the SN spectrum with host-galaxy light. We removed the host galaxy from the spectrum by subtracting a section of the galaxy free from SN light, but the combined noise from the SN and host-galaxy spectra made a spectral classification inconclusive, even with substantial host-galaxy smoothing.

As an alternative approach that avoids adding additional host-galaxy noise to the SN spectrum, we generated a synthetic host spectrum that was not subject to observational noise. We fit SEDs, using a library of spectral templates, to optical and near-IR Subaru, ACS, WFC3, and UKIRT host-galaxy photometry following Dahlen et al. (2010). We then simulated the observed grism host spectrum with the aXeSim software package.[3] The aXeSim software convolves the SED with the shape of the host galaxy and *HST* PSF and samples the spectrum at the G141 spectral resolution of 46.5 Å pixel^{-1}.

One would not necessarily expect emission lines to be the same strength in the template as in the real galaxy due to its differing metallicity, star formation rate, and population of massive stars. Therefore, we replaced the pixels covering the [O 3] line in our simulated host galaxy with those covering the prominent [O 3] line from the grism spectrum. We omitted these pixels (the shaded region in Fig. 2.3) when we later fit spectral templates to the SN spectrum, as we did not have a SN-free

[3] `http://axe.stsci.edu/axesim/.`

line measurement to subtract from the observations. We then rescaled the aXeSim output spectrum to match the F160W magnitude of the host galaxy as measured in the last epoch of follow-up imaging after the SN had faded. Our simulated host-galaxy spectrum is shown in Figure 2.3 (upper left).

After subtracting the host-galaxy model from the SN spectrum contaminated with host light, we used the Supernova Identification (SNID) code[4] from Blondin & Tonry (2007) to match the UDS10Wil spectrum with Type Ia, Type Ib/c, and Type II SN template spectra to determine the best-fit spectrum for each class. For SN Ia fits, we only used templates within ± 3 rest-frame days of the age of the SN UDS10Wil spectrum. The age is based on the SALT2 fit in §4.2, which gives $\sim 12 \pm 1$ day after maximum (rest frame). For CC SN fits, we used any templates which put the time of maximum between the first two epochs of observation (the same as our prior in §3.1). When fitting the spectrum to templates, SNID removes the continuum using a high-order polynomial fit and only matches the spectral features, making the fit independent of reddening and brightness.

SNID returns the $r$lap parameter, which is meant to quantify the quality of the correlation (see Blondin & Tonry, 2007 for details). Blondin & Tonry (2007) suggest that $r$lap values less than 5 are inconclusive. Note that SNID does not apply a broadening symmetric function (Tonry & Davis, 1979), which should be used when the widths of SN features are comparable to the resolution of the spectrum. As the

[4] `http://www.oamp.fr/people/blondin/software/snid/index.html`.

rest-frame G141 resolution is ~ 16 Å pixel^{-1} and significant SN features have a typical width ~ 50 Å, this is not a major concern. However, the inclusion of this function for grism data could improve future SNID classifications, especially those at lower redshift.

The right side of Figure 2.3 shows the best-fit Type Ia, Ib/c, and II SN templates with $r$lap values of 4.8, 2.7, and 1.9, respectively. We show median bins to emphasize the spectral features, but we fit spectra to the unbinned data. The data can be fit by 6 other normal SNe Ia with $r$lap values of at least 4. Five other SN Ib/c fits have an $r$lap of at least 2, and only two other SN II fits have an $r$lap of greater than 1.5.

The χ^2 values for the fits, now including continuum, to Type Ia, Ib/c, and II SNe are 95.9, 97.9, and 104.0 (respectively) with 106 degrees of freedom. We note that both SNe Ia and SNe Ib/c can provide good fits, although the former give a slightly better match. However, all SN II templates yield a poor correlation; the rest-frame features at ~ 4600 and ~ 5200 Å (which are created by neighboring Fe 2, Fe 3, Si 2, and S 2 absorption in SNe Ia; Filippenko, 1997) are not well fit by the spectra of SNe II. We note that although not all of the SNID SNe II are as featureless as the best-fit spectrum shown in Figure 2.3, they all have difficulty matching the strength or location of the spectral features. Even Type II-P templates, which typically have stronger features, have a maximum $r$lap of only 1.4.

Because the best $r$lap value is less than 5, this SN cannot be considered to be spectroscopically confirmed. In addition, the "lap" parameter, which describes the

overlap in wavelength space between the template and SN spectrum, is 0.39 for each of the best-fit SN Ia and CC SN templates. This is below the minimum lap of 0.4 used by Blondin & Tonry (2007) for spectral confirmation. However, the SN UDS10Wil spectrum still favors classification as a SN Ia and its $r$lap is comparable to that of other high-redshift SNe Ia. SN Primo (Rodney et al., 2012; $z = 1.55$) had an $r$lap of only 3.7. We also fit the spectrum of SN SCP-0401 (Rubin et al., 2012; $z = 1.71$), finding that it is best matched by featureless SNID Type Ia and Type Ib/c spectra. However, if we require a match to at least one spectral feature or a lap value greater than 0.1, the maximum SN Ia $r$lap is 4.6 (SN 1993ac, +7 days; lap of 0.2). SNID templates begin at $\lambda_{\rm rest} = 2500\,\text{Å}$, so the first $\sim 500\,\text{Å}$ of the SN SCP-0401 spectrum were not included in the SNID fit.

2.5 Analysis

Taken together, the photometric evidence suggests that UDS10Wil is a SN Ia with high confidence. The spectroscopic evidence independently favors a Type Ia classification. We now proceed to derive its shape and color-corrected magnitude, taking into account the possibility that the SN light has been gravitationally lensed by foreground structure.

2.5.1 Lensing

Our ability to use SNe Ia as accurate distance indicators to constrain cosmological parameters requires us to determine the impact of foreground-matter inhomogeneities on the flux of the SN (e.g., Jönsson et al., 2006). Even without multiple images, gravitational lensing can significantly magnify the SN, altering our measurement of its distance. SN UDS10Wil is close in projection to another galaxy (see Fig. 2.1) separated by only $1''.54$. Therefore, it is necessary to estimate the possible magnification of the SN which could lead to a bias in the derived SN Ia distance. All other foreground sources are greater than $4''.5$ away and cause negligible magnification.

We fit the SED of the lens galaxy as described by Wiklind et al. (2008) to characterize its physical properties. We used a Chabrier initial mass function (IMF; Chabrier, 2003) rather than the Salpeter IMF cited by Wiklind et al. (2008); the former gives a slightly smaller stellar mass but is a more accepted model. To account for photometric uncertainties, we drew Monte Carlo samples for the measured photometry of the galaxy and used the best-fitting SED models to characterize the SED. The SED fit indicates a low-mass galaxy with a photometric redshift 0.283 ± 0.080 and a stellar mass $\log(M_*/M_\odot) = 7.968 \pm 0.222$. We used these parameters to create a plausible mass model of the galaxy and estimate the magnification of the SN.

We modeled the stellar component of the galaxy as an exponential disk using parameters measured from GALFIT (Peng et al., 2002) and the dark-matter halo using a Navarro-Frenk-White (NFW) profile (Navarro et al., 1997). We used the

broken power law given by Yang et al. (2012) to relate the stellar mass M_* to the halo mass and the mass-concentration relation given by Macciò et al. (2008) when modeling the halo.

Both the mass-concentration and stellar-to-halo mass relations have significant scatter around the median relations. To account for this scatter, we took 10,000 Monte Carlo realizations of lensing potentials to calculate the expected magnification distribution. We also drew a photo-z and stellar mass distribution from the Monte Carlo realizations of our SED fits.

Despite the proximity of the galaxy, its low mass makes magnification a minor effect. The median magnification from the above analysis is $2.8^{+2.3}_{-1.2}\%$, where the lower and upper uncertainties represent the 16^{th} and 84^{th} percentiles ($\pm 1\sigma$), respectively. These models do assume a spherical NFW profile, but adding ellipticity to the halo does not significantly change our results. This analysis shows that the systematic offset due to lensing is much smaller than the photometric uncertainties; we applied the lensing correction to our derived magnitude, but it does not have a significant effect on our distance modulus.

2.5.2 Light-curve Fit

We fit the light curve using the SALT2 implementation (Guy et al., 2010) contained in SNANA (Fig. 5.7). Note that although the ACS data provide a valuable color constraint for classification purposes, we have omitted them from our cosmolog-

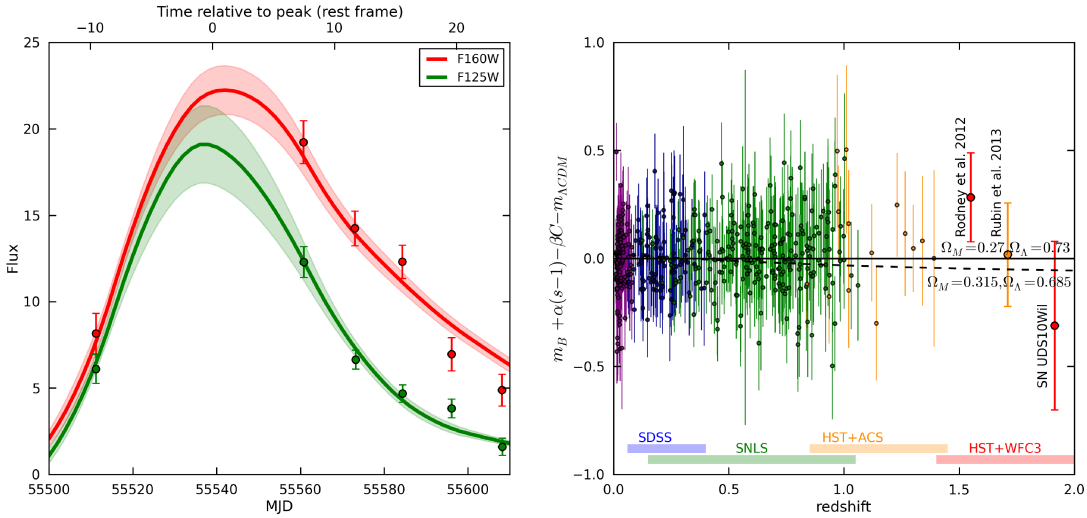

Figure 2.4: On the left, the SALT2 light-curve fit to SN UDS10Wil. SALT2 gives a normal set of light-curve parameters along with a corrected magnitude of 26.15 ± 0.39 (consistent with ΛCDM) and a reduced χ^2 of 1.5. On the right, we place SN UDS10Wil on the Hubble residual diagram using cosmological parameters from Sullivan et al. (2011) and $H_0 = 71.6\,\mathrm{km\,s^{-1}\,Mpc^{-1}}$. For comparison, we also show the compilation of $\sim$ 500 SNe from Conley et al. (2011). Lastly, using Sullivan et al. (2011) values for α and β, we include the other two SNe Ia with spectroscopic evidence for classification discovered at a redshift greater than 1.5 (Rodney et al., 2012; Rubin et al., 2012). The dotted line indicates the difference in $m_{\Lambda CDM}$ when using the recent cosmological parameters from the Planck collaboration ($\Omega_\Lambda = 0.685$, $\Omega_M = 0.315$; Planck Collaboration et al., 2013).

ical analysis. At $z = 1.914$, the ACS bands sample rest-frame wavelengths of 2400–3300 Å, where SNe Ia are more heterogeneous (Ellis et al., 2008) and may evolve with redshift (Foley et al., 2012). Furthermore, the rest-frame UV has been problematic for SN Ia light-curve fitters (Kessler et al., 2009b). Given these concerns, we discarded the ACS data for our light-curve fitting in order to avoid introducing a bias in the derived distance. The ACS observations provided only a single measurement with positive flux (F814W at MJD = 55801.1), so this does not exclude a large fraction of useful data.

The light-curve parameters for SN UDS10Wil are typical of SNe Ia; we derive values of $x_1 = -1.50 \pm 0.51$ and $C = -0.071 \pm 0.11$, which are consistent with the parameters described by Kessler et al. (2009b) ($\bar{C} = 0.04$, $\sigma_C = 0.13$, $\bar{x}_1 = -0.13$, $\sigma_{x_1} = 1.24$). SNANA also gives a peak magnitude $m_B^* = 26.20 \pm 0.11$. We then converted our SALT2 values into SiFTO values (Conley et al., 2008), using the relations of Guy et al. (2010), in order to use the shape and color constants from SNLS ($\alpha = 1.367$, $\beta = 3.179$; Sullivan et al., 2011). We derived a light-curve shape and color-corrected magnitude ($m_{\rm corr}$) using

$$m_{\rm corr} = m_B^* + \alpha \times (s - 1) - \beta \times C, \tag{2.1}$$

where $m_{\rm corr}$ is equal to the distance modulus plus the SN absolute magnitude, M. Here m_B^* is the peak SN magnitude, s is the SiFTO stretch parameter, and C describes the color; also, m_B^* includes the lensing correction of $0.030^{+0.024}_{-0.013}$ mag.

This analysis gives a corrected magnitude of 26.15 ± 0.39. We compare to the corrected magnitude for ΛCDM, $m_{\Lambda CDM}$, by using the cosmological parameters from Sullivan et al. (2011) ($\Omega_\Lambda = 0.73$, $\Omega_M = 0.27$, $w = -1$, $\mathrm{H}_0 = 71.6\,\mathrm{km\,s^{-1}\,Mpc^{-1}}$) and a least-squares fit to the Conley et al. (2011) SNe. We added an offset of 0.27 mag to the value of m_B for the Conley et al. (2011) SNe in order to match the normalization of the SALT2 fitter contained in SNANA, finding $m_{\Lambda CDM} = 26.46$ mag (including the offset, this gives an absolute SN magnitude $M = -19.39$). SN UDS10Wil is less than 1σ from ΛCDM.

We also fit the light curve with MLCS (Jha, Riess, & Kirshner, 2007), after using SDSS SNe to determine, and correct for, the $m_{\rm corr}$ offset between MLCS and SALT2 fits. MLCS gives the same corrected magnitude with a somewhat smaller uncertainty, $m_{\rm corr} = 26.15 \pm 0.27$ mag (with $\Delta = 0.30 \pm 0.18$ and $A_V = 0.01 \pm 0.05\,\mathrm{mag}$). This value is slightly brighter than expected from ΛCDM, but consistent at 1.15σ. We verified that the MLCS and SALT2 parameters are consistent with each other using relations from Kessler et al. (2009b).

2.6 Discussion

The observations of SN UDS10Wil presented here demonstrate that the *HST* WFC3 now allows the cosmological study of SNe Ia at higher redshifts than ever before. The analysis presented above is enabled by the photometric classification

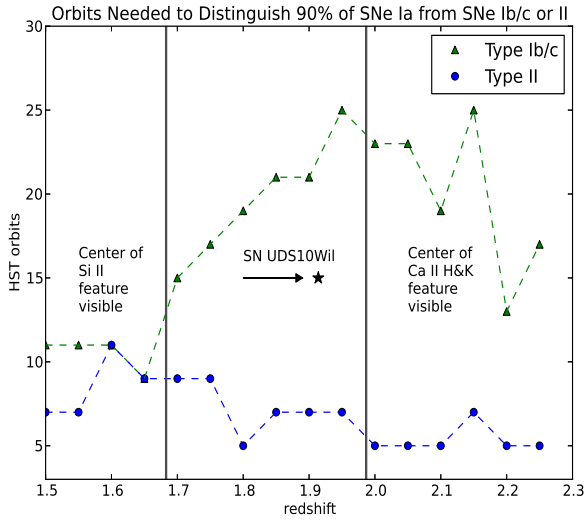

Figure 2.5: The number of HST orbits necessary to rule out the possibility of a SN II or SN Ib/c 90% of the time when observing a SN Ia. Using aXeSim, we simulated a variety of exposure times in the redshift range 1.5–2.3. We found that ∼5–10 orbits can rule out a SN II, but that the number of orbits required to rule out a SN Ib/c possibility is significantly greater. The number of orbits to rule out a SN Ib/c is much lower in the region where Si 2 and Ca 2 H&K are completely visible. These results indicate the need for photometric evidence in SN Ia classification at high redshift, although the *HST* grism can also be valuable in determining SN redshifts.

methods we employ. However, SN science, especially cosmology, has in the past relied heavily on spectroscopic evidence for classification.

At $z > 1.5$, deriving a spectral classification with *HST* requires a large number of orbits to obtain a high S/N. In addition, the *HST* IR grisms cover a relatively small rest-frame wavelength range. In the case of SN UDS10Wil, the G141 grism wavelength range ($\sim$ 1.12–1.65 μm; rest frame $\sim$ 3840–5660 Å) does not include either the Si 2 absorption at $\sim$ 6150 Å or the Ca 2 H&K trough at $\sim$ 3750 Å, which are some of the deepest SN Ia features (the features have equivalent widths $\sim$ 100 Å). This means that spectral classifications of high-redshift SNe using SNID will have lower-significance correlations with SN Ia template spectra, and thus often yield $r$lap values much less than the suggested minimum of 5 (Blondin & Tonry, 2007).

Host-galaxy contamination can be a significant source of noise in high-z SN grism spectra. In this work we have used aXeSim to remove host-galaxy light from the SN+host spectrum. However, even in a situation where a SN is well separated from its host galaxy, spectral evidence alone may not be enough to unequivocally classify the SN as Type Ia. Figure 2.5 shows the number of *HST* orbits with the G141 IR grism that are needed for SNID to correctly distinguish a SN Ia from a SN Ib/c or a SN II 90% of the time, in the redshift range 1.5–2.3. For this figure, we used aXeSim to simulate 100 SN Ia observations per unit redshift with 2.6 ks per orbit, from 0 to 100 orbits (2-orbit intervals). The background flux was set to 95 $e^- s^{-1}$, and the simulated SN magnitude was fixed at the peak magnitude of SN Primo (an F160W

Vega magnitude of 23.98; Primo was observed closer to maximum than UDS10Wil). Each simulated grism spectrum was then processed with SNID, and the classification was deemed correct if the best $r$lap for a SN Ia template was larger than the best SN Ib/c or SN II $r$lap (we allow $r\mathrm{lap} < 5$).

Figure 2.5 shows that, similar to the case of SN UDS10Wil, ruling out a SN II possibility requires only ∼5–10 orbits ($1.5 < z < 2.3$). For a large program like CANDELS, with 200 follow-up orbits and a desired sample of ∼10 SNe, this is a feasible number. Ruling out a SN Ib/c, however, can require up to 25 orbits, becoming most costly at those redshifts where Si 2 and Ca 2 H&K are not completely visible. At very high redshift, such as $z \approx 2.2$–2.3, Figure 2.5 shows that the G141 exposure time required to distinguish a SN Ia from a SN Ib/c begins to drop. The value of spectroscopic confirmation for such high-redshift SNe may warrant the necessary investment of orbits, especially if additional high-value targets can be simultaneously observed within the grism field of view. We note that simulating CC SN observations shows that SNID can occasionally misclassify CC SNe as SNe Ia, an effect we have not taken into account in this analysis.

The G102 grism can also be useful for picking out features such as Si 2 and Ca 2 H&K in the redshift ranges where the G141 grism does not contain them. Unfortunately, the consequence of its more limited wavelength range (~ 0.8–$1.15\,\mu$m; rest frame ~ 2750–3950 Å at $z = 1.91$) is that a SN Ib/c template is more likely to match a SN Ia G102 spectrum well.

HST grism spectroscopy can be good at determining SN redshifts or host-galaxy properties. However, for reliable SN classification, photometric evidence is often important. In the case of SN UDS10Wil we improved upon the photometric methods of Rodney et al. (2012) by introducing a quantitative Bayesian method that returns probabilities for each SN type. With both photometric and spectroscopic methods, we can be confident in our classification and subsequent analysis.

2.7 Conclusions

At a redshift of 1.914, SN UDS10Wil is the most distant SN Ia yet known. Classification of this SN rests on photometry and grism spectroscopy, which rules out the possibility of a CC SN. The spectral evidence alone disfavors the possibility of a SN II, while supporting a SN Ia or SN Ib/c hypothesis. The combined SN colors and rapid decline rate are inconsistent with a CC SN and in good agreement with a SN Ia model.

We find that SN UDS10Wil is not significantly lensed, and its light-curve fit (with SALT2) is consistent with ΛCDM. An alternative fit with MLCS (Jha et al., 2007) is slightly brighter than ΛCDM, but consistent at 1.15σ.

When the full analysis of the CANDELS SNe is complete and combined with the data from the Cluster Lensing and Supernova survey with Hubble (PI: Postman; Postman et al., 2012), we expect that SN UDS10Wil will be one of a sample of

$\sim$ 10 SNe Ia above a redshift of 1.5 to be found by these programs. This SN is an example of an object in a new area of SN cosmology, one which has only begun to be explored in the last few years with the advent of WFC3 on *HST* and one with unique classification challenges. However, with the full sample of SNe at redshift greater than 1.5, new limits on the evolution of dark energy, the DTD, and the evolution of the SN Ia population will become possible.

2.8 Appendix: Photometric Classification Method

We began our classification procedure by using SNANA (Kessler et al., 2009a) to generate a Monte Carlo simulation of 30,000 SNe at redshift 1.91. 10,000 simulated SNe Ia were based on the SALT2 model (Guy et al., 2010), with values of the shape parameter x_1 drawn uniformly in the range -3 to 3 and the color parameter C from -0.4 to 0.6. These ranges cover the observed distribution of SALT2 parameter values (Kessler et al., 2009b), and the C term accounts for both intrinsic SN color and host-galaxy extinction (Guy et al., 2007). The remaining 20,000 simulated SNe were split evenly between the two principal CC SN classes, with light curves based on 16 Type Ib/c and 27 Type II SN templates that comprise the SNANA non-SN Ia library (including subtypes Ib, Ic, II-P, IIn, and II-L). Host-galaxy reddening was applied to each simulated CC SN using $R_V = 3.1$, with a random draw of A_V in the range 0

to 7 mag using the Cardelli et al. (1989) reddening law. For both the SN Ia and the CC SN simulations we chose random values for the date of the light-curve peak, using a range spanning the first to the second epoch of UDS10Wil observations.

To compare each of the 30,000 synthetic light curves to the $N = 15$ photometric observations of SN UDS10Wil, we computed the χ^2 statistic given by

$$\chi^2 = \sum_{i=1}^{N} \frac{(F_{\mathrm{obs},i} - A \times F_{\mathrm{sim},i})^2}{\sigma_{\mathrm{obs},i}^2 + \sigma_{\mathrm{sim},i}^2}, \tag{2.2}$$

where $F_{\mathrm{obs},i}$ and $\sigma_{\mathrm{obs},i}$ are the fluxes and uncertainties for each observation. Here $F_{\mathrm{sim},i}$ and $\sigma_{\mathrm{sim},i}$ are the fluxes and uncertainties (respectively) for a single simulated SN on each observation date. The variable A is a scaling parameter, described below. For SNe Ia, most of their intrinsic variability can be described by the SALT2 model's shape and color parameters. Additional variability causes scatter about the Hubble diagram, and is given by Guy et al. (2010) as 8.7% in distance modulus. We treat this variability as approximately equal to the model uncertainty, which in flux space translates to $\sigma_{\mathrm{simIa},i} = 0.08A \times F_{\mathrm{sim},i}$.

CC SNe have greater heterogeneity, such that our relatively small set of discrete templates cannot describe the entire population. By setting a nonzero $\sigma_{\mathrm{simCC},i}$, our limited CC SN template library can more accurately represent this diverse class. Considering a similar problem, Rodney & Tonry (2009) estimated $\sigma_{\mathrm{simCC},i}$ by measuring the flux difference between all possible pairwise comparisons of templates of the same subclass and taking the median. We classify SN UDS10Wil using more templates

than Rodney & Tonry (2009), such that the CC SN population is better sampled and less uncertainty is present. However, we adopt their value of $\sigma_{\mathrm{simCC},i} = 0.15A \times F_{\mathrm{sim},i}$ as a conservative estimate.

We next chose the optimal distance or absolute magnitude of every simulated SN, therefore removing the assumptions on cosmology and SN luminosity functions that are built into the SNANA simulations. Here we have multiplied $F_{\mathrm{sim},i}$ by A, a free parameter that introduces a coherent flux scaling across all bands. We find a separate value for A with each of the 30,000 comparisons, using χ^2 minimization to match the simulated magnitudes to the data with the equation

$$A = \frac{\sum_{i=1}^{N} F_{\mathrm{sim},i} F_{\mathrm{obs},i} / \sigma^2_{\mathrm{obs},i}}{\sum_{i=1}^{N} F^2_{\mathrm{sim},i} / \sigma^2_{\mathrm{obs},i}}. \tag{2.3}$$

We then converted the measured χ^2 values into a Type Ia SN classification probability using a simple Bayesian framework, similar to Poznanski et al. (2007), Kuznetsova & Connolly (2007), and Sako et al. (2011). The *likelihood* that the data (D) match a simulated SN of type T_j with parameters $\boldsymbol{\theta}$ (shape x_1, color C for SN Ia or A_V for CC SN types, and time of maximum light) is given by

$$p(D|\boldsymbol{\theta}, T_j) = \frac{e^{-\chi^2/2}}{\prod_{i=1}^{N} \sqrt{2\pi(\sigma^2_{\mathrm{obs},i} + \sigma^2_{\mathrm{sim},i})}}, \tag{2.4}$$

where χ^2 is given in Equation 1. Multiplying by prior probability distributions for each of the model parameters then gives us the *posterior probability* for each point

in parameter space, $p(\boldsymbol{\theta}|T_j)p(D|\boldsymbol{\theta}, T_j)$. As we are interested in model selection, not parameter estimation, we can marginalize over all of the nuisance parameters $\boldsymbol{\theta}$. Approximating the marginalization integral with a discrete sum, the probability of SN type T_j given the model is

$$p(D|T_j) = \sum_{i=1}^{N_{\rm sim}(T_j)} p(\boldsymbol{\theta}|T_j)p(D|\boldsymbol{\theta}, T_j)\delta\boldsymbol{\theta}. \tag{2.5}$$

For SN Ia parameters x_1 and C, we applied Gaussian priors based on the values given by Kessler et al. (2009b) ($\bar{C} = 0.04$, $\sigma_C = 0.13$, $\bar{x}_1 = -0.13$, $\sigma_{x_1} = 1.24$). For the CC SNe parameter A_V, we used the Monte Carlo recipe provided by Riello & Patat (2005) and implemented by Dahlen et al. (2012) for a random galaxy orientation. The distribution is peaked at $A_V = 0$ mag and falls off quickly such that $A_V \gtrsim 3$ mag is very unlikely. We used a flat prior for the time of peak brightness.

Note that for computational efficiency we have used SNANA to sample the multi-dimensional model parameter space using a Monte Carlo simulation with uniform sampling distributions (instead of the more typical approach, using a grid of parameter values). Thus, we must approximate $\delta\boldsymbol{\theta}$ – the vector of step sizes along each dimension of parameter space – using the range over which each parameter is sampled:

$$\delta\boldsymbol{\theta} = \frac{1}{N_j}\prod_{k=1}^{N_\theta}\Delta\theta_k, \tag{2.6}$$

where $\Delta\theta_k$ is each range, N_j is the number of simulated SNe in the class (we used

10,000), and the product is over N_θ, the number of parameters θ for the model: 3 for SNe Ia (x_1, c, t_{pk}) and 2 for CC SNe (A_V, t_{pk}).

Lastly, we multiplied each model by a SN rate prior $P(T_j)$. This prior is the fraction of SNe at redshift 1.91 that we expect to be a given type. We began by adopting the rate measurement from Dahlen et al. (2008) for SNe Ia and the local rates from Li et al. (2011) for CC SNe. We scaled the CC SN rates according to the cosmic star-formation history of Hopkins & Beacom (2006) using the form of Cole et al. (2001) and a modified Salpeter IMF (Baldry & Glazebrook, 2003). The normalized rates showed, as an estimate, that one could expect only $\sim 2\%$ of SNe at this redshift to be of Type Ia. The SN UDS10Wil host galaxy SED (§3.2) is consistent with a starburst galaxy, so it is possible that these average rates overestimate the SN Ia rate in this galaxy. In addition, SN rates are very uncertain at this redshift, and the Dahlen et al. (2008) rates at this redshift are consistent with 0 SNe Ia; however, we note that lowering this rates prior by an order of magnitude still returns a classification probability greater than 99%. Thus the result is largely independent of the uncertainty in SN Ia rates.

Applying Bayes' theorem gives the final probability that SN UDS10Wil is of Type Ia:

$$p(Ia|D) = \frac{p(D|Ia)p(Ia)}{\sum_j p(D|T_j)p(T_j)}, \tag{2.7}$$

where the summation is over Type Ia, Ib/c, and II SN models (T_j). In the case of

SN UDS10Wil, our likelihood function is sufficiently narrow that the priors have only a minor effect. Thus, we found that allowing R_V, SALT2 parameters α and β, or parameter ranges to vary does not substantially alter the high probability that this SN is of Type Ia.

Chapter 3

Reconsidering the Effects of Local Star Formation on Type Ia Supernova Cosmology

3.1 Abstract

Recent studies found a correlation with $\sim 3\sigma$ significance between the local star formation measured by GALEX in Type Ia supernova (SN Ia) host galaxies and the distances or dispersions derived from these SNe. We search for these effects by using data from recent cosmological analyses to greatly increase the SN Ia sample; we include 179 GALEX-imaged SN Ia hosts with distances from the JLA and Pan-STARRS SN Ia cosmology samples and 157 GALEX-imaged SN Ia hosts with distances from

the Riess et al. (2011) H_0 measurement. We find little evidence that SNe Ia in locally star-forming environments are fainter after light curve correction than SNe Ia in locally passive environments. We find a difference of 0.000±0.018 (stat+sys) mag for SNe fit with SALT2 and 0.029±0.027 (stat+sys) mag for SNe fit with MLCS2k2 ($R_V = 2.5$), which suggests that proposed changes to recent measurements of H_0 and w are not significant and numerically smaller than the parameter measurement uncertainties. We measure systematic uncertainties of ∼0.01-0.02 mag by performing several plausible variants of our analysis. We find the greatly reduced significance of these distance modulus differences compared to Rigault et al. (2013) and Rigault et al. (2015) result from two improvements with fairly equal effects, our larger sample size and the use of JLA and Riess et al. (2011) sample selection criteria. Without these improvements, we recover the results of Rigault et al. (2015). We find that both populations have more similar dispersion in distance than found by Rigault et al. (2013), Rigault et al. (2015), and Kelly et al. (2015), with slightly smaller dispersion for locally passive ($\log(\Sigma_{\rm SFR}) < -2.9$ dex) SNe Ia fit with MLCS, the opposite of the effect seen by Rigault et al. (2015) and Kelly et al. (2015). We caution that measuring the local environments of SNe Ia in the future may require a higher-resolution instrument than GALEX and that SN Ia sample selection has a significant effect on local star formation biases.

3.2 Introduction

Type Ia supernovae (SNe Ia) have been a key component in measuring the dark energy equation of state, w, with $\lesssim$6% uncertainty Betoule et al. (2014) and the Hubble Constant, H_0, with 3.3% uncertainty Riess et al. (2011, hereafter R11). With such small error budgets, unknown systematic uncertainties affecting SNe Ia shape- and color-corrected absolute magnitudes could have serious consequences for our understanding of dark energy, neutrino properties, and the global geometry of space.

Although SNe Ia remain accurate distance indicators with $\sim$10% uncertainty per SN, there are concerns about their ability to remain standardizable in galaxies that vary in mass, metallicity, star formation, age, and dust properties Sullivan et al. (2010); Rigault et al. (2013); Johansson et al. (2013); Childress et al. (2013). Even a small dependence of SN Ia luminosities on host galaxy properties may have a non-negligible effect on w due to the redshift evolution of galaxies or differences in sample selection. Such an effect could also bias H_0 due to the different demographics of Cepheid host galaxies compared to SN Ia hosts. The lack of detection of such an effect at $>3\sigma$ with samples of $\sim 10^2$ SNe suggests that such effects are $\lesssim \frac{10\%}{\sqrt{100}} \times 3 \lesssim 0.06$ mag, or that they result from galaxy properties that are difficult to measure robustly. These investigations are hampered by an inability to define the nature of the SN Ia correction *a priori*, complicating the interpretation of the significance of the correlations found *a posteriori*. If enough sources for a possible correlation are examined, a 3σ result will always be found.

The first widely accepted effect of host galaxy properties on SNe Ia was confirmed by the detection of a $\sim$0.07 mag difference in mean corrected magnitude of SNe Ia with host masses $>10^{10} M_{\odot}$. Identified by several independent studies including Lampeitl et al. (2010), Sullivan et al. (2010), and Kelly et al. (2010), this effect has now been detected at $>5\sigma$ by Betoule et al. (2014) with a sample of 740 SNe Ia.

Because it is unclear how the physics of a SN Ia distances could depend on its host galaxy mass, the most likely explanation is that host galaxy mass is merely tracing another physical property that could affect SN luminosity, such as metallicity, stellar age, or dust. Domínguez et al. (2001) suggested that progenitor metallicity could affect the SN luminosity by changing the Carbon-Oxygen ratio in the progenitor white dwarf, thus resulting in a lower Nickel mass synthesized in the explosion. Hayden et al. (2013) found that a correction using a star formation-based metallicity indicator reduced Hubble diagram residuals more than a simple host mass correction. Childress et al. (2013) found that dust and stellar age are also plausible explanations because they evolve with host galaxy mass.

Different SN Ia progenitor ages could also exhibit systematic differences in corrected magnitude due to the effects of metallicity or explosion mechanism on ^{56}Ni production Maoz et al. (2014). Childress et al. (2014) suggested that progenitor age could be the source of the host mass step, as older progenitors preferentially occur in non star-forming host galaxies. Because progenitor age evolves with redshift, Childress et al. (2014) modeled a potential redshift-dependent bias in cosmological

analyses.

SN Ia light curve fitters may also create biases by assuming a universal relationship between color and absolute magnitude, independent of the dust composition of different SN Ia hosts. Some preliminary evidence has supported these ideas; Scolnic et al. (2014b) found that the correlation between SN Ia color and absolute magnitude has two different slopes for bluer and redder SNe, which may in part be due to dust properties.

If the host mass step is indicative of one or more of these biases, galaxy properties in the vicinity of SN explosions could be more strongly correlated with SN corrected magnitude than properties of the galaxies as a whole. Three recent studies used $\sim$60$-$85 nearby SNe Ia to look at such properties and found that they affect the distances derived from SNe Ia. Rigault et al. (2013) and Rigault et al. (2015) found a correlation between local star formation and SN Ia Hubble residuals from the Nearby Supernova factory Aldering et al. (2002) and the CfA SN survey (Hicken et al., 2009b, hereafter H09) by using the local star formation rate density (Σ_{SFR}) to separate SNe Ia into those with locally passive (SN Iaϵ) and locally star-forming (SN Iaα) environments. Rigault et al. (2015) (hereafter R15) found a mean difference in Hubble residuals between SNe Iaϵ and Iaα (hereafter referred to as the LSF step) of $\sim$0.09$-$0.17 mag at 2-4σ significance with different light curve fitters.

The fraction of SNe Iaϵ is different in the nearby Cepheid-calibrated SN Ia sample compared to the Hubble-flow SN Ia sample, and R15 found that SNe Iaϵ have mean

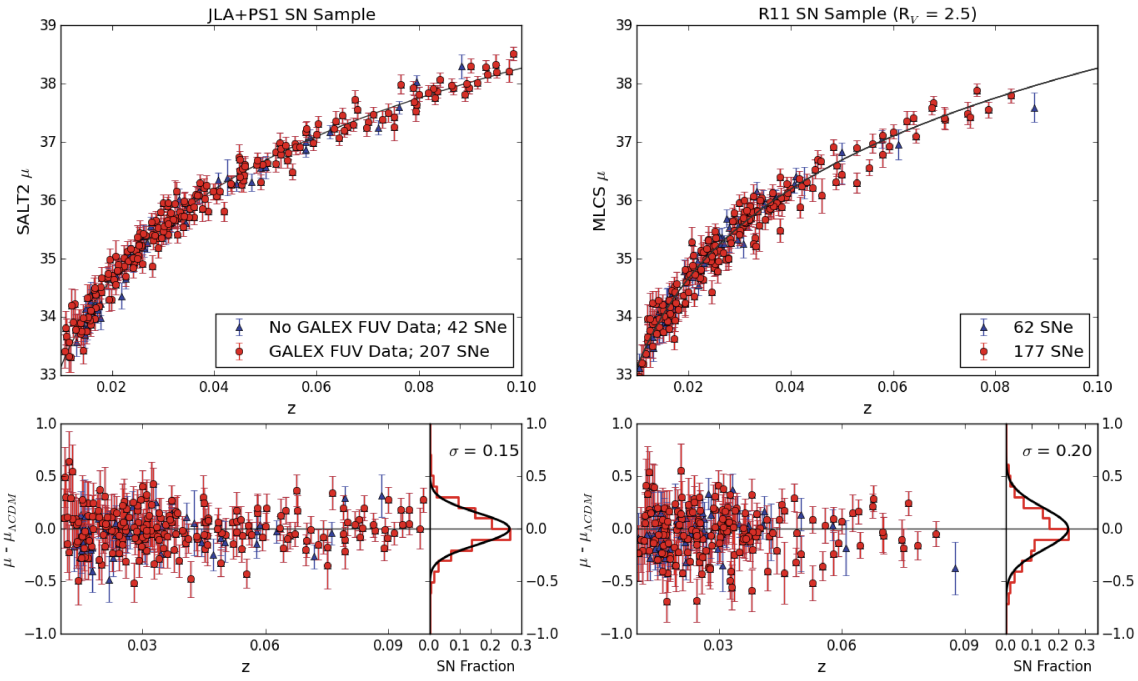

Figure 3.1: Hubble diagrams and Hubble residual diagrams for the JLA+PS1 sample (SALT2 light curve fitter; left) and the R11 sample (MLCS light curve fitter with $R_V = 2.5$; right), with GALEX FUV-imaged hosts in red and SNe without GALEX FUV host images in blue. Out of a total of 249 SNe in the JLA+PS1 sample, 207 were imaged by GALEX within 0.55 degrees of field center. In the R11 sample, 177 out of 239 SNe fit with $R_V = 2.5$ had GALEX FUV images. The MLCS data have slightly higher scatter, but both samples have intrinsic dispersions $\lesssim$0.2.

corrected magnitudes ∼0.15 mag brighter than SNe Iaα when fit with the MLCS light curve fitter and assuming the same R_V as the R11 H_0 baseline analysis. They derived a correction to H_0:

$$\log(H_0^{corr}) = \log(H_0) - \underbrace{\frac{1}{5}(\psi^{HF} - \psi^{C}) \times \delta\langle M_B^{\rm corr}\rangle_{\rm SF}}_{\text{LSF bias correction}}, \tag{3.1}$$

where ψ^{HF} is the fraction of SNe Iaϵ in the Hubble-flow SN sample and ψ^{C} is the fraction of SNe Iaϵ in the Cepheid-calibrated sample. $\delta\langle M_B^{\rm corr}\rangle_{\rm SF}$ is the LSF step of 0.155 mag. By estimating ψ^{HF} (52.1±2.3%) and ψ^{C} (7.0%), R15 estimate that the true value of H_0 is reduced by ∼3%.

R15 also found that SNe in highly star-forming regions fit by MLCS Jha et al. (2007); Riess et al. (1996) have lower dispersion in their Hubble residuals than SNe in locally passive environments. Kelly et al. (2015) came to the same conclusion by examining SNe Ia with high local star formation (Their $\Sigma_{\rm SFR}$ boundary is ∼0.7 dex higher than the R15 Iaϵ/Iaα cut-off). R13 first found this effect using the SALT2 light curve fitter Guy et al. (2007), but they could not reproduce this result with H09 data.

Table 3.1. Studies using local SF data

		SALT2			MLCS			
	SN Surveys	SNe	$\mu_{\rm version}$	β	SNe	$\mu_{\rm version}$	P(A_V)	R$_V$
Rigault+13	SNfactory[a]	82	G07[b]	... [c]	...	...	...	...
Rigault+15	CfA3	77	G07[b]	$2.48^{+0.10}_{-0.12}$	84	v0.06	$e^{-A_V/0.457}$	1.7,2.5,3.1
Kelly+15	LOSS,[d]CfA2-4,CSP	...	...	...	61	v0.07[e]	$e^{-A_V/0.3} * \mathcal{N}(\sigma = 0.02)$[f]	1.8,3.1
This Work	CfA1-4,CSP,CTS,[g]SDSS,SNLS,PS1	187	G10[h]	3.097 ± 0.062	154	v0.06	$e^{-A_V/0.457}$	2.0,2.5,3.1

[a] Aldering et al. (2002).

[b] Guy et al. (2007).

[c] The value of β was blinded in Rigault et al. (2013).

[d] The Lick Observatory Supernova Search Li et al. (2011).

[e] MLCS v0.07 used new spectral templates from Hsiao et al. (2007). This version was implemented in the SuperNova ANAlysis software (Kessler et al., 2009b, SNANA).

[f] An exponential convolved with a normal distribution having $\sigma = 0.02$ mag.

[g] Calan/Tololo Hamuy et al. (1996).

[h] Guy et al. (2010) had improved uncertainty propagation and handling of residual scatter, a new SN Ia spectral energy distribution regularization scheme, and used a larger training sample with higher-z SNe (see their Appendix A for details).

Both R15 and Kelly et al. (2015) used GALEX FUV data to measure the star formation rate within a few kpc of SNe Ia positions. In this work, we use a similar method to examine whether the significance of the LSF step and reduced dispersion from SNe in locally star-forming host galaxies is reduced when we use the most current vintage SNe Ia distance estimates, use a much larger sample size, and vary the priors and assumptions used in the original analyses.

Table 3.1 shows the sizes of the SN samples used in Rigault et al. (2013), R15, Kelly et al. (2015), and this work, along with the light curve fitters used, the SALT2 color parameters, and the MLCS prior on A_V. Rigault et al. (2013) used 82 SNfactory SNe with star formation estimated using local Hα from integral field spectroscopy. Rigault et al. (2015) used $\sim$100 SNe from the CfA3 sample of H09, with $\sim$80 passing GALEX sample cuts. Kelly et al. (2015) used several surveys but made strict sample cuts and only used SNe with Hubble residuals < 0.3 mag, which would amount to a $\sim 1.3\sigma$ cut for R11 data.

By using a sample size $\sim$2-3 times as large as those in the analyses above, we hope to obtain a robust measurement of the magnitude and uncertainty of the effect of local star-formation on SN Ia corrected magnitudes. §3.3 presents our sample selection, and §3.4 discusses our LSF step and dispersion analysis. In §3.5 and §3.6 we present our results and discuss their significance, and our conclusions are in §3.7.

3.3 Data

We used two samples of SNe for this analysis, one from the R11 measurement of H_0 and the other from the dark energy equation of state measurements of Betoule et al. (2014) and Pan-STARRS Rest et al. (2014); Scolnic et al. (2014a, PS1; Scolnic et al. 2015, in prep). These two samples rely on many of the same SNe, but R11 use the MLCS light curve fitter to perform their baseline analysis while Betoule et al. (2014) and PS1 use SALT2 (Guy et al., 2010; Betoule et al., 2014, version 2.4). Each sample is ∼2-3 times as large as the R15 and Kelly et al. (2015) GALEX-imaged host samples and removes the possibility of biases between our sample and the samples used in the most recent measurements of cosmological parameters.

3.3.1 Riess et al. (2011) SNe

The H_0 determination of R11 use the MLCS2k2 light curve fitter for their baseline analysis. We use only their MLCS2k2 distance moduli, as JLA+PS1 consists of a larger SALT2-fit SN Ia sample with more robust light curve cuts and an updated SALT2 model and color parameter, β. The R11 sample consists of 140 SNe between $0.023 < z < 0.1$ from Hicken et al. (2009a) and Ganeshalingam et al. (2010). As one of the variants in their systematics section, R11 extend the lower bound of the redshift range to 0.01 after making peculiar velocity corrections (using results from Neill et al. (2007) and the Pike & Hudson (2005) dipole), giving 240 SNe (with peculiar velocity

uncertainties added in quadrature to the distances). Adopting this redshift range raises H_0 by 0.8 km s^{-1} Mpc^{-1}, or 0.26σ. We adopt this lower redshift limit of 0.01 as it allows us to add more SNe Ia to our sample, although these nearby SNe have less weight in the likelihood approach outlined in §3.4.1 due to their included peculiar velocity uncertainties. In §3.5.1, we examine the effect of restricting the redshift range to $z > 0.023$. R11 remove 4σ Hubble diagram outliers but make no sample cuts based on light curve shape, A_V, or MLCS χ^2.

MLCS2k2 determines the distance modulus for each SN Ia by fitting for the light curve shape and extinction assuming an extinction prior and a value for the total-to-selective extinction ratio, R_V. Common extinction priors include exponential distributions ($e^{-A_V/\tau}$; see Table 3.1), exponential distributions convolved with gaussians, a flat prior (with or without negative A_V allowed), and priors based on host galaxy information. R11 consider the latter two priors in their systematic uncertainty analysis, and use an exponential with scale length 0.457 mag for their baseline analysis. R11 consider dust reddening laws with $R_V = 1.5$, 2.0, 2.5, and 3.1, using $R_V = 2.5$ for their baseline analysis. $R_V = 3.1$ corresponds to the Milky Way reddening law Cardelli et al. (1989). We exclude $R_V = 1.5$ from our analysis as such a low value is not typically used in cosmological analyses (e.g. Kessler et al. (2009a) adopt $R_V = 2.18 \pm 0.5$ for SDSS cosmology); although highly reddened SNe Ia tend to favor low values of R_V Burns et al. (2014), these SNe are usually excluded from samples used to measure cosmological parameters. H09, for example, use only SNe with $A_V < 0.5$.

We queried GALEX[1] for FUV images at the locations of these SNe, keeping only those with a angular distance from the field of view center (FOV radius) < 0.55 deg to ensure accurate photometry and avoid reflection artifacts and distortion of the PSF near the detector edge. Of the 240 SNe used in R11, we found 187 SN host images meeting this criterion, 157 of which remained after the sample cuts described in §3.4.1. A Hubble diagram of the R11 SN Ia sample is shown in Figure 3.1. There is less than 0.01 mag difference in mean Hubble residual between the full sample and the GALEX-detected sample. No bias is expected for SNe with GALEX host images.

3.3.2 Betoule et al. (2014) and Pan-STARRS SNe

The most recent measurements of w Betoule et al. (2014); Rest et al. (2014) use the SALT2 light curve fitter, and compute distance moduli using the equation Tripp (1998):

$$\mu = m_B^* + \alpha \times X_1 - \beta \times C - M, \tag{3.2}$$

where μ is the SN distance modulus, m_B^* is the peak SN B band magnitude, X_1 is the light curve stretch parameter, and C is the light curve color parameter. SALT2 adopts a linear relation between SN Ia color and luminosity with no prior. For consistency with the JLA cosmological analysis, we only use the SALT2 fitter with these data.

The nuisance parameters α, β, and M (in this analysis, a single value independent

[1] `http://galex.stsci.edu/GalexView/`

of host galaxy mass) are simultaneously fit to the full supernova sample. In recent work, the value of β has risen due to changes in the SALT2 model and larger SN Ia samples. The value found by Betoule et al. (2014) is $\beta = 3.102 \pm 0.075$, a difference of $\sim$0.6 relative to the H09 value of $2.48^{+0.10}_{-0.12}$ (used by R15). This could have an important impact on measuring the LSF step, which we discuss further in §3.6.1. In this analysis, we simultaneously fit JLA and PS1 data together, finding $\beta = 3.097 \pm 0.062$. In contrast to Betoule et al. (2014) and following the R15 claim that the LSF step replaces the host mass step, we did not apply the host mass step in deriving this value.

We limited the Betoule et al. (2014) Joint Light-curve Analysis (JLA) to $z < 0.1$ because the large GALEX PSF makes the star formation measurement non-local with FWHM $\sim$8 kpc. This low-z sample includes data from low-redshift surveys such as CfA1-3 Riess et al. (1999); Jha et al. (2006); Hicken et al. (2009a), the Carnegie Supernova Project Hamuy et al. (2006); Stritzinger et al. (2011) and Calan/Tololo Hamuy et al. (1996), and surveys extending to higher z such as SDSS (Kessler et al., 2009a, 25 SNe after sample cuts) and SNLS (Conley et al., 2011, no SNe after sample cuts). We added low-z CfA4 SNe from Hicken et al. (2012, used in the PS1 analysis), PS1 SNe from Rest et al. (2014) and the upcoming 4-year PS1 cosmological analysis (12 SNe after sample cuts; Scolnic et al. 2015, in prep). For both JLA and PS1, peculiar velocities are corrected following Neill et al. (2007) based on the Hudson et al. (2004) model.

The cuts applied to these data are listed in Betoule et al. (2014, their Table 6 and Appendix A). They make light curve shape, color, and SALT2 fit probability cuts (requiring a fit probability >0.01). We applied these same cuts to PS1 SNe, and removed 3.5σ outliers from the full sample, including the 4 $>3\sigma$ outliers removed by Betoule et al. (2014).

The JLA and PS1 samples with $0.01 < z < 0.1$ contain a total of 249 SNe. 207 were found in GALEX with FOV radius <0.55 deg and 179 remained after the sample cuts described in §3.4.1. We found no significant difference (<0.01 mag) between mean Hubble residual of the GALEX-detected sample and the full sample.

Figure 3.1 shows a Hubble diagram for SNe in both samples with and without GALEX imaging. Our cosmological fits used $\Omega_M = 0.3$, $\Omega_\Lambda = 0.7$, $w = -1$, $\mathrm{H}_0 = 70$ km s^{-1} Mpc^{-1} and determined the absolute SN magnitude M from a least squares fit to the Hubble residuals.

3.4 Measuring the Star Formation Density

R15 used the following procedure to measure the *local* star formation density, Σ_{SFR}, and its relation to SN distance estimates. We summarize the principal steps below and describe the differences in our analysis in §3.4.1. §3.4.2 discusses our systematic error treatment. Table 3.2 gives a summary of the quality cuts applied to

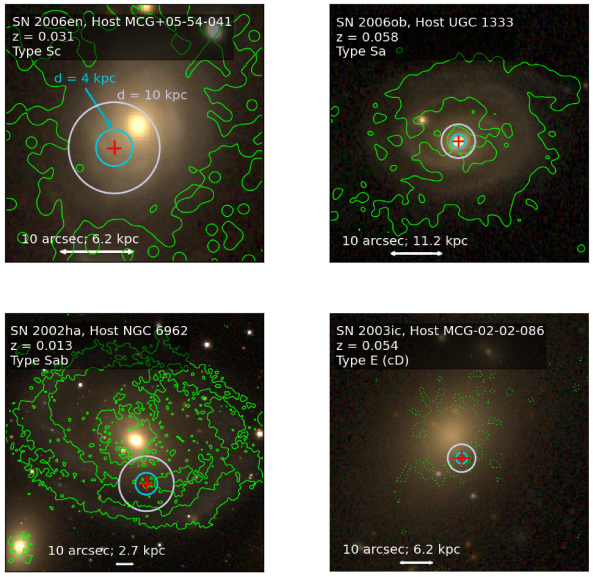

Figure 3.2: Four host galaxies from our sample in SDSS *gri* images, with smoothed GALEX FUV contours marking the star-forming regions ($\log(\Sigma_{\rm SFR}) > -2.9$) and the SN Ia positions marked in red. Two apertures are overlaid, the local aperture size from R15 (4 kpc diameter) and the local aperture size from (Kelly et al. (2015); 10 kpc diameter). We assumed $A_{FUV} = 2.0$ for the three star-forming galaxies. For the passive host of SN 2003ic, none of the galaxy would be considered locally star-forming for $A_{FUV} = 0$, but we show dotted contours to indicate the effect of assuming 2 mags extinction. The 4 kpc diameter aperture appears to be a good approximation for the local star-forming environment while the 10 kpc aperture extends well beyond the local star formation environment for SN 2002ha and encompasses most of the galaxy for SN 2006en. Both the size of our local apertures and our prior on A_{FUV} have an important effect on our results, so we vary both in our systematic error analysis.

Table 3.2. SN Selection Cuts

	JLA+PS1	R11		
No. SNe Ia		R_V =2.0	R_V =2.5	R_V = 3.1
Initial Sample	249	240	239	237
GALEX FUV data exist	212	189	188	187
FOV radius < 0.55 deg	207	181	180	179
Global SFR known	207	178	177	176
Inclined SNe Removed	179	157	156	155

our SN Ia sample and the number of SNe remaining after each cut.

1. R15 measured GALEX FUV aperture photometry at the location of the SN using a 4 kpc aperture diameter. They applied Milky Way dust corrections from Schlegel et al. (1998), where the FUV extinction A_{FUV} is $7.9 \times E(B-V)$ (R15; Cardelli et al. (1989)).

2. The photometry was corrected for host galaxy extinction in the FUV based on the measured FUV−NUV colors, which were converted to extinction using the relation from Salim et al. (2007). A Bayesian prior of $A_{FUV} = 2.0 \pm 0.6$ for star-forming galaxies was also applied (the final A_{FUV} was a weighted mean of the prior and the measured A_{FUV}). R15 made no dust correction for passive galaxies.

   To determine whether each galaxy was globally star-forming or passive, they

used $\Sigma_{\rm SFR}$ measurements from Neill et al. (2009, $\Sigma_{\rm SFR} > -10.5$ is star-forming), who fit synthetic templates to the SN host UV+optical spectral energy distributions (SEDs). Because Neill et al. (2009) SED fits were unavailable for ∼40% of their hosts, R15 used morphology for these, treating galaxy types Sa and later as star-forming (a less accurate method).

3. To minimize the effects of locally passive regions projected on top of locally star-forming regions (see R15, Appendix B.2), R15 removed SNe with host inclination angles >80° from their sample.

4. Based on their photometric and dust correction uncertainties, R15 calculated the probability of a SN Ia being above (P(Iaα)) or below (P(Iaϵ)) the $\log(\Sigma_{\rm SFR})$ $= -2.9$.

5. R15 used a maximum likelihood approach (outlined in §3.8.1) to determine the difference in corrected magnitude and dispersion between SNe Iaα and Iaϵ.

3.4.1 Our Analysis

We largely used the same methodology as R15, but improved the following aspects of the analysis:

1. We used the Schlafly & Finkbeiner (2011) dust corrections instead of the Schlegel et al. (1998) corrections used by R15, resulting in a ∼14% reduction in our extinction values.

2. We used SDSS NUV$-r$ color instead of morphology as a diagnostic of global SFR when UV+optical SED fits were unavailable.

3. For SNe outside the isophotal radii of their host, we did not make a dust correction as we expect these SNe to be minimally affected by extinction.

4. We made a slightly more conservative inclination cut, removing galaxies with inclinations $>70°$.

5. Using our maximum likelihood model, we fit for both SN Iaα and SN Iaϵ dispersion when determining the LSF step to allow for the possibility that these two quantities are significantly different and affect the magnitude of the step.

We discuss our changes and methodology in further detail below. However, these changes have only minor significance on our results (see §3.5.6). Our method of maximum likelihood estimation for calculating the LSF step is described in detail in the Appendix.

3.4.1.1 FUV Aperture Photometry

We used the same baseline 4 kpc aperture diameter as R15 for our photometry but corrected for Milky Way FUV extinction using the Schlafly & Finkbeiner (2011) dust corrections[2] instead of the Schlegel et al. (1998) corrections used by R15. Schlafly & Finkbeiner (2011) derive a $\sim$14% correction for the Schlegel et al. (1998) dust maps

[2] `http://irsa.ipac.caltech.edu/applications/DUST/`

based on the expected vs. measured colors of SDSS stars.

Using GALEX to estimate local star formation, as in Rigault et al. (2015) and Kelly et al. (2015) is complicated by the large GALEX PSF, 5.4″ full width at half maximum (FWHM) in the NUV and 4.5″ in the FUV, which serves as a lower limit to the size of the local region that we can measure. Kelly et al. (2015) used a 10 kpc aperture diameter to measure local star formation, while Rigault et al. (2015) used a 4 kpc diameter. We adopt the R15 4 kpc diameter in this work.

Figure 3.2 shows representative hosts from our sample with FUV-based $\log(\Sigma_{\rm SFR})$ ≥ -2.9 contours to demonstrate the size of these apertures relative to their star-forming regions. A 4 kpc aperture appears to be a reasonable approximation to the local SN Ia environment in these cases, while a 10 kpc aperture radius encompasses the majority of the SN 2006en host. In the case of SN 2002ha, it is unclear whether either aperture is small enough to capture the star formation environment at the SN location.

3.4.1.2 Host Galaxy Extinction Correction

There are three principal differences between our local dust correction and that of R15. First, for galaxies without star formation rates (SFRs) from Neill et al. (2009) (45% of our sample), R15 used morphological information to determine whether or not a galaxy was globally star-forming. However, GALEX NUV - SDSS r magnitude is a more reliable discriminator between passive and star-forming galaxies (e.g. Salim

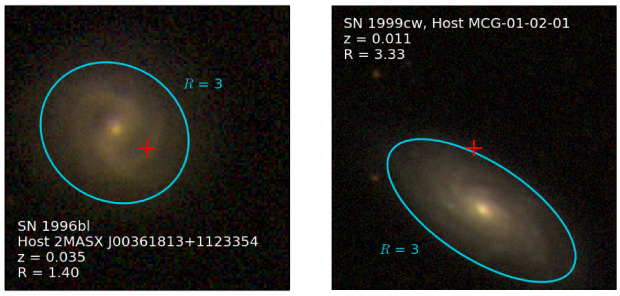

Figure 3.3: SDSS *gri* images of two spiral galaxies from our sample with SN positions marked in red and SExtractor-based isophotal radius estimates ($R = 3$) shown in blue. We corrected SN 1996bl for dust but did not correct SN 1999cw, as it exploded just outside the isophotal radius of its host galaxy and thus is beyond nearly all of its host galaxy's dust.

et al. (2007), their Fig. 1). Passive galaxies have NUV-$r \gtrsim 5$, while star-forming galaxies have NUV-$r \lesssim 4$. For the 45% of our sample with SDSS images, we corrected for dust in galaxies that had NUV-$r < 4.5$ based on SExtractor photometry Bertin & Arnouts (1996). For the final 19% of our sample without Neill et al. (2009) SFR or SDSS images, we used morphology as an estimate of global star formation and performed a local dust correction for Sa and later-type galaxies. We removed 3 morphologically ambiguous hosts from our sample (SN 2005eu, SN 2006ah, and SN 2006is).

Second, SNe Ia near the edges of galaxies should have negligible local dust. We used SDSS and, when necessary, Digitized Sky Survey images[3] to estimate the Sullivan et al. (2006) SExtractor-based R parameter, which gives the SN separation from the host normalized by the size of the host galaxy. For the 28% of SNe approximately

[3] `http://archive.eso.org/dss/dss`

outside the isophotal radius of their host galaxy (R > 3; Sullivan et al. (2006)), we did not correct for local dust regardless of the Salim et al. (2007) extinction estimate, which does not apply for passive, low-dust regions. R15 dust-corrected all SNe in globally star-forming hosts, regardless of the location of the SN. Figure 3.3 shows two examples of spiral host galaxies and their approximate isophotal radii.

In total, our decision to apply or not to apply a dust correction was different from that of R15 for 14% of H09 SNe (13/92 SNe). For 7 of these 13 SNe, we did not apply a dust correction because the SN was outside the isophotal radius of its host. The other 6 SNe had morphology-based SF classifications that disagreed with our NUV-r data.

Finally, we adopted a slightly more conservative inclination cut, removing galaxies with inclinations >70° based on the Tully & Fisher (1977) axial ratio method. This removes an additional 16 SNe from the JLA+PS1 sample and 11 from the R11 sample. In total, the inclination cut removes ∼13% of our sample.

3.4.2 Varying the Baseline Analysis

For a robust result, we performed several plausible variants of our baseline analysis (R15 used a similar method to evaluate the robustness of the LSF step). We used the standard deviation of the measured LSF step from all variations to estimate our systematic error.

Our FUV−NUV color measurements have a median signal-to-noise ratio of 3.02.

Due to such large photometric uncertainties, the dust correction and resulting $\Sigma_{\rm SFR}$ is heavily affected by the 2 mag A_{FUV} prior (e.g. SN 2003ic in Figure 3.2). Because using this prior to correct for dust local to the SN Ia can have up to a $\sim$1 dex effect on the measured $\Sigma_{\rm SFR}$, we examined the effect of changing the Bayesian dust prior to $A_{FUV} = 1.0 \pm 0.6$ and $A_{FUV} = 3.0 \pm 0.6$. These values span the full range of A_{FUV} in blue galaxies measured by Salim et al. (2007, see their Figure 13). Changing this prior serves as a way to alleviate some of the uncertainty associated with our global SFR determination; lowering this prior by 1 mag changes $\sim$10 SNe in our sample from Iaα to Iaϵ.

Following R15, we tried an additional 3 local aperture diameters between 2 and 6 kpc because the choice of a 4 kpc aperture is somewhat arbitrary and other reasonable choices exist. In part, the FWHM of the FUV PSF determines the minimum spatial scale we can probe with GALEX, which is approximately 2 kpc at our median redshift. However, Figure 3.2 shows that it is still possible that a local aperture will encompass components of a galaxy with different star-forming environments. The higher-resolution star formation maps of M33 in Boquien et al. (2015) show large $\Sigma_{\rm SFR}$ variation on much smaller, sub-kpc scales. Nevertheless, we might hope that star-formation within a $\sim$few kpc aperture is still much better correlated with the SN progenitor environment than a global measurement due to the significant fraction of prompt progenitors and low velocity dispersions of young stars de Zeeuw et al. (1999).

The boundary between SNe Iaα and Iaϵ is also somewhat arbitrary. We used values of $\log(\Sigma_{\rm SFR})$ between -3.1 and -2.7. For direct comparison to Kelly et al. (2015), we also examined the boundary between star-forming and passive of $\log(\Sigma_{SFR}) = -1.7$ and -1.85 (accounting for a $\sim$0.4 dex offset between our SFR measurements and Kelly et al. (2015)) when discussing Hubble residual dispersion.

Finally, we tried using global rather than local star formation (global star formation is a less noisy measurement), and with or without 2.5σ-clipping. Our list of analysis variations is given in §3.5, Table 3.5.

3.5 Results

We used 179 GALEX-detected SNe from JLA+PS1 and 157 SNe from R11 to measure the LSF step and distance dispersion. Although for certain variants of the analysis, we see differences between SNe Iaϵ and Iaα at the level of $\sim$1-3σ, the evidence for the LSF step is generally weak.

Although certain peculiar SNe (e.g. SN 1991bg-like and SN 1991T-like) are not explicitly identified and removed from these samples, the shape and color cuts applied by JLA and R11 are sufficient to remove many of them. However, we make no effort to exclude peculiar SNe that JLA/R11 have determined to be cosmologically useful so that we can directly assess the affect of local SF on the JLA/R11 cosmological analyses. In contrast, Rigault et al. (2013) and R15 remove identified SN 1991T

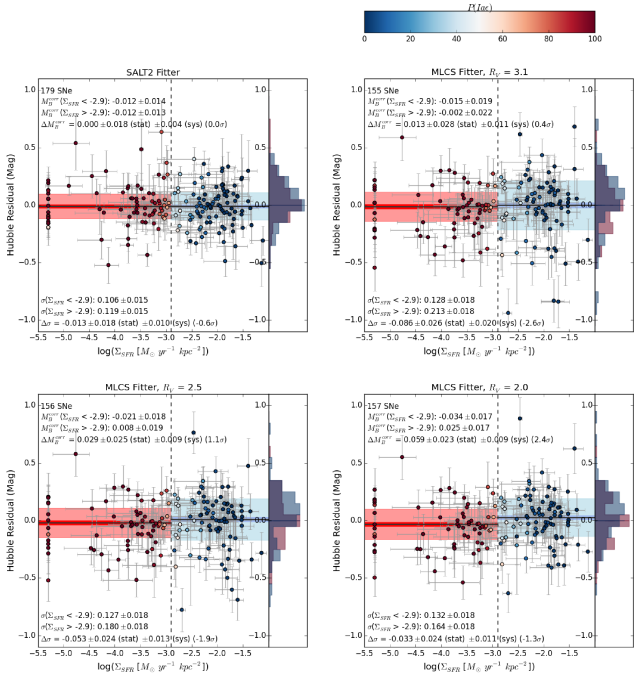

Figure 3.4: Our baseline analysis for the JLA+PS1 sample (SALT2; upper left), and the R11 sample with different values of R_V (MLCS2k2 fitter). The color of each SN indicates the probability that it has a locally passive environment, P(Iaϵ). Shaded bars indicate the uncertainty on the mean (dark shading; statistical error only) and the standard deviation of the maximum likelihood gaussian (the weighted dispersion; light shading). The LSF step is much smaller and has lower significance than the step found by R15, although we detect it at 2.6σ for the $R_V = 2.0$ case (2.4σ with systematic errors). For $R_V = 3.1$ and 2.5, we find lower dispersion among SNe in locally passive environments than those in locally star-forming environments at 3.3σ and 2.2σ, respectively. For consistency with R15, SNe with only Σ_{SFR} upper limits are placed at $\log(\Sigma_{SFR}) = -5.3$. Systematic uncertainties are estimated from several variants of our analysis (Table 3.5).

explicitly (∼3% of their sample).

In this section, we do not examine the effect of correcting for the relationship between host mass and SN distance Sullivan et al. (2010) on the LSF step as only ∼15% of our SNe are low-mass hosts ($\log(M_\odot) < 10$; R15 similarly found that few H09 SNe are in low-mass hosts). However, we briefly consider its effect on H_0 in §3.6.2. A complete table with our GALEX measurements and Hubble residuals is available online[4], with the first 25 rows given in Table 3.4.

3.5.1 The Local Star Formation Step

We find a greatly reduced LSF step compared to R15 for all light curve fitters and values of R_V. Using SALT2, we find an LSF step of 0.000±0.018 mag. With MLCS $R_V = 2.5$ (the value used in the R11 baseline analysis), we find 0.029±0.027 mag. However, we do find mild evidence for an offset of 0.059±0.025 mag with $R_V = 2.0$ (2.4σ significance). For $R_V = 3.1$, we found a value of 0.013±0.030 mag. Our error budget includes systematic errors, which we estimated by measuring the standard deviation of several variants of our analysis.

Figure 3.4 presents our baseline measurement of the LSF step and Hubble residual dispersion for SNe Ia in locally passive and locally star-forming environments (SNe Iaϵ and SNe Iaα, respectively), with colors indicating the probability incorporated in our likelihood model that a given SN Ia has a locally passive environment, P(Iaϵ). We

[4] `http://www.pha.jhu.edu/~djones/lsfstep.html`

find that 47.2% of R11 SNe in our sample are Iaϵ and 46.0% of JLA+PS1 SNe in our sample are Iaϵ. The overall intrinsic dispersion for our full MLCS sample ($\sim$0.13-0.17 mag; 0.14 for $R_V = 2.5$) is higher than for SALT2 (0.12 mag), likely due to the lack of recent calibration of MLCS2k2. Intrinsic dispersion can also be affected by the distribution of light curve parameters in the sample and the robustness of the photometric measurements.

We find no significant difference in dispersion between SNe Iaα and SNe Iaϵ in SALT2. In the R11 MLCS sample, however, we find some evidence that SNe Iaϵ have lower dispersion ($\sigma_{Ia\epsilon}$) than SNe Iaα. For $R_V = 3.1$, the LSF step is the lowest and $\sigma_{Ia\alpha}$ is the highest (0.09 mag $> \sigma_{Ia\epsilon}$; 2.6σ with sys. error). These results disagree with R15 at the 3σ level. For MLCS with $R_V = 2.5$, $\sigma_{Ia\epsilon}$ is $\sim$0.05 mag less than $\sigma_{Ia\alpha}$ (1.9σ significance). For $R_V = 2.0$ we detected only a $\sim$0.03 mag difference in dispersion (1.3σ). Our full results for each analysis variant are presented in Table 3.6.

We found that if we restrict to $z > 0.023$ (the R15 minimum z), we see more evidence for the LSF step. After this cut, there are 135 SALT2 SNe Ia and 104 MLCS SNe Ia. The increased significance of these results is expected because $\sim$3/4 of our MLCS sample is from R15 when we apply this redshift cut. For MLCS $R_V = 2.0$, 2.5, and 3.1 we find LSF steps of 0.086$\pm$0.028 (3.1σ), 0.076$\pm$0.030 ($\sim$50% of R15; 2.5σ), and 0.064$\pm$0.037 (35% of R15; 1.8σ). For SALT2, we only find a very small offset, 0.017$\pm$0.019 (18% of the R15 result) at 0.9σ significance. The MLCS LSF steps are $\sim$50% of those found by R15. Except in the case of MLCS with $R_V = 2.0$, the low-z

data alone ($0.01 < z < 0.023$) show slightly brighter SNe Iaα by $\sim$0.02-0.03 mag but with only 0.5σ significance for MLCS (0.06 mag with 1.4σ for SALT2). This effect is mostly due to $\sim$5 bright low-z SNe, which do not have a large effect on the final result (see the 2.5σ-clipping in Table 3.5). If the peculiar velocity corrections and uncertainties for low-z SNe were in error, we would expect, but do not observe, a significant increase in uncertainty-weighted M_B^{corr} dispersion below $z = 0.023$ (we see $\lesssim$0.015 mag difference). We did not find evidence that our highest-z data ($z > 0.07$) were having a significant effect on our results.

3.5.2 Systematic Uncertainties

Several different variants of our analysis are consistent with the baseline result. The JLA+PS1 variants are shown visually in Figure 3.5, and the R11 variants are shown in Figure 3.6. For the LSF step, the full results from both data sets are presented in Table 3.5 and our dispersion results are presented in Table 3.6. We have added the standard deviation of the LSF step from all variants in quadrature to our measured values (giving each type of variant, e.g. aperture size, SFR boundary, etc., equal weight). Because using the global SFR is not truly a local measurement, we have excluded it from our error computation but include it in our list of variants for comparison.

For nearly all samples, our most significant detections of the LSF step were at a $\log(\Sigma_{\rm SFR})$ boundary of -3.1 and a 3 kpc aperture radius. For a $\log(\Sigma_{\rm SFR})$ boundary

of -3.1, with SALT2 and MLCS $R_V = 2.5$ (the most relevant versions for cosmology), we detected steps of 0.023±0.019 and 0.044±0.029, respectively. These are ∼25% of R15 values and insignificant.

For MLCS with $R_V = 2.5$ and 3.1, our most significant detections came from the variant with 2.5σ-clipping. They had values of 0.060±0.026 mag (2.3σ) for $R_V = 2.5$ and 0.046±0.028 (1.6σ) for $R_V = 3.1$. This may mean that outliers are affecting our measurement. However, we also expect that they affect the R11 H_0 measurement in the same way, and note that $R_V = 2.0$ 2.5σ-clipping has no significant effect.

The variant with the smallest LSF step was the one based only upon global SFR instead of local. However, the significance of the difference is only $\lesssim 1\sigma$ except in the case of $R_V = 2.0$. The difference may stem from the fact that 25% of SNe with globally star-forming environments in our samples had locally passive environments (P(Iaϵ) > 50%). Only 5% of SNe with globally passive environments had a >50% probability of being locally SF. Qualitatively, this agrees with Hα data from Rigault et al. (2013, their Figure 5), who found that globally star-forming hosts often had locally passive regions.

Even after adding the systematic error in quadrature, the MLCS $R_V = 2.0$ LSF step is detected at 2.4σ (0.059±0.025 mag). Future cosmology analyses using MLCS with low R_V should measure the LSF step in their samples to evaluate its effect on cosmology.

The difference in the dispersion between the two SN populations in MLCS is

greatest in those same analysis variants discussed above, but as with our baseline analysis, we see the opposite effect that R15 found. We don't detect any difference in dispersion for SALT2 with the exception of using global instead of local SFR, for which we find a 0.05±0.018 mag (2.8σ) reduction in dispersion for passive hosts. For MLCS $R_V = 2.5$ and 3.1, we find a reduction in dispersion for locally passive SNe of $\sim 0.05-0.1$ mag ($\sim$1-3σ) for a $\log(\Sigma_{\rm SFR})$ boundary of -3.1 and a 3 kpc aperture radius.

3.5.3 Consistency with R15

R15 measured a much larger LSF step of 0.094±0.037 with SALT2, 0.155±0.041 with MLCS2k2 $R_V = 2.5$ and 0.171±0.040 with MLCS2k2 $R_V = 3.1$. We did not directly compare to their $R_V = 1.7$ data, but our $R_V = 2.0$ offset is 50% smaller than theirs. Our measured SALT2 LSF step has a 2.3σ discrepancy with the R15 measurement, our MLCS2k2 $R_V = 2.5$ LSF step has a 2.6σ discrepancy, and our MLCS2k2 $R_V = 3.1$ LSF step has a 3.2σ discrepancy.

Table 3.3 demonstrates the step by step impact of changes in the R15 analysis or data, showing the effects of using the JLA+PS1 and R11 light curve cuts, the JLA+PS1 and R11 distance moduli (with an updated SALT2 light curve fitter for JLA+PS1), our improved $\log(\Sigma_{\rm SFR})$ measurements, and using a larger SN Ia sample (with and without the R15 $z > 0.023$ cut).

Updated distance moduli greatly decrease the significance of the LSF step in

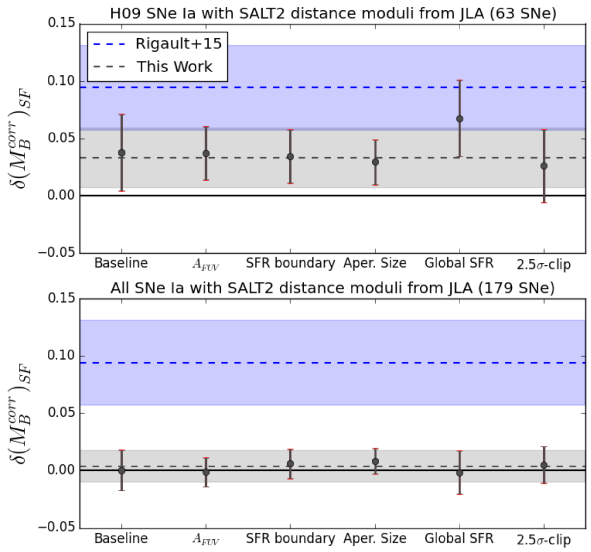

Figure 3.5: The systematic error of the SALT2 LSF step estimated by the effect of different variants of our analysis on the measurement of the LSF step. Red error bars represent the standard deviation of all variants of our analysis added in quadrature to the uncertainties from each individual variant. The top panel shows only H09 SNe included in Betoule et al. (2014), and the bottom panel shows our full SN Ia dataset. The step we detect is $\sim$0.05 mag (1.3σ) with H09 SNe, but shrinks to $<$0.01 when we add in our full SN Ia sample. The blue dashed lines and shaded regions show the R15 LSF step and 1σ uncertainty for SALT2. The results from different variants of our analysis are very consistent; our measured systematic errors are only a small fraction of our statistical errors. The global SFR variant is excluded from the systematic error calculation, as this is not a local measurement.

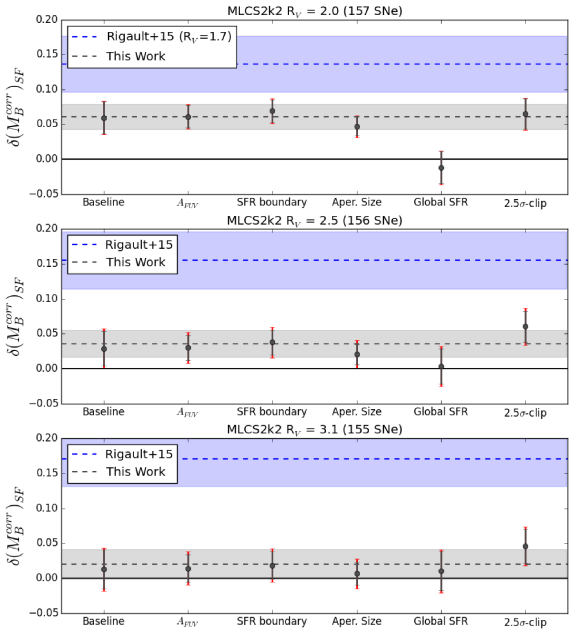

Figure 3.6: The systematic error of the MLCS LSF step estimated by different variants of our analysis for $R_V = 2.0$, 2.5, and 3.1 in the R11 SN Ia sample. The LSF step has 2.4σ significance for $R_V = 2.0$. The baseline analysis used to determine H_0 uses $R_V = 2.5$, for which we see a small LSF step at 1.1σ significance. We see $<1\sigma$ significance for $R_V = 3.1$. The blue dashed lines and shaded regions show the R15 LSF step and 1σ uncertainties for MLCS2k2. The global SFR variant is excluded from the systematic error calculation, as this is not a local measurement.

Table 3.3. The Effect of Step-by-Step Changes in R15 Data, Distances, SFR Measurements, and Sample Cuts

Measurements				SALT2					MLCS R_V=2.5				
SN sample	μ_{resid}	$\Sigma_{\rm SFR}$	SN cuts	SNe	$\delta(M_B^{\rm corr})_{SF}$[a]	Sig.	$\sigma_{Ia\alpha} - \sigma_{Ia\epsilon}$[b]	Sig.	SNe	$\delta(M_B^{\rm corr})_{SF}$[a]	Sig.	$\sigma_{Ia\alpha} - \sigma_{Ia\epsilon}$[b]	Sig.
H09	H09	R15	H09	77	0.093±0.026	3.5σ	-0.034±0.073	-0.5σ	81	0.169±0.026	6.5σ	0.057±0.033	1.7σ
H09	H09	R15	**JPR**[c],H09	59	0.129±0.030	4.3σ	0.012±0.047	0.2σ	74	0.144±0.025	5.6σ	0.038±0.034	1.1σ
H09	**JPR**	R15	JPR,H09	59	0.062±0.032	1.9σ	0.030±0.031	1.0σ	74	0.149±0.025	5.9σ	0.023±0.031	0.7σ
H09	JPR	**Here**[d]	JPR,H09	59	0.071±0.033	2.2σ	0.009±0.031	0.3σ	74	0.119±0.026	4.5σ	-0.010±0.030	-0.3σ
H09	JPR	Here	**JPR**	63	0.045±0.033	1.3σ	0.015±0.030	0.5σ	78	0.097±0.027	3.6σ	-0.029±0.030	-1.0σ
JPR[e]	JPR	Here	JPR,$z >$ **0.023**	135	0.017±0.019	0.9σ	-0.020±0.019	-1.1σ	103	0.076±0.029	2.6σ	-0.041±0.029	-1.4σ
JPR[e]	JPR	Here	JPR	179	0.000±0.018	0.0σ	-0.013±0.018	-0.7σ	156	0.029±0.025	1.2σ	-0.053±0.024	-2.2σ

[a] $\delta(M_B^{\rm corr})_{SF}$ denotes the magnitude of the LSF step.

[b] The difference in uncertainty-weighted dispersion between SNe Iaϵ and Iaα (using the standard deviation of the maximum likelihood gaussians; σ_ϵ and σ_α in Equation 3.3).

[c] **JLA+PS1** $M_B^{\rm corr}$ for SALT2, **R11** $M_B^{\rm corr}$ for $R_V = 2.5$.

[d] Measurements of $\Sigma_{\rm SFR}$ from **this work** (see §3.4.1).

[e] The full **JLA+PS1** (SALT2) and **R11** (MLCS) SN samples.

Note. — We show the difference between our analysis and R15 by improving one element of the analysis at a time. We start with the R15 results and sequentially show the effect of adding light curve cuts from JLA+PS1/R11, using JLA/R11 distance moduli, using our updated SFR measurements, using only JLA/R11 (not H09) light curve cuts, and finally adding in the full SN samples with and without the R15 redshift cut of $z > 0.023$. **The biggest differences come from adding the full sample for both SALT2 and MLCS and using improved SALT2 distance moduli.** The R11 SN light curve cuts also make a 1σ difference in the MLCS results. For consistency, we have used the likelihood minimizer used in the rest of this study to reproduce the R15 results (The SciPy Optimize package). This minimizer returns smaller uncertainties than Minuit, which was used in R15, but we find negligible differences in the maximum likelihood values themselves. The difference in LSF step we find for R15 data with MLCS (our value is 0.014 mag higher) is because we adopt two separate dispersions for SNe Iaα and SNe Iaϵ whereas R15 use a single value for the full sample.

JLA+PS1 data in SALT2, a 50% reduction (a change in significance of 2.4σ). The version of SALT2 used in recent analyses has an improved SN Ia model and uncertainty propagation, a larger training sample, and an updated value for β. R11 distances are nearly identical to H09 distances, so using these has no significant effect on the LSF step.

Using our $\Sigma_{\rm SFR}$ measurements increases the significance of the LSF step by 0.3σ for SALT2 and reduces it by 1.4σ ($\sim$20%) for MLCS. Between our data and the R15 data, there is significant scatter in probability for $10\% < \mathrm{P(Ia}\epsilon) < 90\%$, in large part due to our modest changes in dust correction methodology. However, we find only 3% median offset in P(Iaϵ) between our data and R15 and in §3.5.6 we find that our method of $\Sigma_{\rm SFR}$ measurement has little impact on the final results. Our full set of $\Sigma_{\rm SFR}$ measurements can be compared to R15 using the data we provide online and in Table 3.4.

There are 4 SNe in R11 and 4 SNe in JLA that pass R11/JLA light curve cuts but *do not* pass H09 cuts (SNe 1992j, 1993h, 1999aw, 2001ic, 2006bd, 2006gt, 2007ba, and 2007cg). We found that including them reduces the SALT2 LSF step by a significant 37% (0.9σ) and reduces the MLCS LSF step by $\sim$15% (0.9σ). When applying any LSF-dependent effect to cosmology, it is appropriate to match the cuts used in the cosmological analysis to those used in the measurement.

For both the LSF step and the dispersion in MLCS, there is a $>1\sigma$ change when we use the full SN Ia sample. Although the total statistical change from 3.6σ to 1.2σ

is large, we do not expect this to be a result of peculiar velocity bias from our low-z data. Some of the change may result from a greater sample dispersion, which reduces the significance of small offsets. A dispersion term is typically added in quadrature to distance modulus uncertainties in cosmological analyses, including R11 and Betoule et al. (2014), and has the same effect. In addition, Table 3.3 does not incorporate systematic error, which may have an impact; high-z data effectively have a larger aperture size due to a PSF width that is a greater fraction of the 4 kpc aperture diameter. Figure 3.6 shows that aperture variations may have up to a 1σ effect on the measured LSF step, and to expand our sample size we have preferentially added low-z data with smaller effective apertures ($0.01 < z < 0.023$).

Table 3.3 shows that the MLCS increase in Iaα dispersion is mostly caused by the addition of new SNe rather than to our $\Sigma_{\rm SFR}$ measurements or new distance moduli. The surveys that comprise our sample typically have larger dispersion than H09, which reduces the significance of the H09 sample. There are a number of possible sources for increased dispersion of a SN Ia sample, including underestimating photometric difference image uncertainties near bright hosts and nightly or absolute photometric calibration uncertainties Scolnic et al. (2014a). For MLCS, R11 may also have higher sample dispersion because they make no cut on the χ^2 of the MLCS light curve fits, while H09 remove SNe with reduced $\chi^2 > 1.5$.

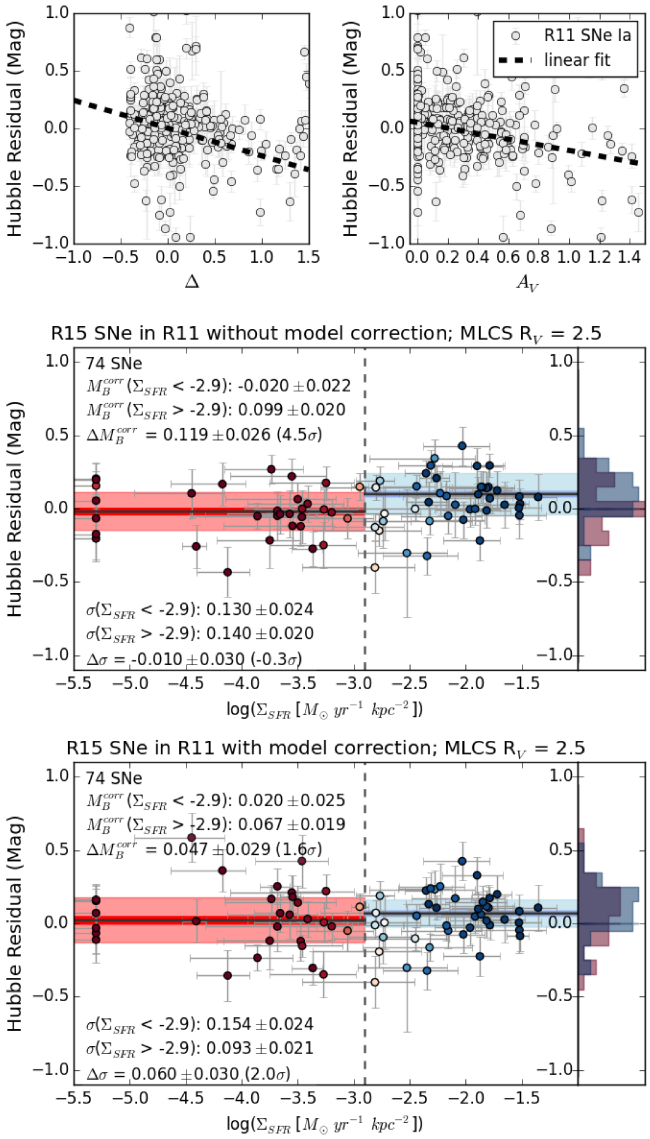

Figure 3.7: A simple linear correction for Hubble residual trends in MLCS reduces the significance of the R15 LSF step. In the top panels, we show MLCS Δ and A_V fit to R11 SNe. In the middle panel, we show our measured SF bias using R11 SNe in H09. In the bottom panel, we make a linear correction for the MLCS Hubble residual trends, and the LSF step is reduced from 4.5σ to 1.6σ significance. Colors indicate P(Iaϵ), with P(Iaϵ)$\sim$100% in red and P(Iaϵ)$\sim$0 in blue.

3.5.4 The Effect of MLCS Sample Cuts

In MLCS, the total difference of ∼0.14 mag between our analysis and R15 may appear surprising, but in addition to the possible reasons discussed above, much of the change between the R15 measurement and ours appears to arise from the different demographics of the two samples and the peculiarities of the MLCS light curve fitter. H09 find that for both high-A_V SNe and high-Δ SNe, MLCS tends to overcorrect leading to negative residuals, and these negative residuals are not subtle. In our $R_V = 2.5$ sample, SNe with $A_V > 0.5$ have a mean residual of -0.22 mag, which has been seen elsewhere as evidence for a lower R_V in high extinction environments. Likewise, SNe with $\Delta > 0.7$, where the relation between light curve shape and luminosity becomes non-linear and is poorly sampled especially when MLCS2k2 was trained, have a mean residual of -0.23 mag. Accordingly, the balance of rare high A_V SNe to rare high Δ SNe can affect an apparent LSF step as the frequency of these objects correlates with host properties.

Passive hosts have preferentially higher Δ than SF hosts (H09, their Figure 19), while SF hosts have preferentially higher A_V. In R15, the H09 data that have GALEX imaging and pass their cuts contain several SNe with large Δ but only two SNe with $A_V > 0.45$ for $R_V = 1.7$ (for $R_V = 3.1$, only two SNe with $A_V > 0.7$). Therefore a sample like R15 without high-A_V hosts but *with* high-Δ hosts will have brighter passive SNe Ia on average, producing a larger apparent LSF step.

One approach to decrease sensitivity to MLCS Hubble residual trends is to first

remove the trends, and then determine the LSF step. In Figure 3.7, we fit a simple linear model to MLCS Hubble residuals as a function of Δ and A_V, using R11 SNe in H09 (with $A_V < 1.5$ and $\Delta < 1.5$ to match H09). When we correct for those slopes, we see that the measured SF step using R11 SNe in H09 shrinks by a factor of 2.5 and is reduced from 4.5σ to 1.6σ significance.

SALT2 does not have the strong residual trends with X_1 and C that MLCS does with A_V and Δ, and we also find that restricting our sample to the H09 "best" SALT2 cuts ($-0.1 < C < 0.2$) does not introduce an LSF step (but changing β may; see §3.6.1). However, it is likely that recent substantial improvements to the SALT2 model have removed some of the biases in its derived distances. Due to the lower dispersion of SALT2-fit SNe, the lack of these residual trends, and because MLCS fits assume an extinction law, it is likely that SALT2 is more effective at standardizing SNe Ia.

In a future update of MLCS using a larger training sample, it would be important to verify that these trends with host, A_V and Δ are diminished.

3.5.5 Kelly et al. (2015) Scatter

Using MLCS, Kelly et al. (2015) see reduced Hubble residual scatter of only 3.5% in distance in highly star-forming regions ($\log(\Sigma_{\rm SFR}) >$ -2.1 and $\log(\Sigma_{\rm SFR}) >$ -2.25). Due to differences in methodology, there is a $\sim$0.4 dex offset in Σ_{SFR} measurements between our data and Kelly et al. (2015). Because of this, we adopt $\log(\Sigma_{\rm SFR}) >$ -1.7

and $\log(\Sigma_{\rm SFR}) > -1.85$ as our Σ_{SFR} boundaries for comparison.

In part, the low scatter seen by Kelly et al. (2015) is because they explicitly remove SNe with Hubble diagram residuals >0.3 mag (>15% in distance). Because of this and because the R11 sample does not cut SNe with high extinction or large Δ, our unweighted standard deviation is a significantly larger $\sim$0.25 (12% in distance) for the R11 sample at $\log(\Sigma_{\rm SFR}) > -1.7$ and $\log(\Sigma_{\rm SFR}) > -1.85$. For SALT2, the standard deviation is a slightly lower 0.20 mag, or 10% in distance, with no difference between SNe in locally passive/locally star-forming environments.

We also see no difference in uncertainty-weighted dispersion for these $\Sigma_{\rm SFR}$ boundaries in SALT2, and we find that the dispersion for SNe in both passive and star-forming environments in SALT2 data is smaller than the *lowest* dispersions we observe with MLCS. The scatter in our sample is much higher than in Kelly et al. (2015), and we find a $\lesssim$0.02 mag ($\sim$14%; $\sim$0.1-0.5σ) reduction in dispersion for MLCS with $R_V = 2.0$. SNe in star-forming environments have *higher* dispersion with low significance for MLCS $R_V = 2.5$. For $R_V = 3.1$, SNe in star-forming environments have $\sim$0.07 mag higher dispersion at $\sim 1\sigma$ significance. A summary of our intrinsic dispersion measurements are in Table 3.7.

If we apply H09 Δ and A_V cuts to our data, we still see the opposite effect as Kelly et al. (2015). We can only reproduce the Kelly et al. (2015) results using their strict Δ and A_V cuts, which have not been used in any cosmological analysis to date. However, these cuts may prove useful in the future if this low-scatter population

persists when additional SNe are added to the data.

3.5.6 Additional Consistency Checks

We performed several consistency checks to verify that individual SN datasets and differences between our analysis and R15 did not bias our results. First, we removed SNe discovered prior to the year 2000, leaving 130 SNe from JLA/PS1 and 116 SNe from R11. Our results were consistent with our baseline analysis; we measured a SALT2 LSF step of 0.010±0.025 mag and an MLCS $R_V = 2.5$ step of 0.040±0.031 mag. The $R_V = 2.0$ step was a slightly higher, but consistent, 0.079±0.030 mag (2.7σ). The dispersion of SNe in highly SF regions was not significantly reduced.

Second, the photometry and calibration from low-z surveys is not as robust as recent data from SDSS and PS1. The JLA/PS1 sample has 37 SNe with redshifts less than 0.1 that have GALEX data and pass our cuts, while the R11 sample includes no SDSS/PS1 SNe as it predates them. For comparison, we fit SDSS and PS1 SNe with MLCS to see if the LSF step derived from these surveys alone are consistent with the R11 results. With SALT2, we find an LSF step of 0.034±0.028 mag with lower SF dispersion by 0.049±0.024 mag (2.0σ). With MLCS, we find a *large* LSF step with 35 SNe of ∼0.14±0.055 mag with 1.7-2.9σ significance. As the sample consists of only ∼10-15 locally passive SNe, this step could still be caused by low statistics or a limited range of light curve parameters comprising the sample. As discussed in §3.5.4, the trends MLCS residuals have with different light curve parameters may be

a factor, as the size and significance of the LSF step is somewhat reduced when this sample is restricted to low Δ and A_V. This step is also unlikely to affect recent cosmological analyses, which are based on SALT2 or comprised mainly of low-z data (e.g. R11, H09). However, it is an interesting result that should be explored further with photometric PS1 SNe and future DES data. This sample is too small at $\log(\Sigma_{\rm SFR}) >$ -1.85 for a reliable check on our Kelly et al. (2015) comparison.

If we make a host galaxy inclination cut at $>80^\circ$ following R15 (instead of our more conservative cut of $>70^\circ$), the results are consistent with our baseline result, with MLCS LSF steps ranging from 0.00 mag ($R_V = 3.1$) to 0.045 mag ($R_V = 2.0$) with uncertainties $\sim$0.025 mag. The SALT2 LSF step is -0.016 mag ($<1\sigma$ significance).

Finally, we apply a dust correction to the FUV flux from *all* SN regions in star-forming hosts when determining $\Sigma_{\rm SFR}$, now including the 20 R11 SNe and 25 JLA/PS1 SNe with $R > 3$ (see §3.4.1.2). We again find a comparable result; the SALT2 LSF step is 0.012$\pm$0.019 mag, and the MLCS $R_V = 2.5$ LSF step is 0.040$\pm$0.028 mag.

3.6 Discussion

We find that local star formation has at little to no effect on SN Ia distances in the R11 and JLA+PS1 samples. Our results have several important implications for cosmological analyses, H_0, and future measurements of relationships between SNe Ia and their host galaxy properties.

3.6.1 The Effect of β and R_V on SN Ia Distances

Although the modest differences we observe in mean magnitude and dispersion for MLCS with certain values of R_V could be due to the relation between SN Ia progenitor properties and derived distances, we consider it much more likely that host galaxy extinction, which is highly correlated with star formation, is causing any observed bias. We propose that some of the effects seen in R15, Kelly et al. (2015), and our data may be due to dust rather than to a secondary effect such as the progenitor age (e.g. Childress et al. (2014)).

With MLCS, the LSF step we found is 0.046 ± 0.039 mag higher assuming $R_V = 2.0$ than assuming $R_V = 3.1$ (systematic errors added). The $R_V = 2.0$ LSF dispersion is 0.053 ± 0.044 (stat+sys) mag lower than $R_V = 3.1$. It has been observed by several groups (e.g. Burns et al. (2014)) that SNe Ia in high-extinction environments have lower values of R_V. Because of this, it seems likely that the $R_V = 3.1$ extinction law is failing to properly correct for the dust in some star-forming regions.

For SALT2, our value of β has a value $\sim$0.6 higher in the latest cosmological analyses than the value found in H09. This can have an important effect on the measured LSF step. For example, a SNe Ia in a locally star-forming environment with $\sim$0.17 magnitudes of A_V, would have its corrected magnitude shifted by 0.1 mag with this new value of β. For comparison, R15 SNe with locally star-forming environments have a mean fitted $A_V = 0.25$ for $R_V = 3.1$ and $A_V = 0.22$ for $R_V = 1.7$. We don't see such a large effect in our data, and would not expect β to have the exact

effect of R_V, but we do find that using a lowered β of 2.5 (the value used in H09) in our analysis raises the SALT2 LSF step to 0.024±0.018 (1.3σ significance).

In future cosmological analyses, it may be possible to separate star-forming and passive hosts and fit for two different values of β or R_V. This could reduce scatter and provide more precise SN Ia distances for subsets of the population, provided the systematic uncertainties in such an analysis are well-understood.

The SALT2 light curve fitter shows the least difference between SNe Iaϵ and SNe Iaα M_B^{corr} and also has the lowest dispersion in both star-forming and passive regions. The lowest dispersion we find using MLCS is still higher than the SALT2 dispersion for both SNe Iaϵ and Iaα. For this reason, SALT2 may be a more reliable light curve fitter for cosmological analyses. In its current version, MLCS fails to standardize SNe Ia to the extent that SALT2 does and has fitter biases that correlate with host properties (such as Hubble residual nonlinearities with high Δ and an assumed value for R_V). Perhaps a re-trained version of MLCS that incorporates terms such as random SN color scatter Scolnic et al. (2014b) would reduce the MLCS outlier fraction and provide more precise distances.

3.6.2 The Effect on Measuring H_0

Because our final measurement of the LSF step with $R_V = 2.5$ is only a 1.2σ detection, there are no grounds in the Bayesian sense to correct H_0 for the LSF step. However, a useful test of systematic uncertainties in the future will be to use only

star-forming hosts in the Hubble flow sample, which have similar physical properties to the nearby Cepheid-calibrated sample and will better control for unknown biases in metallicity, dust, or progenitor age.

Adopting the 47.2% SN Iaϵ fraction we find for R11 and the 7.0% SN Iaϵ fraction found by R15 for the Cepheid sample with Equation 3.1, we find no evidence for a reduced value of H_0. Following R15, if we were to replace the host mass step with the LSF step, our measurement suggests a 0.1% increase in H_0 because the size of the LSF correction is slightly less than the size of the host mass correction.

One caveat is that R11 added the MLCS intrinsic SN Ia dispersion but not the full apparent intrinsic dispersion in quadrature to the distance modulus uncertainties in their Hubble flow SNe. We find that forcing our maximum likelihood gaussian model to use only the MLCS intrinsic dispersion of 0.08 mag raises the magnitude of the $R_V = 2.5$ LSF step we derive to 0.045±0.019 (a 2.4σ detection, but 2.1σ with systematic uncertainty added). This could be because it allows outliers to have a greater effect on the measurement. However, applying this correction after removing the host mass step still only results in a reduction in H_0 of 0.11 km s^{-1} Mpc^{-1}. The R11 value for H_0 is within the 1σ uncertainty of the LSF step. The highest LSF step we are able to find using all our analysis variants with 0.08 mag dispersion is 0.066±0.22 mag (the 2.5σ-clipped variant), and even this extreme measurement lowers H_0 by only 0.4 km s^{-1} Mpc^{-1}.

Finally, if we measure the LSF step *after* host mass correction using masses from

Neill et al. (2009, 53% of the R11 sample) and again using a dispersion of 0.08 mag, we find a LSF step of 0.023±0.027 (stat+sys) mag for $R_V = 2.5$. This results in a small reduction of 0.3 km s^{-1} Mpc^{-1}. Because we detect this effect at $<1\sigma$ (with systematic error added in quadrature), we do not believe a correction is justified.

3.6.3 Future Measurement of the LSF Step

Although we have only detected the LSF step at low significance with GALEX FUV data, GALEX alone is not the best tool for studying local regions due to its large PSF width and the uncertain UV extinction correction. The LSF step would be best identified in local Hα (e.g. Rigault et al. (2013)), high-resolution UV data from the *Hubble Space Telescope* (HST), or local SED fitting.

Table 3.3 shows that sample selection has a significant effect on our results. We suggest that studies examining host galaxy effects use the same SN Ia samples and selection criteria as the latest cosmology analyses when possible. It may be possible to detect the LSF step or differences in dispersion at higher significance using different light curve or distance modulus cuts, but the results of such analyses would not necessarily apply to typical measurements of cosmological parameters.

Local SED fitting may be the optimal approach for studying the relation between host galaxy properties and SN Ia distances, as it can put simultaneous (albeit sometimes degenerate) constraints on a number of parameters that may correlate with SN Ia distances such as stellar age, extinction, star formation history, and mass con-

tained in a local region. Approaches that don't depend entirely on GALEX data will also be able to measure local regions at higher redshifts and put better contraints on possible redshift-dependent biases.

The size of the samples with which we can examine the effects of host galaxy properties on SN Ia corrected magnitudes will increase dramatically in the next few years. The PS1 photometric sample alone will consist of up to ∼2,000 SNe Ia with cosmologically-useful light curves. The Dark Energy Survey (DES) will contribute thousands more up to redshifts of ∼1. Although measurements of local regions become more difficult at high-z, a ground-based optical survey with PSF FWHM ∼1 arcsec will be able to use a much larger SN sample provided the absence of UV data is not prohibitive. Surveys such as PS1 or DES are able to examine local regions of 5 kpc diameter, similar in size to the apertures used in this study, up to $z \simeq 0.35$.

3.7 Conclusions

Analyzing the same SNe Ia used to determine the most recent values of w and H_0, we find little evidence for a LSF step, which suggests that correcting cosmological parameters for this effect is not necessary. There is only 1.1σ evidence for the LSF step in R11 MLCS data assuming $R_V = 2.5$ (the R_V R11 used in their baseline analysis) and 0.0σ evidence for the LSF step in JLA+PS1 SALT2 data. Our most significant detection uses MLCS data assuming $R_V = 2.0$, for which we find 2.4σ

evidence for a step. The sizes of both of these steps are greatly reduced compared to the measurement of R15. Lower values of β in SALT2 and R_V in MLCS may increase the size and the significance of the LSF step.

Compared to R15, differences in our Σ_{SFR} measurement and dust correction technique reduced the size of the MLCS LSF step by $\sim$20% and increased the SALT2 LSF step by $\sim$15%. Using MLCS sample cuts from R11 reduced the offset by an additional $\sim$20% and adding the full R11 sample reduced the offset to 0.029$\pm$0.027 mag, likely due to the higher dispersion and better statistics of the full sample. Using new distance moduli and sample cuts from only Betoule et al. (2014) (and not H09) reduced the SALT2 LSF step by 60% and using the full JLA+PS1 sample reduced the SALT2 step to a value of 0.000$\pm$0.018 mag.

MLCS sample cuts have a significant impact on the results. MLCS Hubble diagram residuals are more negative at greater A_V and Δ, which must be carefully taken into account in cosmological analyses. In particular, passive hosts are known to have preferentially higher Δ but lower A_V (H09). We suspect that because the R15 sample had few high-A_V SNe but a wide range of Δ, their locally star-forming SNe had preferentially fainter Hubble residuals.

We found that JLA+PS1 SNe fit with SALT2 had lower dispersion than MLCS-fit R11 SNe in star-forming *or* passive environments. We also found that locally star-forming SNe in our sample did not have lower dispersion at $\log(\Sigma_{\rm SFR}) > -2.9$. In MLCS with $R_V = 3.1$, SNe Ia in locally passive environments have lower dispersion

than those in locally star-forming environments by ∼0.09 mag, a 2.5σ result. Using MLCS with $R_V = 2.5$, we see a 0.053±0.029 mag difference.

The lowest SN Ia dispersions come from using SALT2 distance moduli. In contrast to Kelly et al. (2015), with MLCS we found no evidence that SNe in highly star-forming environments have lower dispersion than locally passive SNe using $R_V = 2.0$. With $R_V = 3.1$ we found that SNe in star-forming environments had *greater* dispersion (∼1-2σ significance), but note that we did not make the Kelly et al. (2015) sample cuts. We can only reproduce the Kelly et al. (2015) results by using their strict cuts on the SN light curve parameters Δ and A_V and removing SNe with Hubble residuals >0.3 mag, which restricts our sample to largely the same data as Kelly et al. (2015).

The LSF step may also be difficult to detect because of the large PSF width of GALEX and it may also be that the LSF step is only apparent in analyses with certain types of light curve selection or outlier rejection. Future studies with local Hα, SED fitting, or HST UV observations will have an improved ability to detect local effects. Our results also show that certain SN sample cuts may inadvertently increase biases in cosmology. We expect that with the large SN Ia samples from PS1 and DES that will be published in the next few years, the systematic uncertainties on H_0 and the dark energy equation of state will come into clearer focus.

3.8 Appendix

3.8.1 Calculation of Probabilities and Maximum Likelihood Estimation

The only significant difference between our method of measuring the maximum likelihood LSF step and Hubble residual dispersions and the R15 method is that we allowed the intrinsic dispersion of both SN Ia populations (Iaϵ and Iaα) to be fit by our maximum likelihood model. We describe our full procedure below.

We first converted the dust-corrected FUV flux into $\Sigma_{\rm SFR}$ following R15 (their Equation 1). We set the boundary between the locally star-forming and locally passive population at $\log(\Sigma_{SFR}) = -2.9$ as in R15, and measured the probability that the SN Ia exploded in a locally passive environment based on the full probability distribution from our dust-corrected photometric measurements.

We used these probabilities to construct a maximum likelihood model assuming two gaussian populations of SNe with different mean Hubble residuals and dispersions. The likelihood is determined by the equation:

$$\begin{aligned}\mathcal{L}_i = P(Ia\alpha) \times \frac{1}{\sqrt{2\pi(\sigma_i^2+\sigma_\alpha^2)}} \exp(-\frac{(M_{B,i}^{corr}-\mu_\alpha)^2}{2(\sigma_i^2+\sigma_\alpha^2)}) \\ +P(Ia\epsilon) \times \frac{1}{\sqrt{2\pi(\sigma_i^2+\sigma_\epsilon^2)}} \exp(-\frac{(M_{B,i}^{corr}-\mu_\epsilon)^2}{2(\sigma_i^2+\sigma_\epsilon^2)}),\end{aligned} \tag{3.3}$$

where $M_{B,i}^{corr}$ is the corrected magnitude and σ_i is the corrected magnitude uncertainty of a given SN Ia. P(Iaα) and P(Iaϵ) are the probabilities that the SN environment

is locally star-forming or locally passive, respectively. μ_α, μ_ϵ, σ_α and σ_ϵ are free parameters equal to the means and standard deviations of the normal distributions of SNe Iaα and Iaϵ. To determine what these parameters are, we found the maximum likelihood model by minimizing:

$$\log(\mathcal{L}) = -2\sum_{i=1}^{N}\log(\mathcal{L}_i) \tag{3.4}$$

where N is the number of SNe Ia in the sample.

Instead of adding an intrinsic dispersion term in quadrature to the Hubble residuals such that the reduced χ^2 of the sample is 1, as is commonly done in cosmological analyses (and in R15), we fit to the standard deviations of our gaussian maximum likelihood model for SNe Iaα and Iaϵ. We verified that allowing the dispersion to be fit by our model instead of specifying it beforehand does not affect our results.

Table 3.4. The LSF Step Sample

Name	Survey[a]	z	JLA+PS1	R11 MLCS2k2 $\Delta M_B^{\rm corr}$			GALEX data		Global	R[b]	Dust Corr.	$\log(\Sigma_{\rm SFR})$	P(Iaϵ)	Cuts
			SALT2 $\Delta M_B^{\rm corr}$	R_V =2.0	R_V =2.5	R_V = 3.1	Exp.	FUV	Host Class					
							(s)	(mag)				($M_\odot kpc^{-2}yr^{-1}$)	(%)	
010010	PS1	0.100	0.270±0.113	···	···	···	10629	24.90±0.21	SF	5.37	N	$-3.072^{+0.081}_{-0.076}$	98	Incl
010026	PS1	0.032	0.092±0.159	···	···	···	16222	21.75±0.04	SF	1.28	Y	$-2.239^{+0.054}_{-0.050}$	0	···
070242	PS1	0.064	0.167±0.129	···	···	···	92341	28.82±1.09	SF	35.00	N	$-4.898^{+0.259}_{-0.460}$	100	···
10028	SDSS	0.064	-0.102±0.117	···	···	···	3272	25.68±0.60	Pa	0.46	N	$-3.712^{+0.194}_{-0.223}$	100	···
10805	SDSS	0.044	-0.198±0.128	···	···	···	8006	21.02±0.04	SF	0.88	Y	$-1.501^{+0.062}_{-0.053}$	0	···
1241	SDSS	0.088	-0.092±0.108	···	···	···	1670	26.04±1.50	SF	4.84	N	$-3.321^{+0.254}_{-0.422}$	97	···
12779	SDSS	0.079	0.055±0.122	···	···	···	206	24.47±2.07	SF	1.91	Y	$-1.983^{+0.384}_{-0.592}$	15	···
12781	SDSS	0.083	0.191±0.119	···	···	···	3354	>26.43	Pa	3.34	N	< -3.670	100	···
12898	SDSS	0.083	0.002±0.107	···	···	···	1627	23.38±0.24	SF	0.94	Y	$-2.166^{+0.170}_{-0.295}$	4	···
12950	SDSS	0.081	0.078±0.102	···	···	···	4954	22.01±0.08	SF	0.55	Y	$-1.817^{+0.112}_{-0.105}$	0	···
130308	PS1	0.082	0.037±0.123	···	···	···	4024	24.99±0.32	∼SF	0.90	Y	$-2.451^{+0.208}_{-0.329}$	12	Incl
17240	SDSS	0.071	-0.159±0.143	···	···	···	3053	>27.31	Pa	4.15	N	< -3.970	100	···
17258	SDSS	0.088	-0.188±0.118	···	···	···	4130	23.73±0.20	SF	0.88	Y	$-1.900^{+0.159}_{-0.251}$	1	···
17745	SDSS	0.062	-0.000±0.117	···	···	···	1643	23.34±0.26	SF	0.89	Y	$-1.973^{+0.176}_{-0.271}$	2	···
18241	SDSS	0.094	0.176±0.165	···	···	···	544	24.19±0.95	SF	1.07	Y	$-1.888^{+0.292}_{-0.403}$	5	···
19899	SDSS	0.090	-0.048±0.107	···	···	···	2147	25.57±0.92	SF	5.88	N	$-3.220^{+0.187}_{-0.334}$	96	···
1990af	JRK07	0.050	-0.063±0.160	-0.213±0.170	-0.204±0.178	-0.205±0.188	336	>24.09	Pa	1.77	N	< -3.230	100	···
1990o	JRK07	0.031	-0.107±0.150	-0.071±0.140	-0.050±0.144	-0.037±0.147	145	22.13±0.67	SF	2.95	Y	$-2.156^{+0.300}_{-0.422}$	9	···

Note. — The full table is available online at `http://www.pha.jhu.edu/~djones/lsfstep.html`.

[a]JRK refers to the Jha et al. (2007) sample, which includes SNe from the CfA1, CfA2, and Calan/Tololo SN surveys Riess et al. (1999); Jha et al. (2006); Hamuy et al. (1996).

[b]SN separation from the host galaxy, normalized by the SExtractor-measured host galaxy size Sullivan et al. (2006). We did not apply a local dust correction for SNe with R > 3, as these are outside the isophotal radius of the host.

*Visual inspection found that this SN Ia was within the isophotal radius of it's host. A dust correction was applied.

Table 3.5. Local Star Formation Step

	SALT2			MLCS R_V=2.0			MLCS R_V=2.5			MLCS R_V=3.1		
Analysis Change	SNe	$\delta(M_B^{\rm corr})_{SF}$	Sig.	SNe	$\delta(M_B^{\rm corr})_{SF}$	Sig.	SNe	$\delta(M_B^{\rm corr})_{SF}$	Sig.	SNe	$\delta(M_B^{\rm corr})_{SF}$	Sig.
None	179	0.000±0.018	0.0σ (0.0σ)	157	0.059±0.023	2.6σ (2.5σ)	156	0.029±0.025	1.2σ (1.0σ)	155	0.013±0.028	0.5σ (0.4σ)
$P(A_{FUV})$=1.0±0.6	179	-0.008±0.017	-0.4σ (-0.4σ)	157	0.062±0.023	2.7σ (2.6σ)	156	0.029±0.025	1.1σ (1.0σ)	155	0.012±0.028	0.4σ (0.4σ)
$P(A_{FUV})$=3.0±0.6	179	0.005±0.018	0.3σ (0.3σ)	157	0.060±0.023	2.6σ (2.5σ)	156	0.031±0.025	1.3σ (1.1σ)	155	0.016±0.027	0.6σ (0.5σ)
Σ_{SFR} boundary = -3.1	179	0.017±0.018	1.0σ (0.9σ)	157	0.071±0.023	3.1σ (2.9σ)	156	0.044±0.025	1.8σ (1.6σ)	155	0.028±0.027	1.0σ (0.9σ)
Σ_{SFR} boundary = -2.7	179	-0.005±0.018	-0.3σ (-0.3σ)	157	0.067±0.022	3.0σ (2.8σ)	156	0.031±0.025	1.3σ (1.1σ)	155	0.009±0.028	0.3σ (0.3σ)
1 kpc aper. radius	179	-0.005±0.018	-0.3σ (-0.3σ)	157	0.051±0.023	2.2σ (2.1σ)	156	0.018±0.025	0.7σ (0.6σ)	155	0.005±0.029	0.2σ (0.2σ)
3 kpc aper. radius	179	0.022±0.018	1.2σ (1.2σ)	157	0.057±0.024	2.4σ (2.3σ)	156	0.031±0.025	1.3σ (1.1σ)	155	0.016±0.027	0.6σ (0.5σ)
4 kpc aper. radius	179	0.007±0.019	0.4σ (0.4σ)	157	0.034±0.025	1.4σ (1.3σ)	156	0.012±0.026	0.5σ (0.4σ)	155	-0.001±0.028	-0.0σ (-0.0σ)
Global instead of local SFR	179	-0.001±0.019	-0.1σ (-0.1σ)	157	-0.013±0.023	-0.6σ (-0.5σ)	156	0.002±0.025	0.1σ (0.1σ)	155	0.008±0.029	0.3σ (0.2σ)
2.5σ-clipping	171	0.005±0.016	0.3σ (0.3σ)	151	0.047±0.021	2.2σ (2.1σ)	147	0.046±0.022	2.1σ (1.8σ)	148	0.039±0.024	1.6σ (1.4σ)
Sys. Error[a]		0.004			0.007			0.014			0.014	

[a]The systematic error is computed from the standard deviation of each type of variant (e.g. aperture size variants, SFR boundary variants, etc.). The global SFR variant is excluded.

Table 3.6. Star Formation Dispersion

	SALT2			MLCS R_V=2.0			MLCS R_V=2.5			MLCS R_V=3.1		
Analysis Change	SNe	$\sigma_{SF} - \sigma_{passive}$	Sig.	SNe	$\sigma_{SF} - \sigma_{passive}$	Sig.	SNe	$\sigma_{SF} - \sigma_{passive}$	Sig.	SNe	$\sigma_{SF} - \sigma_{passive}$	Sig.
None	179	-0.013±0.018	**-0.7σ (-0.7σ)**	157	-0.033±0.024	**-1.4σ (-1.2σ)**	156	-0.053±0.024	**-2.2σ (-1.8σ)**	155	-0.086±0.026	**-3.3σ (-2.5σ)**
$P(A_{FUV})$=1.0±0.6	179	-0.003±0.017	**-0.2σ (-0.2σ)**	157	-0.035±0.024	**-1.5σ (-1.3σ)**	156	-0.061±0.025	**-2.5σ (-2.1σ)**	155	-0.096±0.027	**-3.6σ (-2.8σ)**
$P(A_{FUV})$=3.0±0.6	179	-0.016±0.018	**-0.9σ (-0.9σ)**	157	-0.028±0.024	**-1.2σ (-1.1σ)**	156	-0.047±0.024	**-1.9σ (-1.6σ)**	155	-0.077±0.026	**-3.0σ (-2.3σ)**
Σ_{SFR} boundary = -3.1	179	-0.006±0.018	**-0.3σ (-0.3σ)**	157	-0.032±0.024	**-1.3σ (-1.2σ)**	156	-0.054±0.025	**-2.1σ (-1.8σ)**	155	-0.087±0.026	**-3.3σ (-2.6σ)**
Σ_{SFR} boundary = -2.7	179	-0.017±0.018	**-1.0σ (-0.9σ)**	157	-0.031±0.024	**-1.3σ (-1.1σ)**	156	-0.053±0.025	**-2.2σ (-1.8σ)**	155	-0.087±0.026	**-3.3σ (-2.6σ)**
1 kpc aper. radius	179	-0.004±0.018	**-0.2σ (-0.2σ)**	157	0.024±0.023	1.0σ (0.9σ)	156	-0.009±0.025	**-0.4σ (-0.3σ)**	155	-0.058±0.027	**-2.1σ (-1.7σ)**
3 kpc aper. radius	179	-0.003±0.019	**-0.2σ (-0.2σ)**	157	-0.023±0.024	**-0.9σ (-0.8σ)**	156	-0.042±0.025	**-1.7σ (-1.4σ)**	155	-0.074±0.026	**-2.9σ (-2.2σ)**
4 kpc aper. radius	179	-0.016±0.021	**-0.8σ (-0.8σ)**	157	-0.016±0.025	**-0.6σ (-0.6σ)**	156	-0.029±0.026	**-1.1σ (-1.0σ)**	155	-0.057±0.027	**-2.1σ (-1.7σ)**
Global instead of local SFR	179	-0.038±0.018	**-2.1σ (-2.1σ)**	157	0.013±0.023	0.6σ (0.5σ)	156	0.025±0.024	1.0σ (0.9σ)	155	0.012±0.026	0.4σ (0.3σ)
2.5σ-clipping	173	-0.015±0.017	**-0.9σ (-0.9σ)**	153	-0.008±0.022	**-0.3σ (-0.3σ)**	151	-0.018±0.023	**-0.8σ (-0.6σ)**	151	-0.032±0.025	**-1.3σ (-1.0σ)**
Sys. Error[a]		0.003			0.013			0.016			0.022	

[a]The systematic error is computed from the standard deviation of each type of variant (e.g. aperture size variants, SFR boundary variants, etc.). The global SFR variant is excluded.

Table 3.7. Star Formation Dispersion with Kelly et al. (2015) SFR Boundaries

		SALT2			MLCS R_V=2.0				MLCS R_V=2.5				MLCS R_V=3.1			
Σ_{SFR} boundary	SNe	$\sigma_{passive}$	σ_{SF}	Sig.	SNe	$\sigma_{passive}$	σ_{SF}	Sig.	SNe	$\sigma_{passive}$	σ_{SF}	Sig.	SNe	$\sigma_{passive}$	σ_{SF}	Sig.
-1.7 dex	179	0.127±0.010	0.118±0.034	0.3σ	157	0.145±0.013	0.141±0.046	0.1σ	156	0.193±0.014	0.138±0.065	0.9σ	155	0.198±0.014	0.265±0.061	-1.1σ
-1.85 dex	179	0.114±0.010	0.118±0.026	-0.1σ	157	0.146±0.013	0.129±0.035	0.5σ	156	0.169±0.014	0.171±0.040	-0.0σ	155	0.177±0.014	0.256±0.044	-1.8σ

Chapter 4

Measuring the Properties of Dark Energy with Photometrically Classified Pan-STARRS Supernovae. I. Systematic Uncertainty from Core-Collapse

Supernova Contamination

4.1 Abstract

The Pan-STARRS (PS1) Medium Deep Survey discovered over 5,000 likely supernovae (SNe) but obtained spectral classifications for just 10% of its SN candidates. We measured spectroscopic host galaxy redshifts for 3,147 of these likely SNe and estimate that ∼1,000 are Type Ia SNe (SNe Ia) with light-curve quality sufficient for a cosmological analysis. We use these data with simulations to determine the impact of core-collapse SN (CC SN) contamination on measurements of the dark energy equation of state parameter, w. Using the method of Bayesian Estimation Applied to Multiple Species (BEAMS), distances to SNe Ia and the contaminating CC SN distribution are simultaneously determined. We test light-curve based SN classification priors for BEAMS as well as a new classification method that relies upon host galaxy spectra and the association of SN type with host type. By testing several SN classification methods and CC SN parameterizations on large SN simulations, we estimate that CC SN contamination gives a systematic error on w (σ_w^{CC}) of 0.014, 29% of the statistical uncertainty. Our best method gives $\sigma_w^{CC} = 0.004$, just 8% of the statistical uncertainty, but could be affected by incomplete knowledge of the CC SN distribution. This method determines the SALT2 color and shape coefficients, α and β, with ∼3%

bias. However, we find that some variants require α and β to be fixed to known values for BEAMS to yield accurate measurements of w. Finally, the inferred abundance of bright CC SNe in our sample is greater than expected based on measured CC SN rates and luminosity functions.

4.2 Introduction

Since the discovery of cosmic acceleration (Riess et al., 1998; Perlmutter et al., 1999), measuring the properties of dark energy with Type Ia supernovae (SNe Ia) has been predicated on the spectroscopic confirmation of SN Ia candidates. However, as the size of individual SN Ia samples surpasses 1,000 SNe, obtaining spectra for each Type Ia candidate is becoming prohibitively expensive. Only a small fraction of SNe Ia from current and future surveys such as the Dark Energy Survey (DES) and the Large Synoptic Survey Telescope (LSST) will have spectroscopic classification. Without spectroscopic classification, core-collapse SN (CC SN) contamination can bias our estimates of cosmological parameters (Falck et al., 2010, Kunz, Bassett, & Hlozek, 2007).

Without SN spectroscopy, the shape and color of a photometric SN light curve can be used as a less precise diagnostic of the type. Campbell et al. (2013) used SDSS *ugriz* light curves to classify 752 SNe as likely Type Ia, enough to measure the dark energy equation of state, w, with $\sim$10% statistical uncertainty. Their sample was

selected from light curve properties and a classifier that compares each observed light curve to SN Ia and CC SN templates (PSNID; Sako et al., 2011). Their final sample comprised just 3.9% CC SNe. While Campbell et al. (2013) is the *only* SN Ia-based measurement of w to date that does not use spectroscopic classification for its SNe, the measurement did not include systematic uncertainties. In addition, contaminating CC SNe bias their measurements of SN Ia dispersion and the correlation between SN luminosity and light curve rise/decline rate by $\sim$60%.

Many light curve classifiers use the "naïve Bayes" approximation, which assumes all observables that indicate SN type are uncorrelated. Machine learning techniques can often outperform these classifiers, yielding higher SN Ia classification efficiency (the fraction of SNe Ia classified correctly) and lower CC SN contamination (Lochner et al., 2016; Möller et al., 2016). On SDSS SN data, the Sako et al. (2014) kd-tree nearest neighbor (NN) method has a purity comparable to Campbell et al. (2013) but accurately classifies $\sim$1.4 times as many real SNe Ia in a given sample.

An important caveat is that nearly all classifiers are optimized on simulations with little evaluation on real data. Simulations, in turn, depend on CC SN templates and knowledge of the CC SN luminosity functions (LFs) and rates. CC SNe are diverse, far more so than SNe Ia, and only a limited number of high-quality templates are publicly available. Training a classifier directly on survey data is possible but can be sub-optimal due to limited numbers of CC SNe observed and the dependence of classifier results on the specific survey characteristics (e.g. observing cadences, filters,

and signal-to-noise ratios).

We can make SN classification less dependent on CC SN templates, LFs, and rates by incorporating host galaxy data. Because many SNe Ia have a $\gtrsim$1 Gyr delay time between progenitor formation and explosion (Rodney et al., 2014), they are the only type of SNe found in early-type galaxies (with very few known exceptions; Suh et al., 2011). Foley & Mandel (2013) found that it was possible to accurately classify the $\sim$20% of SNe Ia found in elliptical galaxies if the morphology of their host galaxy is known.

Though these results are encouraging, light curve and host galaxy classification alone may not be enough to enable a measurement of w as precise as measurements using spectroscopically classified SNe (e.g. Betoule et al., 2014, $w = -1.027 \pm 0.055$). A difference in w of 5% corresponds to a change of 0.02 mag from $z = 0$ to $z = 0.5$; if CC SNe are 1 mag fainter than SNe Ia on average, a bias of 0.02 mag can be induced by just 2% CC SN contamination in a high-z sample such as PS1. If the contaminating distribution of CC SNe is more than 1 mag fainter (this depends on survey Malmquist bias), it takes even fewer CC SNe to bias w by an equivalent amount.

A Bayesian method, however, could use the probabilities that SNe are of type Ia as priors to simultaneously determine distances to Ia and CC SNe without bias. We refer to this method as Bayesian Estimation Applied to Multiple Species (BEAMS) following Kunz, Bassett, & Hlozek (2007) (hereafter KBH07; see also Press, 1997 and Rubin et al., 2015). KBH07 test BEAMS on a simplistic SN simulation and find that

it gives near-optimal accuracy and uncertainties on SN Ia distances.

Hlozek et al. (2012) test BEAMS further with Monte Carlo simulations of the Sloan Digital Sky Survey SN survey (SDSS-SN; Frieman et al., 2008; Kessler et al., 2009a). BEAMS biases measurements of the cosmic matter and dark energy densities, Ω_M and Ω_Λ, by less than the statistical uncertainties measured from their simulations. Their results demonstrated that SDSS SNe without spectroscopic classification can significantly improve cosmological constraints relative to the SDSS spectroscopic sample (Kessler et al., 2009a). Hlozek et al. (2012) did not measure the systematic uncertainties from their method.

As with SDSS, Pan-STARRS (PS1) discovered far more SNe Ia than could be observed spectroscopically. Spectroscopically-confirmed SNe Ia from the first $\sim$1/3 of PS1 have been used to measure cosmological parameters but constitute only a small fraction of the available data (Rest et al., 2014, hereafter R14; Scolnic et al., 2014b). In this study, we use PS1 SNe with and without spectroscopic classification as a tool for testing SN classifiers, understanding CC SN contaminants and measuring the systematic error due to CC SN contamination. In total, PS1 has 1,145 SNe with high quality light curves and spectroscopic redshifts − both host galaxy and SN redshifts − that can be used to measure cosmological parameters (including a $\sim$few percent CC SN contamination). Here, we focus on the 1,020 likely SNe Ia with spectroscopic host galaxy redshifts, 143 of which are spectroscopically confirmed, in order to study a sample with fewer selection biases (§4.3.1).

The goal of this study is to develop the methods necessary to measure cosmological parameters robustly using PS1 SNe without spectroscopic classifications (hereafter referred to as photometric SNe). Our full cosmological results from these data will be presented in a future analysis.

In §4.3, we present the sample and our host galaxy redshift followup survey. §5.3.2.1 discusses our SNANA simulations of the PS1 sample and our assumptions about the CC SN population. §4.5 describes our Bayesian parameter estimation methodology. In §4.6 we test BEAMS on simulations and subsamples of PS1 photometric SNe. In §4.7 we test the robustness of these results by exploring several variants of the method. The uncertainties in our simulations and methodology are discussed in §4.8 and our conclusions are in §5.10.

4.3 The Pan-STARRS Photometric Supernova Sample

The Pan-STARRS medium deep survey covers 10 7-square degree fields in five broadband filters, with typical $griz_{P1}$ observational cadences of 6 images per 10 days and a 5 day gap during bright time during which y_{P1} images are taken. Typical 5σ detection limits are $\sim$23 AB mag for $griz_{P1}$, albeit with significant variation. For a complete description of the PS1 survey, see Kaiser et al. (2010) and R14.

PS1 images are processed using an image subtraction pipeline that is described

in detail in Rest et al. (2005) and R14. To measure final light curves for the PS1 photometric sample (and the full spectroscopic sample; Scolnic et al. in prep), we made several improvements to that pipeline. We more than doubled the typical number of images that are combined to create a deep template for subtraction, we refined our method of selecting stars to build the point spread function (PSF) model, and we improved the zeropoint calibration. These improvements will be described in detail in Scolnic et al. (in prep.).

Pan-STARRS discovered 5,235 likely SNe during its four years of operation and obtained spectra for 520 SNe. We collected 3,147 spectroscopic host galaxy redshifts of these likely SNe (§4.3.1). In addition to SN candidates, we observed spectra for thousands of variable stars, AGN, flaring M dwarfs, and other transients that will be published in future work.

4.3.1 Host Galaxy Redshift Survey

During the PS1 survey, many SN host redshifts were measured using the Hectospec multi-fiber instrument on the MMT (Fabricant et al., 2005; Mink et al., 2007). Near the end of PS1 operations, we began an additional survey with Hectospec to obtain redshifts for as many host galaxies as possible. Redshifts were also obtained with the Apache Point Observatory 3.5m telescope[1] (APO), the WIYN telescope[2], and for the

[1] `http://www.apo.nmsu.edu/arc35m/`

[2] The WIYN Observatory is a joint facility of the University of Wisconsin-Madison, Indiana University, the National Optical Astronomy Observatory and the University of Missouri.

Table 4.1. Redshift Follow-up Summary

Telescope	Instrument	SN Redshifts[a]	$\lambda_{min} - \lambda_{max}$ Å	Avg. Exp. Time min.	Approx. Resolution Å pix^{-1}	$z_{\rm median}$
AAT	AAOmega	512	3700 − 8500	180	6	0.15
APO	DIS	10	3500 − 9800	60	2.5	0.24
MMT	Hectospec	2348	3700 − 9200	90	5	0.33
SDSS	BOSS	250	3800 − 9200	45	2.5	0.20
WIYN	Hydra	45	3700 − 6500	180	4.5	0.34
Other[b]	···	361	···	···	···	0.19
Total	···	3,147	···	···	···	0.30

Note. — Some transient hosts were observed with multiple telescopes. Numbers include host galaxy observations of both spectroscopically confirmed and unconfirmed SN candidates.

[a]Number of SN candidates with reliable redshifts.

[b]Includes redshifts from 2dFGRS (Colless et al., 2003), 6dFGS (Jones et al., 2009), DEEP2 (Newman et al., 2013), VIPERS (Scodeggio et al., 2016), VVDS (Le Fèvre et al., 2005), WiggleZ (Blake et al., 2008) and zCOSMOS (Lilly et al., 2007).

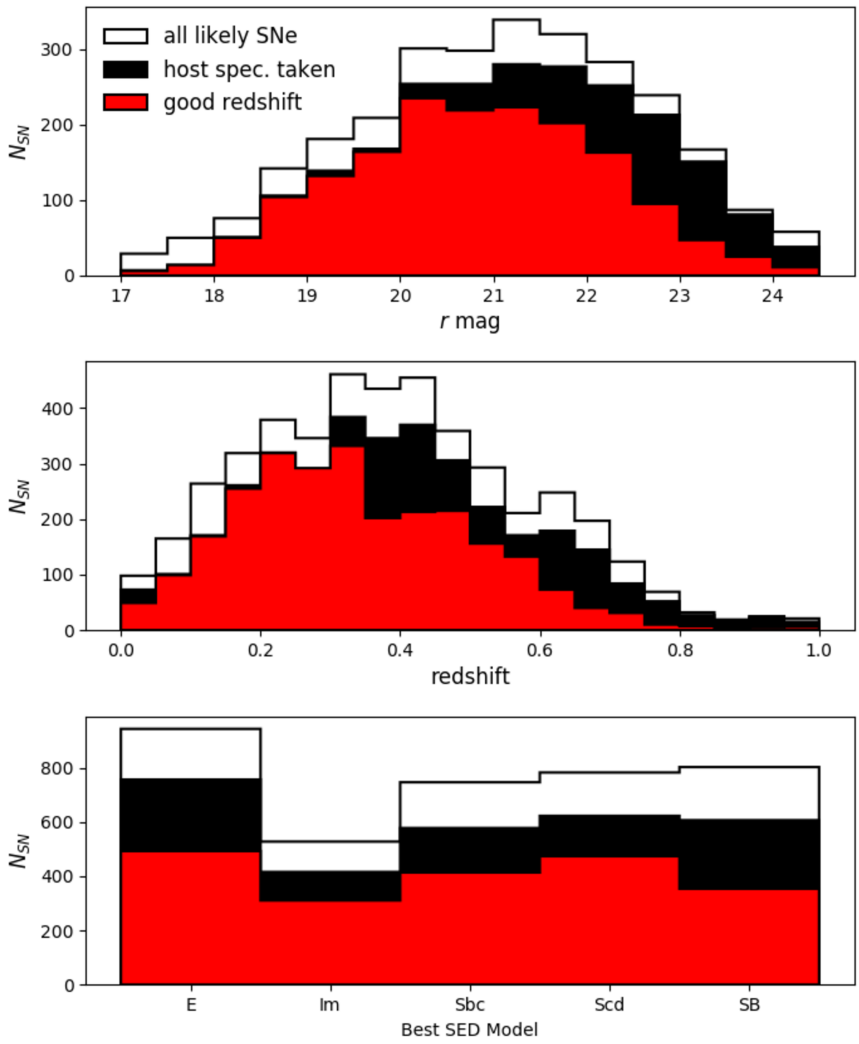

Figure 4.1: Host properties from PS1 as a function of r mag, redshift, and best-fit SED model. Out of the full sample of 5,235 PS1 SNe (white; host galaxy photo-z), we observed 3,930 hosts (black; photo-z) and measured accurate redshifts for 3,147 (red; spec-z). Our redshift survey has nearly 100% success to $r = 21$ and has a median redshift of 0.30. We obtained redshifts for a large number of both emission-line and absorption-line galaxies.

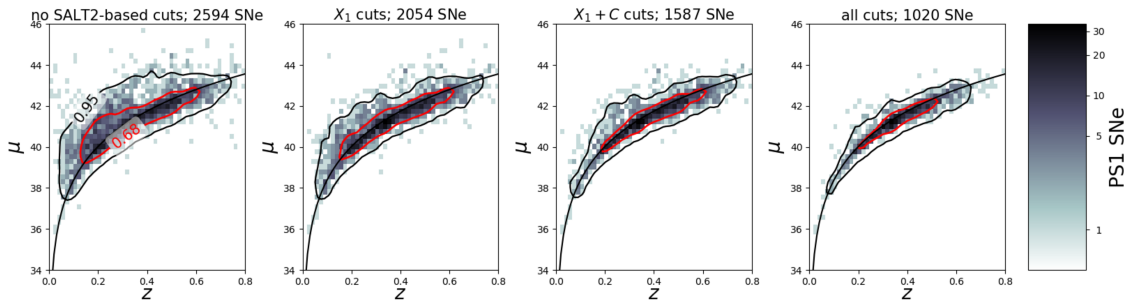

Figure 4.2: The effect of Betoule et al. (2014) cuts on the PS1 photometric Hubble diagram. Distance moduli are measured using the Tripp estimator (Eq. 5.1) with nuisance parameters from R14. Of the 2,594 SNe that are fit by SALT2 and are not possible AGN, shape and color cuts remove 1,007, while χ^2-based fit probability cuts and SNR-type cuts (shape uncertainty and time of maximum uncertainty) remove an additional 567 SNe, leaving 1,020. Each set of cuts removes a mix of SNe Ia with poor light curve quality and CC SNe.

southern-most PS1 field, the Anglo-Australian Telescope (AAT). We chose candidate host galaxies for follow-up in a largely unbiased way; we did not prioritize SNe based on their magnitudes, colors, or whether or not a SN spectrum had previously been obtained. Approximately 600 of our redshifts come from SDSS (Smee et al., 2013) or other public redshift surveys[3].

We used the galaxy size- and orientation-weighted R parameter to identify the most likely host galaxy for each SN (Sullivan et al., 2006). The isophotal limit of a galaxy corresponds to $R \sim 3$. We use the redshift of the host galaxy with the lowest R if it has $R \leq 5$ following Sullivan et al. (2006). See Gupta et al. (2016) for a similar but more rigorous method of identifying SN host galaxies.

[3]We include redshifts from 2dFGRS (Colless et al., 2003), 6dFGS (Jones et al., 2009), DEEP2 (Newman et al., 2013), VIPERS (Scodeggio et al., 2016), VVDS (Le Fèvre et al., 2005), WiggleZ (Blake et al., 2008) and zCOSMOS (Lilly et al., 2007).

To estimate the fraction of SNe for which we incorrectly determined which galaxy was the host, we compared redshifts derived from the spectroscopic redshifts of SNe to the spectroscopic redshifts of their most likely host galaxies. We found that only 2 of 169 hosts with reliable redshifts had evidence of a host galaxy mismatch, $|z_{SN} - z_{host}| > 0.02$. Both of these hosts had multiple large, nearby galaxies with $R < 5$. This mismatch fraction suggests that 1.2±0.5% of our redshifts are incorrect due to mismatched hosts.

Compared to spectroscopically confirmed SNe, it is unlikely that photometric SNe have a higher fraction of mismatched hosts. The spectroscopic targeting preferentially followed SNe with a larger separation from the center of their host galaxies or SNe with fainter hosts, as these SNe have spectra with less galaxy light contamination. Just 11% of photometrically classified SNe are outside the isophotal radii of their host galaxies compared to 24% of the 169 SN-host pairs. However, we also note that the 169 SN-host pairs have preferentially brighter hosts than the full sample and have a median redshift of 0.21 compared to the median redshift of 0.3 for the full sample. It may be somewhat easier to mismatch a host galaxy at high-z as galaxies are more difficult to detect, but we expect this to be a subdominant effect as Gupta et al. (2016) finds the fraction of mismatched hosts to be approximately constant at $z < 0.6$ in a DES-like survey (which has similar depth to PS1 templates).

The other source of incorrect redshifts is the measurement of velocities from host galaxy spectra. We measured redshifts by cross-correlating our spectra with galaxy

templates (The RVSAO package; Kurtz & Mink, 1998) and visually inspecting the results. Over the course of the survey, we observed over 1,500 transient hosts multiple times. For ∼250 of these hosts, at least one observation yielded a redshift with a high Tonry & Davis (1979) cross-correlation parameter (TDR; $\gtrsim 9-10$).

By restricting our sample to hosts with TDR > 4 and redshifts of $0.01 < z < 0.75$, we measure a false redshift fraction of $1.4 \pm 1.3\%$. At $z > 0.75$, few SNe could be discovered by PS1 or have their host redshifts measured with our program (Figure 4.1). Including mismatched hosts, the total percent of incorrect redshifts we expect is $2.6 \pm 1.4\%$. In §5.3.2.1 we simulate this fraction of false redshifts so that this effect will be incorporated in our BEAMS systematic error budget.

In total, we observed 3,930 host galaxies and have 3,147 reliable redshifts. The telescopes and instruments comprising our redshift survey are summarized in Table 4.1. Figure 4.1 shows the r magnitudes, redshifts, and best-fit SED model for the PS1 photometric sample. 87% of PS1 SNe with detectable host galaxies were observed with our redshift follow-up program and reliable redshifts were measured for 73% of those galaxies. We measured redshifts for a large number of both emission-line and absorption-line galaxies. These data have a median redshift of 0.30.

4.3.2 SALT2 Selection Requirements

Throughout this work, we use the SALT2.4 model (Guy et al., 2010, implemented in B14) to measure SN light curve parameters. We use these light curve parameters

Table 4.2. Sequential PS1 Data Cuts

	Removed	Remaining	This Cut Only	Without This Cut	Comments
Total candidates	···	5235	···	···	···
Host Sep. $R < 5$	774	4461	···	···	likely host galaxy can be identified
Good host redshifts	1314	3147	···	···	···
Fit by SALT2	457	2690	···	···	SALT2 parameter fitting succeeds
Possible AGN	96	2594	2594	1040	separated from center or no long-term variability
$-3.0 < X_1 < 3.0$	540	2054	2119	1092	SALT2 light curve shape
$-0.3 < C < 0.3$	467	1587	1903	1215	SALT2 light curve color
$\sigma_{\mathrm{peakMJD}} < 2$	30	1557	2630	1021	uncertainty in time of max. light (rest frame days)
$\sigma_{X_1} < 1$	379	1178	1930	1386	X_1 uncertainty
fit prob. ≥ 0.001	158	1020	2096	1178	χ^2 and N_{dof}-based prob. from SALT2 fitter
$\mathrm{E(B\text{-}V})_{MW} > 0.15$	0	1020	2690	1020	Milky Way reddening

to standardize SNe Ia and select the SNe Ia that can best measure cosmological parameters. The Tripp estimator uses SALT2 light curve parameters to infer the SN distance modulus, μ (Tripp, 1998):

$$\mu = m_B + \alpha \times X_1 - \beta \times C - M. \tag{4.1}$$

m_B is the log of the light curve amplitude, X_1 is the light curve stretch parameter, and C is the light curve color parameter. These parameters are all measured by the SALT2 fitting program, but deriving the distance modulus from them depends on the nuisance parameters α, β, and M. M is degenerate with the Hubble Constant, H_0, and will be marginalized over during cosmological parameter estimation.

To avoid unexpected biases in our sample selection, we use light curve selection requirements (cuts) from previous analyses using spectroscopically confirmed SNe.

We make the same series of cuts to PS1 SN light curves as Betoule et al. (2014) and add one additional cut on the SALT2 fit probability following R14. These cuts include uncertainty-based cuts that ensure the shape and time of maximum light of each SN is well-measured, and shape and color cuts that restrict our sample to SNe Ia for which the SALT2 model is well-trained. Our cuts are summarized in Table 5.1 and Figure 4.2. Out of 3,147 SNe with reliable host redshifts, SALT2 fits run successfully on 2,690 SNe (SALT2 parameter fitting often fails due to lack of light curve data before or after maximum). 1,020 SNe pass all of our cuts.

Omitting the SALT2 σ_{X_1} cut has the largest single impact on our final sample. Without it, there would be nearly 1,400 SNe in the sample but also twice as many SNe with Hubble residuals > 0.5 mag (poorly measured SNe Ia or CC SNe). The cut with the second largest reduction is the cut on C, without which there would be $\sim$1,200 SNe (though many would be CC SNe). Although it may be possible to increase the SN sample size with relaxed cuts, the extent to which SNe Ia with low signal-to-noise ratio (SNR) and unusual colors are standardizable is not well characterized.

In addition to the Betoule et al. (2014) cuts, we implement an additional set of cuts to remove possible AGN that were not flagged during the PS1 transient search. We tuned our long-term variability criteria to find known AGN in PS1 data. We found that sources where >25% of background epochs have 2σ deviations from 0 are likely AGN (we define background epochs as <20 days before or >60 days after the discovery epoch). 86 SNe with both evidence of long-term variability and SN

positions within $0.5''$ of their host centers were removed. After light curve cuts, removing likely AGN reduces our sample by just 18 SNe. To have a sample with uniform selection, we make these cuts (and all cuts) regardless of whether or not a given SN Ia is spectroscopically confirmed.

4.3.3 Low-z SNe

Cosmological parameter constraints are greatly improved when a large, low-z SN Ia sample is included to anchor the Hubble diagram. We use the same 197 low-z SNe Ia used in R14 though we anticipate adding additional low-z SNe in our full cosmological analysis. These SNe are spectroscopically confirmed and are assumed to have no CC SN contamination.

The R14 PS1 cosmology analysis has a low-z sample with higher intrinsic dispersion than the PS1 sample. The intrinsic dispersion, σ_{int}, is defined as the value added in quadrature to the SN Ia distance modulus uncertainty such that the Hubble diagram reduced χ^2 is equal to 1 (Guy et al., 2007). Differences in SN Ia intrinsic dispersion from survey to survey are typical, with the likely source of the variation including underestimated photometric difference image uncertainties and excess scatter from bright host galaxy subtractions (as seen in R14 and Kessler et al., 2015). Redshift evolution of the SN Ia population could also play a role. We added 0.05 mag in quadrature to the m_B uncertainties of the low-z SNe to resolve the discrepancy. Once added, this additional uncertainty term gives both the PS1 and low-z SNe from

R14 the same intrinsic dispersion of ∼0.115 mag.

4.4 Simulating the Pan-STARRS Sample

To robustly determine how CC SN contamination affects PS1 measurements of w, we require a simulation that encapsulates as many elements of the PS1 SN survey as possible. We used the SuperNova ANAlysis software (SNANA[4]; Kessler et al., 2009b) to generate Monte Carlo realizations of the PS1 survey. SNANA simulates a sample of SNe Ia and CC SNe using real observing conditions, host galaxy noise, selection effects, SN rates, and incorrect redshifts from host galaxy mismatches or measurement error. Simulations assume a flat ΛCDM cosmology with $H_0 = 70$ km s^{-1} Mpc^{-1}, $\Omega_M = 0.3$, $\Omega_\Lambda = 0.7$, and $w = -1$.

We choose not to simulate one significant effect: the correlation between SN luminosity and host mass (the host mass bias; Kelly et al., 2010; Lampeitl et al., 2010). We do not simulate the host mass bias because R14 did not include it (finding it had low significance in their sample), and we wish to compare our PS1 photometric results directly to R14. This effect has been identified at $>5\sigma$ by Betoule et al. (2014) and we will include it in our future cosmological analysis with these data.

Each major component of our simulation is discussed in detail below:

1. **Observing conditions**. SNANA generates SN observations based on a simu-

[4] `http://snana.uchicago.edu/`

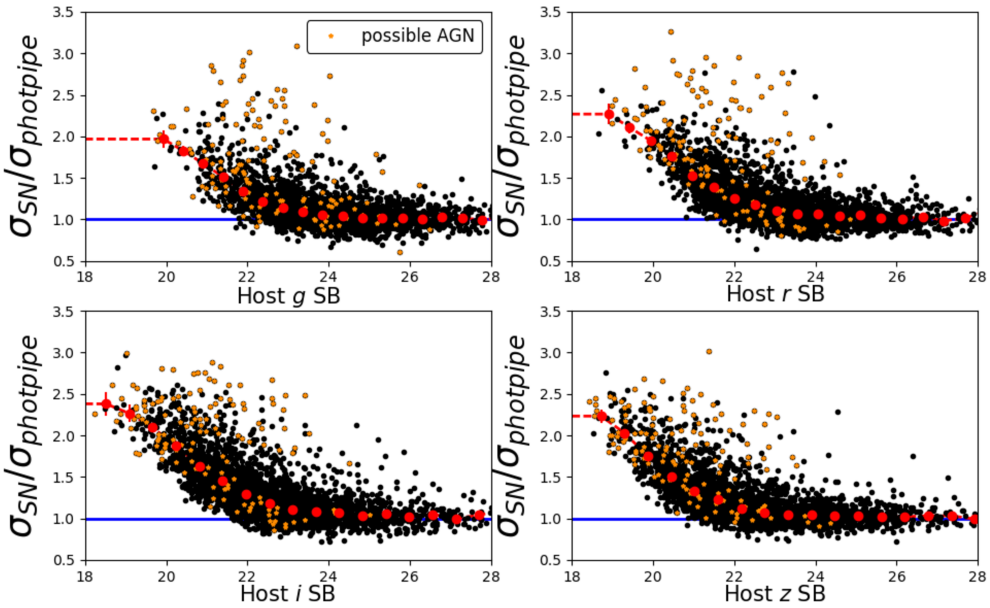

Figure 4.3: The ratio between "true" and DAOPHOT-derived photometric noise as a function of host galaxy surface brightness in the $griz_{PS1}$ filters. We computed the host galaxy surface brightness by averaging over one PSF FWHM at the SN location. We computed the true photometric noise by inflating the errors from DAOPHOT (which do not include host galaxy noise) such that light curve epochs without SN light had $\chi^2 = 1$. Possible AGN (gold stars) comprise many of the outliers in this relation. We incorporated this relationship into our SNANA simulations to yield an accurate prediction of photometric uncertainties.

lation library file with observation dates, filters, sky noise, zeropoints, and PSF sizes that we measure from PS1 nightly images.

2. **Host galaxies**. The observed flux scatter of SNe found in bright galaxies exceeds what is expected from Poisson noise alone (R14; Kessler et al., 2015). To correct for this, SNANA adds host galaxy noise to SN flux uncertainties by placing each SN in a simulated host galaxy. The SN is placed at a random location that has been weighted by the galaxy surface brightness profile. The distribution of PS1 host galaxies was determined from PS1 data; we measured the magnitudes and shape parameters of PS1 SN host galaxies using SExtractor, with zeropoints measured from the PS1 pipeline. We then use the noise model from Kessler et al. (2015, their Equation 4):

$$\tilde{\sigma}_{flux} = \sigma_{flux} \times R_{\sigma}, \tag{4.2}$$

where R_{σ} is a function of host galaxy surface brightness (the vertical axis of Figure 4.3). We determine R_{σ} for PS1 by comparing host surface brightness to the flux error scaling that gives light curve epochs without SN flux a reduced $\chi^2 = 1$.

3. **Selection effects**. Two primary selection effects come into play in a photometric SN Ia survey. The first is detection efficiency, the fraction of single-epoch detections as a function of the photometric SNR. The detection efficiency is computed by dividing the number of epochs detected by PS1 at a given SNR by

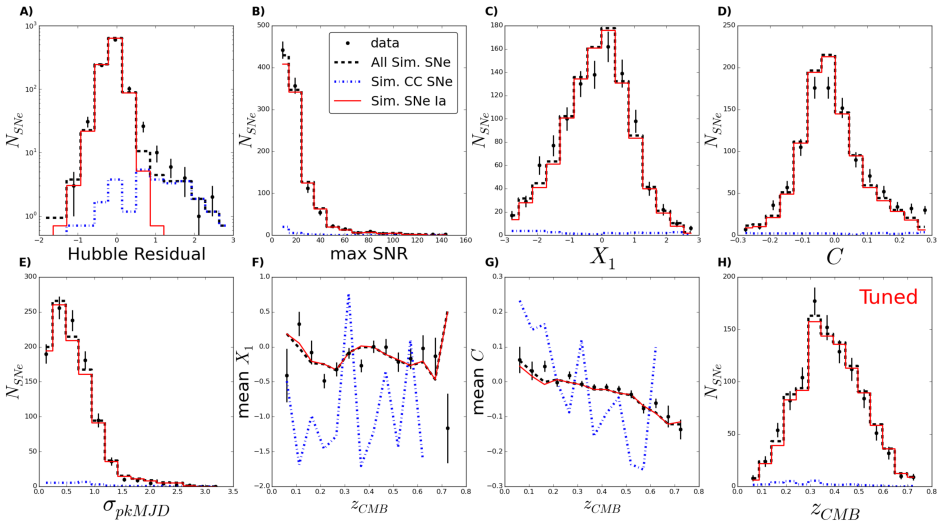

Figure 4.4: SNANA simulations of a PS1 photometric sample compared to PS1 data. The simulated Hubble residuals (A) of the CC SN distribution are flatter and fainter than the data. The simulated SNR (B), shapes (C), colors (D), uncertainties (E) and X_1/C redshift dependences (F and G) match our data closely, albeit with $\sim 3\sigma$ discrepancies in the time of maximum uncertainty and SN color. We tuned the simulated redshift distribution (H) to match our data.

the total number of epochs at that SNR. SNANA uses the efficiency vs. SNR, measured by PS1, to determine which simulated epochs are detected. SNANA then applies the PS1 survey requirement of three detections to "discover" a SN. The PS1 detection efficiency is ∼50% for epochs with a SNR of 5 in the final light curves.

The second effect is host galaxy redshift selection. To model this effect, we incorporated a redshift-dependent "host galaxy efficiency" distribution in our simulations, which we adjusted such that the redshift distribution of the simulations matched our data.

4. **Uncertainty adjustment**. SNANA allows its simulated uncertainties to be scaled as a function of SNR such that the mean uncertainties in simulations match the mean uncertainties of our data. In PS1, this requires a modest $\sim 5-10\%$ noise increase at low SNR (after excess host galaxy noise is added). This adjustment is necessary due to the non-Gaussian wings of the PS1 PSF and the PSF fitting radius used by the PS1 pipeline.

5. **Mismatched host galaxies and incorrect redshifts**. As discussed in §4.3.1, we expect $2.6 \pm 1.4\%$ of our redshifts to be incorrect due to mismatched host galaxies and redshift measurement uncertainties. We used SNANA to simulate incorrect host redshifts by assigning false, "measured" redshifts to 2.6% of our SNe. These redshifts are drawn from a flat, random distribution between $z =$

0.01 and $z = 0.75$. This is the range of redshifts at which PS1 can discover SNe, with the exception of rare superluminous SNe. Superluminous SNe typically have hosts too faint for our follow-up survey to measure their redshifts (Lunnan et al., 2015).

We find that $\sim$50% of SNe with incorrect redshifts fail our sample cuts, giving a final contamination fraction of $\sim 1 - 1.5\%$. In large part, this reduction is due to cuts on the SALT2 color parameter. If a SN has an incorrect redshift, SALT2 is twice as likely to infer that its observed-frame colors are inconsistent with normal SNe Ia when transformed to the wrong rest frame.

6. **SN Ia model**. The SN Ia model used in these simulations is the Guy et al. (2010) model with SN Ia nuisance parameters from R14 (SALT2 $\alpha = 0.147$, $\beta = 3.13$). The parent X_1 and C distributions were determined by Scolnic & Kessler (2016) for the PS1 spectroscopic sample. We adjusted the parent means of the X_1 and C distributions by 1σ to better match our data, making X_1 lower by 0.17 and C higher by 0.023. This difference is likely physical; on average, X_1 is lower and C is higher in massive host galaxies (e.g. Childress et al., 2013). Our host follow-up program preferentially obtained redshifts of massive galaxies.

7. **CC SN templates and diversity**. CC SNe are simulated based on a library of 43 templates in SNANA. The templates we use were originally created for

the SN Photometric Classification Challenge (Kessler et al., 2010) and also used by Bernstein et al. (2012). Templates are based on bright, spectroscopically-confirmed SDSS, SuperNova Legacy Survey (SNLS; Conley et al., 2011; Sullivan et al., 2011), and Carnegie Supernova Project (Hamuy et al., 2006; Stritzinger et al., 2011) CC SNe with well-sampled light curves. Templates were created from the light curves by warping a model spectrum for each SN subtype to match the light curve fluxes in every broadband filter (see §4.10.1.1).

SNANA has 24 II-P templates, 2 IIn templates, 1 II-L template, 7 Ib templates and 9 Ic templates. In this work, we make the assumption that reddening in the templates is approximately equal to reddening in our data. This assumption allows us to use the Li et al. (2011) LFs, which have not been corrected for reddening, and SNANA templates, which also include intrinsic reddening. Correcting these templates, the Li et al. (2011) rates and the Li et al. (2011) LFs for reddening is an important avenue for future work.

We added a subtype-specific magnitude offset to each CC SN template such that the mean simulated absolute magnitude of the subtype matched the mean of its Li et al. (2011) luminosity function (LF). By applying a uniform offset to every template in a subtype, the brightness of different templates relative to their subtype is incorporated in our simulations[5]. We also matched the dispersions

[5]We tweaked this procedure for SNe Ib, which had one anomalously bright template. All SN Ib templates were adjusted by individual magnitude offsets such that each template matched the mean magnitude of SNe Ib given by Li et al. (2011).

of the Li et al. (2011) LFs by adding an additional, random magnitude offset to each simulated CC SN. This offset was drawn from a Gaussian with a width we adjusted such that the dispersion of simulated absolute magnitudes for each subtype matched Li et al. (2011).

8. **SN Rates**. SNANA creates a combined SN Ia+CC simulation, with each SN type normalized by its rate. The redshift-dependent SN rates used in this work are the same as the baseline model of Rodney et al. (2014). SNe Ia follow measured rates, while CC SNe follow the cosmic star formation history. Relative rates of SN types and subtypes are anchored at $z = 0$ by Li et al. (2011) and evolve $\propto (1 + z)^{\gamma}$, where γ is a free parameter tuned to match theory and observations (only a single value for γ is needed over the redshift range of PS1). We used $\gamma_{Ia} = 2.15$ and $\gamma_{CC} = 4.5$ (Rodney et al., 2014).

Figure 4.4 compares our simulations to the data after fitting all SNe with the SALT2 model. Note that CC SN information in this simulation is obtained without any PS1 analysis or input. SALT2 fitting is an effective way to examine both SNe Ia and the light curve parameters of Ia-like CC SNe. Discrepancies in Figure 4.4 indicate potential biases when measuring cosmological parameters with a CC SN-contaminated sample.

Our simulations agree closely with the data for most light curve parameters. The maximum SNR of simulated light curves matches the data (4.4B), as does the distribution of SALT2 X_1 (4.4C). However, there are too few simulated SNe with red

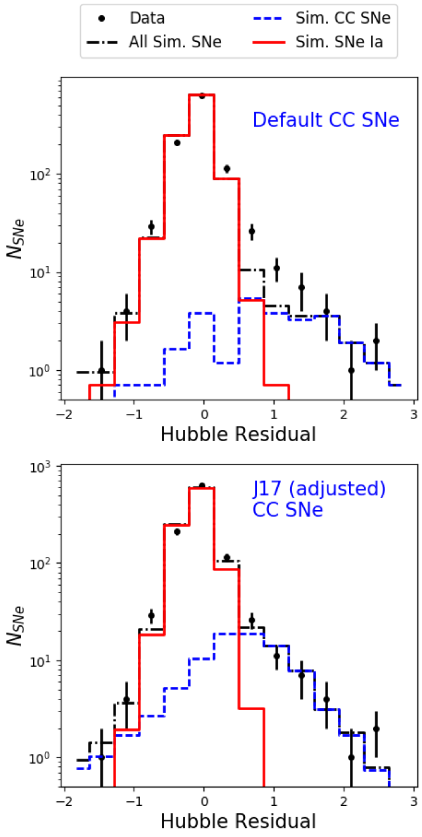

Figure 4.5: Comparison of Hubble residuals before and after empirical adjustments to CC SN LFs. We enlarge Figure 4.4A (top) and compare to our adjusted J17 simulations (bottom). Before empirical adjustments, the simulations contain just 2.4% CC SNe and are a poor match to the data. After adjustments, the simulations have 8.9% CC SNe. Discrepancies between data and simulations in the red end of the SALT2 C distribution can be explained by additional CC SNe.

SALT2 colors (4.4D). The simulated redshift evolution of X_1 and C matches the data well (4.4F and 4.4G).

Though most simulated light curve parameters match our data well, the Hubble residuals (4.4A) show a discrepancy. We see $\sim$3 times more SNe than expected between $0.5 \lesssim \mu - \mu_{\Lambda CDM} < 1.5$ mag (these SNe are fainter than SNe Ia at their redshifts). For this reason, we used light curve-based classifications of our data to adjust the CC SN luminosity functions. The details of this procedure are discussed in Appendix 4.10. We find that the peak of the CC SN LF must be brightened by 1.2 mag for SNe Ib/c and 1.1 mag for SNe II in order for our simulations to match our data (Figure 4.5). The dispersion of CC SN templates must be reduced by 55% for SN Ib/c. We also add four 1991bg-like SN Ia templates and four SN IIb template to SNANA to include a broader range of SN types.

The CC SNe LFs in our adjusted simulation are $\sim 5\sigma$ brighter than Li et al. (2011). However, these results do not necessarily imply that the true LFs of CC SNe show a $\sim 5\sigma$ inconsistency with Li et al. (2011). Rather, they indicate that our SALT2-based shape and color cuts isolate a region of CC SN parameter space that is not the average. Although we find it plausible that the CC SNe with shapes and colors most similar to SNe Ia have brighter and lower-dispersion LFs than CC SNe as a whole, further work is required to understand the diversity of CC SN sub-populations. Larger sets of high-cadence, high quality spectral time series from which to construct templates are also necessary. An additional factor is that the low statistics in the LOSS volume-

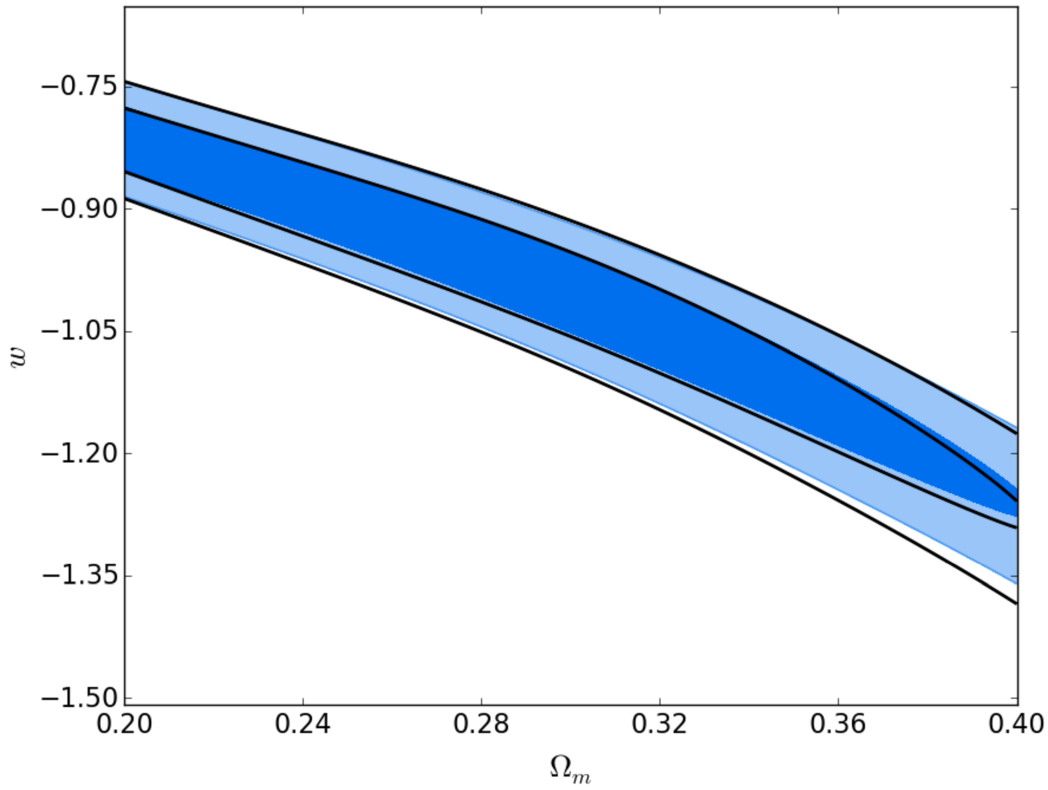

Figure 4.6: Comparing the full SN Ia likelihood (filled contours) to the binned Ia likelihood (black).

limited sample require that the shape of the CC SN LFs be extrapolated in some way. We treat CC SN LFs as Gaussian, most likely a flawed assumption (see Figure 16 of Li et al., 2011).

4.5 Estimating SN Ia Distances with BEAMS

We use the Bayesian Estimation Applied to Multiple Species (BEAMS) method to obtain SN Ia distance measurements that are corrected for the CC SNe contam-

inating our data (KBH07). The implementation of BEAMS suggested in KBH07 solved for distances and cosmological parameters in a single step; here, we first use BEAMS to solve for binned SN Ia distances and then use CosmoMC (Lewis & Bridle, 2002) to determine cosmological parameters. This procedure will allow us to more easily combine SN data with complementary CMB and BAO data in our forthcoming cosmological analysis. We summarize the method below.

BEAMS simultaneously determines Ia and CC SN distances by sampling a posterior probability distribution that includes both SN Ia and CC SN populations in the likelihood. The BEAMS posterior, the probability of the free parameters θ given the data, D, is proportional to the product of the individual likelihoods for each SN multiplied by the priors on the free parameters:

$$P(\theta|D) \propto P(\theta) \times \prod_{i=1}^{N} \mathcal{L}_i. \tag{4.3}$$

The simplest suggested likelihood from KBH07 uses Gaussian distributions to represent CC SN and SN Ia populations:

$$\begin{aligned} \mathcal{L}_i = \mathrm{P_i(Ia)} \times \frac{1}{\sqrt{2\pi(\sigma_{i,Ia}^2 + \sigma_{Ia}^2)}} \exp(-\frac{(\mu_{i,Ia} - \mu_{Ia}(z_i))^2}{2(\sigma_{i,Ia}^2 + \sigma_{Ia}^2)}) \\ +\mathrm{P_i(CC)} \times \frac{1}{\sqrt{2\pi(\sigma_{i,CC}^2 + \sigma_{CC}(z_i)^2)}} \exp(-\frac{(\mu_{i,CC} - \mu_{CC}(z_i))^2}{2(\sigma_{i,CC}^2 + \sigma_{CC}(z_i)^2)}). \end{aligned} \tag{4.4}$$

$\mathrm{P_i(Ia)}$ is the prior probability that the ith SN is of type Ia. $\mathrm{P_i(CC)}$, the probability that the SN is a CC SN, is equal to $1 - \mathrm{P_i(Ia)}$. $\mu_{i,Ia}$, $\mu_{i,CC}$ and $\sigma_{i,Ia}$, $\sigma_{i,CC}$ are the

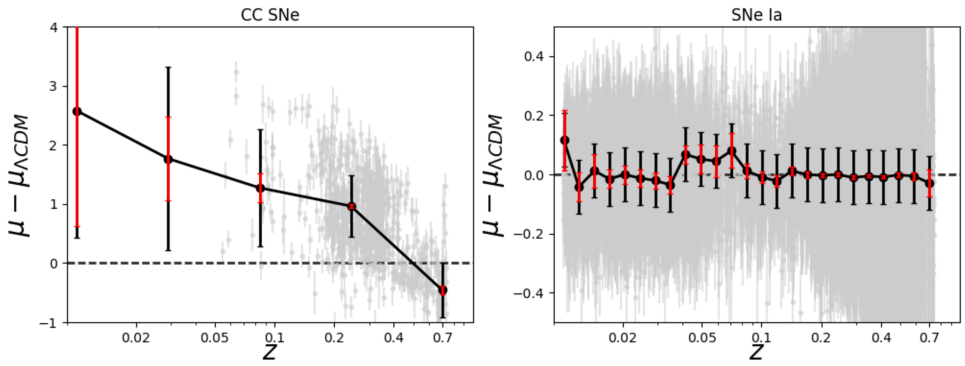

Figure 4.7: An illustration of BEAMS. Simulated CC SNe (left) and SNe Ia (right) with the redshift-dependent BEAMS parameters μ_{CC}, μ_{Ia} (black points) and σ_{CC}, σ_{Ia} (black bars). Uncertainties on μ_{CC} and μ_{Ia} are in red. We use correct prior probabilities of P(Ia) = 1 for SNe Ia with correct redshifts and P(Ia) = 0 for all others.

distance modulus and distance modulus uncertainties for the ith SN, derived using the Tripp estimator (Eq. 5.1). We differentiate between measured Ia and CC distance moduli from the data because we will allow the Tripp estimator to use different nuisance parameters for the SN Ia and CC SN terms in the likelihood (§4.5.1). μ_{Ia}, σ_{Ia} and μ_{CC}, σ_{CC} are the means and standard deviations of the SN Ia and CC SN Gaussians, respectively.

The variables μ_{Ia} and μ_{CC} are a function of the redshift, z, of the ith SN and of cosmological parameters. The variable σ_{CC} is redshift dependent as well, primarily due to the changing mix of CC SN subtypes that PS1 is able to discover as a function of redshift. We fit for $\mu_{Ia}(z)$, $\mu_{CC}(z)$ and $\sigma_{CC}(z)$ by allowing BEAMS to treat them as free parameters at certain fixed redshifts z_b. We refer to the set of fixed redshifts

as "control points" following Betoule et al. (2014)[6]. Between two control points, the distance modulus (and dispersion) is interpolated by a linear function of $\log(z)$ defined by:

$$\begin{aligned} \mu(z) &= (1-\xi)\mu_b + \xi\mu_{b+1} \\ \xi &= \log(z/z_b)/\log(z_{b+1}/z_b), \end{aligned} \tag{4.5}$$

where μ_b is the distance modulus at redshift z_b.

Betoule et al. (2014) fit to a set of 30 log-spaced redshift control points, and found that the difference between ΛCDM and the interpolation is always smaller than 1 mmag. We used 25 control points for the smaller PS1 redshift range of $0.01 < z < 0.7$ (we restrict our sample to $z < 0.7$, as very few PS1 SNe can be found at higher redshifts). In Figure 4.6, we compare the cosmological constraints from 1,000 individual SNe Ia to the approximate results derived from the SN Ia distances at 25 control points (P(Ia) = 1 for all SNe Ia). We find that the cosmological constraints are nearly identical.

We use 5 log-spaced redshift control points for CC SNe. If true SN type probabilities are known, 5 CC SN control points allows BEAMS enough flexibility to avoid biasing the Ia likelihood with a poor determination of the CC SN distribution. We allow the intrinsic width of the CC SN Gaussian distribution (σ_{CC}) to vary with redshift, but keep the intrinsic width of the SN Ia Gaussian fixed. By using the `SALT2mu` pro-

[6]Note that Betoule et al. (2014) use this method to increase computational efficiency when combining SN Ia data with Planck priors. However, their method of reducing SN data to a set of distances at redshift control points is well-suited for a BEAMS-like algorithm.

cedure (Marriner et al., 2011), we verified that the (simulated) uncertainty-weighted dispersion of SNe Ia does not change with redshift for PS1 (this is also a typical assumption in cosmological analyses; Guy et al., 2010). This physically realistic assumption gives BEAMS more leverage to discriminate between SNe Ia and CC SNe, which have much higher dispersion than SNe Ia.

In total, our baseline implementation of BEAMS has 38 free parameters: 25 SN Ia distance moduli at Ia control points, 5 CC SN distance moduli at CC control points, 5 CC SN dispersion parameters, 1 SN Ia dispersion parameter[7], and the SALT2 nuisance parameters α and β which are used to compute μ_i and σ_i (discussed below). BEAMS free parameters can be efficiently estimated by sampling the logarithm of the posterior with a Markov Chain Monte Carlo (MCMC) algorithm. This work uses `emcee`[8], a `Python` MCMC implementation (Foreman-Mackey et al., 2013). We use `emcee`'s Parallel-Tempered Ensemble Sampler to explore the multimodal peaks of the likelihood robustly. Figure 4.7 illustrates the Hubble residual diagram from BEAMS using simulated SNe and correct prior probabilities (all SNe Ia with correct redshifts have P(Ia) = 1 and all other SNe have P(Ia) = 0). Note that if few or no CC SNe are in a given redshift bin, the magnitude and uncertainty of CC SN distances are primarily determined by the priors.

We apply loose Gaussian priors on most BEAMS free parameters, but find that

[7]Throughout, we have written this dispersion parameter as σ_{Ia} to distinguish it from σ_{int}, the global uncertainty term used in many previous analyses. σ_{int}, defined in §4.3.3, has a different definition than the BEAMS free parameter σ_{Ia}.

[8]`http://dan.iel.fm/emcee/current/`

with samples of 1,000 SNe or more, the difference between Gaussian and flat priors is negligible. For SN Ia distances, we apply flat priors. Though we assume some prior knowledge of the CC SN distribution, our priors on CC SN distance (μ_{CC} in Eq. 5.3) are very loose; we use broad Gaussians of width 3 mag that are centered at 2 mag fainter than SNe Ia at each control point. SALT2 nuisance parameters have Gaussian priors of width 5 times the uncertainties from R14. Our code is available online[9].

4.5.1 SALT2 Light Curve Parameters

We use a SALT2 fitting program to measure SN light curve parameters for our sample. However, SALT2 parameters do not directly measure the distance modulus (Eq. 5.1). For BEAMS to measure distances using SALT2 light curve fits, the nuisance parameters α and β must either be fixed to the value from a spectroscopic sample or incorporated into BEAMS as free parameters. We allow α and β to be free parameters here as it is a more general test of the method. Different survey methods, detection efficiencies, and selection criteria can significantly bias recovered SN parameters (Scolnic & Kessler, 2016), which could make it necessary for future analyses to be able to fit for these parameters. In the CC SN component of the BEAMS likelihood, we fixed α and β to the nominal value for SN Ia spectroscopic samples (allowing them to float has no effect on our results).

Because we include α and β as free parameters, the likelihood presented in Eq.

[9]See Jones (2017), with recent updates at https://github.com/djones1040/BEAMS. Example input files are also provided.

5.3 has a term in the Gaussian normalization factor, σ_i, that depends on α and β. The result is a significant bias in the derived SN parameters (March et al., 2011). This bias grows for larger SN samples (see Appendix B of Conley et al., 2011 and Kelly, 2007 for details). The solution adopted in Conley et al. (2011) is to neglect the normalization term when determining α, β, and σ_{int} by using a simple likelihood $\mathcal{L} \propto \exp(-\chi^2/2)$. For 1,000 SNe, Conley et al. (2011) find that the bias from this likelihood is well below the statistical error. Though we cannot use this solution without biasing determinations of the CC SN and SN Ia distributions, we use an alternative formalism and treat the uncertainties on the distance modulus as fixed in the denominator of the normalization term (independent of α and β). Fixing distance modulus uncertainties in the denominator does not bias α, β, or w and is a very modest approximation; in the PS1 sample, varying α and β within their 1σ errors from R14 gives a mean change in uncertainty of only 2 mmag. No individual SN has its uncertainty change by >20 mmag. See Kessler & Scolnic, 2017, §8.1 for an alternative solution.

4.5.2 Prior Probabilities

The BEAMS formalism requires an estimate of the prior probability that a given SN is of Type Ia. This prior can be measured by a SN classifier or it can be as simple as setting P(Ia) = 1/2 for all SNe. For our baseline analysis, we adopt the PSNID light curve fitter, as implemented in SNANA (Sako et al., 2011, 2014). In

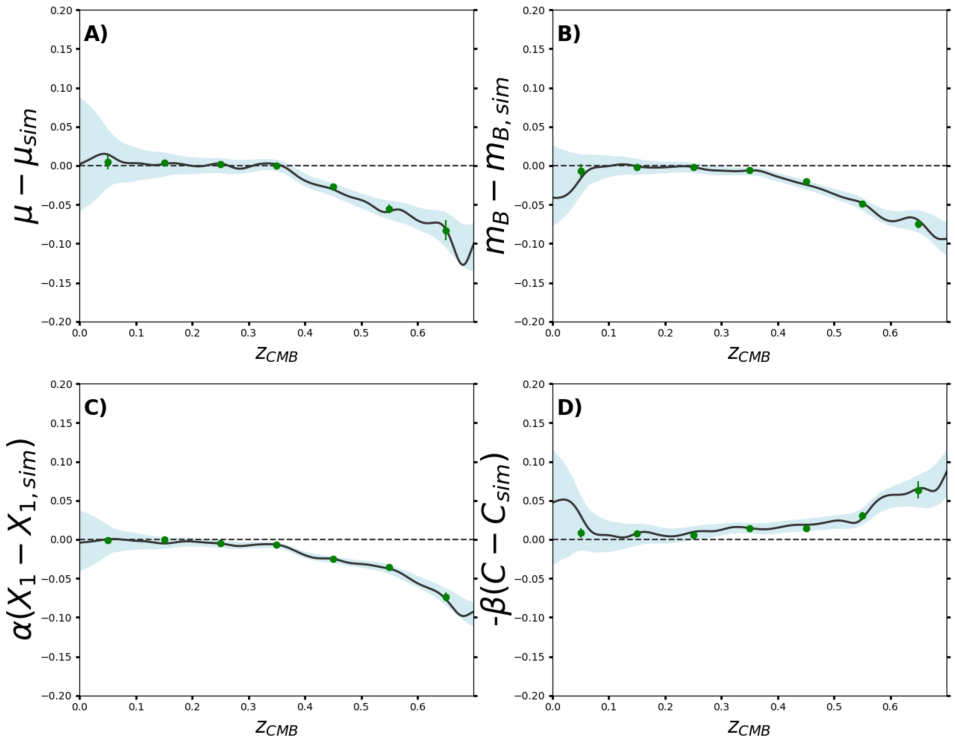

Figure 4.8: The simulated redshift-dependent bias in distance (A), peak B magnitude (B), αX_1 (C), and $-\beta C$ (D) for the PS1 photometric sample using non-parametric spatial averaging (black lines with 95% confidence intervals in blue) with median bins (points) shown for comparison. The PS1 sample has negligible distance (Malmquist) bias until $z \sim 0.3$ and a maximum bias of $\sim$0.1 mag at $z \gtrsim 0.6$.

PSNID, observed SN light curves are fit with perfect, noise-free simulations of the SALT2 SN Ia model and SNANA's CC SN templates to determine the probability that each SN is of type Ia[10]. PSNID estimates P(Ia) from the χ^2 of the fit and includes type, redshift, and luminosity priors. The set of SNe with P(Ia) > 0.5 has 2.9% contamination by CC SNe while including 92% of real SNe Ia.

We allow a re-mapping of the PSNID prior probabilities by adding two parameters to BEAMS: one that re-normalizes the probabilities, and a second that shifts them linearly. The first parameter is a scaling factor that corrects for globally skewed prior probabilities following Hlozek et al. (2012). This normalization term allows BEAMS to correct for effects such as incorrect redshift-dependent SN rates, inaccurate classifier training, or other P(Ia) biases. The second parameter is a global, linear shift in probability to handle incorrect typing near P(Ia) $= 0$ or P(Ia) $= 1$ (but requiring $0 <$ P(Ia) < 1). This is necessary in cases where uncertainty in P(Ia) $\simeq 1$ or P(Ia) $\simeq 0$ is significant (KBH07). The relationship between the normalization factor, A, the shift parameter, S, and the probability P(Ia) is given by:

$$\tilde{P}(\mathrm{Ia}) = \frac{\mathrm{A} \times (\mathrm{P(Ia)} + \mathrm{S})}{1 - (\mathrm{P(Ia)} + \mathrm{S}) + \mathrm{A} \times (\mathrm{P(Ia)} + \mathrm{S})} \qquad 0 < \tilde{P}(\mathrm{Ia}) < 1. \tag{4.6}$$

Another solution suggested by KBH07 that could be explored in future work is adding

[10]Because the simulated CC SN models in SNANA are the same as the CC SN models in the PSNID template library, we used an option in PSNID (SNANA v10_47m and later) that ensures a CC SN simulated using a given template cannot be classified using a noise-free version of that same template. This option increases the CC SN contamination by ∼1%.

a probability uncertainty term to the likelihood.

4.5.3 Malmquist Bias

$\mu_{i,Ia}$, the SALT2-derived distance modulus for the ith SN, is subject to Malmquist bias for magnitude-limited surveys such as PS1. We account for the SN Ia Malmquist bias using PS1 and low-z simulations to determine the redshift-dependent bias of derived SN Ia distances. We used Monte Carlo simulations of $\gtrsim$10,000 SNe and non-parametric spatial averaging to determine and correct for the trend in distance modulus. Our spatial averaging algorithm uses local polynomial smoothing to interpolate the mean distance modulus trend across the redshift range.

Our simulations of the spectroscopically-confirmed low-z SN sample follow R14, who use the same α and β as our PS1 simulations. The details of these low-z simulations and the determination of the spectroscopic selection function are discussed in detail in Scolnic et al. (2014a, see their Figure 6 for a comparison between simulations and data).

Figure 4.8 shows the simulated, redshift-dependent measurement bias in distance modulus, m_B, αX_1, and $-\beta C$. The average high-z distance modulus bias in PS1 is nearly identical to the bias measured for PS1 spectroscopically-confirmed SNe by R14. One difference is that the Malmquist bias is almost negligible in our sample until $z \sim 0.35$. Some differences in bias are expected because the R14 bias is dominated by their spectroscopic SN follow-up selection function.

At $z > 0.5$, we find the bias in X_1, C, and μ becomes large as flux uncertainties near the epoch of peak brightness are up to a factor of 2 larger than in the lower-z data. Greater than 50% of the m_B and C bias at these redshifts is due to our cut on X_1 uncertainty, which is effectively a SNR cut that increases the selection bias. Distance biases due to cuts on X_1 and C are also expected as the data become noisier and statistical fluctuations cause more SNe that fall outside the luminosity-correlated range to appear on our Hubble diagram (Scolnic & Kessler, 2016, see their Figure 4). Our simulations also show that requiring lower X_1 uncertainty tends to select narrower measured light curve shapes. Accordingly, Figure 4.4F shows that the measured X_1 distribution remains largely flat with redshift; though SNe with larger X_1 values are intrinsically more luminous and thus more likely to be discovered, the measurement bias shown in Figure 4.8 has an opposite, and approximately equal, effect.

A discussion of systematic error in Malmquist bias determination will be presented in our forthcoming cosmological analysis. This will include incorporating α and β uncertainties, which can cause differences in the distance bias of $\sim$5 mmag at $z > 0.5$. Although Scolnic et al. (2014a) found that the Malmquist bias is not one of the dominant sources of error, the photometric sample may be subject to different biases than a typical spectroscopic sample due to its lower average SNR.

We correct all SNe, but only for the SN Ia Malmquist bias (we do not attempt bias corrections based on P(Ia)). It is not necessary to correct for the CC SN Malmquist bias, as CC SNe are not used to derive cosmological parameters. However, we im-

plicitly model the CC SN Malmquist bias using BEAMS because BEAMS allows the CC SN mean and dispersion to vary with redshift.

4.5.4 Cosmological Parameter Fitting

Finally, once distance moduli at the 25 redshift control points have been measured with BEAMS, BEAMS distances and distance covariance matrices can be used as inputs into the Cosmological Monte Carlo software for cosmological parameter fitting (CosmoMC; Lewis & Bridle, 2002). For computational efficiency, we did not use the full Planck chains in this analysis and instead ran CosmoMC on our BEAMS results with a Planck-like prior of $\Omega_M = 0.30 \pm 0.02$.

4.6 Cosmological Results from BEAMS

4.6.1 Tests with Simulated Data

We generated 25 simulations of 1,000 PS1 SNe each (25,000 total SNe) in order to test BEAMS on samples the size of the PS1 photometric sample. We add simulated low-z samples of 250 SNe Ia each, the approximate number that will be included in our forthcoming cosmological analysis. The results presented here use the J17 CC SN simulations (Appendix 4.10), as they have CC SN LFs that match our data.

To focus on biases from CC SN contamination, we define the CC SN bias Δ and

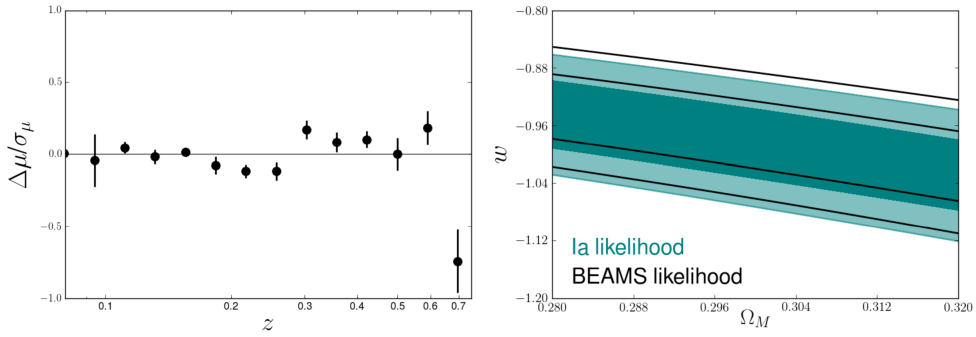

Figure 4.9: Left: Average distance modulus bias due to CC SN contamination (Eq. 4.7) as a fraction of the statistical uncertainty. Error bars are the uncertainty on the median bias from 25 samples. The average absolute biases at $z > 0.2$ are $\sim$3 mmag, with the point at $z \simeq 0.6$ having the largest bias of 6 mmag (with the exception of the final high-uncertainty point at $z \simeq 0.7$). There is a slight z-dependent slope, which could bias cosmological parameters, with at 2.3σ significance. Right: 1σ cosmological parameter likelihood contours from BEAMS compared to the true likelihood using a representative sample of 1,000 PS1 SNe.

Table 4.3. Results from BEAMS

	PS1 Simulations					PS1 Data				
	bias	$\sigma_{\rm bias}$[a]	$\sigma_{\rm stat}$[b]	bias/$\sigma_{\rm stat}$	$\Delta\sigma_{\rm stat}$	bias	$\sigma_{\rm bias}$[a,c]	$\sigma_{\rm stat}$[b]	bias/$\sigma_{\rm stat}$	$\Delta\sigma_{\rm stat}$
μ[d]	0.000	0.001	0.031	0.0	0.001 (3%)	-0.040	0.019(±0.09)	0.074	-0.4	0.010 (14%)
α	0.004	0.000	0.006	0.6	0.000 (3%)	0.001	0.001(±0.005)	0.012	0.1	0.001 (5%)
β	0.088	0.008	0.073	1.2	0.004 (6%)	0.199	0.018(±0.10)	0.154	1.4	0.009 (6%)
w	-0.005	0.004	0.048	-0.1	0.002 (3%)	-0.040	0.012(±0.084)	0.095	-0.4	0.008 (8%)

Note. — Bias and increase in uncertainty due to CC SN contamination. All quantities shown are taken from the median of 25 samples. Bias is defined in Eq. 4.7 for simulations and Eq. 4.8 for data (bias in data is relative to R14 parameter measurements).

[a]Uncertainty on the median bias.

[b]Statistical uncertainty on each parameter from a single sample.

[c]In parentheses, we show the estimated uncertainty on the R14 values. Because our PS1 data are correlated with R14 (they share the low-z sample), we take Monte Carlo samples of 100 simulated PS1 SNe and combine each with the R14 low-z sample, taking the standard deviation of measurements from these combined data as the uncertainty.

[d]Averaged over $0.08 < z < 0.7$.

the increase in statistical uncertainty due to CC SNe, $\Delta\sigma_{stat}$, for a given parameter P:

$$\begin{aligned} \Delta &= P_m - P_{Ia}, \\ \Delta\sigma_{stat} &= \sigma(P_m) - \sigma(P_{Ia}) \end{aligned} \tag{4.7}$$

where P_m is the measured parameter from the BEAMS method and P_{Ia} is the measured parameter from the BEAMS method using SNe Ia alone and setting all prior probabilities equal to one. For the 25 simulated samples, the average w_{Ia} value is -1.001±0.009. The RMS of w_{Ia} is 0.045, consistent with the mean statistical uncertainty (0.048).

We compare the Ia-only distances, SN parameters, and w measurements against our results from the BEAMS method in Table 4.3. Figure 4.9 shows that the binned distances are biased by less than 20% of their uncertainties with the exception of the final control point. Typical biases are ∼3 mmag and the largest average bias from the 25 samples (aside from the final high-uncertainty control point) is 6 mmag at $z \simeq 0.6$.

The SN parameters α and β are biased by 3%, or 1-1.5 times the average statistical error. $\sigma_{\rm Ia}$ is biased by 4%, 0.3 times the average statistical error. Note that σ_{Ia} (in Eq. 5.3) is functionally similar to the SN intrinsic dispersion, σ_{int}. These biases are small enough that they would be difficult to measure in real data. A possible cause of these biases is that Ia-like CC SNe have color laws more consistent with Milky Way dust ($\beta \sim 4.1$) and different shape-luminosity correlations.

We find w has a median bias of -0.005±0.004 due to CC SN contamination, 10% of the statistical error on w. While our analysis is consistent with no bias, we assign a systematic uncertainty on w of 0.005+0.004 = 0.009, though the true systematic uncertainty could be higher due to uncertainties in CC SN simulations (§4.7). The statistical uncertainty on w in this case is just 3% higher than the statistical uncertainty from SNe Ia alone. This result is consistent with KBH07, who find that BEAMS can yield nearly optimal uncertainties (we discuss BEAMS uncertainties further in §4.8.3).

If we compare the bias on w to a naïve method of measuring w with photometrically classified SNe, the advantage of using BEAMS is obvious. For our 25 1,000-SN samples, we take likely SNe Ia ($P_{PSNID}(Ia) > 0.5$) and estimate cosmological parameters assuming that all of these SNe are Type Ia (Campbell et al., 2013 used a similar method of cutting the sample based on PSNID classifications). Making this cut removes 8% of true SNe Ia in our sample and yields a final sample contaminated by 2.9% CC SNe. In spite of having a sample comprised of >97% SNe Ia, the average bias on w is -0.025±0.004, a factor of five higher than our BEAMS results. The bias is >50% of the statistical uncertainty on w and has 6σ significance, while the BEAMS result is consistent with no bias. The statistical uncertainty on w from this method is 6% higher, compared to 3% higher from BEAMS. Even a cut of $P_{PSNID}(Ia) > 0.9$ yields a bias on w of 0.011±0.003 ($>3\sigma$ significance) at the cost of removing 17% of real SNe Ia. Furthermore, while BEAMS allows these probabilities to be adjusted by

the method, treating them as fixed in this simplistic method increases the possibility of biased classifications due to incompleteness in the CC SN template library. It is clear that BEAMS outperforms this simple cut-based analysis, though this naïve method could still be effective with significantly improved classification methods.

4.6.2 Comparing Real Pan-STARRS Photometric Supernovae to Rest et al. (2014)

Rather than analyzing the full PS1 sample, we analyze 25 random draws of PS1 SNe to compare R14 measurements − and uncertainties − directly to measurements from CC SN-contaminated samples of the same size. Because 96 R14 SNe Ia pass our sample cuts, we draw samples of 104 photometric SNe in order that our subsamples each contain an average of 96 SNe Ia (and 8 CC SNe; we also use reprocessed R14 light curves). We don't explicitly require these random samples to have the same redshift distribution as the PS1 spectroscopic sample. However, the redshift distribution of the PS1 photometric sample is similar to that of R14 (a nearly identical range and median redshift, though the photometric sample does include more faint SNe Ia with red colors).

For subsamples of PS1 data, we report parameter biases relative to R14:

$$\Delta = P_m - P_{R14}$$
$$\Delta\sigma_{stat} = \sigma(P_m) - \sigma(P_{R14}) \tag{4.8}$$

where P_{R14} and $\sigma(P_{R14})$ refer to a parameter and its uncertainties from R14.

Although R14 does not have enough SNe to test for small biases in w, the data still allow for a consistency check that is independent of the myriad assumptions made in simulations. In addition, the 96 SNe from R14 with low-z SNe can provide constraints on the bias of nuisance parameters α, β, and σ_{Ia} due to the BEAMS method. We include low-z SNe because BEAMS is more robust when it has a spectroscopically-confirmed sample as part of the data and has difficulty measuring accurate SN Ia dispersions for small samples.

We find that measured distances, SN nuisance parameters α and β, and w are consistent with R14 (Table 4.3). We may be seeing the same hints of a bias toward higher values of β that we find in simulations but they have under 2σ significance. The bias in α is not statistically significant (0.1σ).

The average of w from 25 104-SN samples is consistent with the measurements from reprocessed R14 light curves (0.4σ lower, where σ is the statistical uncertainty from R14). The uncertainties on w are 15% higher and distance modulus uncertainties are 14% higher, likely due to the lower average SNR of photometric PS1 light curves. The median SNR at peak is 22 for all PS1 SNe, compared to a median SNR at peak of 38 for spectroscopically classified SNe.

4.7 Results from BEAMS Variants

The BEAMS method measures w with no significant bias due to CC SN contamination and a statistically insignificant bias in PS1 data. However, the reliability of these results could depend on the assumptions that we made when generating CC SN simulations and implementing BEAMS. We now expand our study of systematic uncertainties in simulations by applying alternative SN classification methods, including ones with less dependence on the accuracy of our CC SN simulations, and adjusting the CC SN likelihood model.

4.7.1 Analysis Variants

In total, we test three additional methods of determining the prior probability P(Ia) (Eq. 5.3) − the Nearest Neighbor, *Fitprob*, and GalSNID classifiers − and two additional CC SN models. The two additional CC SN models include a two-Gaussian model and a single, asymmetric Gaussian model. Nearest Neighbor (NN) and *Fitprob* are light curve-based classification methods. NN uses SALT2 light curve parameters to classify SNe based on whether they lie nearer to simulated SNe Ia or simulated CC SNe in X_1, C and redshift space while *Fitprob* uses the χ^2 and degrees of freedom of the SALT2 light curve fit to measure a probability. GalSNID (Foley & Mandel, 2013) uses the fact that, unlike CC SNe, many SNe Ia explode in galaxies with old stellar populations, and thus uses only host galaxy properties to derive a SN type

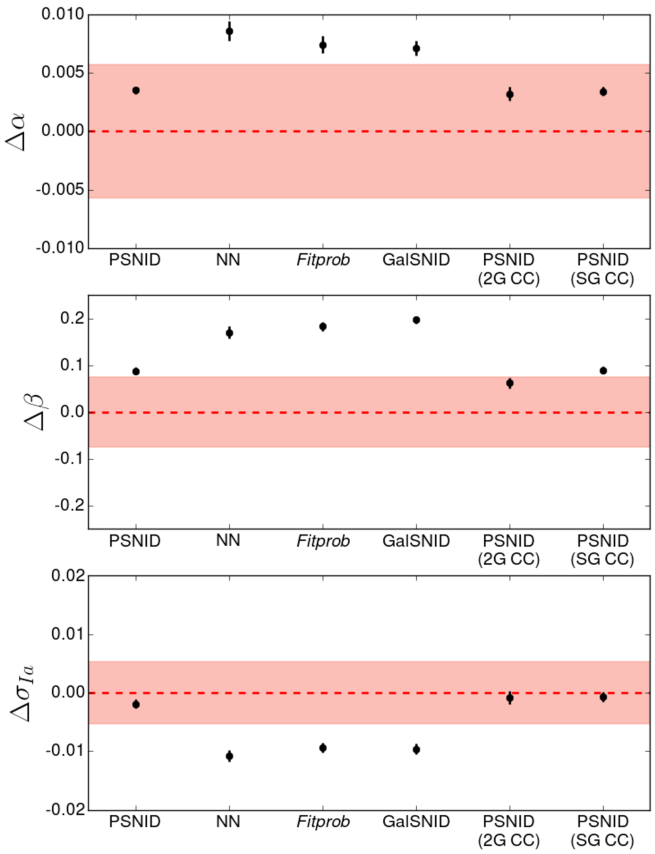

Figure 4.10: The bias in SALT2 α, β, and σ_{Ia} measured from 25 simulations of 1,000 SNe each, with shaded regions indicating typical uncertainties on each parameter from SN Ia-only samples. σ_{Ia} is too low by $\sim 0.005 - 0.01$, while α and β are too high by ∼0.005-0.01 and ∼0.1-0.2, respectively (∼1-2σ). It is likely that reddened CC SNe are responsible for the higher color term (more consistent with Milky Way dust than the SN Ia color law). "2G CC" and "SG CC" refer to the 2-Gaussian and skewed Gaussian CC SN parameterizations, respectively.

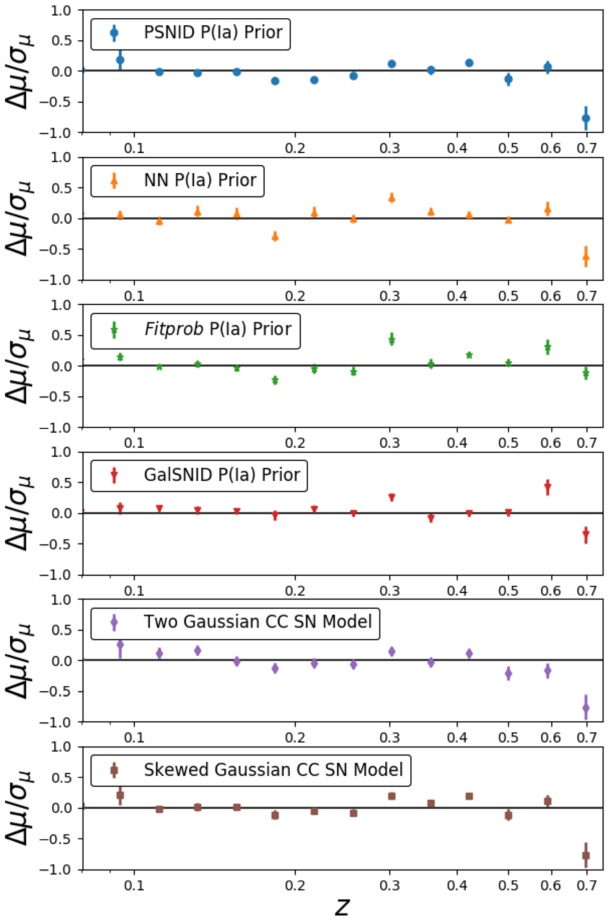

Figure 4.11: Distance bias due to CC SN contamination as a fraction of the distance uncertainty for each BEAMS variant. Small systematic discrepancies begin to appear at $z \geqslant 0.3$.

probability. We expand the GalSNID method to use observables from host galaxy spectroscopy in addition to photometric observations. PSNID is the best method; NN yields a sample with 6.5% contamination at P(Ia) > 0.5 and 3.8% contamination at P(Ia) > 0.9, *Fitprob* yields a sample with 6.1% contamination at P(Ia) > 0.5 (4.1% at P(Ia) > 0.9) and GalSNID gives a sample with 9.3% contamination (7.2% at P(Ia) > 0.9; the total contamination in the sample is 9.7%). The details of these variants are given in Appendix 5.5.

We note that the best approach would be a hybrid one that takes advantage of all classifiers. Though we keep these classifiers as separate here in order to explore the effect of different classification assumptions, Kessler & Scolnic (2017), for example, combine a *Fitprob* > 0.05 cut with the NN classifier. Combining GalSNID priors with a light curve-based classifier is another promising option for future work.

We test each variant on 25 samples of 1,000 simulated PS1 SNe. Though we discuss the ways in which distances and nuisance parameters are affected by these variants, we focus primarily on measurements of w. The RMS of these variants gives an estimate of the systematic uncertainty on w, σ_w^{CC}, an error which could be reduced in the future by improved SN classification methods. It could also be reduced by testing our best single classifier on a robust set of CC+Ia SN simulations that include a larger set of CC SN templates and several methods of adjusting CC SN rates and LFs to match the data.

4.7.2 Systematic Uncertainty on w

We examine two situations in this section: one where α and β are measured by the BEAMS method, and one where α and β are fixed to the values measured from spectroscopic samples. In the case where α and β are measured by the BEAMS method, Figure 4.10 shows the bias on α and β from each classifier. β biases in particular can cause large distance biases at $z > 0.5$, as the average SN color at these redshifts is $\sim$-0.1 (for a bias in β of 0.2, $\Delta\beta \times \overline{C} = 20$ mmag).

If α and β are fixed, BEAMS requires very little information to give robust measurements of w. We test the effect of fixing α and β for all variants and also compare to the case where BEAMS has minimal prior information: we set P(Ia) = 1/2 for all photometric SNe while still fixing P(Ia) = 1 for low-z SNe. If α and β are fixed, the largest absolute bias on w is -0.018 (the *Fitprob* classifier) and the P(Ia) = 1/2 case gives a w-bias of only -0.011. The biases are approximately twice as high if we instead allow BEAMS to fit for α and β, and four times as high for the P(Ia) = 1/2 case, worse than all other methods (a w-bias of -0.043).

Table 4.4 and Figure 5.3 show the median bias and increase in uncertainty on w due to each P(Ia) method and CC SN model. Figure 5.3 shows the bias before and after fixing α and β. We find that alternate CC SN models have only a small effect on the measurement of w. Our lowest w-bias of -0.001$\pm$0.003 comes from the skewed Gaussian CC SN model; however, the results from these three CC SN treatments are statistically consistent (with the exception of the two-Gaussian model with α and β

fixed, which appears to have difficulty robustly measuring both CC SN Gaussians).

Using all variants, σ_w^{CC} has an average value of 0.014±0.007 (30% of the statistical error) if α and β are fixed for the NN, GalSNID, and *Fitprob* classifiers (these classifiers give twice the bias on α and β as PSNID does). The uncertainty is due to the dispersion of the systematic uncertainty from sample to sample. BEAMS distances (Figure 4.11) and nuisance parameters (Figure 4.10) are consistent to within 1σ, regardless of the method.

We note that in some cases fixing α and β may subject the sample to additional systematic uncertainty. For example, α and β could be different in a photometric sample because the host galaxy spectroscopic follow-up selects bright hosts. Host properties correlate with shape and color, which in turn can affect measured α and β (Scolnic et al., 2014b). However, these biases are well-known and can in principle be simulated and corrected for (see Scolnic & Kessler, 2016).

Current measurements of w (e.g. B14) have approximately equal statistical and systematic uncertainties. Therefore, a measurement of w biased by less than ∼half the statistical uncertainty (0.024 in this work), such as the value of $\sigma_w^{CC} = 0.014$ measured here, does not prohibit a robust measurement of w. Any bias larger than that − such as the alternative classifiers discussed in this section without α and β fixed − will dominate the systematic error budget and make it unlikely that photometric SN samples can be competitive with spectroscopically classified samples. For future surveys, such as DES and LSST, this bias may be approximately equal to the

Table 4.4. Cosmological Results from BEAMS Variants

Method	Δw[a]	$\sigma_{\rm stat}$[b]	$\Delta w/\sigma_{\rm stat}$	$\Delta\sigma_{\rm stat}$
one Gaussian[c]	-0.005±0.004	0.050	-0.1	0.002 (3%)
two Gaussians[c]	0.004±0.004	0.051	0.1	0.003 (6%)
skewed Gaussian[c]	**-0.001±0.003**	0.050	-0.0	0.001 (2%)
		P(Ia) Method[d]		
	Δw	$\sigma_{\rm stat}$	$\Delta w/\sigma_{\rm stat}$	$\Delta\sigma_w$
PSNID	**-0.005±0.004**	0.050	-0.1	0.002 (3%)
NN[e]	-0.009±0.004	0.047	-0.2	-0.001 (-2%)
Fitprob[e]	-0.018±0.004	0.047	-0.4	-0.001 (-1%)
GalSNID[e]	-0.011±0.004	0.048	-0.2	-0.000 (0%)

[a]The median bias on w and its uncertainty.

[b]The statistical uncertainty on w from a single sample of 1,000 PS1 SNe.

[c]Using PSNID for the P(Ia) prior probabilities.

[d]Using a single Gaussian CC SN model.

[e]For these classifiers, we keep α and β fixed to their known values. $\Delta\sigma_w$ is negative in some cases, because fixing α and β neglects the contribution of nuisance parameter uncertainties to the uncertainty on w.

Note. — Bias of w in simulations from each CC SN model and prior probability method. We take the median of 25 samples of 1,000 PS1 SNe. For each increase in uncertainty ($\Delta\sigma_w$), we show its percent increase in parentheses. Methods with the lowest bias are highlighted in bold.

statistical error and must be reduced through improved classification methods or a better understanding of CC SNe to yield accurate results.

4.8 Discussion

The PS1 photometric SN sample is the largest SN Ia sample, but using it to optimally measure cosmological parameters − particularly if nuisance parameters α and β are unknown or observationally biased − requires accurate SN type probabilities. These in turn rely on our understanding of the PS1 sample and the CC SNe in it. Evaluating how our incomplete knowledge of CC SNe could bias the results is difficult. In this section, we discuss how CC SN simulations could be improved in the future. We also present alternatives to our implementation of BEAMS and measure the degree to which different methods and priors affect the statistical uncertainty on w.

4.8.1 Generating Reliable CC SN Simulations

Evaluating the reliability of our method would be subject to fewer uncertainties if CC SN simulations were more robust. These simulations are currently subject to two primary limiting factors: the assumption that the CC SN LF is Gaussian with measured mean and RMS from Li et al. (2011) and the limited CC SN template diversity.

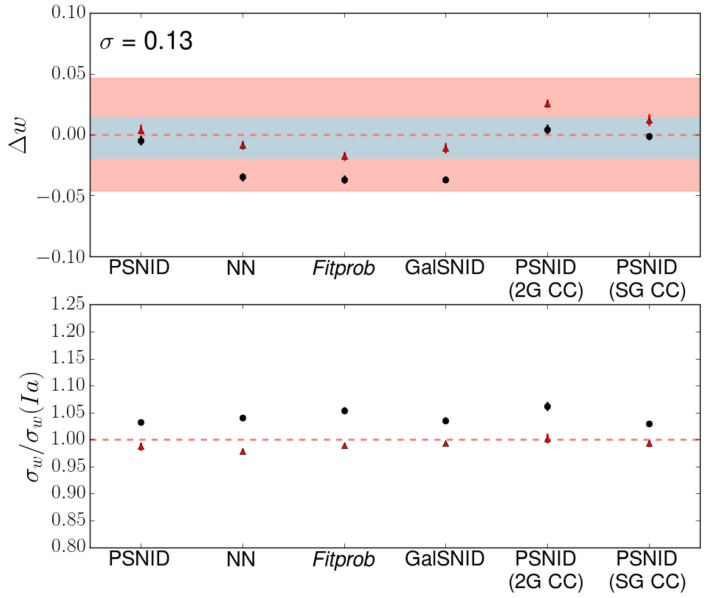

Figure 4.12: The w bias (top) and increased uncertainties (bottom) due to different P(Ia) priors and CC SN parameterizations in BEAMS (black points). We show the median from 25 samples of 1,000 simulated SNe. Red points show the biases with α and β fixed. In the top panel, the statistical error on w from SNe Ia is shown in the red band and the dispersion of the values given in Table 4.4 in blue. Red points have lower uncertainties than the Ia-only uncertainties because fixing α and β neglects their uncertainties. "2G CC" and "SG CC" refer to the 2-Gaussian and skewed Gaussian CC SN parameterizations, respectively.

Figure 4.13 shows that the assumption of the shape of CC SN LFs could have a strong impact on the fraction of bright CC SNe. While the Malmquist bias for SNe Ia is ∼0.1 mag at maximum, Type II SNe observed at the median PS1 survey redshift are up to 3 magnitudes − and 2-3 standard deviations − brighter than the peak of their LF. Determining the frequency of such bright CC SNe requires measuring the shapes of their LFs with better precision than what is currently available from volume-limited surveys such as Li et al. (2011). Due to low statistics, our current simulations treat the LFs of each SN subtype as Gaussian, a flawed assumption.

Generating more robust simulations also requires additional, diverse CC SN templates. Our simulations sample the luminosity, shape, and color distribution of most CC SN subtypes with just a few templates. In addition, the luminosity distribution of these templates is heavily biased; nearly all CC SNe currently used as templates are much brighter than the mean luminosity of their subtypes. Our method makes these bright templates fainter to match the Li et al. (2011) LFs, implicitly assuming that faint CC SNe have similar light curves to bright CC SNe. A better approach would be based on CC SN templates that sample the full range of luminosity space for CC SNe.

We note that additional high-SNR CC SN light curves and spectra exist, but require careful smoothing, interpolation, and spectral mangling to be a reliable addition to the SNANA template library. We have added SNe Ia-91bg and SN IIb templates to SNANA (Appendix 4.10.1.1), but assembling and mangling all available CC SN light curves and templates is beyond the scope of this work.

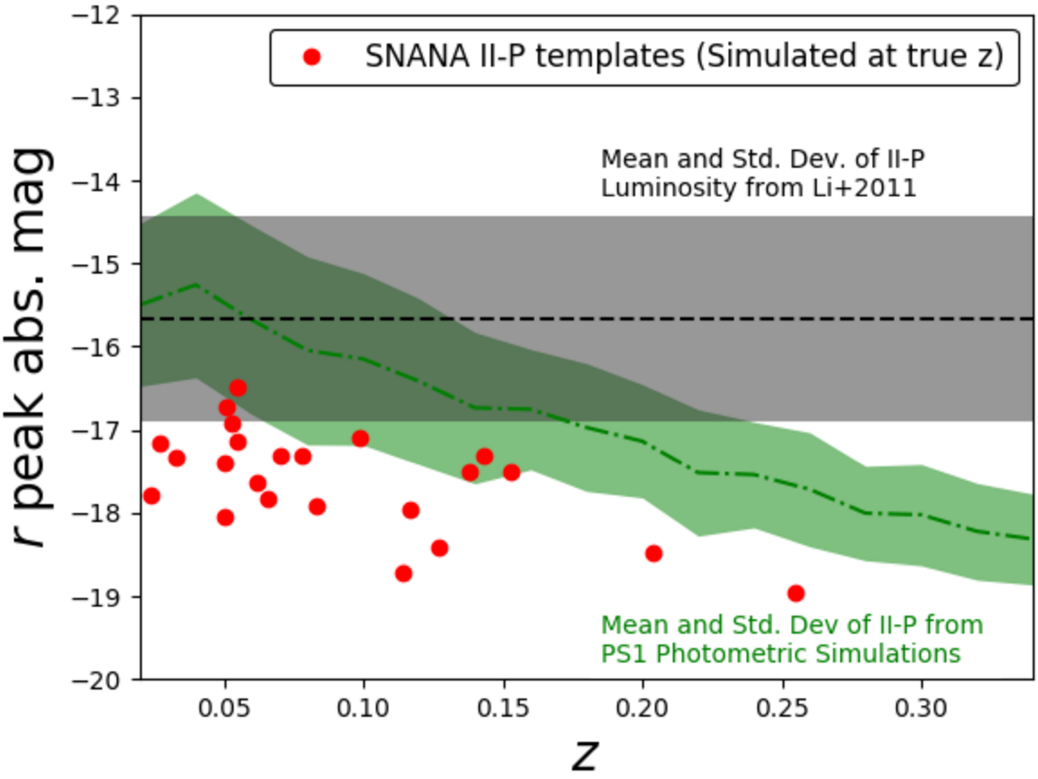

Figure 4.13: In this work, SNANA II-P templates from SDSS (red) are made fainter to match Li et al. (2011) LFs (gray) and then used to generate simulations of the PS1 survey (green). SNANA II-P templates are typically 2-3σ brighter than the mean magnitude of the population from Li et al. (2011).

In the absence of additional templates and improved LF measurements, we can use GalSNID and *Fitprob* classifications to give measurements of w some degree of independence from these sources of uncertainty. Though these classifiers are sub-optimal compared to classifiers such as PSNID, they give a unique set of probabilities that do not rely on simulations for training (though *Fitprob* is implicitly dependent on the nature of CC SN light curves contaminating our sample). *Fitprob* and GalSNID *explicitly* depend on simulations only through their rates priors. Adjusting these priors by a factor of 2 biases w by $\sim$20% of the statistical uncertainty or less.

4.8.2 Alternatives in Implementing BEAMS

In determining cosmological parameters with the BEAMS method we made a set of choices with a modest number of free parameters that reproduced the full cosmological parameter likelihoods. We found that most choices, e.g. varying priors or adding additional CC SN bins, made little difference provided that we had a large number of MCMC steps and few enough parameters.

Two additional choices can improve the systematic error due to CC SN contamination. First, though fixing α and β does not improve the accuracy of the BEAMS method when using PSNID priors, it does improve the accuracy when using NN, *Fitprob* and GalSNID, methods with less accurate classifications. With α and β fixed, NN, *Fitprob* and GalSNID are competitive with the more sophisticated light curve based methods. If we choose to either keep α and β fixed when measuring w

from these classifiers, we find that the σ_w^{CC} decreases by ∼30% on average. In Pan-STARRS, spectroscopically-confirmed SNe can measure these parameters with low uncertainty, and fixing them for our future cosmology analysis in some or all methods could be advantageous.

The second method of improving BEAMS is by cutting additional likely CC SNe from the sample. Following Kessler & Scolnic (2017), we tested a cut on the NN prior probability by requiring $0.5 < P_{NN}(Ia) < 1$. Our simulations show that this cut removes ∼33% of contaminants but just 5% of SNe Ia. The rejected sample has ∼40% CC SN contamination. We found that an NN probability cut yields no improvements to our results using the NN classifier. However, when this cut is added to our other classification methods, it reduces σ_w^{CC} by ∼30% on average. We have not included this cut in our systematic error analysis (§4.7) as it makes our classification methods more correlated and adds an additional dependence on uncertain simulations to the measured systematic error. However, it is likely that this cut will increase the consistency of the full PS1 cosmological results. Kessler & Scolnic (2017) use a hybrid classification approach by requiring $Fitprob > 0.05$. In our simulations, this cut reduces the CC SN contamination by an additional 30% compared to using the NN classifier alone.

A third option for BEAMS is to estimate SN Ia distances with a more strict CC SN model. Kessler & Scolnic (2017) adopt an approach where BEAMS CC SN distributions are determined directly from simulations. For our PS1 analysis, we have adopted

a more general approach to CC SNe at the cost of several additional parameters to marginalize over and a simpler form of the likelihood (Kessler & Scolnic, 2017 also suggest free CC SN parameters as a possible improvement to their method). Tests show our parameterization is capable of marginalizing over the simulated CC SNe such that the Ia likelihood is recovered, and our method is slightly more general than a simulation-based method. A simulation-based mapping of CC SNe may be more robust, but validating it thoroughly is beyond the scope of this paper. In particular, the influence of inaccurate simulations on its recovered results must be explored fully.

4.8.3 Uncertainties in BEAMS Distances

By setting P(Ia) = 1/2 for all photometric SNe, the BEAMS method measures w with a bias of -0.01, 0.2 times the statistical uncertainty on w. The statistical uncertainty on w from setting P(Ia) = 1/2, even with no prior information as to which SNe are of Type Ia, is just 5% higher than using SNe Ia alone (comparing to SNe Ia alone in a case where α and β are fixed to known values). This is primarily due to two factors: the loose priors we employ and the fact that we include a sample of low-z spectroscopically-confirmed SNe Ia for which P(Ia) is fixed to 1. These low-z SNe Ia help to set the SN Ia dispersion and the SN parameters α and β, which are fixed as a function of redshift.

If we remove the low-z sample, distance and SN parameter biases increase. Distance uncertainties, which are higher by just $\sim$5% when using the P(Ia) = 1/2 prior,

increase by nearly 50%. Nevertheless, BEAMS does remarkably well at determining the Gaussian distributions of SNe Ia and CC SNe with relatively little information. This is helped by the fact that because SNe Ia have a factor of $\sim$20 lower dispersion than CC SNe, a loose prior on BEAMS free parameters is sufficient to find the most probable Gaussian distributions.

If we use a more flexible CC SN model (a two Gaussian or skewed Gaussian CC SN model), the requirements on our prior probabilities must become more stringent to yield precise distances. In the case of the two Gaussian model, prior probabilities can no longer be re-normalized or shifted (Eq. 4.6) − these are parameters which can greatly improve the results for alternative prior probability methods. Second, our prior probabilities must be significantly more accurate to yield results with low uncertainties. With the two-Gaussian CC SN model, the uncertainty on w increases by 20% when using GalSNID priors and by 100% when setting P(Ia) = 1/2 for all photometric SNe. Using the skewed Gaussian model, GalSNID and P(Ia) = 1/2 priors increase the uncertainties by 13% and 27%, respectively.

Fortunately, a single Gaussian model for CC SNe appears to yield unbiased distances even though the simulated distribution is not perfectly Gaussian. In essence, BEAMS attempts only to determine the Gaussian distributions of two types of SNe and fortunately, those distributions are relatively well-separated in dispersion even if they are not always well-separated in distance.

4.9 Conclusions

We measured spectroscopic redshifts for 3,147 SN host galaxies in Pan-STARRS, over 1,000 of which are cosmologically-useful, likely SNe Ia. When combined with the full PS1 spectroscopic sample (Scolnic et al. in prep.), we will have 1,145 cosmologically-useful SNe Ia from PS1.

We find that currently available CC SN templates and luminosity functions are biased or incomplete. Our results suggest there are too few bright CC SNe in our simulations.

We generate 25 simulations that closely resemble the PS1 sample. Each has 1,000 photometric PS1 SNe and 250 low-z spectroscopically-confirmed SNe Ia. These simulations show that our method can measure w with a bias due to CC SN contamination as low as -0.001$\pm$0.003. This equates to a systematic uncertainty on w of just 0.004, 8% of the statistical uncertainty, but this uncertainty could be affected by incomplete knowledge of the CC SN distribution. The SN Ia dispersion, σ_{Ia}, is biased by -0.005 ($\sim 0.5\sigma$), the SALT2 shape parameter α is biased by $\sim$0.005 ($\sim 1\sigma$), and the color parameter β is biased by $\sim$0.1 ($\sim 1.5\sigma$). The statistical uncertainties on w are nearly equivalent to those using only SNe Ia.

Using several variants of the method and a CMB-like prior on Ω_M, we estimate the systematic error introduced by CC SN contamination to be 0.014$\pm$0.007 (29% of the statistical error). This systematic error would constitute only a 3% increase on the uncertainty on w in a JLA-like analysis with CMB priors ($\sigma_w = 0.057$ (stat+sys),

and $\sqrt{0.057^2 + 0.014^2} = 0.059$). However, this systematic error assumes that α and β can be fixed to known values from a spectroscopic sample for the alternate classification methods. If α and β are fixed, our least accurate classifiers − including an uninformative prior probability P(Ia)=1/2 for all simulated PS1 SNe − give a median bias on w between -0.01 and -0.02. Systematic error could be reduced further by using a cut on prior probabilities from one variant to reduce CC SNe in the sample for the other variants. We caution that due to uncertainties in CC SN simulations and statistical fluctuations, the CC SN contamination systematic affecting our forthcoming cosmological results may be somewhat lower or higher than the one estimated in this work. However, that analysis will also include a subset of PS1 SNe with known (spectroscopic) classifications as part of the data, a scenario which will likely reduce the systematic uncertainty due to CC SN contamination.

Included in these variants are a total of four different classification methods to measure cosmology, including a host galaxy spectrum-based version of GalSNID (Foley & Mandel, 2013) that we introduce in this work (see Appendix 4.11.1.3). GalSNID is based only on SN Ia host galaxy observables and a rates prior. GalSNID provides a method of measuring w from photometric data that does not depend on SN light curves and training on simulated data. Machine learning techniques may be able to improve on the efficiency of this method in the future. We caution that even with these multiple variants, if CC SN simulations are inaccurate it could cause the systematic error to be underestimated in real data. Additional CC SN templates

and a better measurement of the shape of CC SN luminosity functions could help to ameliorate these concerns.

By drawing random samples from real PS1 data, we tested whether the BEAMS method can work on real data within the confidence intervals of Rest et al. (2014). We found that our measurements of w were fully consistent with Rest et al. (2014), as were the SN nuisance parameters α and β.

Though our results are robust, w is an extremely sensitive measurement and the burden of proof for BEAMS is high. Future validation tests could include SDSS and SNLS photometric data, as well as simulated tests with a variety of CC SN LFs. Additional light curve classification methods could also help to improve the reliability of the BEAMS method.

Future SN Ia samples from DES and LSST will be unable to rely solely on spectroscopic classification to measure cosmological parameters. With the light curve classification and Bayesian methodologies presented here, we validate some of the techniques that will be used in future surveys, and anticipate that PS1 photometric SNe can provide a robust measurement of w using the largest SN Ia sample to date.

4.10 Appendix A: The Dearth of Simulated CC SNe

4.10.1 Core-Collapse SNe

There are a few potential explanations for the difference in Hubble residuals ($0.5 < \mu - \mu_{\Lambda CDM} < 1.5$) between simulations and data. In this Appendix, we attempt to identify the cause of the discrepancy.

First, a large percentage ($\gtrsim$20%) of inaccurate SN Ia redshifts could explain the data. However, in addition to disagreeing with our measurements, this would give too many simulated SNe with very bright and very faint Hubble residuals. Requiring a high TDR minimum and a small separation between the SN location and host galaxy center in our data does not resolve the conflict.

A second option is that the relative rates or magnitude distributions from Li et al. (2011) are erroneous or are biased by the targeted nature of the survey (LOSS searched for SNe in a set of pre-selected bright galaxies). These rates also do not take into account that the relative fractions of different CC SN subtypes could change with redshift. Modest adjustments, such as "tweaking" the mean magnitudes or dispersions of CC SNe by $\lesssim$0.5 mag, cannot explain the discrepancy. Simulating CC SNe using LFs from Richardson et al. (2014), which are typically $\sim$0.3-1.0 mag brighter than Li et al. (2011), produces far too many bright CC SNe compared to our data. The

effect of weak lensing on the data is expected to be an order of magnitude less than the size of the offset we see here (Smith et al., 2014). It is also unlikely that strongly lensed SNe contribute significantly to the discrepancy (Oguri & Marshall, 2010).

By re-classifying LOSS SNe, Shivvers et al. (2017) recently found that SN Ib relative rates were more than double the fraction found by Li et al. (2011). This change could reduce the Hubble residual discrepancy by half or more. However, Shivvers et al. (2017) determined these rates by re-classifying a number of LOSS SNe Ic as SNe Ib, which in turn means that the SN Ib LF should be made fainter. Making the SN Ib LF fainter will increase the discrepancy in Hubble residuals. We continue to use Li et al. (2011) in this work, as we can be sure that the LFs and relative rates are self-consistent.

Finally, we consider that our results could be biased if SNANA templates have lower average reddening than PS1 data. There are likely substantial differences between the reddening distribution of the templates and the data. However, we find that adding additional reddening to our simulations tends to make the magnitude distribution of CC SNe more broad (we approximately adjust the Li et al., 2011 LFs for dust following Rodney et al., 2014). This *increases* the discrepancy between simulations and data. Correcting for the unknown intrinsic reddening of these templates is an important future objective that can allow SNANA simulations to be more realistic. See §4.8.1 for further discussion of biases in our simulations and templates.

4.10.1.1 Adding New Supernova Templates to SNANA

Several CC SN or peculiar Ia subtypes are missing from the SNANA simulation library but could be present in the PS1 data. Missing SN types include superluminous SNe, SNe IIb, SNe Ibc-pec, and peculiar, faint SNe Ia such as 1991bg-like SNe Ia (Ia-91bg) and SNe Iax (Foley et al., 2013). Superluminous SNe are unlikely to help resolve the discrepancy, as they are brighter than SNe Ia and occur preferentially in faint hosts for which redshifts are difficult to measure (Lunnan et al., 2015). SNe Ibc-pec have similar LFs to SNe II-P but are much less common, so it is unlikely that many would fall on the Hubble diagram so near the SN Ia distribution. SNe Iax are red, fast-declining SNe that may be relatively common but have faint (albeit uncertain) LFs more similar to SNe II-P and Ibc-pec. These also tend to be poorly fit by SALT2, and would frequently fail our cuts.

SNe IIb and SNe Ia-91bg both have LFs only $\sim$1 mag fainter than SNe Ia, though they are relatively uncommon and would need a high fraction to pass SALT2 light curve cuts to be major contributors to our Hubble diagram. We investigated their impact by adding Ia-91bg and IIb templates to SNANA.

To simulate CC SNe over a wide range of redshifts and passbands, SNANA templates require relatively high-SNR, high-cadence spectral and photometric sampling, which exists for a paucity of CC SNe. Simulating SN light curves at high redshift often necessitates near-ultraviolet data as well. To create a template, an interpolated, flux-calibrated spectral time series is "mangled" to match the observed photometry

by using wavelength-dependent splines with knots at the effective wavelengths of the photometric filters. Least-squares fitting determines the the best-fit spline that scales the spectrum to match the photometry. Hsiao et al. (2007) describes the "mangling" procedure in detail.

To improve the SNANA CC SN simulation, we add four SN IIb templates − SNe 1993J, 2008ax, 2008bo, and 2011dh − using spectra and light curves consolidated by the Open Supernova Catalog (Guillochon et al., 2017)[11]. Each of these templates have well-sampled spectra and optical light curves. We also add Ia-91bg templates using the SN 1991bg spectrum from Nugent et al. (2002)[12], warped to match SNe Ia-91bg with well-sampled light curves before and after maximum (SNe 1991bg, 1998de, 1999by, 2005bl[13]). Using multiple SN templates helps us obtain better sampling of the shape-luminosity relation for SNe 91bg (steeper than the relation for normal SNe Ia; Taubenberger et al., 2008).

Figure 4.14 shows the interpolated light curves, mangled spectra and Hubble residual histograms for SNe IIb and Ia-91bg. For Ia-91bg, we assume their rates have the same redshift dependence as SNe Ia. SNe Ia-91bg have magnitude distributions that

[11]References for the spectra and photometry are listed here. SN 1993J: Richmond et al. (1996); Metlova et al. (1995); Barbon et al. (1995); Jerkstrand et al. (2015); Modjaz et al. (2014). SN 2008ax: Modjaz et al. (2014); Brown et al. (2014); Taubenberger et al. (2011); Tsvetkov et al. (2009); Pastorello et al. (2008). SN 2008bo: Modjaz et al. (2014); Brown et al. (2014); Bianco et al. (2014). SN 2011dh: Ergon et al. (2015, 2014); Shivvers et al. (2013); Arcavi et al. (2011). Secondary sources: Yaron & Gal-Yam (2012); Richardson et al. (2001); Silverman et al. (2012) and the Sternberg Astronomical Institute Supernova Light Curve Catalogue.

[12]`https://c3.lbl.gov/nugent/nugent_templates.html`

[13]References for the photometry are listed here. SN 1998de: Silverman et al. (2012); Ganeshalingam et al. (2010); Modjaz et al. (2001). SN 1999by: Silverman et al. (2012); Ganeshalingam et al. (2010); Garnavich et al. (2004). SN 2005bl: Contreras et al. (2010). Secondary sources: the Sternberg Astronomical Institute Supernova Light Curve Catalogue.

could explain the data, but their rates are inconsistent with the data. SNe IIb are far too rare, as nearly all simulated SNe IIb have measured colors that are too red to be SNe Ia. Though we find that Ia-91bg and IIb SNe are not frequent enough to resolve the difference between PS1 data and simulations, we incorporate these subtypes in our simulations hereafter.

4.10.1.2 Measuring CC SN Luminosity Functions with PSNID

There is an additional procedure by which PS1 data can inform CC SN LFs: we use the PSNID light curve classifier (Sako et al., 2011, 2014) to separate the likely contributions of SNe Ia, Ib/c, and II. The SNANA implementation of PSNID compares the SALT2 SN Ia model and SNANA's CC SN templates to the observed data. PSNID determines the fit χ^2- and prior-based probability that a given SN is Type Ia, Type Ib/c, or Type II. Though the set of templates we use for PSNID is the same set we use to generate CC SNe in our simulations, broad priors allow these templates to be shifted in magnitude and extinction to fit our data.

We compare PSNID's classifications of PS1 data and simulations by examining the distribution of $m_B - \mu_{\Lambda CDM}$, a proxy for absolute magnitude at peak (Figure 4.15). We find that likely SNe Ib/c are much brighter and have lower dispersion than the simulations. To bring our simulations into agreement with the data, we adjusted the simulated SN Ib/c and II distributions such that the mean and standard deviations of the *simulated* SNe that PSNID classified as Type Ib/c and II matched the mean

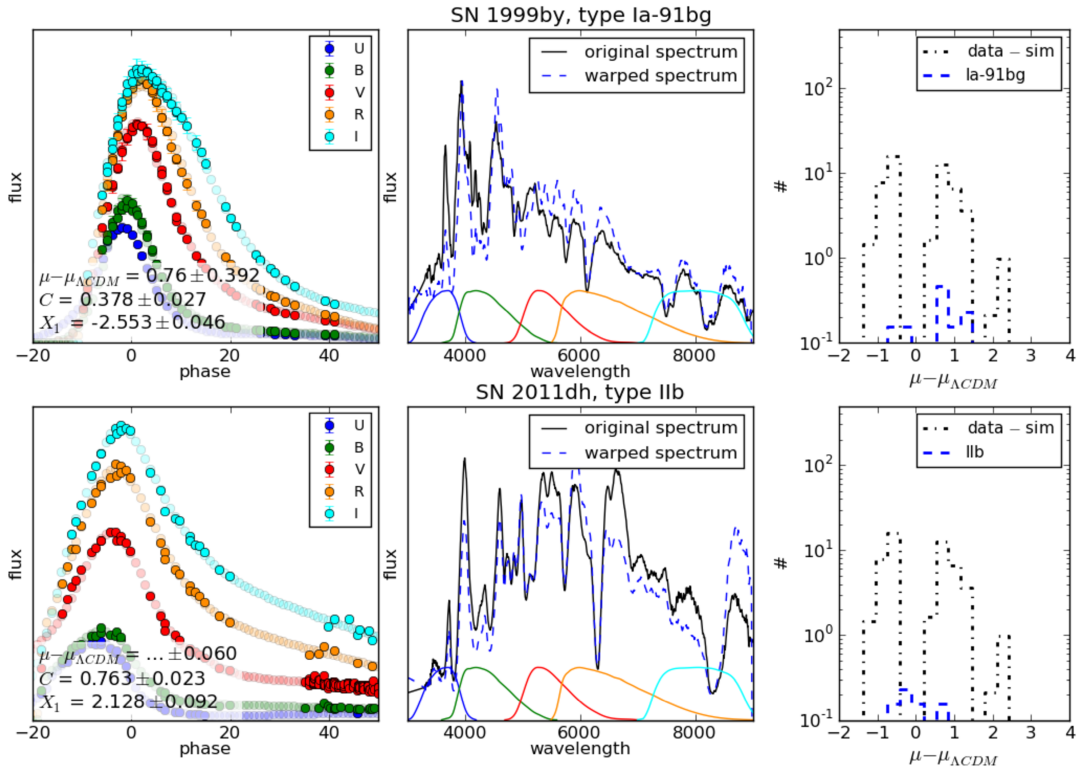

Figure 4.14: New templates for SNe Ia-91bg (top panels) and IIb (bottom panels) were added to SNANA by mangling a template spectrum to match light curve data. From left to right, we show the interpolated SN light curves (light shading indicates interpolated points), the warped template spectra at peak brightness, and the Hubble residuals of *all* templates of the new subtype. We compare the Hubble residuals of the new templates to the difference between the data and our simulations; the new templates cannot explain the discrepancy we observe. Because SN 2011dh has $z < 0.01$, its distance modulus residual is not shown in the left panel.

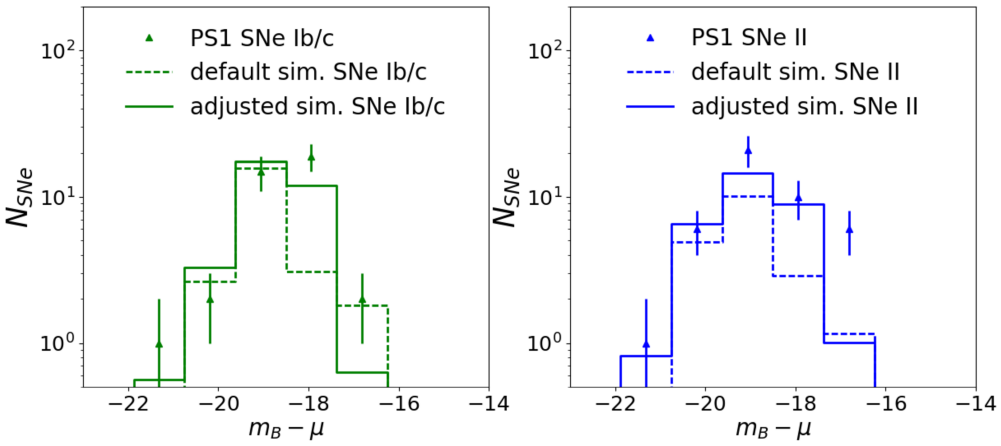

Figure 4.15: Empirical adjustments to SNANA simulations motivated by PSNID classifications, shown using histograms of SN absolute magnitude (SALT2 $m_B - \mu_{\Lambda CDM}$). PSNID-classified PS1 SNe and PSNID-classified simulations suggest that SNe Ib/c, after shape and color cuts, are brighter than expected. Our adjusted simulations (solid lines) match the data after we reduce the simulated dispersions and brighten LFs by $\sim$1 mag.

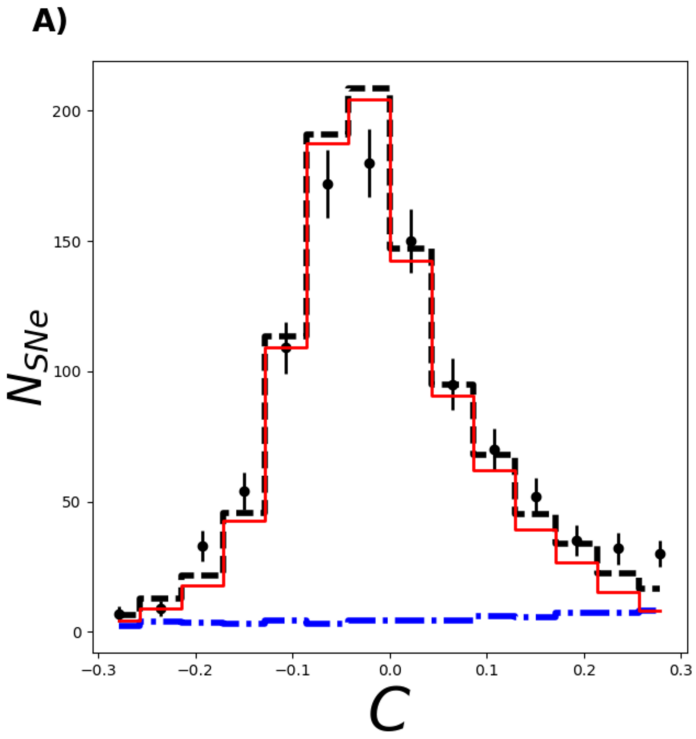

Figure 4.16: Simulated SALT2 C (right), compared to data in the J17 (adjusted) simulations. Compared to the original simulations (Figure 4.4D and 4.4E), the red end of the C distribution is more consistent with our data in the J17 simulations.

and standard deviations of *real* PS1 SNe that PSNID classified as Type Ib/c and II. This requires reducing the dispersion of CC SN templates by 55% for SNe Ib/c. It also requires brightening the simulated LFs by 1.2 mag for SNe Ib/c and 1.1 mag for SNe II. We made shape and color cuts (§4.3.2) in this analysis but neglected σ_{X_1} and $\sigma_{\rm peakMJD}$ cuts to increase our SN statistics.

Figure 4.15 shows the distributions of PSNID-classified PS1 SNe (P(SN Type) > 95%) compared to our simulations before and after absolute magnitude and dispersion adjustments. We apply shape and color cuts but neglect additional cuts to increase our CC SN sample size.

After these adjustments, simulated CC+Ia SNe are consistent with our data. Figure 4.5 shows Hubble residual histograms before and after our PSNID-based adjustments. After correction, CC SNe are 8.9% of our final sample and SNe Ia-91bg comprise 0.2%. Additional CC SNe can explain the red tail of the SALT2 C distribution in Figure 4.4C (Figure 4.16). No CC SN rate adjustments were made. Although the simulated absolute magnitudes have been brightened by ∼1 mag, CC SN in the adjusted simulations are only ∼0.5 mag brighter than the original simulation on average. This is because as we brighten the CC SN distribution, the number of detectable faint SNe − which are nearer to the peak of the LF, and thus occur more frequently − increases, reducing the mean absolute magnitude. Note that the ∼2-3σ discrepancy on the left (bright) side of the Hubble diagram can be reduced by simulating a nominal host mass correction, which tends to very slightly broaden the simulated

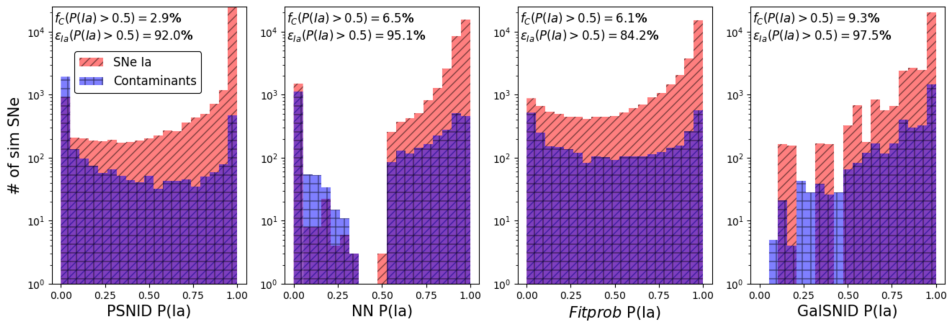

Figure 4.17: Simulated prior probabilities from the four classification methods discussed in this work for SNe Ia (red) and contaminants (blue; includes CC SNe and SNe Ia with incorrect redshifts). For each method, we show the percentage of contaminants f_C and the fraction of SNe Ia included, ϵ_{Ia}, in a P(Ia) > 0.5 sample.

distribution of SNe Ia.

Our adjusted simulation matches the Hubble residuals of the PS1 data. It also resolves the discrepancies in the PS1 C distribution (Figure 4.16). Hereafter, we refer to the adjusted simulation, which adds new CC SN templates and uses PSNID to infer the true SN Ib/c distribution, as the J17 simulation[14].

4.11 Expanding the BEAMS Method

We discuss the methodology behind alternative BEAMS variants in this section. The results from these variants are given in §4.7.

[14]Templates and simulation input files for this simulation have been added to the SNANA library.

4.11.1 Additional P(Ia) Priors

In addition to the PSNID prior probabilities in our baseline method, we use three additional methods of estimating P(Ia): *Fitprob*, NN, and GalSNID. The effectiveness of each method is illustrated in Figure 4.17. The NN, *Fitprob*, and PSNID classifiers all determine probabilities by fitting to the photometric SN light curve. *Fitprob* relies on only the SALT2 model for fitting, while PSNID and NN depend on CC SN simulations for templates and training, respectively. GalSNID uses host galaxy information and depends on SNANA simulations only through the SN rates prior.

4.11.1.1 NN

The Nearest Neighbor (NN) classifier (Sako et al., 2014) uses a set of observables to define how close a given SN is to the CC SN and SN Ia populations. In our implementation, we use the SALT2 color (C), stretch (X_1), and redshift (z). The equation:

$$d_i^2 = \frac{(z - z_i)^2}{\Delta z_{\max}^2} + \frac{(C - C_i)^2}{\Delta C_{\max}^2} + \frac{(X_1 - X_{1,i})^2}{\Delta X_{1,\max}^2} \tag{4.9}$$

defines a list of NN distances between the ith SN and simulated training data. For the ith SN, neighbors are defined as all simulated events with $d_i < 1$. NN training finds the parameters $\Delta C_{\max}$, $\Delta X_{1,\max}$ and $\Delta z_{\max}$ that optimize the classification metric (efficiency $\times$ purity) of simulated training data. NN is an efficient and accurate classifier in PS1 simulations: the set of SNe with $P_{NN}(\mathrm{Ia}) > 0.9$ has 3.8% contamination

compared to 9.7% contamination for the full sample (including CC SNe and SNe Ia with incorrect redshifts). This set includes 74% of all SNe Ia. See Kessler & Scolnic (2017) for details on the NN classification method.

4.11.1.2 *Fitprob*

The *Fitprob* method estimates P(Ia) from the χ^2 and number of degrees of freedom of the SALT2 light curve fit (the SALT2 fit probability). Because the SALT2 fit χ^2 has no knowledge about the relative frequency of different SN types, we multiplied $P_{fp}(Ia)$, the *Fitprob* probability, by a redshift-dependent SN rates prior, $P(Ia|z)$. $P(Ia|z)$ is the number of SNe Ia divided by the total number of SNe at a given redshift (after sample cuts; measured using the J17 simulations):

$$\tilde{P}_{fp}(Ia) = \frac{P(Ia|z)P_{fp}(Ia)}{P(CC|z)(1 - P_{fp}(Ia)) + P(Ia|z)P_{fp}(Ia)} \tag{4.10}$$
$$P(CC|z) = 1 - P(Ia|z).$$

Compared to the PSNID (baseline) classifier, *Fitprob* has twice the fraction of contaminants at $P(Ia) > 0.5$. The fraction of CC SNe with high P(Ia) is also higher by a factor of $\sim$2.

4.11.1.3 GalSNID

SNe Ia have much longer average delay times between progenitor formation and explosion than CC SNe. Because of this, SNe Ia are the only SN type found in early type hosts. This allows methods such as GalSNID (Foley & Mandel, 2013) to classify SNe with host galaxy information. The GalSNID method in Foley & Mandel (2013) is based on photometric information and is highly dependent on host morphology. Because measuring galaxy morphologies at typical PS1 redshifts requires $\sim 0.1''$ image resolution, we modified the method by adding spectral observables. Though GalSNID is a very inefficient classifier, it measures SN Ia probabilities in a way that is only minimally subject to light curve and LF uncertainties.

To train GalSNID, we used 602 host galaxy spectra from the Lick Observatory Supernova Search (LOSS; Leaman et al., 2011) and 354 host galaxy spectra of PS1 spectroscopically-confirmed SNe. The equivalent widths of spectral emission lines, and Hα in particular, correlate with SN type. Another useful diagnostic is the template that cross-correlates best with the observed host spectrum. Finally, we include host galaxy R (labeled effective offset in Foley & Mandel, 2013), $B - K$ colors and absolute K magnitudes from Foley & Mandel (2013).

We trained GalSNID on spectral information using LOSS host galaxy spectra and spectroscopically confirmed PS1 SNe for which we have host galaxy spectra. Relative to the PS1 spectroscopic sample, LOSS has a greater number of total SNe, and a greater diversity and number of CC SNe on which to train the data.

Spectra for ∼1/3 of the LOSS sample are available from SDSS/BOSS (Alam et al., 2015; 297 spectra), and we found an additional ∼1/3 (305 spectra) by querying the NASA/IPAC Extragalactic Database. In total, 67% of the 905 SNe discovered by LOSS have host galaxy spectra. In general, the SNR of these data are high (much higher on average than our redshift survey data).

PS1 spectroscopically classified 520 SNe of which ∼150 are CC SNe and the rest are SNe Ia. Of the CC SNe, ∼30 are SNe IIn (Drout et al. in prep), 76 are II-P or II-L (Sanders et al., 2015) and ∼20-30 are SNe Ib or Ic. We obtained host galaxy spectra for 354 of these SNe.

We searched for a number of prominent, observational galaxy diagnostics that correlate with the age of the host, and found that the equivalent widths of bright emission lines such as OII, OIII, Hα and Hβ are measurable in many of our spectra. We required continuum SNR > 5 near a given line measurement for an observable to be used in training or classification. As a way to incorporate additional information in a single diagnostic, we included the best matched spectral template based on cross-correlation as an observable.

Although these diagnostics are correlated, in this work we follow Foley & Mandel (2013) in treating them as independent. Final probabilities for a given SN can therefore be computed by multiplying the probability of a Ia given each observable (Foley & Mandel, 2013):

$$\mathrm{P(Ia|D)} = k^{-1}\mathrm{P(Ia}|z)\prod_{i=1}^{N}\mathrm{P(D_i|Ia)}, \tag{4.11}$$

where N is the number of observables and $\mathrm{P(D}_i\mathrm{|Ia)}$ is the probability of an observable given that the SN is Type Ia (Table 4.5). $\mathrm{P(D}_i\mathrm{|Ia)}$ is easy to compute; it is the fraction of SN Ia host galaxies that have observable D_i. $\mathrm{P(Ia}|z)$ is a rates prior informed by our SNANA simulations. k is a normalization factor that requires $\mathrm{P(Ia|D)} + \mathrm{P(CC|D)} = 1$. See Foley & Mandel (2013) for additional details on the methodology. In the future, machine learning techniques may be able to improve our results by relaxing the assumption that observables are uncorrelated.

The probabilities from our LOSS+PS1 training sample are provided in Table 4.5. We also include effective offset, $B - K$ colors, and K absolute magnitudes using probabilities measured from Foley & Mandel (2013) and SED fits using PS1 host galaxy photometry. Note that because Hα and Hβ are almost perfectly correlated (the correlation coefficient is 0.94), we do not use Hβ as an observable when Hα is present in optical spectra ($z \lesssim 0.35$). Figure 4.17 shows the GalSNID probabilities of SNe Ia and CC SNe in PS1 and our simulations (we redshift and add noise to LOSS spectra to determine simulated GalSNID probabilities). Figure 4.18 shows GalSNID probabilities for real spectroscopically classified PS1 SNe.

To create GalSNID probabilities for the simulated sample, we artificially redshifted LOSS host galaxy spectra, added noise to make them consistent with the SNR of PS1 host spectra, and used GalSNID to measure the probability that each host observed

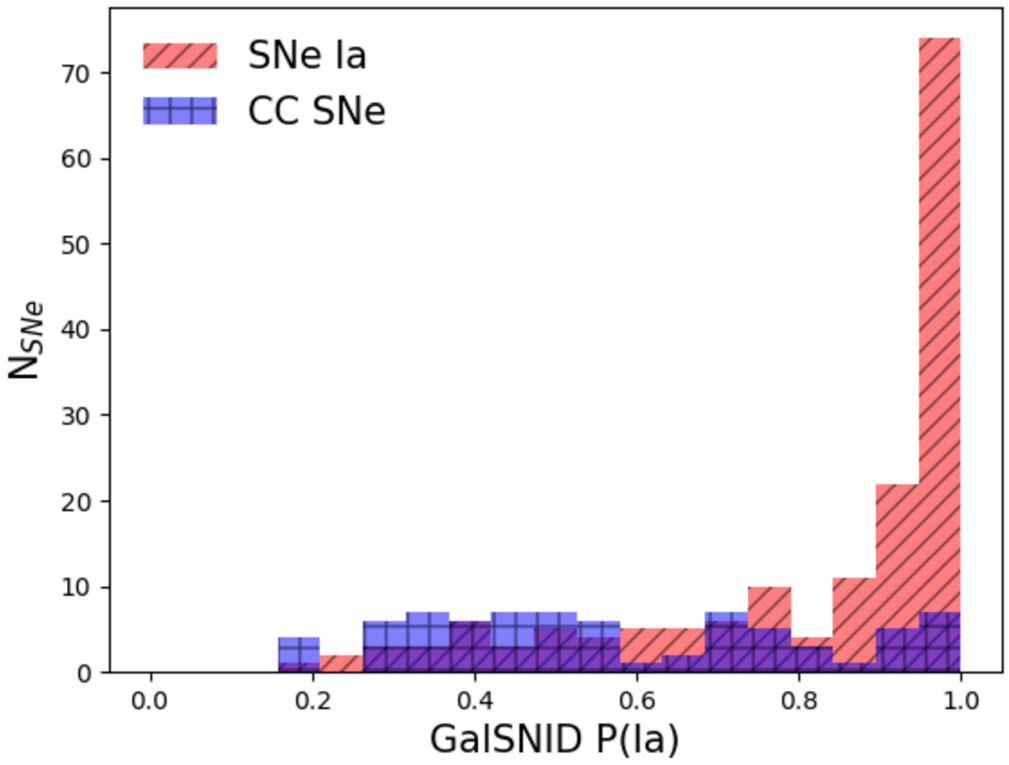

Figure 4.18: GalSNID classifications of spectroscopically classified CC SNe and SNe Ia in Pan-STARRS, neglecting rates priors.

a SN Ia. We took the distributions of GalSNID probabilities for the redshifted, noisy spectra corresponding to LOSS SNe II, Ib/c and Ia hosts in each simulated redshift bin and assigned the probabilities drawn from those distributions to simulated SNe II, Ib/c and Ia. This gave our simulated SNe the same probability distributions as the redshifted LOSS data. Figure 4.17 shows that GalSNID is a relatively imprecise classifier, but it provides constraints that are independent of SN light curves and their associated uncertainties. We have not taken into account the redshift evolution of SN host galaxies in this work.

On PS1 data, GalSNID is by far the least efficient classifier. Because classifications are highly influenced by the rates prior, GalSNID considers just 5% of contaminants to be likely CC SNe. If we set a higher threshold of P(Ia) > 0.9, GalSNID removes $\sim$25% of CC SNe and keeps $\sim$70% of SNe Ia. GalSNID is also most effective at $z \lesssim 0.35$, where Hα is present in our optical spectra (the best indicator of SN type in our spectra). Unfortunately, the largest SN Ia distance biases are at $z > 0.4$, where the CC SN distribution becomes blended with the SN Ia distribution.

GalSNID would also be useful as an additional prior on SN type in conjunction with other methods. However, due to uncertainty in CC SN models and LFs, in the present analysis we consider it most powerful as a stand-alone tool that can measure SN Ia probabilities without using light curve data.

4.11.2 Varying the CC SN Model

PS1 and other spectroscopic data show that SNe Ia are well-represented by a Gaussian Hubble residual model, but CC SNe are not. We investigated replacing the CC SN likelihood in Eq. 5.3 with two likelihoods that are more consistent with our CC SN simulations. We tested a two-Gaussian model with ten additional free parameters for CC SNe (the means and standard deviations of the second Gaussian at five redshift control points). We also tested a single, asymmetric Gaussian model with five additional free parameters (skewness at each CC SN control point).

If we allow BEAMS to shift and/or rescale the prior probabilities that a SN is of type Ia (Eq. 4.6), BEAMS can give unphysical results. The alternative CC SN models are significantly more flexible and that flexibility must be constrained by accurate, fixed prior probabilities such as those from NN (see §4.8.3). We fix the parameters that allow BEAMS to adjust the priors ($A = 1$ and $S = 0$ in Eq. 4.6) or else the uncertainties on SN Ia distances will inflate to >0.1 mag for even our best-measured redshift control points.

Table 4.5. Probability of Host Properties Given Type

Bin	$P(D_i\|\text{Ia})$	$P(D_i\|\text{Ibc})$	$P(D_i\|\text{II})$
	Cross-Correlation Template		
absorption	$0.502\ ^{+0.054}_{-0.048}$	$0.256\ ^{+0.069}_{-0.055}$	$0.286\ ^{+0.036}_{-0.033}$
ellipt+A stars	$0.431\ ^{+0.050}_{-0.045}$	$0.598\ ^{+0.097}_{-0.085}$	$0.609\ ^{+0.051}_{-0.048}$
late-type	$0.029\ ^{+0.017}_{-0.012}$	$0.037\ ^{+0.035}_{-0.020}$	$0.030\ ^{+0.015}_{-0.010}$
emission	$0.029\ ^{+0.017}_{-0.012}$	$0.098\ ^{+0.047}_{-0.034}$	$0.071\ ^{+0.021}_{-0.016}$
	Hα Equivalent Width		
<-5.0	$0.005\ ^{+0.011}_{-0.004}$	$0.000\ ^{+0.033}_{-0.000}$	$0.000\ ^{+0.010}_{-0.000}$
-5.0 – 0.0	$0.323\ ^{+0.045}_{-0.039}$	$0.054\ ^{+0.051}_{-0.029}$	$0.116\ ^{+0.031}_{-0.024}$
0.0 – 5.0	$0.219\ ^{+0.038}_{-0.033}$	$0.250\ ^{+0.086}_{-0.066}$	$0.217\ ^{+0.039}_{-0.034}$
5.0 – 10.0	$0.095\ ^{+0.026}_{-0.022}$	$0.125\ ^{+0.067}_{-0.046}$	$0.143\ ^{+0.033}_{-0.027}$
>10.0	$0.358\ ^{+0.047}_{-0.042}$	$0.571\ ^{+0.120}_{-0.100}$	$0.524\ ^{+0.058}_{-0.052}$
	Hβ Equivalent Width		
<-5.0	$0.000\ ^{+0.007}_{-0.000}$	$0.000\ ^{+0.026}_{-0.000}$	$0.000\ ^{+0.007}_{-0.000}$
-5.0 – 0.0	$0.504\ ^{+0.046}_{-0.043}$	$0.338\ ^{+0.084}_{-0.068}$	$0.333\ ^{+0.040}_{-0.035}$
0.0 – 5.0	$0.399\ ^{+0.041}_{-0.038}$	$0.451\ ^{+0.094}_{-0.079}$	$0.441\ ^{+0.044}_{-0.041}$
5.0 – 10.0	$0.069\ ^{+0.019}_{-0.016}$	$0.070\ ^{+0.048}_{-0.030}$	$0.149\ ^{+0.028}_{-0.023}$
>10.0	$0.029\ ^{+0.014}_{-0.010}$	$0.141\ ^{+0.060}_{-0.044}$	$0.077\ ^{+0.021}_{-0.017}$
	OII Equivalent Width		
<-5.0	$0.000\ ^{+0.027}_{-0.000}$	$0.000\ ^{+0.183}_{-0.000}$	$0.000\ ^{+0.056}_{-0.000}$
-5.0 – 0.0	$0.103\ ^{+0.055}_{-0.038}$	$0.000\ ^{+0.183}_{-0.000}$	$0.152\ ^{+0.101}_{-0.066}$
0.0 – 5.0	$0.676\ ^{+0.115}_{-0.098}$	$0.400\ ^{+0.315}_{-0.191}$	$0.545\ ^{+0.161}_{-0.126}$
5.0 – 10.0	$0.132\ ^{+0.060}_{-0.043}$	$0.300\ ^{+0.290}_{-0.163}$	$0.182\ ^{+0.108}_{-0.072}$
>10.0	$0.074\ ^{+0.049}_{-0.032}$	$0.300\ ^{+0.290}_{-0.163}$	$0.121\ ^{+0.096}_{-0.058}$
	OIII Equivalent Width		
<-5.0	$0.000\ ^{+0.007}_{-0.000}$	$0.000\ ^{+0.027}_{-0.000}$	$0.000\ ^{+0.007}_{-0.000}$
-5.0 – 0.0	$0.215\ ^{+0.032}_{-0.028}$	$0.101\ ^{+0.055}_{-0.037}$	$0.079\ ^{+0.021}_{-0.018}$
0.0 – 5.0	$0.674\ ^{+0.054}_{-0.050}$	$0.739\ ^{+0.118}_{-0.103}$	$0.728\ ^{+0.058}_{-0.053}$
5.0 – 10.0	$0.067\ ^{+0.019}_{-0.016}$	$0.058\ ^{+0.046}_{-0.028}$	$0.059\ ^{+0.019}_{-0.015}$
>10.0	$0.041\ ^{+0.016}_{-0.012}$	$0.101\ ^{+0.055}_{-0.037}$	$0.134\ ^{+0.027}_{-0.023}$

Chapter 5

Measuring Dark Energy Properties with Photometrically Classified Pan-STARRS Supernovae. II. Cosmological Parameters from 1,344 Supernovae

5.1 Abstract

We use over 1,100 photometrically classified supernovae (SNe) from Pan-STARRS and ∼200 low-z ($z < 0.1$) SNe Ia to measure cosmological parameters. The current

generation of wide-angle time domain surveys are discovering far more Type Ia supernovae (SNe Ia) than can be classified with SN spectroscopy. However, in a previous paper (I), we demonstrated that SNe without spectroscopic classifications can still be used to infer unbiased cosmological parameters by using a Bayesian methodology that marginalizes over core-collapse (CC) SN contamination. Our sample contains 71% more SNe than the largest previous compilation of SNe Ia. It has a redshift range of $0.01 \lesssim z \lesssim 0.7$ with a median survey redshift of $\sim$0.3 and we estimate that $\sim$95% of SNe in the sample are bona fide SNe Ia. From these data, we measure the difference in derived SN Ia distances between low-mass and high-mass host galaxies to be 0.101$\pm$0.026 mag (stat+sys), consistent with previous measurements. Combining SNe with cosmic microwave background (CMB) constraints from the Planck satellite, we measure the dark energy equation of state parameter w to be -1.018$\pm$0.063 (stat+sys). Combining these data with additional constraints from baryon acoustic oscillations (BAO) and local H_0 measurements yields w = -1.047$\pm$0.051. If we allow w to evolve with redshift as $w(a) = w_0 + w_a(1-a)$, we find $w_0 = -0.952 \pm 0.147$ and w_a = -0.185$\pm$0.445 from the combination of SNe, BAO, CMB, and local H_0 measurements. These results are consistent with the Joint Lightcurve Analysis constraints on w and have $\sim$10% larger uncertainties due to noisier SN data and a more conservative treatment of the selection bias systematics. We try four different photometric classification priors for Pan-STARRS SNe and two alternate ways of modeling the CC SN contamination, finding that no variant gives a w that differs by more than 3.3% from

the baseline measurement. Uncertainty in the CC SN contamination model is only the fourth largest systematic uncertainty in this analysis ($\sigma_w^{\rm CC} = 0.010$), after uncertainty in the SN Ia dispersion model ($\sigma_w^{\rm disp} = 0.028$), photometric calibration ($\sigma_w^{\rm cal} = 0.028$), and the SALT2 model calibration uncertainty, all of which are not specific to photometrically classified SN samples. We also find $\sim 3\sigma$ evidence for evolution in the correlation between SALT2 color and luminosity as a function of redshift, a potential new source of systematic uncertainty that could become significant at $z \sim 0.5$-1 (just 1σ evidence for evolution had been seen previously). Our data provide one of the best current constraints on w, demonstrating that even samples with $\sim$5% CC SN contamination can give competitive cosmological constraints when marginalized over in a Bayesian framework.

5.2 Introduction

The cause of the universe's accelerating expansion at late times is one of the fundamental questions in astrophysics today. Twenty years ago, distances from Type Ia supernovae (SNe Ia) revealed that approximately $\sim$70% of the energy in the present day universe must consist of "dark energy" to explain its acceleration (Riess et al., 1998; Perlmutter et al., 1999). In the time since this discovery, large SN surveys with up to $\sim$750 spectroscopically confirmed SNe Ia have measured the expansion history of the universe at $z \lesssim 1$ with increasing precision (Riess et al., 2004; Kessler et al., 2009a;

Hicken et al., 2009b; Conley et al., 2011; Sullivan et al., 2011; Suzuki et al., 2012; Rest et al., 2014; Betoule et al., 2014). Because SNe Ia are observed in the cosmic epochs when dark energy is most dominant, they have more leverage to measure dark energy than most other cosmological probes. In conjunction with baryon acoustic oscillation (BAO) and cosmic microwave backround (CMB) constraints (e.g. Eisenstein et al., 2005; Bennett et al., 2003; Anderson et al., 2014; Planck Collaboration et al., 2015), these SNe Ia are used to infer the dark energy equation of state parameter w (its pressure to density ratio, $P/\rho c^2$).

The simplest model of dark energy is a cosmological constant, a vacuum energy that exerts a spatially and temporally constant negative pressure ($w = -1$). However, if w is measured to be greater than -1 it would be an indication of "quintessence" dark energy, a dynamic scalar field. A w of less than -1 would imply so-called "phantom" dark energy, which requires extremely exotic physics (Amendola et al., 2013).

Nearly all SN Ia analyses have measured a dark energy equation of state consistent with $w = -1$. The most precise measurement to date is that of Betoule et al. (2014, hereafter B14), who combined 740 spectroscopically confirmed SNe Ia from the Sloan Digital Sky Survey (SDSS; Alam et al., 2015), the SuperNova Legacy Survey (SNLS; Astier et al., 2006) high-z SNe from HST (Riess et al., 2007) and low-z SNe (Hamuy et al., 1996; Riess et al., 1999; Jha et al., 2006; Hicken et al., 2009c,a; Contreras et al., 2010; Folatelli et al., 2010) to form the Joint Light-curve Analysis (JLA). JLA SNe Ia, when combined with CMB data from the Planck satellite and BAO constraints from

Anderson et al. (2014) and Ross et al. (2015), yield $w = -1.006 \pm 0.045$ (Planck Collaboration et al., 2015).

Statistical and systematic uncertainties on the JLA measurement of w are approximately equal. Though a great deal of recent progress has been made to lower systematic uncertainties, including the leading systematic of photometric calibration error (Scolnic et al., 2015), lower uncertainties are also possible just by adding more SNe Ia. Although a significant reduction of the statistical uncertainty now requires hundreds of additional SNe Ia, *thousands* of SNe Ia have already been discovered by Pan-STARRS (PS1; Kaiser et al., 2010). Thousands more are currently being discovered by the Dark Energy Survey (DES; Flaugher, 2005) and tens of thousands will be discovered by the Large Synoptic Survey Telescope (LSST) in the near future.

Obtaining spectroscopic classifications for all of these SNe is prohibitively expensive. SN Ia spectra cannot be efficiently obtained with multi-object spectroscopy as they have a sparse density on the sky: their rate is $\sim$10 yr^{-1} deg^{-2} for those with $R \lesssim 22$ and spectral classifications must be obtained within $\sim$2 weeks of maximum light. At the median PS1 redshift of $z \sim 0.3$, spectroscopic classifications also necessitate $\sim$1 hour or more of 4m-class telescope time per SN. In addition, $\sim$30% of these SNe Ia will fail sample selection requirements *after* their spectrum has been observed and thus cannot be placed on the Hubble diagram (§5.3). Assuming poor weather on $\sim$30-50% of nights, 100 nights of 4m-class telescope time will result in a cosmologically useful sample of just $\sim$400 SNe Ia. In future surveys, such as LSST, the cost of

obtaining tens of thousands of SN Ia will far exceed the available resources.

The alternative to spectroscopic classifications is using classifications based only on photometric SN light curves, but this subjects the sample to contamination by core-collapse (CC) SNe. However, if cosmological distances can be measured without bias from CC SN contamination, photometrically classified SNe Ia could be used to measure w without penalty. To this end, SN light curve classification algorithms have improved greatly in the last few years. The advent of LSST has provided additional motivation to develop quick, robust classification methods that rely only on limited photometric data (e.g Saha et al., 2016). Machine learning algorithms in particular have been found to yield both efficiencies (few bona fide SNe Ia are misclassified) and sample purities $\gtrsim$96% in cases where the classifier can be trained on a representative SN sample (Sako et al., 2014; Lochner et al., 2016).

The first measurement of w with photometrically classified SNe, Campbell et al. (2013), used 752 SDSS SNe lacking spectroscopic classifications to measure cosmological parameters. They reduced CC SN contamination using the PSNID Bayesian light curve classifier (Sako et al., 2011), among other sample cuts, and estimated that their final sample had 3.9% CC SN contamination. However, Campbell et al. (2013) did not include a systematic uncertainty budget in their measurements. Because CC SNe are 1-2 mag fainter than SNe Ia, a contamination fraction of just 2% would shift the mean distance by 0.02-0.04 mag, equivalent to a 5-10% difference in w over the redshift range $0 < z < 0.5$.

For this reason, Kunz, Bassett, & Hlozek (2007) proposed the Bayesian Estimation Applied to Multiple Species (BEAMS) method to simultaneously determine the SN Ia and CC SN distributions. BEAMS models photometrically selected SN samples as a combination of SNe Ia and CC SNe, simultaneously fits for the contributions of each and marginalizes over nuisance parameters to give cosmological parameters. BEAMS should yield cosmological parameter measurements with less bias and nearly optimal uncertainties (Kunz, Bassett, & Hlozek, 2007). Hlozek et al. (2012) used the BEAMS method to measure the cosmic matter density Ω_M from SDSS SNe lacking spectroscopic classifications, but again did not include a systematic uncertainty budget in their measurements.

We expanded on this work in Jones et al. (2016, hereafter J17). J17 undertook a series of MC simulations to test the application of a BEAMS-like algorithm to a Pan-STARRS photometrically classified SN sample and made a first estimate of the systematic uncertainty on w due to CC SN contamination. We found a small bias of $\Delta_w^{CC} = 0.003 \pm 0.002$ and a modest systematic uncertainty of 0.014, which we estimated using four different SN classification methods and three different contamination models.

In the current work, we apply the J17 methodology to PS1 SNe to measure cosmological parameters with robust systematic uncertainties. To date, only 10% of PS1 SNe Ia − half of the spectroscopically classified SN Ia sample − have been used to measure cosmological parameters (Rest et al., 2014; Scolnic et al., 2014a). The

present sample is drawn from 350 spectroscopically classified SNe Ia and 3,073 PS1 SNe with spectroscopic host galaxy redshifts and unknown classifications. We anchor our Hubble diagram with a compilation of spectroscopically confirmed low-z SNe Ia from the CfA1-4 and Carnegie Supernova Project samples (Riess et al., 1999; Jha et al., 2006; Hicken et al., 2009c,a; Contreras et al., 2010; Folatelli et al., 2010; Stritzinger et al., 2011). We exclude SDSS and SNLS SNe from this sample in order to give cosmological constraints that are independent of previous high-z data. After applying conventional light curve cuts (e.g., B14), 1,344 PS1+low-z SNe remain. Statistically, we expect $\sim$5% of these SNe to be CC SN contaminants (J17).

A companion paper, Scolnic et al. (in prep.; hereafter S17), combines spectroscopically classified PS1 SNe with JLA SNe to give cosmological constraints from nearly 1,000 spectroscopically classified SNe Ia. S17 presents the PS1 spectroscopic sample, including improvements in the PS1 pipeline that are used in this work. This work also relies heavily on the detailed analysis and simulations of the low-z sample in S17 as well as their improvements to the relative and absolute photometric calibration of all surveys.

The sample of PS1 SNe with host galaxy redshifts was presented in J17, and in §2 we briefly discuss this sample and present the low-z and PS1 spectroscopically classified SNe that are included in this analysis. We derive bias-corrected distance measurements and estimate classification priors for these samples. In §3, we discuss contributions to our systematic uncertainty budget and in §4 we summarize our cos-

mological parameter estimation methodology. In §5, we perform consistency checks on the methodology. In §6, we give measurements of Ω_M and w from SN Ia+CMB constraints. In §7 we present combined cosmological constraints after combining SNe with CMB, BAO and local H_0 measurements. In §8 we discuss possible biases in the measurement and unknown sources of systematic error, and our conclusions are in §9.

5.3 Distances and Photometric Classifications from the Supernova Data

The PS1 medium deep survey covers 10 7-square degree fields in 5 filters, with typical observing cadences in a given field of 6 observations per 10 days. The PS1 SN discovery pipeline is described in detail in Rest et al. (2014). Likely SNe were flagged based on three signal-to-noise ratio (SNR) ≥ 4 observations in the $griz_{PS1}$ filters and no previous detection of a SN at that position. The PS1 survey overview is given in Kaiser et al. (2010).

Over its four years of operation PS1 flagged 5,200 likely SNe. Spectroscopic followup was triggered for $\sim$10% of SNe, typically those with $r \lesssim 22$ mag, on a wide variety of spectroscopic instruments (see Rest et al., 2014). For 520 of these candidates, spectroscopic observations of the SN near maximum light allowed their type to be determined. $\sim$350 of these 520 were spectroscopically classified as Type Ia (S17).

During the last year of PS1, we began a survey to obtain spectroscopic host galaxy

Table 5.1. SALT2-Based Data Cuts

	Number of SNe			Comments
	PS1 Host-z	PS1 Spec-z	Low-z	
Total candidates	5235	160	316	···
Host Sep $R < 5$	4461	···	···	likely host galaxy can be identified
Good host redshifts	3147	···	···	···
Fit by SALT2	2602	···	···	SALT2 parameter fitting succeeds
Not an AGN	2513	···	···	separated from center or no long-term variability
$-3.0 < X_1 < 3.0$	1978	153	297	SALT2 light curve shape
$-0.3 < C < 0.3$	1563	147	259	SALT2 light curve color
$\sigma_{\rm peakMJD} < 2$	1538	146	255	uncertainty in time of max. light (rest frame days)
$\sigma_{X_1} < 1$	1175	134	254	x_1 uncertainty
fit prob. ≥ 0.001	1038	125	181	χ^2 and N_{dof}-based prob. from SALT2 fitter
E(B-V)$_{MW} < 0.15$	1038	125	181	Milky Way reddening

redshifts for the majority of the sample, both those with SN spectra and those without. We chose targets independent of SN type in order to build a sample without any color or shape selection bias. Of 3,930 targets, 3,073 SN candidates had strong enough spectral features and high enough SNR to yield reliable spectroscopic redshifts. An estimated 1.4% incorrect redshift fraction contributes to the "contamination" systematic uncertainty and is discussed in J17. Though our sample contains a mix of galaxy types (and comprises $\sim$25% absorption line galaxies), we are unable to obtain redshifts for SNe in low surface brightness hosts. The preponderance of bright, massive host galaxies gives our sample significantly different SN and host demographics compared to previous high-z data, but makes it more similar to the targeted nature of the current low-z sample.

After SN discovery and redshift follow-up, the PS1 light curves were reprocessed with an enhanced version of the discovery pipeline that included a more accurate (non-Gaussian) PSF model. The PS1 photometric pipeline has been improved further for this analysis and the complementary analysis of S17. The improvements include deeper templates, more accurate astrometric alignment, and better PSF modeling. The zeropoint calibration has also been improved by using the Ubercal process (Schlafly et al., 2012; Padmanabhan et al., 2008). Ubercal uses repeat observations of stars in PS1 to solve for the system throughput, atmospheric transparency and detector flat field in the $griz_{PS1}$ filters. It has a photometric accuracy of better than 1% over the entire PS1 3π survey area. Pipeline improvements are discussed in further

detail in S17.

We use a compilation of low-z SNe observed over the last ∼20 years to anchor the Hubble diagram. Nearly all of these SNe are all included in the JLA analysis, including the CfA1-3 SN samples (Riess et al., 1999; Jha et al., 2006; Hicken et al., 2009c,a) and Carnegie Supernova Project SNe from the first data release (CSP; Contreras et al., 2010; Folatelli et al., 2010)[1]. We exclude Calan/Tololo SNe (Hamuy et al., 1996) as most lie below the PS1 3π survey area and therefore cannot take advantage of the PS1-based photometric calibration system we use in this paper (Supercal; Scolnic et al., 2015). We also include the most recent CfA SN compilation (CfA4; Hicken et al., 2012) and the second CSP data release (Stritzinger et al., 2011), which were not included in the JLA analysis but are used in the Rest et al. (2014) PS1 cosmological analysis.

5.3.1 SALT2 Model

To derive distances from the SNe in this sample, we use the SALT2 light curve fitter (Guy et al., 2010, hereafter G10) to measure the light curve parameters of SNe Ia and to restrict our sample to SNe that can be well standardized. We use the most recent version of SALT2, which was re-trained by B14 to include additional high-z SNe and improve the photometric calibration (SALT2.4).

We restrict our sample to SNe with shapes and colors consistent with normal

[1]See B14 for a detailed description of these data and their respective photometric systems.

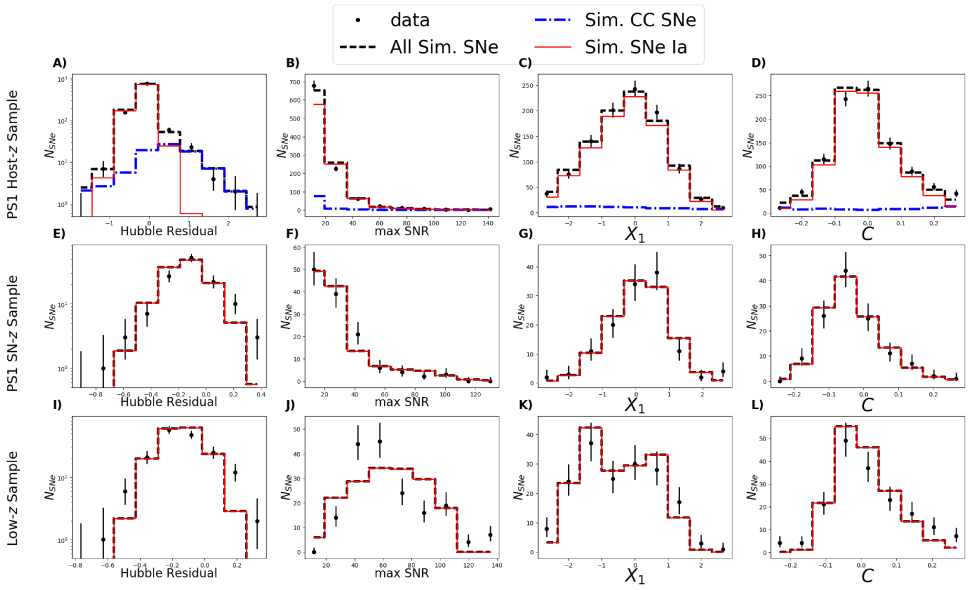

Figure 5.1: Simulations of the PS1 host galaxy redshift sample (host-z sample), the PS1 SN redshift only sample (SN-z sample), and the low-z SN sample compared to the real SNe used to measure cosmological parameters in this work. The PS1 host-z sample consists of $\sim$9% CC SN contamination (blue), the details of which are discussed in J17 (CC SN contamination is not relevant for distance bias correction).

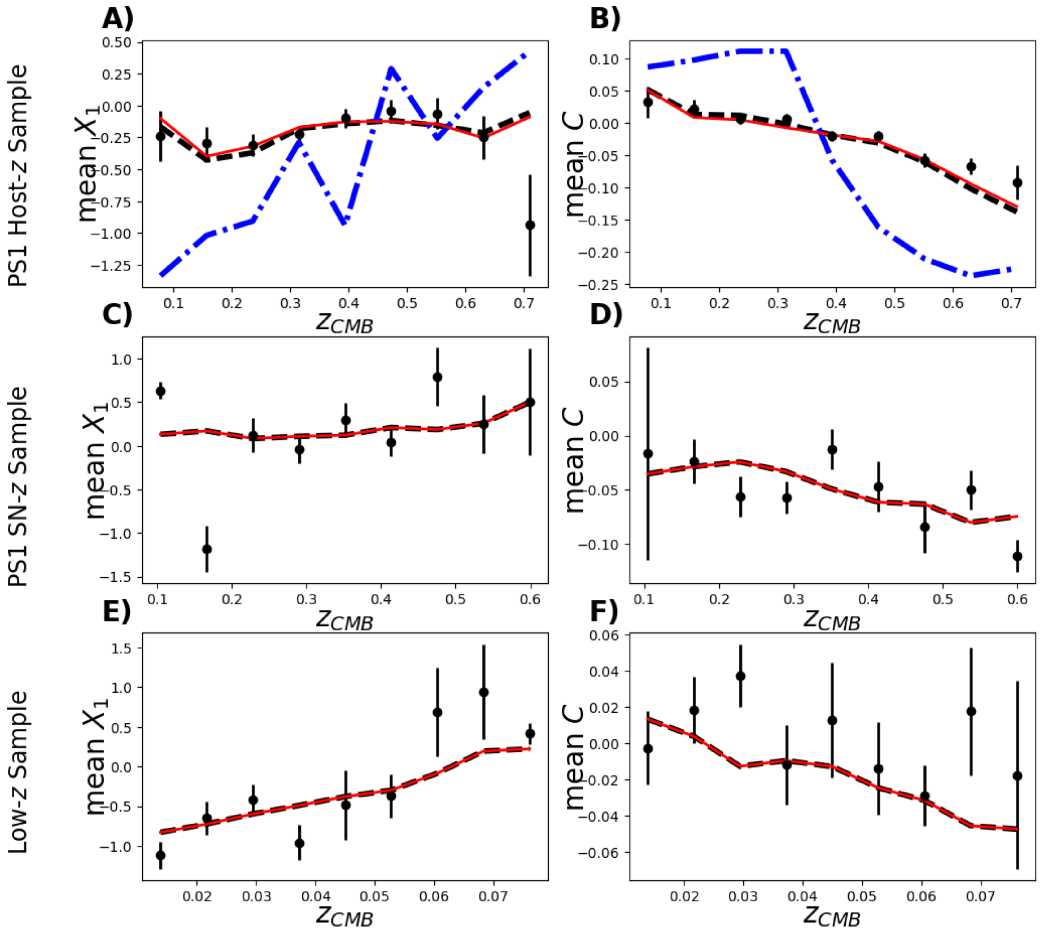

Figure 5.2: Similar to Figure 5.1, but showing the dependence of x_1 and c on redshift for each survey.

SNe Ia ($-0.3 < c < 0.3$, $-3 < x_1 < 3$) and well-measured shapes and times of maximum light. As measuring cosmological parameters from SNe without spectroscopic classifications adds the potential for new biases to this work, we strive for consistency with previous cosmological analyses whenever possible. For this reason, our cuts are identical to those of B14 with the exception of one additional cut on the χ^2 and degrees of freedom of the SALT2 light curve fit (SALT2 fit probability >0.001) that was applied by Rest et al. (2014). This cut serves to remove CC SNe as well as SNe Ia with poor light curve fits.

These cuts reduce the PS1 spectroscopically confirmed SNe Ia sample by ∼30%. They reduce the number of PS1 SNe Ia without spectroscopic classifications by 60%, as these SNe have lower average signal-to-noise ratios (SNRs; thus more frequently failing the shape uncertainty cut[2]) and, due to high initial CC SN contamination, a much lower fraction with SN Ia-like shapes and colors. The effect of each sample cut is shown in Table 5.1, including both the cuts described in J17 on the separation between the SN and its likely host galaxy (the R parameter, Sullivan et al., 2006) and removal of possible active galactic nuclei (AGN).

Once light curve parameters have been measured with SALT2, we use the Tripp estimator (Tripp, 1998) to infer the SN distance modulus from these light curve parameters:

[2]In PS1, SNe with x_1 uncertainty < 1 have a mean SNR at maximum light of 15.6. SNe with x_1 uncertainty > 1 have a mean SNR at maximum light of 8.3.

$$\mu = m_B - \mathcal{M} + \alpha \times x_1 - \beta \times c + \Delta_M + \Delta_B. \quad (5.1)$$

x_1 is the light curve stretch parameter, c is the light curve color parameter, and m_B is the log of the light curve amplitude (approximately the peak SN magnitude in B). The distance to a given SN also depends on the global nuisance parameters α, β, and $\mathcal{M}$. $\mathcal{M}$, a combination of the absolute SN magnitude and the Hubble constant, α, and β are typically marginalized over when fitting to the cosmological parameters (e.g. B14, Conley et al., 2011). Δ_M is a correction based on the mass of the SN host galaxy, discussed in §5.3.1.1, and Δ_B is the distance bias correction, often referred to as the selection bias or Malmquist bias (§5.3.2.2).

After fitting with SALT2, SNe Ia have ∼10% scatter in shape- and color-corrected magnitude even after their photometric uncertainties are taken into account. This is traditionally referred to as the intrinsic dispersion, σ_{int} (Guy et al., 2007). σ_{int} is defined as the global uncertainty that must be added in quadrature to the distance errors σ_μ of each SN such that the reduced χ^2 of the Hubble residuals equals 1. We follow B14 and Conley et al. (2011) in correcting for the intrinsic dispersion of the low-z samples separately from high-z data; the current low-z compilation may have underestimated photometric difference image uncertainties or uncorrected scatter from bright host galaxies, and has a measured σ_{int} that is ∼0.02 mag higher than PS1. Therefore, we increase the m_B uncertainties of low-z SNe from SALT2 light curve fits (effectively increasing the uncertainties on the inferred distances) so that

they have the same σ_{int} as the PS1 spectroscopically confirmed SN Ia sample. The distance uncertainties must also include redshift uncertainty and lensing uncertainty ($\sigma_{lens} = 0.055z$; Jönsson et al., 2010).

5.3.1.1 Host Galaxy Masses

It has been shown that SNe Ia after shape and color correction are $\sim$ 0.05-0.1 mag brighter in high mass host galaxies ($\log(M_*/M_\odot) > 10$) than lower-mass host galaxies (the mass step; Kelly et al., 2010; Lampeitl et al., 2010; Sullivan et al., 2010). The difference in inferred distance between SNe Ia in low-mass versus high mass hosts has recently been measured at $>3\sigma$ significance in photometrically classified SN samples even though such samples (including PS1) have strong selection biases toward high-mass host galaxies (Campbell et al., 2016; Wolf et al., 2016). We model the mass step using the parameter Δ_M, the difference in inferred distance modulus between SNe Ia in low-mass versus high-mass hosts. Because the underlying physics behind the mass step are unclear, we allow it to evolve with redshift in our systematic error analysis (§5.5.7).

Computing Δ_M robustly requires measuring the host galaxy masses of every SN in a self-consistent way. We measured host masses using the SED-fitting method of Pan et al. (2014) with PS1 and low-z host galaxy photometry. For PS1, we use SExtractor (Bertin & Arnouts, 1996) to measure the photometry from PS1 templates. The PS1 templates use $\sim$3 years of co-added PS1 data, omitting only the year in which the

SN Ia occurred. The likely host of each SN is assumed to be the galaxy with the lowest R parameter relative to the SN position, as discussed in J17. The R parameter defines a separation between the SN and a galaxy center and is normalized by the size of the galaxy in the direction of the SN[3]. If the nearest host has $R > 5$ (i.e, the SN spectrum gives the only redshift), we assume the true host was undetected following Sullivan et al. (2006). Undetected galaxies of spectroscopically classified SNe Ia are placed in the $\log(M_*/M_\odot) < 10$ bin. Because we cannot be sure these SNe have $\log(M_*/M_\odot) < 10$, we add a systematic uncertainty of 0.07 mag in quadrature to their distance uncertainties following B14.

For the low-z sample, we use $ugrizBVRIJHK$ photometry from 2MASS (Skrutskie et al., 2006) and SDSS. Following B14 and S17, low-z SNe without nearby photometric catalog matches are likely hostless and are assumed to have $\log(M_*/M_\odot) < 10$. To these low-z SNe, we again add 0.07 mag in quadrature to their distance uncertainties.

Finally, we use the low-z and PS1 host galaxy photometry to estimate M_* with the `Z-PEG` SED-fitting code (Le Borgne & Rocca-Volmerange, 2002), which in turn is based on spectral synthesis models from `PEGASE.2` (Fioc & Rocca-Volmerange, 1997). Galaxy SED templates correspond to spectral types SB, Im, Sd, Sc, Sbc, Sa, S0 and E. We simultaneously marginalize over E(B-V), which is allowed to vary from 0 to 0.2 mag. Uncertainties are determined from the range of model parameters that are

[3]We predict that for $\sim$1% of SNe, this method will incorrectly determine the host galaxy, but in J17 we determined that this fraction of mismatches does not bias the cosmology.

able to fit the data with similar χ^2, and are typically $\sim$0.1-0.3 dex.

5.3.2 Supernova Selection Bias

5.3.2.1 Simulating Pan-STARRS and Low-z Supernovae

A magnitude-limited sample of SNe will have a distance bias, frequently referred to as a Malmquist or selection bias, that is typically measured from rigorous simulations of the survey (see, e.g., B14, Scolnic et al., 2014a, Conley et al., 2011). We use three survey simulations in this analysis: simulations of the set of PS1 SNe with redshifts from their host galaxies (the host-z sample), the set of PS1 SNe Ia with redshifts from SN spectroscopy alone (the SN-z sample; these SNe have been spectroscopically classified), and the compilation of low-z SNe Ia. We use the SNANA software (Kessler et al., 2010) to simulate SNe Ia based on the SALT2 model, with detection efficiencies, zeropoints, PSF sizes, sky noise, and other observables from the real surveys. Simulations of the PS1 host-z sample are presented in J17 (including CC SN contamination, which we discuss in detail in J17), while the SN-z and low-z samples are presented in S17.

Because SN spectroscopy is only attempted for bright SNe, a lower magnitude limit than the PS1 survey detection limit comes into play for the SN-z sample. The SN-z sample includes only the portion of our data without host galaxy redshifts and thus is comprised almost entirely of $r_{pk} < 22$, spectroscopically classified SNe in faint

hosts. On the other hand, the host-z sample consists of SNe in brighter ($r \lesssim$ 22-23) hosts. SN Ia distances are a function of the biased host galaxy demographics in these samples, and we must correct them using the host mass step (Δ_M; variants given in the systematic error analysis, §4).

The host-z sample is host galaxy magnitude-limited. Because SN shape and color correlate with host galaxy brightness (e.g. Childress et al., 2013), the SN shape and color distribution in the host-z sample has a z dependence that is difficult to model. Similarly, the SN-z sample consists of spectroscopically classified SNe for which host galaxy redshifts could not be measured, and therefore will also have a biased, z-dependent host galaxy distribution. Because of this, we add one additional component to the host-z and SN-z simulations: we allow the means of the simulated SALT2 parameters x_1 and c to evolve slightly with redshift to better match the data. We discuss the details and impact of this method in the Appendix, and find that it changes the distance bias by up to $\sim$0.02 mag in the highest redshift bins.

For each survey, the simulations are compared to the data in Figure 5.1 and 5.2. The distributions of x_1, c and their redshift dependences are consistent with the data, as is the maximum SNR distribution. The biggest discrepancies between simulation and data are found in the low-z simulations. The low-z surveys are exceptionally difficult to model due to the heterogeneous nature of the surveys, multiple photometric systems and analysis pipelines, their semi-arbitrary spectroscopic selection functions, and their targeting of NGC galaxies. Because of this, we also simulate a

"volume-limited" variant of the low-z survey, which matches the observed data with a "host galaxy targeting" selection function − fraction of hosts observed as a function of redshift − instead of a selection function due to SN spectroscopy. We improve the simulations using redshift-dependent x_1 and c distributions due to the redshift-dependent host galaxy properties (x_1/c and host properties are correlated; Childress et al., 2013). These simulations are discussed in more detail in S17, and are included in our systematic error analysis (§4).

5.3.2.2 Using Simulations to Correct for Selection Bias

Due to their intrinsic dispersion, SNe Ia in magnitude-limited surveys become preferentially brighter at greater distance even after shape and color correction. Even the low-z SN Ia surveys used here may be biased toward selecting brighter targets (see B14, their Figure 5). The bias in distance is given by the SNANA simulations discussed above and is defined by (Mosher et al., 2014):

$$\Delta_B(z) = \langle \mu_{fit} - \mu_{sim} \rangle_z. \tag{5.2}$$

For low-z surveys, the bias can be up to ∼0.035 mag ($z > 0.05$), while PS1 has distance biases of nearly 0.1 mag at $z > 0.5$.

The host-z and SN-z biases are very similar, which is surprising given that the SN-z sample has a much lower magnitude limit. The reason is that the lower average SNR of the host-z sample exacerbates a bias due to the x_1 uncertainty cut. At a

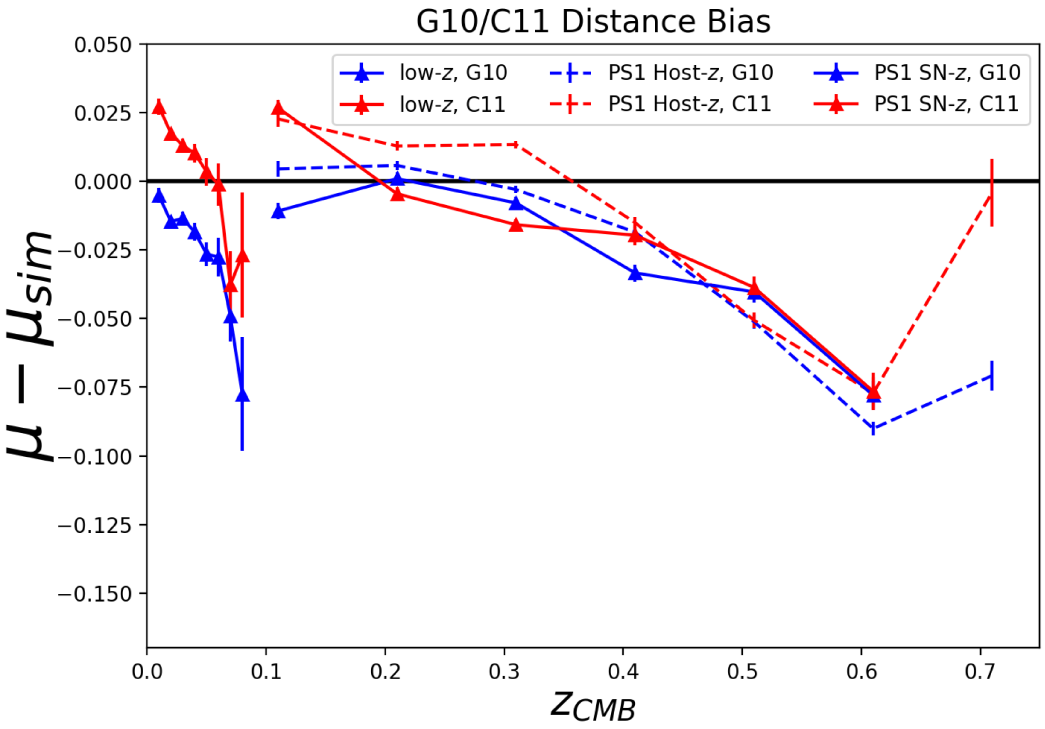

Figure 5.3: Difference in SN Ia distance bias for the G10 and C11 scatter models. Low-z SNe have a bias of up to 0.035 mag while PS1 SNe have a bias of up to ∼0.1 mag at the highest survey redshifts. Bias prediction curves for the low-z and spectroscopic PS1 data are not as smooth as in previous cosmological analyses because of the limited number of SNe Ia from which simulated shapes, colors and redshifts are drawn (§5.3.2.1).

given SNR, SNe with narrower (measured) light curve shapes are fit with lower x_1 uncertainties by SALT2, introducing this non-intuitive bias in the case where many x_1 uncertainties are near the cutoff point of 1. As discussed in J17 (see their Figure 8), a $\sigma_{x_1} < 1$ sample cut biases the recovered values of x_1 by up to $\alpha(x_1 - x_{1,sim}) = -0.1$ at high-z. This bias has the opposite effect of the m_B bias of spectroscopically confirmed SNe Ia (a difference of $\sim$0.05 mag at $z \sim 0.5$ between SN-z and host-z simulations).

Uncertainty in the intrinsic dispersion model is the dominant uncertainty in the bias corrections. The uncertainty is encapsulated by two primary scatter models that are both consistent with the data. First, the G10 SALT2 model assumes that 70% of the $\sim$0.1 mag intrinsic dispersion in derived SN Ia distances is uncorrelated with the shape or color of the SN (achromatic dispersion). An alternative model is that of Chotard et al. (2011, hereafter C11), which finds an equally good fit to SN data by assuming 75% of SN dispersion can be attributed to chromatic variation.

The SALT2 nuisance parameter β is 25% higher in the C11 model than the G10 model (Scolnic & Kessler, 2016), and these two models can give very different predictions for the distance bias as a function of redshift (Figure 5.3). Due to the chromatic nature of the C11 dispersion, the difference in bias is a strong function of the (z-dependent) SN c distribution in a given survey. This is especially apparent when examining the difference between the G10/C11 biases for the different samples. Low-z and photometrically classified SNe have median c between -0.01 and 0.01, giving an average $\beta^{C11}c - \beta^{G10}c = 0.015$ mag for low-z and 0.003 mag for PS1 photometrically

classified SNe. In contrast, PS1 spectroscopically confirmed SNe Ia have a median c of -0.04, giving an average difference of $\beta^{C11}c - \beta^{G10}c$ = -0.028 mag in distance.

Unfortunately, there are not enough spectroscopically classified SNe to distinguish between the G10/C11 scatter models in our data. As we have no reason to prefer the C11 model over the G10 model or vice versa, we take the average of the two as our baseline bias correction for cosmology analysis. We incorporate the difference between these model predictions in our systematic error budget.

5.3.3 Photometric Classification

We use PSNID (Sako et al., 2014) to classify each SN in this sample as Type Ia, Ib/c or II based on its light curve. PSNID matches observed SN light curves to simulated SN Ia and CC SN light curves to determine the χ^2 and prior-based probability that each SN is of type Ia. We use the version of PSNID that has been implemented in SNANA[4], which uses the SALT2 model as its SN Ia template. For CC SNe, PSNID marginalizes over 51 CC SN templates when classifying SNe and includes a grid of reddening values for each template (because templates have not been de-reddened, we allow just $0 < A_V < 1$ of additional reddening).

We also use three alternate classification methods, including two light curve-based methods, NN (Sako et al., 2014) and *Fitprob*. The NN classifier uses the proximity of a given SN to the SALT2 x_1, c, and redshift of simulated CC and Ia SNe to

[4]Version 10.48l.

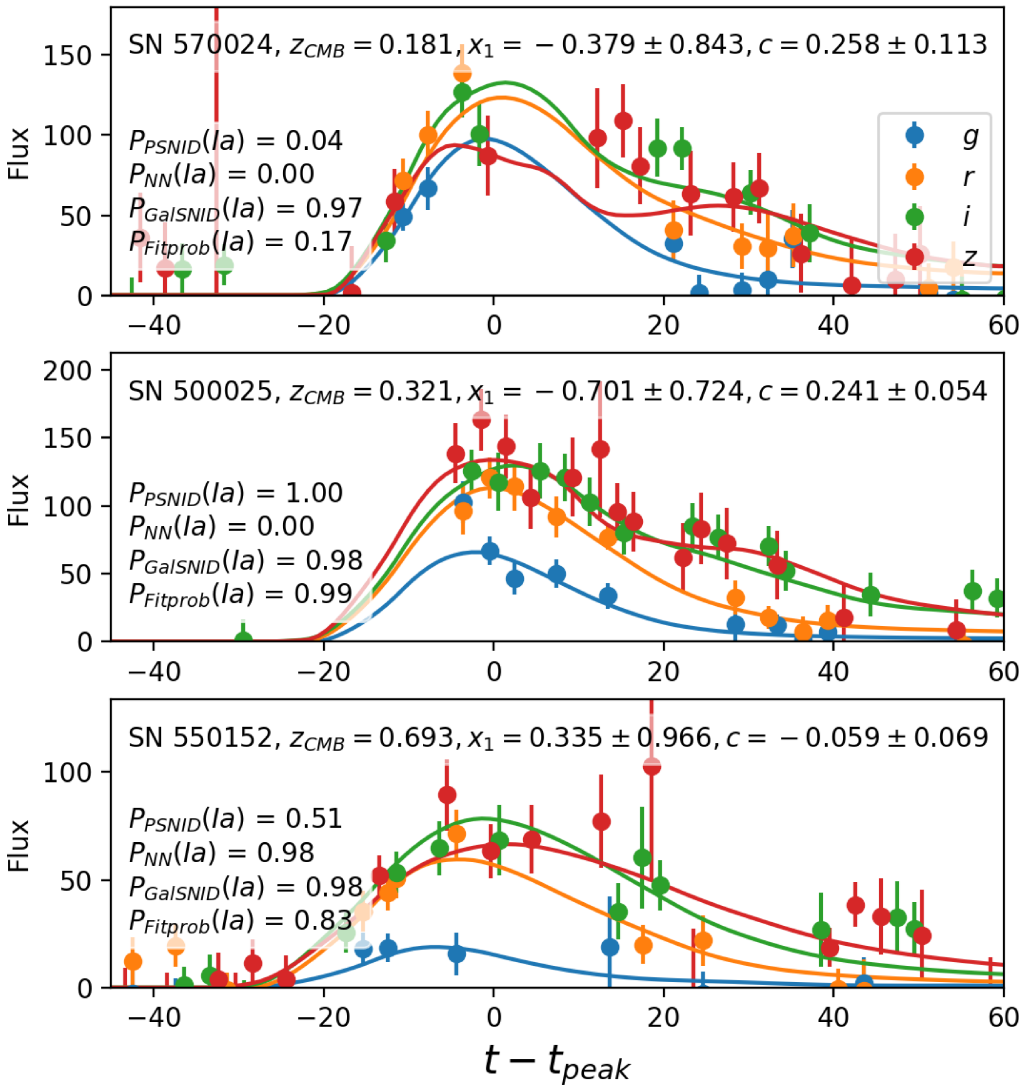

Figure 5.4: Three PS1 light curves with ambiguous classifications included in our sample and shown with their best-fit SALT2 light curve fits.

determine the likely SN type. *Fitprob* is simply the fit probability from the SALT2 light curve fit multiplied by a redshift-dependent SN type prior based on the CC SN and SN Ia rates. One additional method, GalSNID (Foley & Mandel, 2013; J17), estimates the type probability using only host galaxy properties by taking advantage of the paucity of CC SNe in low-star formation environments. *Fitprob* and GalSNID are sub-optimal but independent of uncertainties in CC SN simulations. In J17, we suggest that uncertainties in the shape of CC SN luminosity functions and the dearth of CC SN templates for several subtypes necessitate the use of methods that do not rely on simulations.

Figure 5.4 shows classification probabilities for three PS1 SNe with ambigous types. For SN 570024 (top panel), all light curve-based classification methods agree that this SN is most likely a CC SN due to its unusual z-band light curve. GalSNID, however, finds that this is most likely a bona fide Ia due to the lack of strong star formation indicators in its host galaxy spectrum. For SN 500025 (middle panel), PSNID and *Fitprob* agree that the SN is of Type Ia due to the low χ^2 of its light curve fit. However, the NN classifier finds it most likely to be a CC SN due to its very red SALT2 color. For SN 550152 (bottom panel), the shapes/colors are consistent with a SN Ia but the light curve fit χ^2 is too high to definitively prefer a SN Ia. This diversity in classifications adds robustness to our methodology. We revisit the effect of different classifiers on our results in §5.6.

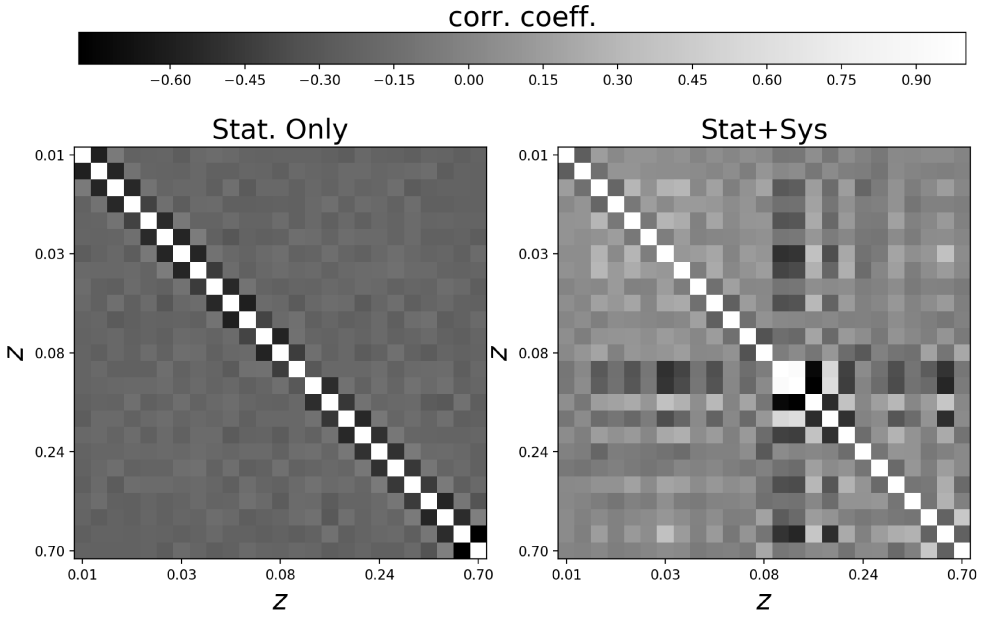

Figure 5.5: Statistics-only and stat+sys correlation matrices from the PS1+low-z SN sample. The statistics-only correlation matrix shows the strong anti-correlation between neighboring bins. The stat+sys correlation matrix shows larger-scale correlations due to systematic uncertainties and large uncertainties in the bins with minimal data ($z \sim 0.1 - 0.2$). The correlation matrix is equal to $C_{ij}/\sqrt{C_{ii}C_{jj}}$ for covariance matrix C.

5.4 Cosmological Parameter Estimation Methodology

In the previous section we measured the SALT2 light curve parameters, host galaxy masses, classification probabilities, and bias corrections that will be used to generate distances from PS1 and low-z SNe Ia. For each SN in our sample, these parameters are given in Table 5.7.

With these data, we measure cosmological parameters from the 1,163 PS1 SNe and 181 low-z SNe Ia in two steps: (1) marginalizing over CC SNe and reducing the data to a set of distance measurements at 25 redshifts (log-spaced between $0.01 < z < 0.7$) and (2) using those distances, redshifts, uncertainties and covariances to infer cosmological parameters with the cosmological Monte Carlo software (CosmoMC; Lewis & Bridle, 2002). CosmoMC allows us to easily include the latest CMB, BAO, and/or H_0 priors in our cosmological constraints. This two-step procedure also follows B14 (see their Appendix E).

5.4.1 The Likelihood Model

The SN likelihood model used here is discussed and tested comprehensively in J17 and is based on the Bayesian Estimation Applied to Multiple Species (BEAMS) algorithm presented in Kunz, Bassett, & Hlozek (2007). We summarize the model below.

To measure distances from SNe Ia, we sample a posterior distribution $P(\theta|D)$ that is proportional to a set of priors $P(\theta)$ and the product over N SNe of the likelihoods (of the model given the data) for each individual SN. D is the data, while θ is the set of free parameters in the model. The specific free parameters comprising θ are discussed in the paragraphs below.

We use a three-Gaussian form of the SN likelihood, $\mathcal{L}$. SNe Ia are represented by two Gaussians: one for SNe Ia in low-mass hosts, $\mathcal{L}_i^{Ia,M<10}$, and one for SNe Ia

in high-mass hosts, $\mathcal{L}_i^{Ia,M>10}$. CC SNe are represented by the third Gaussian, $\mathcal{L}_i^{CC}$ (alternative CC SN models are given in §5.5.5):

$$
\begin{aligned}
P(\theta|D) &\propto P(\theta) \times \prod_{i=1}^{N} (\mathcal{L}_i^{Ia,M<10} + \mathcal{L}_i^{Ia,M>10} + \mathcal{L}_i^{CC}), \\
\mathcal{L}_i^{Ia,M<10} &= \frac{\mathrm{P_i(M<10)P_i(Ia)}}{\sqrt{2\pi(\sigma_{i,Ia}^2 + \Sigma_{Ia}^2)}} \exp\Big[-\frac{(m_{i,Ia}^{corr} + \Delta_M - f(z_i))^2}{2(\sigma_{i,Ia}^2 + \Sigma_{Ia}^2)}\Big], \\
\mathcal{L}_i^{Ia,M>10} &= \frac{\mathrm{P_i(M>10)P_i(Ia)}}{\sqrt{2\pi(\sigma_{i,Ia}^2 + \Sigma_{Ia}^2)}} \exp\Big[-\frac{(m_{i,Ia}^{corr} - f(z_i))^2}{2(\sigma_{i,Ia}^2 + \Sigma_{Ia}^2)}\Big], \\
\mathcal{L}_i^{CC} &= \frac{\mathrm{P_i(CC)}}{\sqrt{2\pi(\sigma_{i,CC}^2 + \Sigma_{CC}(z_i)^2)}} \exp\Big[-\frac{(m_{i,CC}^{corr} - g(z_i))^2}{2(\sigma_{i,CC}^2 + \Sigma_{CC}(z_i)^2)}\Big].
\end{aligned}
\tag{5.3}
$$

$m_{i,Ia}^{corr}$ and $m_{i,CC}^{corr}$ (in the exponential terms) are shape- and color-corrected magnitudes for the ith SN that we compute from the SALT2 parameters m_B, x_1, c, and Δ_B using the Tripp estimator. They depend on nuisance parameters α and β (Eq. 5.1; $m_{i,Ia}^{corr} = \mu_i + \mathcal{M}$). Because we only wish to measure SALT2 nuisance parameters from SNe Ia, we allow separate values of α and β in the Ia and CC components of the likelihood. $m_{i,Ia}^{corr}$ values are computed using free parameters α_{Ia} and β_{Ia}. $m_{i,CC}^{corr}$ values use α_{CC} and β_{CC}, which are fixed to the values for SNe Ia given by B14 (allowing these to be free parameters does not improve the robustness of the cosmological results). $\sigma_{i,Ia}$ and $\sigma_{i,CC}$ are the uncertainties on the corrected magnitudes of the ith SN using (α_{Ia}, β_{Ia}) or (α_{CC}, β_{CC}), respectively.

Δ_M, the mass step, is a free parameter that adjusts the magnitudes of SNe Ia in low-mass hosts to match those in high-mass hosts. In the $\mathcal{L}_i^{Ia,M<10}$ and $\mathcal{L}_i^{Ia,M>10}$ terms above, $\mathrm{P}_i(M > 10)$ and $\mathrm{P}_i(M < 10) = 1 - \mathrm{P}_i(M > 10)$ are the probabilities from our host masses and host mass measurement uncertainties that a given SN has a

host galaxy with mass >10 dex or <10 dex, respectively. We treat the uncertainties as Gaussian, an approximation that predominantly affects only the minority (∼25%) of SNe that have host masses within 1σ of $\log(M_*/M_\odot) = 10$. In previous cosmological analyses (e.g. B14), the uncertainties on $\log(M_*/M_\odot)$ were neglected.

$f(z_i)$ is the variable of interest for cosmological parameter estimation. It is the continuous, z-dependent model for the SN Ia corrected magnitudes − the mean of the SN Ia Gaussian − and is allowed to vary across the redshift range of the survey ($0.01 < z < 0.7$). We evaluate the model at any z across this redshift range by choosing a fixed set of 25 log-spaced redshift "control points" ($\vec{z_b}$; $\Delta\log_{10}(z) = 0.077$) at which the corrected SN Ia magnitudes $f(\vec{z_b}) = \mu(\vec{z_b}) + \mathcal{M}$ are free parameters. For any redshift z_i, we interpolate between the redshift control points below (z_b) and above (z_{b+1}):

$$\begin{aligned} \mu(z_i) &= (1-\xi)\mu_b + \xi\mu_{b+1} \\ \xi &= \log(z_i/z_b)/\log(z_{b+1}/z_b), \end{aligned} \tag{5.4}$$

where μ_b is the distance modulus at redshift z_b. Interpolating with a simple linear model instead of ΛCDM produces differences of <1 mmag at all redshifts. The SN Ia dispersion Σ_{Ia} plays the same role as the intrinsic dispersion and is kept fixed at all redshifts.

The z-dependent mean and standard deviation of the CC SN Gaussian model ($g(z_i)$ and $\Sigma_{CC}(z_i)$) are interpolated between 10 log-spaced redshift control points.

Unlike SNe Ia, the dispersion of the heterogeneous CC SN population changes drastically with redshift due to to strong detection biases at high z.

Each Gaussian is multiplied by the prior probability ($\mathrm{P}_i(\mathrm{Ia})$ and $\mathrm{P}_i(\mathrm{CC}) = 1-\mathrm{P}_i(\mathrm{Ia})$) that a given SN is or is not of type Ia. We use the PSNID classifier to estimate these probabilities. Alternative classification methods are included as part of our systematic error budget (§5.5.5).

For those SNe without spectroscopic classifications, our method allows the type priors to be shifted and scaled to account for incorrect classifications (see J17). For spectroscopically classified SNe Ia, we set the prior probabilities, $\mathrm{P}_i(\mathrm{Ia})$, equal to one and do not allow them to be adjusted. We include broad Gaussian priors on all free parameters with the exception of SN Ia corrected magnitudes. We apply no priors (i.e. flat priors) to the SN Ia control point magnitudes $f(\vec{z_b})$ to avoid any possibility of cosmological bias.

We estimate the free parameters by sampling the log of the posterior with a Markov Chain Monte Carlo (MCMC) algorithm. As in J17, we use the Parallel-Tempered Ensemble Sampler from `emcee` as our MCMC method (Foreman-Mackey et al., 2013).

5.4.2 Constraining Cosmological Parameters

From the methods presented above, we infer the corrected magnitudes of SNe Ia at 25 redshift control points, $f(\vec{z_b})$, using the baseline SN light curve parameters,

bias corrections, and J17 methodology. We also generate $f(\vec{z}_b)$ for each systematic uncertainty (§5.5). From these values, a systematic error covariance matrix C_{sys} is created (Scolnic et al., 2014a; Conley et al., 2011):

$$C_{sys}^{jk} = \sum_{n=1}^{N} \frac{\partial f(z_j)}{\partial S_n} \frac{\partial f(z_k)}{\partial S_m} \sigma(S_n^2). \tag{5.5}$$

The sum is over all N systematics and $\frac{\partial f(z_j)}{\partial S_n}$ is the change in corrected magnitude after applying a single systematic S_m to the individual light curves. $\sigma(S_n)$ is the size of each systematic uncertainty. The systematic covariance matrix is then combined with the statistical covariance matrix:

$$C_{tot} = D_{stat} + C_{sys}. \tag{5.6}$$

Note that the statistics-only covariance matrix, D_{stat}, includes both diagonal and off-diagonal components because the corrected magnitudes from BEAMS are anti-correlated with the corrected magnitudes at neighboring control points:

$$D_{stat}^{ij} = \sum_{k}^{N_{MCMC}} \frac{(f_k(z_{b,i}) - \overline{f(z_{b,i})})(f_k(z_{b,j}) - \overline{f(z_{b,j})})}{N_{MCMC}}. \tag{5.7}$$

N_{MCMC} is the length of the MCMC chain that samples free parameters $f(\vec{z}_b)$. $f_k(z_{b,i})$ is the value of f at the ith control point from the kth MCMC sample. $\overline{f(z_{b,i})}$ is the mean of f at the ith control point from the full MCMC chain. Figure 5.5 shows the correlation matrices from statistical uncertainties alone (left) and statistical and systematic uncertainties combined (right).

We then use the cosmological Monte Carlo software (CosmoMC; Lewis & Bridle, 2002) to measure cosmological parameters by minimizing the following χ^2:

$$\chi^2 = (\mu'(\vec{z_b}) - \mu_{\Lambda CDM}(\vec{z_b}; \Omega_M, w, ...))^\dagger C_{tot}^{-1} (\mu'(\vec{z_b}) - \mu_{\Lambda CDM}(\vec{z_b}; \Omega_M, w, ...)), \quad (5.8)$$

where $\mu'(\vec{z_b}) = f(\vec{z_b}) - \mathcal{M}$ (we marginalize over $\mathcal{M}$ using CosmoMC). The vector of model distances, $\mu_{\Lambda CDM} = 5\log(d_L) - 5$, is a function of the cosmology:

$$\begin{aligned} d_L(z, w, \Omega_M, \Omega_\Lambda, \Omega_K) &= (1+z)\frac{c}{H_0}\int_0^z \frac{dz}{E(z)}, \\ E(z) &= [\Omega_M(1+z)^3 + \Omega_k(1+z)^2 + \Omega_\Lambda(1+z)^{3(1+w)}]^{1/2}. \end{aligned} \quad (5.9)$$

Ω_M is the cosmic matter density, Ω_Λ is the dark energy density, and Ω_k is the curvature of space. w is the redshift-independent dark energy equation of state parameter (z-dependence will be added in §5.7).

5.5 Systematic Uncertainties

The SNe in this sample are affected by systematic uncertainties that can broadly be attributed to 8 sources of error: Milky Way extinction, distance bias correction, photometric calibration, SALT2 model calibration, CC SN contamination, low-z peculiar velocity corrections, the redshift dependence of SN nuisance parameters, and

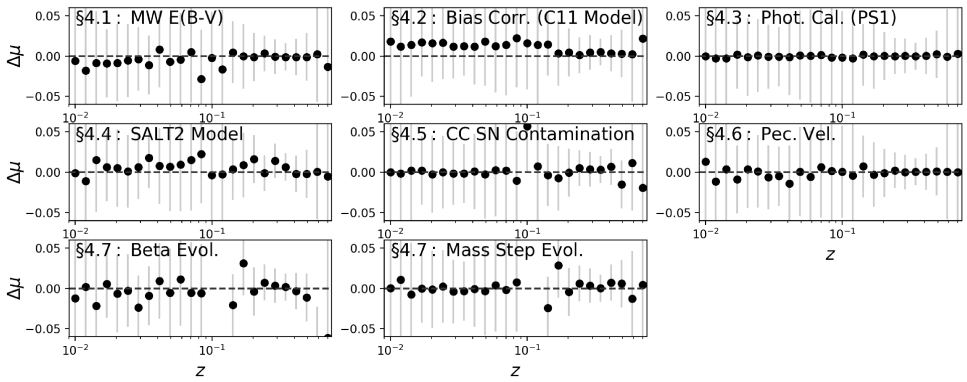

Figure 5.6: The average change in distance modulus $\Delta\mu$ due to each type of systematic uncertainty in this analysis. Error bars show the statistical uncertainty on the distance of each bin. Deviations at $z \simeq 0.01$ and $\simeq 0.1$ are due to low SN statistics in these bins and have little effect on the cosmological constraints.

the dependence of SN Ia luminosities on their host galaxies. Figure 5.6 shows the average redshift dependence of each type of systematic uncertainty. We discuss each of these uncertainties in detail below.

5.5.1 Milky Way Extinction

Milky Way extinctions for each SN are given by Schlafly & Finkbeiner (2011), who use the colors of stars with spectra in SDSS to derive a 14% correction to the reddening maps of Schlegel, Finkbeiner, & Davis (1998). We assume a conservative, fully correlated 5% uncertainty on these measurements, which could be caused by selection biases in the SDSS stars chosen for spectroscopic follow-up and use of stars that lie in front of some fraction of the Galactic dust (Schlafly & Finkbeiner, 2011).

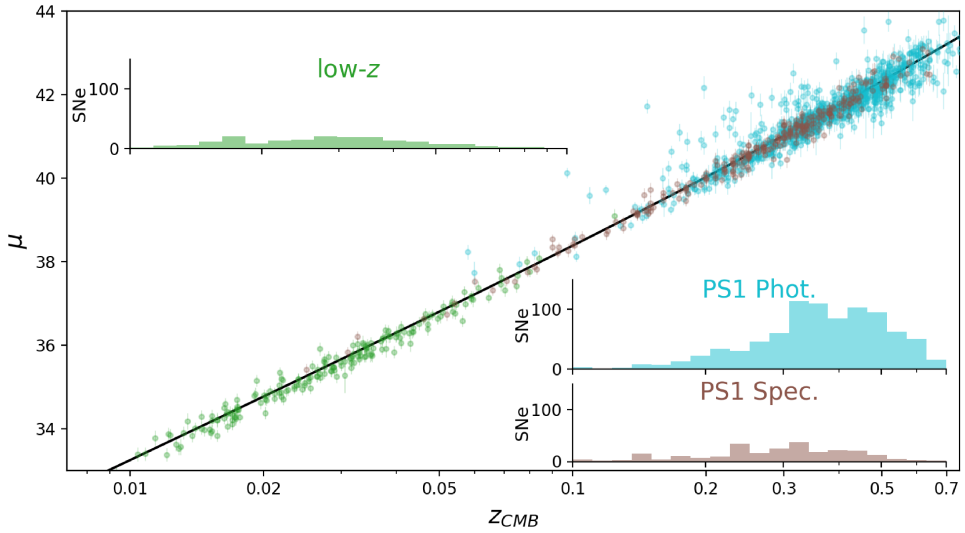

Figure 5.7: The PS1+low-z Hubble diagram with low-z SNe (green), spectroscopically classified SNe (brown) and photometrically classified SNe (blue).

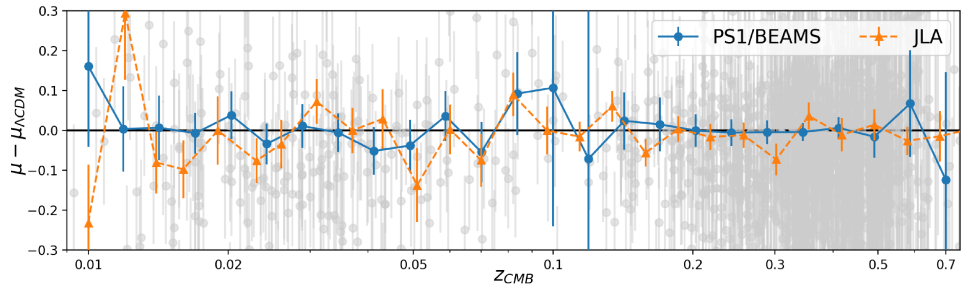

Figure 5.8: The PS1+low-z Hubble residual diagram, with a comparison to the binned SN Ia distances given by B14. We see excellent agreement with B14 across the redshift range, with slight discrepancies at low-z due to the addition of the CfA4 sample and a stronger prediction for the distance bias correction.

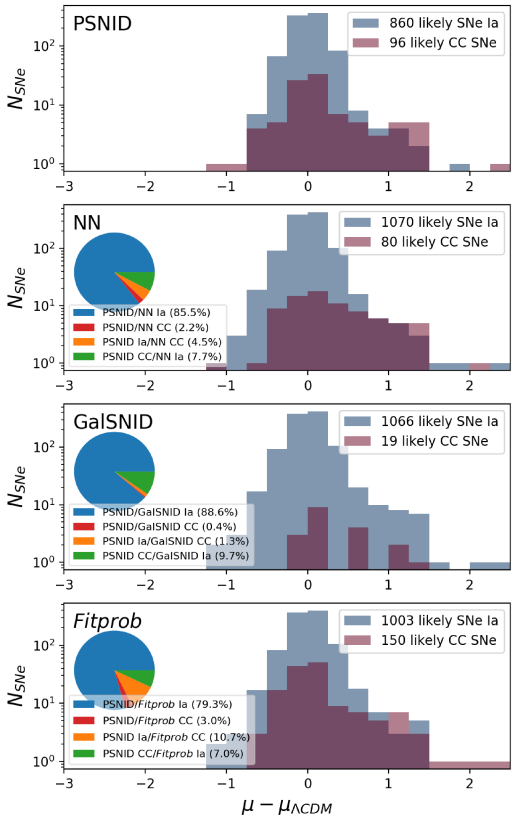

Figure 5.9: Log-scaled histograms of Hubble residuals for likely PS1 SNe Ia (P(Ia) > 0.5; blue) and likely PS1 CC SNe (P(Ia) < 0.5; red) from each classifier considered in this work. *Fitprob* classifies the most real SNe Ia as CC SNe, while GalSNID likely classifies the most real CC SNe as SNe Ia. PSNID appears to be the most effective, but can be prone to overconfident, incorrect classifications. In spite of large classification differences, the output distances given by our method are consistent with the spectroscopically confirmed PS1 sample and each other (Figure 5.10).

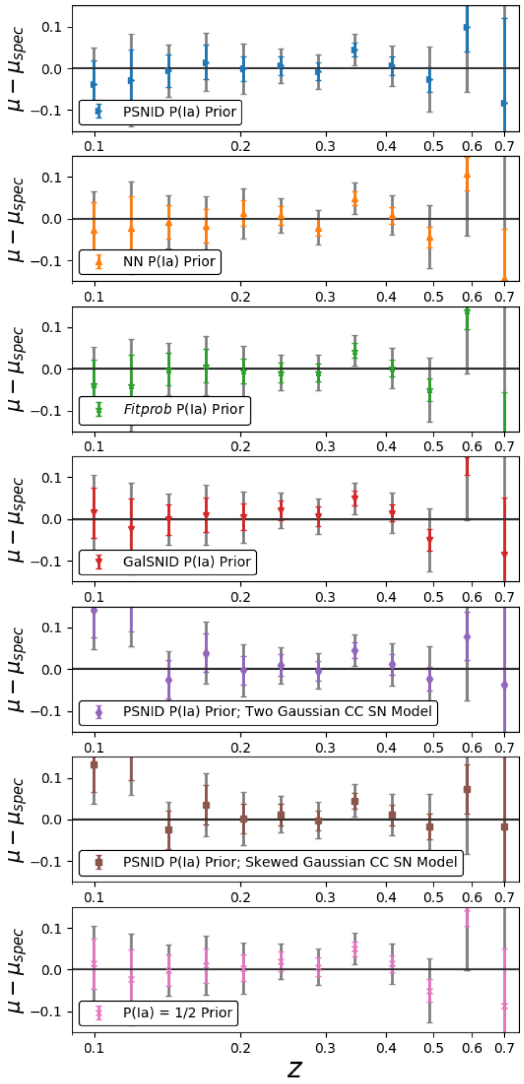

Figure 5.10: The difference in derived distance of the full photometric sample compared to distances from the subset of ∼250 spectroscopically classified PS1 SNe Ia. Grey (large) error bars are the uncertainties on spectroscopic and photometric distances added in quadrature, while the smaller errors are from the photometric sample alone. Distances are remarkably consistent between methods, with a small bump at $z \sim 0.35$ that could be due to high CC SN contamination at this redshift but is also consistent with statistical fluctuation. For comparison to the predicted biases from simulations, see Figure 11 of J17.

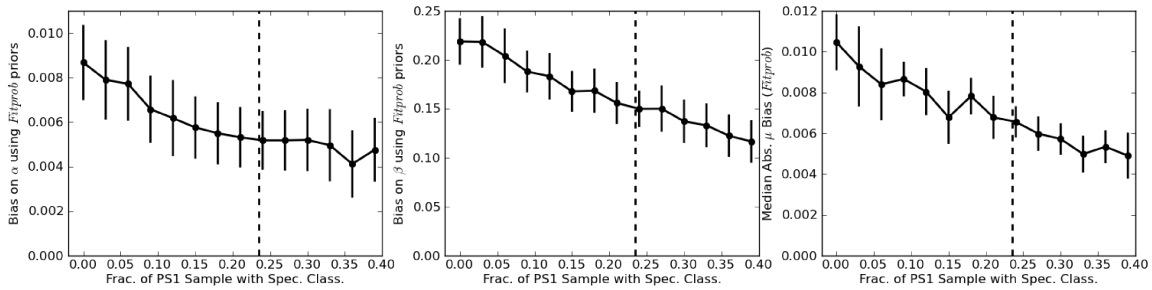

Figure 5.11: For *Fitprob* P(Ia) priors, one of the least precise classification methods, we used simulations (§5.3.2.1) to show the bias on α, β, and distance due to BEAMS as a function of the fraction of spectroscopically classified SNe Ia in the data. In this work, ∼24% of the PS1 sample is spectroscopically classified (vertical lines), giving a predicted reduction in α/β bias and $|\mu - \mu_{true}|$ of ∼30-40%.

5.5.2 Distance Bias Correction

Two effects lead to systematic uncertainties in distance bias corrections. The dominant effect is the difference in distance bias predictions between the G10 and C11 dispersion models. The difference between the G10 and C11 models is up to $\Delta\mu(z) \sim 0.03$ mag (with the exception of the highest-z data, which are subject to large c biases; Figure 5.3). As there is no *a priori* reason to choose one dispersion model over the other, we choose to adopt the average of the two bias predictions for our baseline distance bias correction. The systematic error then becomes half the difference between the G10/C11 bias.

A secondary effect is that uncertainty in the survey detection limit or spectroscopic follow-up selection function can cause the simulated distance bias to be inaccurate. We adjust the detection efficiency (for the PS1 host-z sample) and the spectroscopic

selection efficiency (for the PS1 SN-z sample) such that SNR at maximum light for simulated SNe matches the data with a $\sim$20% higher reduced χ^2 (a 1σ difference). These efficiencies are well-contrained by the data; the detection efficiency adjustment for the host-z sample corresponds to lowering the magnitude limit of the survey by just $\sim$4 mmag.

For the low-z distance bias, which is measured from low-z simulations that are a less convincing match to the data, we use the "volume-limited" simulations discussed in §5.3.2.1 for the systematic uncertainty. The volume limited variant has $<$0.01 mag distance bias using the G10 scatter model (small biases due to the correlation of Hubble residuals with x_1 and c still arise; Scolnic & Kessler, 2016), and a bias of $\sim$0.02 mag using the C11 model because $\beta_{fit} - \beta_{sim} = 0.7$. The systematic uncertainty due to the detection limit and spectroscopic follow-up selection function is subdominant to the G10/C11 systematic uncertainty.

5.5.3 Photometric Calibration Uncertainties

In this work, the systematic uncertainties in the photometric calibration are the same as the S17 analysis. They are due to uncertainty in the survey filter functions, uncertainty in the calibration of HST CALSPEC standard stars, and uncertainty in the calibration of the PS1/low-z photometric systems relative to HST.

Uncertainties in the survey filter functions are modeled as uncertainties in the zeropoints and effective wavelengths of each filter. PS1 has a nominal effective wave-

length uncertainty of 7Å per filter (Scolnic et al., 2015). The low-z filter uncertainties are typically $\sim$6$-$7Å but are survey- and filter-dependent. They can be as high as 25$-$37Å (exact values are given in Scolnic et al., 2015; see their Table 1).

The relative calibration uncertainties are given by the Supercal method. Supercal uses the excellent (sub-1%) relative calibration of PS1 across 3π steradians to compare the photometry of tertiary standard stars in previous SN surveys to their photometry on the PS1 system. Typical corrections are on the order of 1%, but can be up to 2.5% for B band low-z data. Uncertainties in the Supercal procedure are typically 3-4 mmag per filter but can be up to 10 mmag for low-z surveys such as CfA1.

Finally, there is uncertainty in the AB magnitude system itself as measured using HST CALSPEC standard stars. We follow B14 by assuming a global 0.5% slope uncertainty for the flux as a function of wavelength, which was determined by comparing white dwarf models to the HST data (Bohlin, 2014; Betoule et al., 2013). In total, we use 62 individual systematic uncertainties to describe the uncertainty in the photometric calibration. Most are due to the relative calibration: there is one systematic for the filter zeropoint and the filter λ_{eff} $\times$ number of surveys $\times$ number of filters per survey.

5.5.4 SALT2 Model Calibration Uncertainties

The training of the SALT2 model is subject to the same photometric calibration uncertainties discussed above. B14 created variants of the SALT2.4 light curve fitter

by applying zeropoint and filter function shifts to the training data and subsequently re-training SALT2. These account for 10 individual systematics, which are averaged to give the SALT2 model systematic error. These uncertainties are discussed in §5.4 of B14.

Re-training SALT2 using the improved calibration from Supercal will lower the SALT2 systematic uncertainty in future analyses. However, we do not re-train the SALT2 light curve fitter for this analysis, as the SALT2 training data are not public.

5.5.5 Core-Collapse Supernova Contamination

Systematic error due to marginalizing over the ∼5% CC SN contamination in our sample is a new source of uncertainty caused by our use of photometrically classified SNe. Our method of measuring distances from SNe Ia while marginalizing over CC SNe is subject to errors in the prior probabilities that a given SN is of type Ia and differences between the CC SN model and the true distribution of CC SNe. The systematic error estimation from CC SN contamination was presented in detail in J17 and relies on varying these components.

We use the four methods of estimating prior probability discussed above (§5.3.3) and three parametric models for the CC SN distribution. The baseline likelihood model for CC SNe, $\mathcal{L}_i^{CC}$ (Eq. 5.3), is a Gaussian with a mean and standard deviation − $g(z_i)$ and $\Sigma_{CC}(z_i)$ for the ith SN − that are both functions of redshift. The two alternate CC SN parametric models are a two-Gaussian and skewed Gaussian

model. We demonstrated in J17 that these models typically agree well with single Gaussian results; all three CC SN distributions tend to be much broader than the SN Ia distribution, therefore encompassing most outliers.

5.5.6 Peculiar Velocity Correction

The magnitude of SN peculiar velocities − due to bulk flows and nearby superclusters − becomes $\gtrsim$5% of the Hubble flow at $z \lesssim 0.03$. We correct for peculiar velocities using the nearby galaxy density field measured by the 2M++ catalog from 2MASS (Lavaux & Hudson, 2011). The uncorrelated uncertainty associated with each correction is ± 150 km s^{-1}. The peculiar velocity model is parameterized by the equation $\beta_I = \Omega_M^{0.55}/b_I$, where b_I describes the light-to-matter bias. (β_I is unrelated to the SALT2 nuisance parameter). Carrick et al. (2015) measure $\beta_I = 0.43 \pm 0.021$. We adopt a conservative ± 0.1 systematic on β_I for our peculiar velocity systematic uncertainty. Peculiar velocity uncertainty is one of the smallest systematics in most SN cosmology analyses.

5.5.7 SN Ia Demographic Shifts

Though SN Ia have been shown to be excellent standardizable candles at low-z, it has been suggested that the relationship between their luminosities, colors, or host galaxy properties may change with redshift. We address these possibilities by adding

two systematic tests. For these tests, we add two additional parameters to our model for estimating cosmological parameters (§5.4). The first is to allow a linear evolution of the mass step as a function of redshift. Mass step evolution was proposed by Childress et al. (2014), and could be observed if the mass step is caused by physical differences in SNe Ia with different progenitor ages. The second is to allow a linear evolution in the SALT2 shape and color standardization parameters, α and β, as a function of redshift. This was suggested as a possible concern by Conley et al. (2011). Δ_M and β in Equations 5.1 and 5.3 then become:

$$\begin{aligned} \Delta_M &= \Delta_{M,0} + \Delta_{M,1} \times z, \\ \beta &= \beta_0 + \beta_1 \times z. \end{aligned} \tag{5.10}$$

$\Delta_{M,0}$, $\Delta_{M,1}$, β_0 and β_1 are free parameters. They are measured simultaneously with SN Ia distances in §5.6.

An additional potential systematic is the relation between SN Ia corrected magnitudes and their *local* host galaxy environments. Several papers have recently asserted that SN Ia corrected magnitudes are correlated with their local star formation environments on a scale of ∼1-2 kpc (the LSF step; Rigault et al., 2013, 2015). Due to the $\sim 1''$ PSF of PS1 and the lack of ultraviolet or u-band observations for much of our sample, it is impossible to measure robust local star formation rates over the PS1 redshift range. However, Jones, Riess, & Scolnic (2015) re-examined the evidence for the LSF step, finding that the re-training of SALT2 in B14/G10 reduced or

eliminated many of the biases in the SALT2 model. Jones, Riess, & Scolnic (2015) found no evidence for a LSF step in the B14 low-z sample. Though our data are not optimal for investigating local properties, we plan to use PS1 data to more robustly determine the relationship between SNe Ia and their global host galaxy properties in future work. We discuss the potential for other evolutionary systematics in the discussion (§5.9).

5.6 First Results and Consistency Checks

The PS1+low-z Hubble diagram is shown in Figure 5.7 and the SN Ia distances from our likelihood model are compared to the JLA sample in Figure 5.8 (using the correlated bins given in B14, Appendix F). The agreement is close, with a difference in median Hubble residual of just 9 mmag at $z > 0.2$. At low-z, our distances are just 5 mmag fainter. This difference can also be explained by improvements in the bias correction methodology as well as the addition of CfA4 SNe, which are not included in B14. CfA4 SNe are $\sim$26 mmag fainter than the other low-z SNe on average and comprise 24% of the low-z sample. Light curve parameters for our full sample are given in Table 5.7.

Our likelihood model is simultaneously used to measure α, β, and the dispersion σ_{Ia}, which are given in Table 5.2. α is higher than measured by previous analyses by up to $\sim 2.5\sigma$. It is unclear whether this could be due to observational bias or

another cause, but PS1 spectroscopically confirmed SNe and SDSS spectroscopically confirmed SNe (measured with the `SALT2mu` procedure; Marriner et al., 2011) prefer α of $\sim$0.15-0.16. The systematic error on β is higher than other nuisance parameters due to the predicted biases on β found by J17 when using the GalSNID and *Fitprob* SN classification methods (see §5.6.1).

In J17, we predicted that our method would give α and β that are biased by +3%. This gives a prediction that the α and β measured here will be higher than the α and β measured from spectroscopically confirmed SN Ia alone. Table 5.2 shows that this may indeed be the case; α and β are 4% higher than the values from spectroscopically confirmed PS1+low-z SNe Ia (though at $<1\sigma$ significance if we neglect the partial correlations between these two samples).

We also recover the mass step at nearly 4σ significance (nearly 7σ from statistical errors alone). Our measurement of 0.101 ± 0.026 is consistent with B14 (0.07 ± 0.023). Interestingly, the host mass step Δ_M is higher in the full PS1+low-z sample than in the sample of spectroscopically classified SNe Ia alone (1.9σ significance from statistical uncertainties alone, but these measurements are not independent). It's unclear if this could be due to statistical fluctuation, a bias from the method, or the presence of broader light curve shapes and redder colors in the full sample. x_1 and c correlate with both host mass and Hubble residual (Scolnic & Kessler, 2016) − and could increase the size of the step (S17). We will use simulations to investigate whether our method of marginalizing over CC SN contamination could bias determinations of the

host mass step in future work.

5.6.1 Impact of Different Classification Methods

Figure 5.9 illustrates the prior probabilities that go into the likelihood model, which in turn is used to infer SN Ia distances. We show the PS1 Hubble residual histograms for likely SNe Ia and likely CC SNe as determined by each of the four classification methods considered in this work. Figure 5.9 shows that PSNID, our most reliable classifier from J17, classifies nearly three times as many SNe as likely CC SNe compared to the other methods.

In spite of these large differences in classifier results, the BEAMS measurements of SN Ia distances are remarkably consistent (Figure 5.10). Nearly all distances are within 1σ of distances derived from the PS1 spectroscopically classified SN Ia sample. Additionally, distances from $0.2 \lesssim z \lesssim 0.5$, where most of our data lie, show few discrepancies between the different methods. Even the test case of using an uninformative prior of P(Ia) = 1/2 for all photometrically classified SNe (bottom panel) yields distances within 1σ of the spectroscopic sample in all bins but one. We note that close agreement is predicted by J17; even in a sample without spectroscopically confirmed SNe Ia, J17 predict biases of <10 mmag due to the method. We will revisit this prediction in §**??** to test whether our methodology remains robust and consistent in the case of an "ideal" photometrically classified SN sample; i.e., a sample without spectroscopic classifications.

The nuisance parameters α and β are also more consistent than expected from J17, varying by 30-50% less than the simulation-based predictions in J17 (in this work we observe differences of $\Delta\beta \sim 0.07$ and $\Delta\alpha \sim 0.004$ between the four different classification methods). In Figure 5.11, we use one of the least accurate classification methods (*Fitprob*) to provide a possible explanation for why our results are more consistent than expected. J17 simulations included no subset of spectroscopically classified PS1 SNe, while our data consist of ∼20% spectroscopically classified PS1 SNe. Because of this, we used simulations of the PS1 host-z and SN-z samples (§5.3.2.1) to predict the effect of adding spectroscopically classified subsets of SNe to the data. We find that the predicted biases on α and β due to marginalizing over CC SNe decrease by 30-40% when the PS1 data consist of just 20% spectroscopically classified SNe.

Similarly, the median absolute biases on both low-z and high-z distances decrease by ∼30-40% when 20% of PS1 SNe are spectroscopically classified (low-z distances are not subject to CC SN contamination but can be biased by incorrect α and β). Simulations predict that our best method, PSNID, has no statistically significant bias even in the case where there are no spectroscopically classified PS1 SNe (J17). However, including a subset of spectroscopically classified SNe as part of the data could greatly reduce bias and improve consistency if PSNID classifications are systematically biased or if suboptimal classification methods are used.

Table 5.2. Nuisance Parameters

	All SNe			Spec. Class. SNe	
		σ_{stat}	$\sigma_{stat+sys}$		σ_{stat}
α	0.165	0.007	0.019	0.154	0.008
β	3.118	0.069	0.143	3.013	0.089
σ_{Ia}	0.112	0.011	0.047	0.119	0.023
Δ_M	0.100	0.013	0.027	0.057	0.018

Note. — Nuisance parameters from PS1+low-z SNe. Note that the systematic uncertainty on β is likely overestimated due to the biases from the GalSNID and *Fitprob* classification methods discussed in J17.

5.6.2 Evolution of Nuisance Parameters

Using Equation 5.10 to add linear mass step (Δ_M) evolution to BEAMS, we find no evolution in Δ_M as a function of redshift (we use the baseline classifier, PSNID). However, our uncertainties are large (0.08 mag) due to lack of low-mass hosts at high redshift[5]. In Figure 5.12, we estimate the redshift dependence of the mass step by clipping Hubble residuals at $-0.5 < \mathrm{HR} < 0.5$ to remove most CC SNe and plotting the maximum likelihood mass step in redshift bins of 0.1. This is an incomplete removal of CC SN contamination, but doubles as a simple sanity check on BEAMS. We see possible hints that the high-z mass step is smaller, but find no statistically

[5]S17, however, finds evidence of mass step evolution. The discrepancy could be due to the larger SNLS redshift range and additional SNe Ia in low-mass hosts at $z > 0.5$.

significant measurement of mass step evolution.

We do see 3σ evidence for evolution of the β parameter, however. Fortunately, this does not constitute a significant contribution to our systematic error budget as it predominantly affects the highest survey redshifts where few SNe are found (Figure 5.6). Evidence for β evolution was seen in SNLS data (Conley et al., 2011) and S17, though its significance is disputed in B14. We caution that blue ($c < 0$) SNe Ia have lower observed β (SNe primarily appear blue due to noise and selection biases; (Scolnic & Kessler, 2016)), and our high-z data are dominated by blue SNe (Figure 5.1). However, our methodology does not recover any significant evolution of β when tested on simulated SN samples with a constant β. If this evolution is confirmed, it could suggest an evolution in dust properties or the evolution of SN progenitors with redshift and could contribute significantly to the error budget at $z > 0.5$.

5.7 Cosmological Constraints from Supernova and CMB Data

We first constrain Ω_M using the SN Ia data alone and assuming a flat ΛCDM cosmology. We find $\Omega_M = 0.308 \pm 0.041$, consistent with B14 ($0.295 \pm 0.034$). These results are independent of, but in agreement with, the Planck constraints on Ω_M ($\Omega_M = 0.308 \pm 0.012$).

We combine these data with CMB constraints from the Planck full-mission data

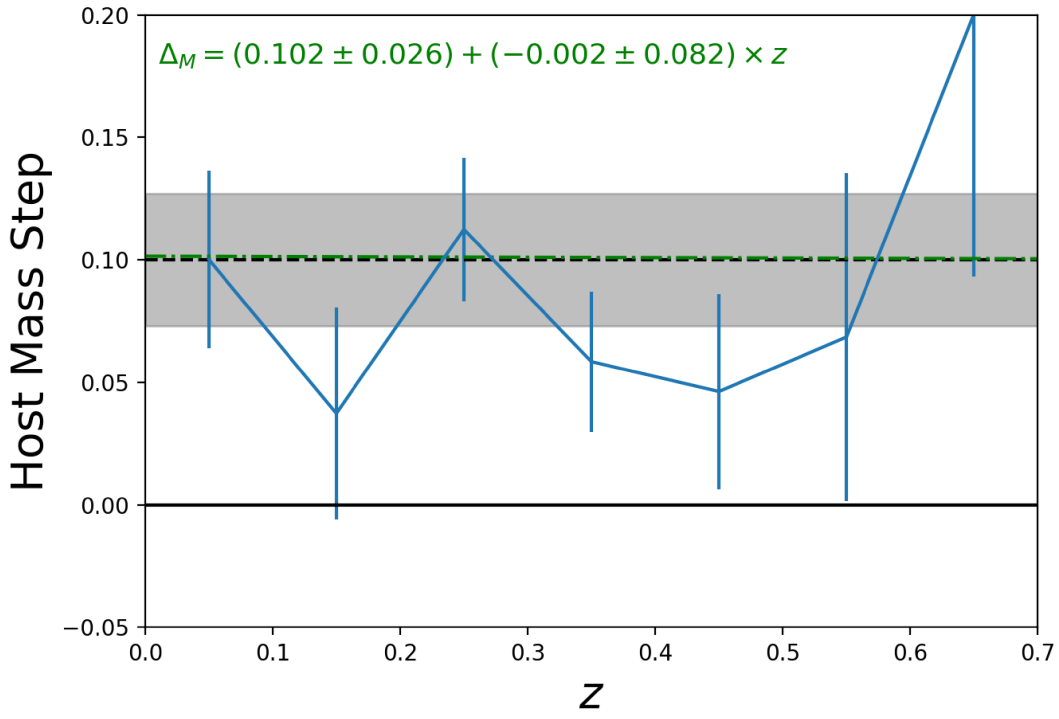

Figure 5.12: Evolution of the host galaxy mass step with redshift. Binned points are shown with the best fit global mass step (black) and linear trend (green). Although $z > 0.4$ data tend to favor a smaller mass step, we see no statistically significant evidence for evolution with these data. A sample with a larger redshift range will have more power to measure the possibility of mass step evolution.

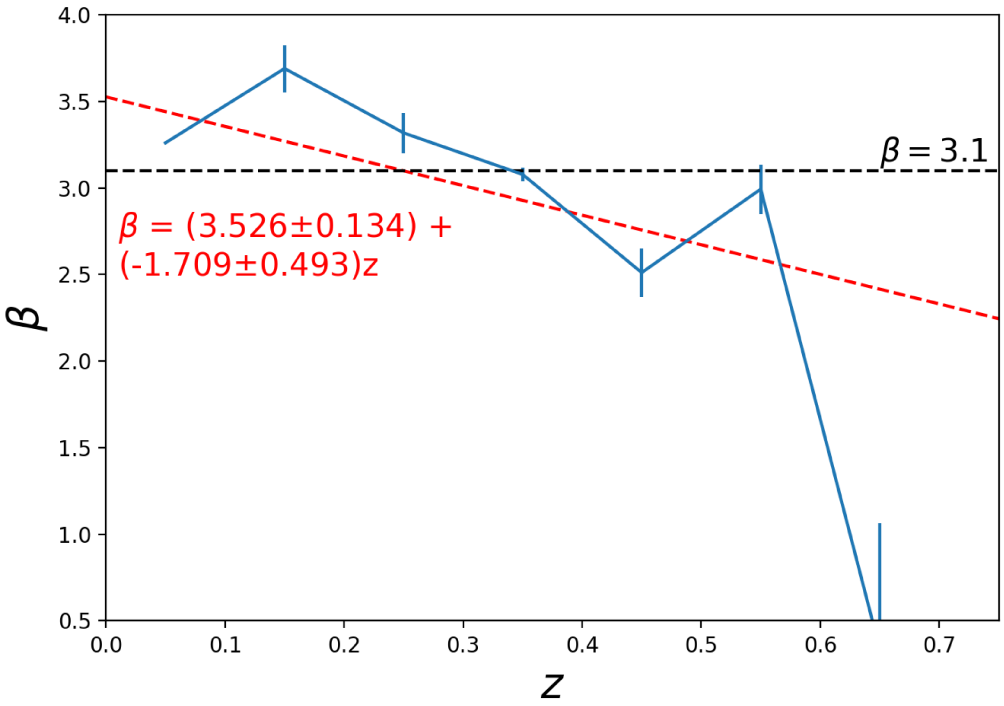

Figure 5.13: Evolution of the SALT2 nuisance parameter β with redshift. Binned points are shown with the best fit β (black) and linear trend (red).

Table 5.3. Summary of Systematic Uncertainties on w

Error	w	$\Delta\sigma_w$[a]	Rel. to σ_w^{stat}
Stat.	-1.008±0.039	0.000	0.000
All Sys.	-1.001±0.062	0.048	1.248
Phot. Cal.	-1.010±0.048	0.028	0.731
Bias Corr.	-1.019±0.048	0.028	0.733
SALT2 Model	-1.007±0.040	0.011	0.287
CC SN Contam.	-1.007±0.040	0.010	0.269
MW E(B-V)	-1.018±0.039	0.009	0.225
Beta Evol.	-1.012±0.039	0.008	0.217
Mass Step	-1.011±0.038	0.000	0.000
Pec. Vel.	-1.005±0.038	0.000	0.000

[a]The additional uncertainty added in quadrature from each source of systematic error.

(Planck Collaboration et al., 2015). In contrast to the Planck Collaboration et al. (2014) constraints used in B14, the full-mission Planck data does not require WMAP polarization measurements. Planck provides the full likelihoods for the CMB spectrum, which can then be combined with SNe Ia using CosmoMC. Planck data greatly improve our constraints on w through the CMB temperature power spectrum, which gives a precise constraint on the cosmic matter density at $z \sim 1090$. Constraints from a matter-dominated cosmic epoch are largely independent of an evolving or non-cosmological constant dark energy, which affects cosmic evolution only at the late times probed by SNe Ia and BAO measurements.

With Planck priors, we measure w = -1.018±0.063 (stat+sys). Systematic uncertainties on this measurement are 25% higher than statistical uncertainties (Table 5.3). Though we have substantially more SNe than B14 and S17, our uncertainty budget is 9% higher than B14. There are three primary reasons for this. First, we have fewer independent surveys to reduce the photometric calibration systematic. Second, we have estimated a more conservative systematic uncertainty on the selection bias correction. Lastly, PS1 photometrically classified SNe have much lower SNR (for PS1, SNR at maximum is an average of 17 for photometrically classified SNe and 39 for spectroscopically classified SNe Ia), and PS1 SNe, unlike SNLS SNe, cannot be found at $z \sim 0.7 - 1$. However, PS1 SNe have the added benefit of being independent from all previous high-z SN samples.

We also use these data to constrain the two-parameter redshift evolution of w

using the most common parameterization:

$$w = w_0 + w_a z/(1+z). \tag{5.11}$$

Eq. 5.11 is a first order Taylor series expansion of w as a function of scale factor a (Linder, 2003). We find $w_0 = -0.952 \pm 0.147$ and w_a =-0.408±0.815. These constraints are slightly better than those of B14, which is due to our use of the most recent chains from Planck. We find much tighter constraints after combining with BAO (§5.8).

5.7.1 Systematic Uncertainties on w

Contributions to the systematic uncertainties on w are summarized in Table 5.3. In spite of recent improvements, the photometric calibration remains tied with the selection bias uncertainty as the largest systematic uncertainty. It was reduced by ∼20% using the Supercal procedure (Scolnic et al., 2014a find a systematic of 0.035 on w for PS1+low-z SNe). Continued improvements will come from a new network of white dwarf standards (Narayan et al., 2016).

The systematic uncertainty on the selection bias of 0.028 is is dominated by the difference between the G10 and C11 scatter models and the uncertain spectroscopic selection function of the low-z surveys. It may be that re-training SALT2 assuming the C11 scatter model, e.g. Mosher et al. (2014), will reduce this systematic (SALT2 training data are not publicly available). This may be an important avenue for future

Table 5.4. w with Different Photometric Classification Priors

Method	w	Δw
PSNID	-1.008±0.038	···
PSNID, Skewed Gaussian CC Model	-1.002±0.038	0.008±0.000
PSNID, 2-Gaussian CC Model	-0.977±0.042	0.031±0.018
NN	-1.001±0.036	0.007±0.000
GalSNID	-1.003±0.037	0.005±0.000
Fitprob	-1.023±0.037	-0.015±0.000

Note. — "SkG" and "2G" and refer to the skewed Gaussian CC SN parameterization and the two-Gaussian CC SN parameterization. The classification systematic error due to CC SNe is lower than expected from J17, likely because our photometric sample comprises ∼25% spectroscopically confirmed SNe.

work. The SALT2 model calibration is also a significant systematic, but can be reduced with larger training samples, new data from surveys such as Foundation, and re-training SALT2 after applying the Supercal calibration.

The systematic due to marginalizing over CC SNe is just the fourth largest systematic − approximately equal in size to MW reddening and the SALT2 model calibration − and is 35% lower than predicted in J17 in spite of the fact that we allow α and β to be fit by BEAMS for all methods. Table 5.4 shows the value of w measured from each variant of the classification priors and the CC SN parameterization discussed in §4. All measurements of w agree to within ∼3% or better.

The better-than-expected consistency on w may be due to sample-to-sample variations, but is more likely explained by tighter constraints on Ω_M from the full Planck chains and the fact that a sizeable portion ($\sim$20%) of our high-z data are spectroscopically classified SNe Ia. With simulations, we found that a subset of SNe with known types can greatly help the BEAMS method to constrain distances and SN Ia nuisance parameters (§5.6). If the amount of CC SN contamination was overestimated in J17, that could also help to explain the low contamination systematic. The magnitude of the CC SN contamination systematic can be further reduced by improved validation of classifiers and a better understanding of the diversity of CC SNe, their luminosity functions, and the inclusion of additional CC SN templates in classifier training as discussed in J17. We expect that within a few years, the advantage of using photometrically classified SNe will be unequivocal.

5.8 Cosmological Constraints with BAO and H_0 Priors

We now combine Planck and PS1+low-z SNe with baryon acoustic oscillation (BAO) constraints and a local prior on the value of H_0 from Riess et al. (2016). The BAO feature, the evolving size of the imprint of acoustic waves on the distribution of cosmic matter, serves as a standard ruler that is independent of SN Ia measurements. The BAO scale is proportional to a combination of the angular diameter distance to

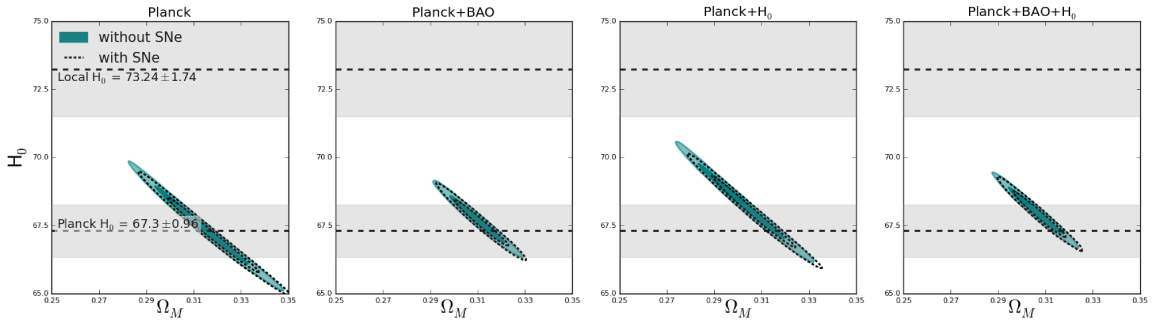

Figure 5.14: Discrepant constraints on H_0 from CMB, BAO, and local measurements assuming ΛCDM. SNe Ia cannot resolve these conflicts.

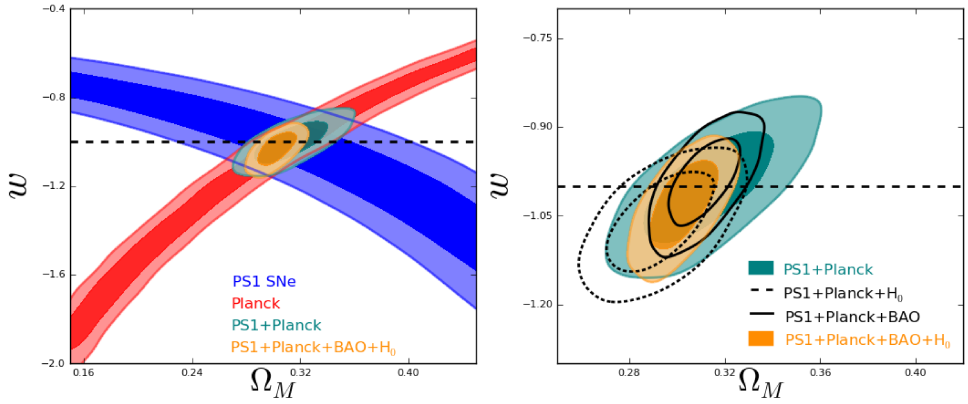

Figure 5.15: Constraints on w and Ω_M from PS1+low-z SNe in conjunction with other probes.

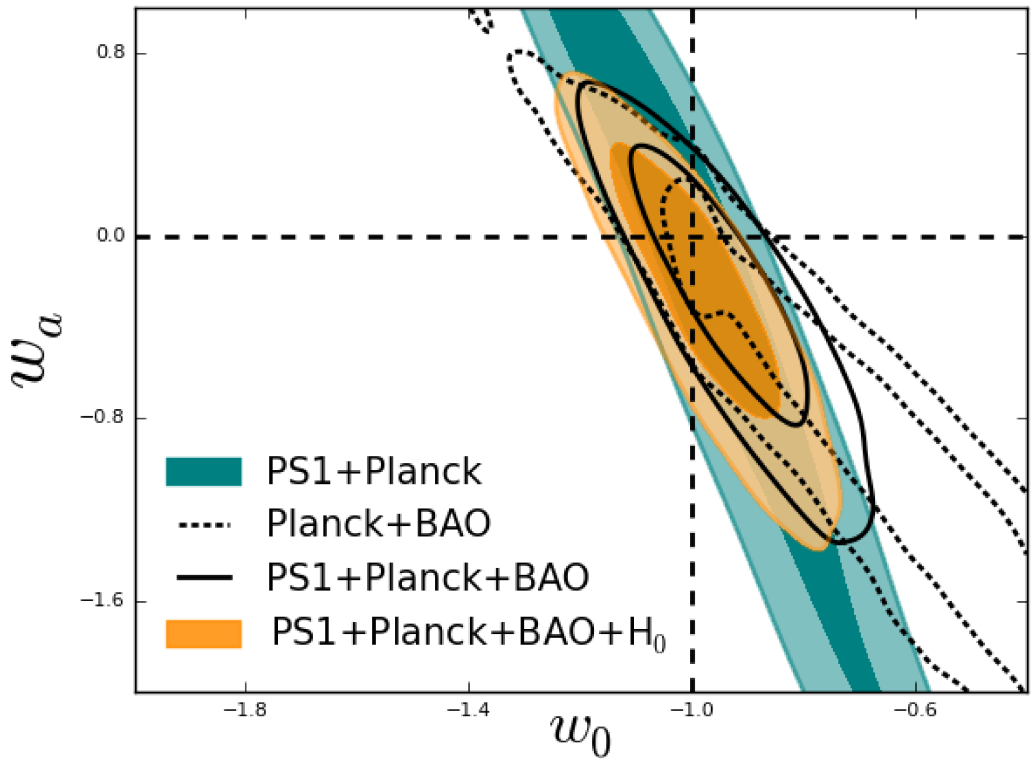

Figure 5.16: Constraints on w_0 and w_a from PS1+low-z SNe, Planck, BAO, and H_0.

a given redshift and the Hubble parameter $H(z)$ at that redshift. Following Planck Collaboration et al. (2015), we use BAO constraints from the SDSS Main Galaxy Sample (MGS; Ross et al., 2015) and the combination of the Baryon Oscillation Spectroscopic Survey (BOSS) and CMASS survey (Anderson et al., 2014). The BAO constraints used here give measurements of the BAO scale to $z = 0.15$, 0.32, and 0.57.

There is a notable internal conflict between these priors: a 3.4σ discrepancy between local and CMB-inferred values of H_0 (Riess et al., 2016). The difference could be due to systematic uncertainties in one or both datasets (e.g. Addison et al., 2016), >3 neutrino species, non-Λ dark energy, or more exotic phenomena. We show this discrepancy in Figure 5.14 for a standard ΛCDM cosmology (reionization optical depth $\tau = 0.078$; Planck Collaboration et al., 2016). PS1+low-z SNe have no significant impact on the disparity in a standard ΛCDM cosmological model.

Following B14, we use SN data to constrain three cosmological models: the o-ΛCDM model removes the assumption of flatness ($\Omega_k = 0$), the w-CDM model allows a fixed, non-cosmological constant value of w, and the w_a-CDM model allows w to evolve with redshift. The constraints on these three models are presented in Table 5.5. All measurements of w and w_a are consistent with ΛCDM (Figures 5.15 and 5.16). With SNe+Planck+BAO+H_0 constraints, we find w = -1.047$\pm$0.051 for the w-CDM model and w_a = -0.185$\pm$0.445 for the w_a-CDM model (Figure 5.16). With just SNe, Planck, and BAO data, we find w = -1.003$\pm$0.051 for the w-CDM model and w_a = -0.191$\pm$0.418 for the w_a-CDM model.

Nearly all measurements of Ω_k are consistent with a flat universe. The lone exception is the combination of SNe, Planck and H_0 without BAO constraints. This choice of priors gives 2.3σ evidence for positive curvature, but the result is entirely due to the local/CMB H_0 discrepancy and becomes insignificant when BAO constraints are added.

As shown from the H_0 measurements in Table 5.5, PS1+low-z SNe and the non-ΛCDM models considered here do not explain the local/CMB H_0 discrepancy. When H_0 priors are omitted, all measurements of H_0 are inconsistent with Riess et al. (2016) at the $\sim$2-3σ level. When only CMB and H_0 priors are included, we measure values of H_0 that are consistent with Riess et al. (2016) only when allowing for positive curvature or evolving w. When we combine with CMB, H_0 and BAO priors, all measurements of H_0 are inconsistent at the 2.6σ to 2.8σ level *even though* H_0 priors are included. Therefore, SNe Ia and the models considered here do not favor a non-ΛCDM universe and cannot currently resolve the H_0 discrepancy.

5.9 Possible Biases

Our Hubble diagram (Figure 5.7) and measurements of w and Ω_M show excellent agreement with B14. For the flat wCDM model, Table 5.6 shows the drift in the values of w we measure with respect to B14. All values are consistent within 0.25σ. Though these measurements are correlated, as B14 use many of the low-z SNe that

Table 5.5. Cosmological Parameters from PS1, BAO, CMB, and H_0

	$o-\Lambda$CDM Constraints			
	Ω_M	Ω_Λ	Ω_k	H_0
PS1+Planck+BAO+H_0	0.306±0.007	0.692±0.008	0.002±0.003	68.390±0.704
PS1+Planck	0.318±0.047	0.683±0.037	-0.001±0.011	67.540±5.206
PS1+Planck+BAO	0.310±0.008	0.689±0.008	0.001±0.003	67.894±0.731
PS1+Planck+H_0	0.271±0.018	0.720±0.015	0.009±0.004	72.671±2.319
	w-CDM Constraints			
	Ω_M	w	H_0	
PS1+Planck+BAO+H_0	0.302±0.009	-1.031±0.050	68.595±1.092	
PS1+Planck	0.314±0.018	-1.001±0.062	67.503±1.781	
PS1+Planck+BAO	0.311±0.010	-0.992±0.049	67.539±1.105	
PS1+Planck+H_0	0.293±0.014	-1.061±0.055	69.633±1.530	
	w_a-CDM Constraints			
	Ω_M	w_0	w_a	H_0
PS1+Planck+BAO+H_0	0.304±0.010	-0.983±0.101	-0.251±0.419	68.608±1.084
PS1+Planck	0.308±0.027	-0.952±0.147	-0.342±0.807	68.184±2.849
PS1+Planck+BAO	0.313±0.011	-0.940±0.106	-0.251±0.411	67.535±1.157
PS1+Planck+H_0	0.280±0.015	-0.863±0.126	-1.090±0.616	71.319±1.699

we do (with the exception of CfA4), and we combine both SN datasets with the same CMB, BAO, and H_0 data, such close agreement is somewhat surprising. Nevertheless, it is prudent to consider whether changes in methodology relative to B14 could be biasing this measurement.

J17 found that CC SN contamination could bias the determination of w, and that these biases are almost always negative. However, even with the least informative classification methods, our simulations showed that the absolute bias on w is $\lesssim$0.035. We expect the bias to be lower still in this work because we include spectroscopically classified SNe as part of the data and a stronger constraint on Ω_M from the full Planck chains. We also test our results by keeping α and β fixed − an option which results in lower biases in J17 − and find that the difference in w is just 0.003.

Our photometric pipeline could cause unexpected systematic uncertainty, but the effectiveness of this pipeline and its calibration have been demonstrated and tested in S17, Rest et al. (2014), and Scolnic et al. (2014a). The Supercal procedure (Scolnic et al., 2015) predicts a 2.6% lower w due to improved calibration (this offset is not tailored to the PS1+low-z survey), but this is well within the statistical uncertainty of our measurement. We also see good agreement between photometric SNe Ia and spectroscopically confirmed SNe Ia; spectroscopically confirmed PS1+low-z SNe give $w = -0.997 \pm 0.046$ (stat. errors only).

The results presented here remain subject to uncertainty in the population of CC SNe contaminating the SN data. However, our cosmological parameter measure-

ments remain consistent when using several uncorrelated methods as part of the BEAMS framework. The consistency of these results with measurements from spectroscopically confirmed PS1 SNe gives us additional confidence in its robustness. In the next few years, we expect additional CC SN templates and better constraints on CC SN luminosity functions will lead to even more robust simulation-based tests for this method and other similar methods.

5.9.1 Evolution of SNe Ia

We include two new systematics in this analysis pertaining to the possible evolution of SN characteristics with redshift. These include evolution of the mass step and evolution of β. However, we find that these have a negligible effect on the cosmology, even though one of them (β evolution) is significant. β evolution could have a greater impact at $z \sim 1$, and should be taken into account in future analyses. It may cause a change in the B14 results.

Another optional test for evolutionary systematics could include changing the location of the mass step. We do not include this here as it is not evident in the data (see Figure 12 of B14). Other possible systematics include replacing the mass step with a host galaxy star formation rate, stellar age, or stellar metallicity step (e.g. Rigault et al., 2013; Hayden et al., 2013; Childress et al., 2014), and these possibilities will be evaluated in detail in future work. The correlation of global host galaxy properties with these physical parameters has only been found to be more significant

than the mass step at the 1-2σ level, and could be due to statistical fluctuations or differences in analysis (Jones, Riess, & Scolnic, 2015). We plan to undertake a separate analysis to determine which of them could affect the determination of cosmological parameters. Note, however, that evolutionary systematics have a reduced effect in our data compared to the JLA sample, whose larger redshift range could result in larger evolutionary effects.

5.9.2 Observational Biases

The well-measured dependence of β on SN color could cause bias at high-z, where PS1 SNe are predominantly blue. We tested a variant of our analysis that uses a different color law for blue SNe Ia and red SNe Ia. This β difference is most likely due to sample selection cuts rather than SN physics as it can be recovered in simulations of the SALT2 model (Scolnic & Kessler, 2016). However, if the simulations of our redshift-dependent color distribution have some error, a two-slope relation between color and luminosity will reduce bias. This two-slope relation favors a nearly identical w of -1.006 $\pm$ 0.038 (stat. error). While it is not clear if additional biases could arise from crudely treating color via a two-slope relation (or a more sophisticated treatment; **?**), a SN light curve fitter that takes selection criteria into account would be a valuable addition to cosmology analyses.

One such method exists already: the "BEAMS with Bias Corrections" (BBC) method of Kessler & Scolnic (2016) uses SN simulations to correct for observational

Table 5.6. Comparison to Betoule et al. (2014)

	w (This Work)	w (JLA)	Difference
SNe+Planck	-1.001±0.062	-1.017±0.056	0.016±0.083 (0.19σ)
SNe+Planck+BAO	-0.992±0.049	-1.003±0.047	0.011±0.068 (0.16σ)
SNe+Planck+H_0	-1.061±0.055	-1.064±0.051	0.003±0.075 (0.03σ)
SNe+Planck+BAO+H_0	-1.031±0.050	-1.038±0.047	0.007±0.068 (0.10σ)
	w_a (This Work)	w_a (JLA)	Difference
SNe+Planck	-0.342±0.807	-0.608±0.748	0.266±1.100 (0.24σ)
SNe+Planck+BAO	-0.251±0.411	-0.280±0.433	0.029±0.597 (0.05σ)
SNe+Planck+H_0	-1.090±0.616	-1.055±0.586	-0.035±0.850 (0.04σ)
SNe+Planck+BAO+H_0	-0.251±0.419	-0.290±0.443	0.039±0.610 (0.06σ)

Note. — Comparison of our results to the JLA measurements after applying updated Planck, H_0 and BAO priors to the JLA sample.

biases in c, x_1, m_B, α and β, while simultaneously marginalizing over CC SN contamination. This approach is promising, and as measurements on w are refined further such a method can help to reduce both the statistical and systematic uncertainties on w. For the present analysis, we consider its treatment of CC SN contamination to be somewhat too rigid given current uncertainties in the CC SN luminosity functions (J17). As this is the first measurement of w with a BEAMS-like methodology, we also favor an approach with more consistency to recent analyses such as B14.

5.9.3 Impact of an Unblinded Analysis

In carrying out this analysis, we note that we did not blind ourselves to the cosmological results. A blinded analysis, such as that of S17, would remove any subconscious bias on the part of the authors to acheive agreement (or disagreement) with ΛCDM cosmology. We note, however that all of the photometry and many of the bias correction simulations were undertaken before the cosmological results were examined. Furthermore, we have strived for consistency with previous analyses whenever possible, which serves to limit the number of qualitative choices that can be tuned to yield a preferred cosmology. Future analyses, such as DES SN Ia cosmology, will be fully blinded. As cosmology with photometrically classified SNe Ia becomes a more mature subject area, the authors will feel more comfortable undertaking blinded analyses.

5.10 Conclusions

The 1,344 cosmologically useful, likely SNe Ia from the PS1 medium deep fields and low-z surveys constitute the largest set of SNe Ia assembled to date. Though the smaller redshift range and lower SNR of these data yield nearly equivalent constraints to the JLA compilation, they are independent of many of the systematic uncertainties that affect SNLS or SDSS. In the future, these data can be used in conjunction with the Foundation low-z SN sample (Foley et al., in prep.) to give independent

constraints on w using *only* the well-calibrated PS1 photometric system.

The PS1 SNe in this sample do not have spectroscopic classifications, necessitating the use of a BEAMS-like algorithm (J17) to marginalize over the CC SN population. Our SN Ia distances from BEAMS ($z > 0.2$) differ from the JLA compilation by just 9 mmag on average. J17 finds that CC SNe in a PS1-like sample bias w by just 0.003±0.002.

After combining with CMB data, we find that these data are fully consistent with a flat ΛCDM cosmology, with w =-1.018±0.063. If we allow w to be parameterized by a constant component (w_0) and a component that evolves with redshift (w_a), we find no evidence for a changing value of w. Combining SNe with CMB and BAO constraints gives w = -1.003±0.051 and w_a = -0.191±0.418. Finally, adding H_0 constraints yields w = -1.047±0.051 and w_a = -0.185±0.445. Our constraints differ from those of B14 by $<0.25\sigma$ regardless of whether CMB, BAO, and/or H_0 priors are included.

CC SN contamination is currently our fourth-largest systematic uncertainty, and this can be improved with new SN classification algorithms and better training samples, as discussed in J17. In future work, our dominant systematics − selection biases and calibration − can be reduced by combining PS1 data with Foundation and/or SNLS and SDSS data.

We recover a mass step of 0.101±0.026, consistent with that of B14 (0.07±0.023). We find no evidence for evolution of the mass step with redshift (e.g. Childress et al.,

2014) but $\sim 3\sigma$ evolution in the SALT2 β parameter (the correlation between SN color and luminosity).

In future years, SN samples from the Dark Energy Survey (DES) and the Large Synoptic Survey Telescope (LSST) will measure w with larger, higher-SNR samples of SNe without spectroscopic classifications. Though CC SN contamination is the third-largest source of systematic uncertainty on w in this analysis, we expect that the systematic uncertainty on w from CC SN contamination will be greatly reduced in the next few years. Improvements will be due to larger samples of CC SN templates that can be used to train SN classification algorithms and a better understanding of the shape of the CC SN luminosity function. We hope that the methods presented here will demonstrate the robustness of measuring w from such samples as we continue to gain a better understanding of the nature of dark energy.

5.11 Appendix

In this appendix, we discuss the improvement to the PS1 simulations due to allowing the mean simulated x_1 and c to evolve with redshift. We consider the standard approach of fixed x_1 and c populations insufficient for our analysis, because the PS1 host-z sample has a redshift-dependent host mass distribution due to our magnitude-limited host galaxy redshift follow-up program. Similarly, the SN-z sample consists of SNe not included in the host-z sample and therefore also has a z-dependent bias.

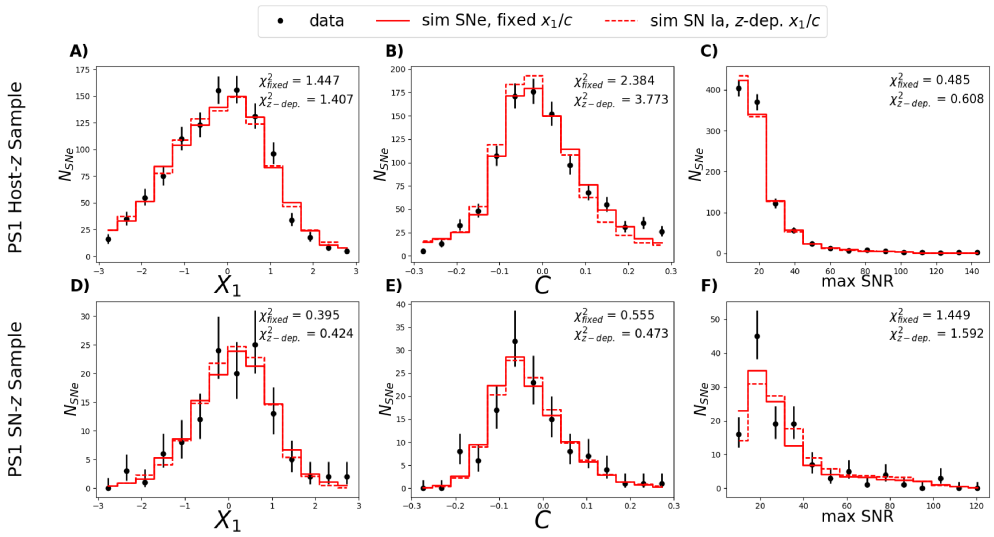

Figure 5.17: Comparing the traditional method of simulating SN Ia samples compared to the data-based method that incorporates host galaxy selection biases. The data-based method is a slightly better match to the data.

Because x_1 and c depend on host mass, their distributions change as a function of z in a way that is not due only to selection biases.

Using the default simulations for the host-z and SN-z samples from J17 and S17, respectively, we fit a 3rd-order polynomial to the difference between the simulations and the data after binning in redshift ($\Delta z = 0.05$). We used these polynomials as inputs to SNANA, allowing them to define the intrinsic evolution of x_1 and c with redshift.

Figure 5.17 shows the change in the distributions of x_1, c, and SNR at maximum light if the simulated x_1/c distributions are allowed to evolve with redshift (G10 scatter model). Figure 5.18 shows the redshift dependence of the x_1 and c distributions

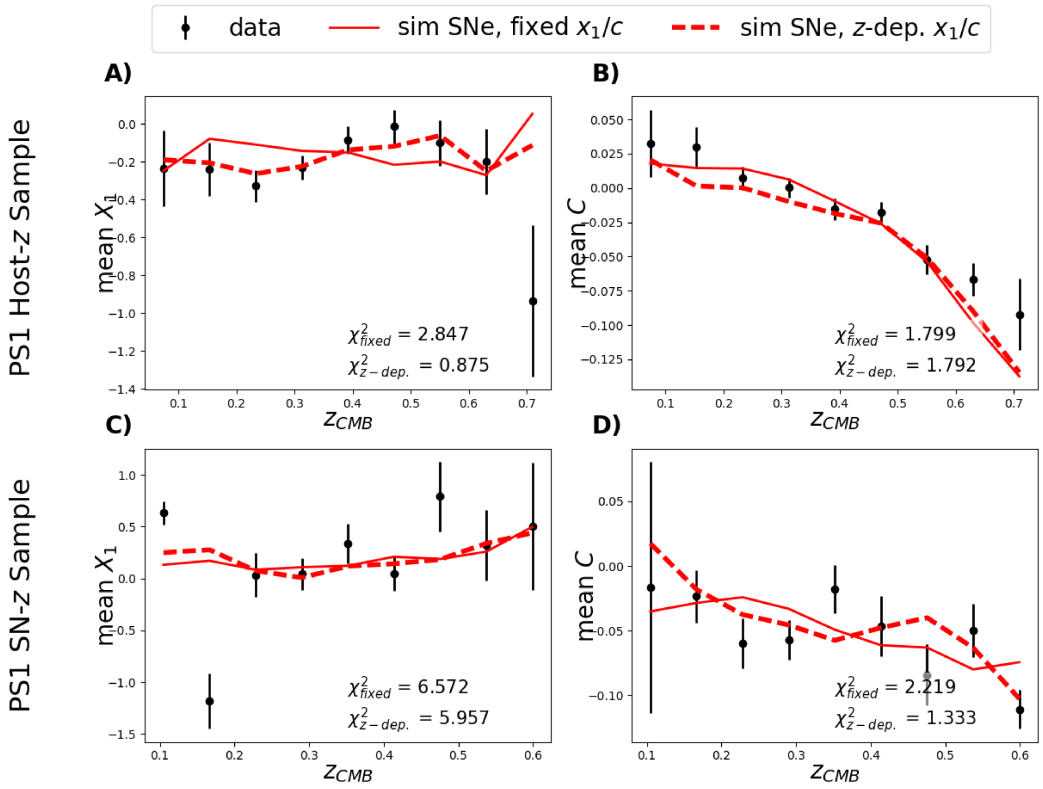

Figure 5.18: The z-dependence of x_1 and c in the SK16 and data-based simulations. The data-based method is a significantly better match to the redshift evolution of the SALT2 shape and color parameters.

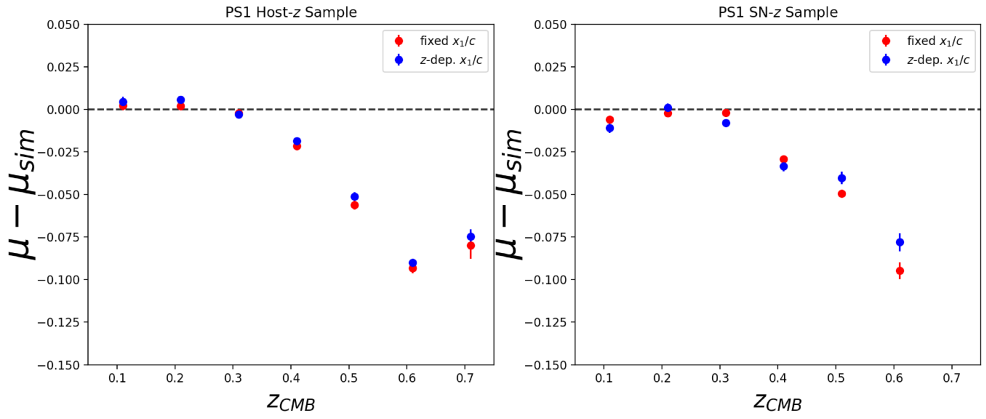

Figure 5.19: Difference in distance bias between the SK16 and data-based simulations. The new simulations predict a smaller distance bias by ∼0.01-0.02 mag at high z.

in simulations with fixed and evolving x_1/c. Though allowing x_1 and c to evolve with redshift does improve the simulations, the new simulations are only a moderately better match to the data.

Figure 5.19 show the difference in bias corrections using the G10 scatter model with and without z-dependent x_1 and c populations. If x_1 and c are redshift dependent, the distance bias is slightly larger for the host-z sample and smaller by up to 0.02 mag at high z for the SN-z sample.

Table 5.7. PS1 Coordinates and Light Curve Parameters

SN	α	δ	z_{CMB}^{SN}	z_{CMB}^{Host}	t_{peak}	x_1	c	m_B	P_{NN}(Ia)	$\log(M_{Host}/M_\odot)$	$\Delta\mu_{bias}$
050298	16:12:38.025	55:43:14.67	···	0.522	55346.10(0.60)	-0.126(0.557)	-0.081(0.052)	22.499(0.014)	0.9906	10.860(0.319)	-0.055
050598	12:16:11.728	46:11:48.97	···	0.293	55372.50(1.10)	0.419(0.811)	0.099(0.050)	21.435(0.088)	0.1725	11.514(0.206)	0.006
050625	16:07:18.198	53:49:47.78	···	0.333	55373.70(0.40)	-0.070(0.440)	0.057(0.041)	21.963(0.055)	1.0000	11.158(0.043)	0.000
050665	16:10:34.502	54:57:25.53	···	0.588	55363.40(0.90)	0.596(0.759)	-0.085(0.047)	22.943(-0.017)	1.0000	11.636(0.210)	-0.076
051109	16:12:11.537	54:00:32.46	···	0.230	55304.60(0.50)	-1.153(0.261)	-0.031(0.035)	21.047(0.048)	1.0000	9.874(0.266)	0.009
060015	16:03:50.262	54:12:36.58	···	0.385	55385.20(0.40)	0.480(0.418)	-0.004(0.042)	22.138(0.040)	0.9911	11.108(0.140)	-0.011
060141	16:09:39.092	54:16:08.95	···	0.190	55393.40(0.20)	-1.382(0.174)	-0.107(0.035)	20.427(0.048)	1.0000	10.781(0.080)	0.010
060169	16:13:15.442	54:26:35.95	···	0.406	55390.90(0.50)	0.299(0.475)	-0.067(0.042)	22.241(0.038)	1.0000	9.692(0.276)	-0.016
060238	22:14:42.32	00:47:51.71	···	0.323	55375.10(2.60)	0.471(0.509)	0.016(0.069)	21.470(0.193)	0.7533	11.466(0.036)	0.002
060249	22:19:51.404	00:53:51.82	0.329	0.329	55374.80(0.50)	-1.641(0.672)	-0.189(0.082)	21.699(0.166)	0.7112	10.974(0.085)	0.001
061192	02:20:30.796	-04:59:51.58	···	0.235	55401.90(2.10)	-0.773(0.452)	0.028(0.068)	21.336(0.155)	1.0000	10.580(0.180)	0.008
061197	02:21:54.589	-04:11:18.99	0.329	0.330	55415.40(0.90)	-0.728(0.565)	0.030(0.042)	21.805(0.049)	0.9997	11.127(0.194)	0.001
070071	22:19:56.443	-00:26:30.93	···	0.369	55421.10(0.40)	-0.703(0.488)	-0.239(0.039)	21.782(0.043)	1.0000	11.716(0.169)	-0.008
070110	02:21:07.819	-05:06:01.50	···	0.280	55412.40(1.10)	0.048(0.447)	0.209(0.045)	22.230(0.077)	1.0000	10.875(0.473)	0.006
070175	16:07:36.819	54:48:35.16	···	0.548	55408.50(1.50)	-1.244(0.874)	-0.070(0.026)	23.251(0.026)	···	11.373(0.070)	-0.063
070200	02:26:38.462	-03:36:57.83	···	0.437	55413.30(1.50)	-1.271(0.771)	0.060(0.058)	22.663(0.044)	0.9999	11.562(0.251)	-0.026
070264	22:13:47.572	00:26:28.25	···	0.332	55426.30(0.20)	0.041(0.234)	-0.038(0.030)	21.873(0.043)	···	9.879(0.385)	0.001
070402	16:13:33.837	54:18:07.88	···	0.316	55428.80(0.20)	0.047(0.257)	-0.019(0.034)	21.658(0.048)	1.0000	10.949(0.109)	0.004
070470	02:19:48.006	-03:42:10.47	···	0.353	55429.90(0.10)	1.359(0.229)	0.003(0.029)	21.872(0.032)	1.0000	9.528(0.360)	-0.004
070515	02:25:51.16	-05:24:17.60	0.475	0.475	55423.80(0.60)	0.760(0.472)	-0.006(0.036)	22.488(0.003)	1.0000	9.470(0.123)	-0.039
070612	16:18:30.721	54:23:11.37	···	0.554	55423.90(0.90)	-0.332(0.766)	-0.011(0.077)	23.373(0.011)	0.9919	11.626(0.262)	-0.065
070719	23:25:53.735	-00:32:13.90	···	0.609	55422.70(0.90)	-1.527(0.782)	-0.067(0.068)	23.284(-0.013)	0.9994	10.495(0.303)	-0.083
070986	23:33:16.318	-00:31:19.64	···	0.345	55442.00(0.30)	0.030(0.234)	-0.067(0.028)	21.756(0.034)	1.0000	9.141(0.284)	-0.002
071060	16:01:16.064	55:28:38.25	···	0.181	55442.20(0.40)	-2.403(0.504)	0.012(0.038)	21.323(0.052)	···	9.679(0.105)	0.011
071113	16:11:44.234	55:08:51.77	···	0.492	55432.70(0.70)	-1.178(0.689)	0.064(0.078)	23.045(0.040)	0.7881	11.312(0.281)	-0.045
080012	22:14:08.482	-00:10:06.88	···	0.526	55444.30(0.50)	0.787(0.483)	-0.010(0.048)	22.888(-0.005)	0.9857	10.961(0.291)	-0.056
080023	23:26:39.152	-00:43:01.94	···	0.459	55448.40(0.50)	-1.103(0.197)	0.172(0.265)	23.132(0.124)	0.9318	10.997(0.078)	-0.034
080031	23:28:17.68	-00:14:59.28	0.293	0.293	55439.70(0.50)	0.798(0.472)	0.282(0.047)	22.668(0.071)	0.0174	9.615(0.117)	0.006
080048	02:24:25.255	-05:00:44.34	0.322	0.322	55442.10(0.10)	-1.454(0.315)	-0.029(0.043)	21.747(0.057)	1.0000	11.471(0.059)	0.003
080087	16:18:28.314	55:14:37.46	···	0.344	55442.30(0.70)	-0.241(0.740)	0.192(0.050)	22.806(0.057)	0.0000	10.733(0.045)	-0.002
080146	03:31:19.116	-26:51:52.43	···	0.457	55449.80(0.80)	0.604(0.540)	-0.065(0.037)	22.351(0.003)	1.0000	10.191(0.160)	-0.033
080241	03:28:32.442	-28:04:17.73	···	0.308	55456.10(0.30)	0.326(0.278)	-0.024(0.029)	21.602(0.041)	1.0000	10.821(0.100)	0.005
080257	03:37:43.958	-27:19:15.27	···	0.187	55436.00(0.80)	0.414(0.723)	0.170(0.064)	21.092(0.119)	1.0000	11.410(0.007)	0.010
080295	02:24:43.482	-04:09:34.95	···	0.625	55452.10(0.20)	1.182(0.730)	-0.003(0.055)	23.145(-0.028)	1.0000	9.816(0.655)	-0.077
080363	03:26:38.822	-27:55:14.34	···	0.317	55448.60(0.80)	-0.006(0.534)	0.232(0.044)	22.095(0.060)	1.0000	11.141(0.133)	0.004
080546	02:21:23.685	-04:00:25.51	0.614	0.614	55448.60(0.50)	1.988(0.609)	-0.168(0.041)	23.037(-0.035)	···	9.849(0.370)	-0.082
080555	02:21:35.496	-03:39:28.37	0.240	0.240	55445.60(0.80)	-2.210(0.523)	-0.003(0.050)	21.149(0.066)	1.0000	11.209(0.052)	0.008
080689	02:25:37.504	-05:14:38.51	0.311	0.310	55454.40(1.10)	0.245(0.922)	-0.004(0.064)	22.647(0.076)	0.0003	10.577(0.297)	0.005

Note. — The full table is available online.

Bibliography

Addison, G. E., Huang, Y., Watts, D. J., et al. 2016, ApJ, 818, 132

Alam, S., Albareti, F. D., Allende Prieto, C., et al. 2015, ApJS, 219, 12

Aldering, G., Adam, G., Antilogus, P., et al. 2002, in Society of Photo-Optical Instrumentation Engineers (SPIE) Conference Series, Vol. 4836, Survey and Other Telescope Technologies and Discoveries, ed. J. A. Tyson & S. Wolff, 61–72

Amendola, L., Appleby, S., Bacon, D., et al. 2013, Living Reviews in Relativity, 16, 6

Anderson, L., Aubourg, É., Bailey, S., et al. 2014, MNRAS, 441, 24

Arcavi, I., Gal-Yam, A., Yaron, O., et al. 2011, ApJl, 742, L18

Astier, P., Guy, J., Regnault, N., et al. 2006, A&A, 447, 31

Baldry, I. K., & Glazebrook, K. 2003, ApJ, 593, 258

Bamba, K., Geng, C.-Q., Lee, C.-C., & Luo, L.-W. 2011, JCAP, 1, 021

BIBLIOGRAPHY

Barbon, R., Benetti, S., Cappellaro, E., et al. 1995, A&AS, 110, 513

Bennett, C. L., Halpern, M., Hinshaw, G., et al. 2003, ApJS, 148, 1

Bernstein, J. P., Kessler, R., Kuhlmann, S., et al. 2012, ApJ, 753, 152

Bertin, E., & Arnouts, S. 1996, A&AS, 117, 393

Betoule, M., Marriner, J., Regnault, N., et al. 2013, A&A, 552, A124

Betoule, M., Kessler, R., Guy, J., et al. 2014, A&A, 568, A22

Bianco, F. B., Modjaz, M., Hicken, M., et al. 2014, ApJS, 213, 19

Blake, C., Brough, S., Couch, W., et al. 2008, Astronomy and Geophysics, 49, 5.19

Blondin, S., & Tonry, J. L. 2007, ApJ, 666, 1024

Bohlin, R. C. 2014, ArXiv e-prints

Boquien, M., Calzetti, D., Aalto, S., et al. 2015, ArXiv e-prints

Brown, P. J., Breeveld, A. A., Holland, S., Kuin, P., & Pritchard, T. 2014, Ap&SS, 354, 89

Burns, C. R., Stritzinger, M., Phillips, M. M., et al. 2014, ApJ, 789, 32

Campbell, H., Nichol, R. C., Olmstead, M. D., et al. 2016, ApJ, 821, 115

Campbell, H., D'Andrea, C. B., Nichol, R. C., et al. 2013, ApJ, 763, 88

BIBLIOGRAPHY

Cardelli, J. A., Clayton, G. C., & Mathis, J. S. 1989, ApJ, 345, 245

Carrick, J., Turnbull, S. J., Lavaux, G., & Hudson, M. J. 2015, MNRAS, 450, 317

Chabrier, G. 2003, PASP, 115, 763

Childress, M., Aldering, G., Antilogus, P., et al. 2013, ApJ, 770, 108

Childress, M. J., Wolf, C., & Zahid, H. J. 2014, MNRAS, 445, 1898

Chotard, N., Gangler, E., Aldering, G., et al. 2011, A&A, 529, L4

Cirasuolo, M., McLure, R. J., Dunlop, J. S., et al. 2007, MNRAS, 380, 585

Cole, S., Norberg, P., Baugh, C. M., et al. 2001, MNRAS, 326, 255

Colless, M., Peterson, B. A., Jackson, C., et al. 2003, ArXiv Astrophysics e-prints

Conley, A., Sullivan, M., Hsiao, E. Y., et al. 2008, ApJ, 681, 482

Conley, A., Guy, J., Sullivan, M., et al. 2011, ApJS, 192, 1

Contreras, C., Hamuy, M., Phillips, M. M., et al. 2010, AJ, 139, 519

Dahlen, T., Strolger, L.-G., & Riess, A. G. 2008, ApJ, 681, 462

Dahlen, T., Strolger, L.-G., Riess, A. G., et al. 2012, ApJ, 757, 70

Dahlen, T., Mobasher, B., Dickinson, M., et al. 2010, ApJ, 724, 425

de Zeeuw, P. T., Hoogerwerf, R., de Bruijne, J. H. J., Brown, A. G. A., & Blaauw, A. 1999, AJ, 117, 354

BIBLIOGRAPHY

Domínguez, I., Höflich, P., & Straniero, O. 2001, ApJ, 557, 279

Eisenstein, D. J., Zehavi, I., Hogg, D. W., et al. 2005, ApJ, 633, 560

Ellis, R. S., Sullivan, M., Nugent, P. E., et al. 2008, ApJ, 674, 51

Ergon, M., Sollerman, J., Fraser, M., et al. 2014, A&A, 562, A17

Ergon, M., Jerkstrand, A., Sollerman, J., et al. 2015, A&A, 580, A142

Fabricant, D., Fata, R., Roll, J., et al. 2005, PASP, 117, 1411

Falck, B. L., Riess, A. G., & Hlozek, R. 2010, ApJ, 723, 398

Filippenko, A. V. 1997, ARA&A, 35, 309

Fioc, M., & Rocca-Volmerange, B. 1997, A&A, 326, 950

Flaugher, B. 2005, International Journal of Modern Physics A, 20, 3121

Folatelli, G., Phillips, M. M., Burns, C. R., et al. 2010, AJ, 139, 120

Foley, R. J., & Mandel, K. 2013, ApJ, 778, 167

Foley, R. J., Filippenko, A. V., Kessler, R., et al. 2012, AJ, 143, 113

Foley, R. J., Challis, P. J., Chornock, R., et al. 2013, ApJ, 767, 57

Foreman-Mackey, D., Hogg, D. W., Lang, D., & Goodman, J. 2013, PASP, 125, 306

Frederiksen, T. F., Hjorth, J., Maund, J. R., et al. 2012, ArXiv e-prints

BIBLIOGRAPHY

Frieman, J. A., Bassett, B., Becker, A., et al. 2008, AJ, 135, 338

Ganeshalingam, M., Li, W., Filippenko, A. V., et al. 2010, ApJS, 190, 418

Garnavich, P. M., Bonanos, A. Z., Krisciunas, K., et al. 2004, ApJ, 613, 1120

Graur, O., Poznanski, D., Maoz, D., et al. 2011, MNRAS, 417, 916

Grogin, N. A., Kocevski, D. D., Faber, S. M., et al. 2011, ApJS, 197, 35

Guillochon, J., Parrent, J., Kelley, L. Z., & Margutti, R. 2017, ApJ, 835, 64

Gupta, R. R., Kuhlmann, S., Kovacs, E., et al. 2016, ArXiv e-prints

Guy, J., Astier, P., Baumont, S., et al. 2007, A&A, 466, 11

Guy, J., Sullivan, M., Conley, A., et al. 2010, A&A, 523, A7

Hamuy, M., Phillips, M. M., Suntzeff, N. B., et al. 1996, AJ, 112, 2398

Hamuy, M., Folatelli, G., Morrell, N. I., et al. 2006, PASP, 118, 2

Hayden, B. T., Gupta, R. R., Garnavich, P. M., et al. 2013, ApJ, 764, 191

Hicken, M., Wood-Vasey, W. M., Blondin, S., et al. 2009a, ApJ, 700, 1097

—. 2009b, ApJ, 700, 1097

Hicken, M., Challis, P., Jha, S., et al. 2009c, ApJ, 700, 331

Hicken, M., Challis, P., Kirshner, R. P., et al. 2012, ApJS, 200, 12

BIBLIOGRAPHY

Hillebrandt, W., & Niemeyer, J. C. 2000, ARA&A, 38, 191

Hlozek, R., Kunz, M., Bassett, B., et al. 2012, ApJ, 752, 79

Hopkins, A. M., & Beacom, J. F. 2006, ApJ, 651, 142

Howell, D. A. 2011, Nature Communications, 2, 350

Hsiao, E. Y., Conley, A., Howell, D. A., et al. 2007, ApJ, 663, 1187

Hudson, M. J., Smith, R. J., Lucey, J. R., & Branchini, E. 2004, MNRAS, 352, 61

Jerkstrand, A., Ergon, M., Smartt, S. J., et al. 2015, A&A, 573, A12

Jha, S., Riess, A. G., & Kirshner, R. P. 2007, ApJ, 659, 122

Jha, S., Kirshner, R. P., Challis, P., et al. 2006, AJ, 131, 527

Johansson, J., Thomas, D., Pforr, J., et al. 2013, MNRAS, 435, 1680

Jones, D. H., Read, M. A., Saunders, W., et al. 2009, MNRAS, 399, 683

Jones, D. O. 2017, Measuring Dark Energy With Photometrically Classified Pan-STARRS Supernova: Bayesian Estimation Applied to Multiple Species Algorithm

Jones, D. O., Riess, A. G., & Scolnic, D. M. 2015, ApJ, 812, 31

Jones, D. O., Rodney, S. A., Riess, A. G., et al. 2013, ApJ, 768, 166

Jones, D. O., Scolnic, D. M., Riess, A. G., et al. 2016, ArXiv e-prints

BIBLIOGRAPHY

Jönsson, J., Dahlén, T., Goobar, A., et al. 2006, ApJ, 639, 991

Jönsson, J., Sullivan, M., Hook, I., et al. 2010, MNRAS, 405, 535

Kaiser, N., Burgett, W., Chambers, K., et al. 2010, in Society of Photo-Optical Instrumentation Engineers (SPIE) Conference Series, Vol. 7733, Society of Photo-Optical Instrumentation Engineers (SPIE) Conference Series, 0

Kelly, B. C. 2007, ApJ, 665, 1489

Kelly, P. L., Filippenko, A. V., Burke, D. L., et al. 2015, Science, 347, 1459

Kelly, P. L., Hicken, M., Burke, D. L., Mandel, K. S., & Kirshner, R. P. 2010, ApJ, 715, 743

Kessler, R., & Scolnic, D. 2016, ArXiv e-prints

—. 2017, ApJ, 836, 56

Kessler, R., Becker, A. C., Cinabro, D., et al. 2009a, ApJS, 185, 32

Kessler, R., Bernstein, J. P., Cinabro, D., et al. 2009b, PASP, 121, 1028

Kessler, R., Bassett, B., Belov, P., et al. 2010, PASP, 122, 1415

Kessler, R., Marriner, J., Childress, M., et al. 2015, AJ, 150, 172

Koekemoer, A. M., Faber, S. M., Ferguson, H. C., et al. 2011, ApJS, 197, 36

Kunz, M., Bassett, B. A., & Hlozek, R. A. 2007, Phys. Rev. D, 75, 103508

Kurtz, M. J., & Mink, D. J. 1998, PASP, 110, 934

Kuznetsova, N. V., & Connolly, B. M. 2007, ApJ, 659, 530

Lampeitl, H., Smith, M., Nichol, R. C., et al. 2010, ApJ, 722, 566

Lavaux, G., & Hudson, M. J. 2011, MNRAS, 416, 2840

Lawrence, A., Warren, S. J., Almaini, O., et al. 2007, MNRAS, 379, 1599

Le Borgne, D., & Rocca-Volmerange, B. 2002, A&A, 386, 446

Le Fèvre, O., Vettolani, G., Garilli, B., et al. 2005, A&A, 439, 845

Leaman, J., Li, W., Chornock, R., & Filippenko, A. V. 2011, MNRAS, 412, 1419

Lewis, A., & Bridle, S. 2002, Phys. Rev. D, 66, 103511

Li, W., Leaman, J., Chornock, R., et al. 2011, MNRAS, 412, 1441

Lilly, S. J., Le Fèvre, O., Renzini, A., et al. 2007, ApJS, 172, 70

Linder, E. V. 2003, Physical Review Letters, 90, 091301

Livio, M. 2001, in Supernovae and Gamma-Ray Bursts: the Greatest Explosions since the Big Bang, ed. M. Livio, N. Panagia, & K. Sahu, Vol. 13, 334–355

Lochner, M., McEwen, J. D., Peiris, H. V., Lahav, O., & Winter, M. K. 2016, ArXiv e-prints

Lunnan, R., Chornock, R., Berger, E., et al. 2015, ApJ, 804, 90

BIBLIOGRAPHY

Macciò, A. V., Dutton, A. A., & van den Bosch, F. C. 2008, MNRAS, 391, 1940

Maoz, D., Mannucci, F., & Nelemans, G. 2014, ARA&A, 52, 107

March, M. C., Trotta, R., Berkes, P., Starkman, G. D., & Vaudrevange, P. M. 2011, MNRAS, 418, 2308

Marriner, J., Bernstein, J. P., Kessler, R., et al. 2011, ApJ, 740, 72

Metlova, N. V., Tsvetkov, D. Y., Shugarov, S. Y., Esipov, V. F., & Pavlyuk, N. N. 1995, Astronomy Letters, 21, 598

Mink, D. J., Wyatt, W. F., Caldwell, N., et al. 2007, in Astronomical Society of the Pacific Conference Series, Vol. 376, Astronomical Data Analysis Software and Systems XVI, ed. R. A. Shaw, F. Hill, & D. J. Bell, 249

Modjaz, M., Li, W., Filippenko, A. V., et al. 2001, PASP, 113, 308

Modjaz, M., Blondin, S., Kirshner, R. P., et al. 2014, AJ, 147, 99

Möller, A., Ruhlmann-Kleider, V., Leloup, C., et al. 2016, ArXiv e-prints

Mosher, J., Guy, J., Kessler, R., et al. 2014, ApJ, 793, 16

Narayan, G., Axelrod, T., Holberg, J. B., et al. 2016, ApJ, 822, 67

Navarro, J. F., Frenk, C. S., & White, S. D. M. 1997, ApJ, 490, 493

Neill, J. D., Hudson, M. J., & Conley, A. 2007, ApJl, 661, L123

Neill, J. D., Sullivan, M., Howell, D. A., et al. 2009, ApJ, 707, 1449

Newman, J. A., Cooper, M. C., Davis, M., et al. 2013, ApJS, 208, 5

Nugent, P., Kim, A., & Perlmutter, S. 2002, PASP, 114, 803

Oguri, M., & Marshall, P. J. 2010, MNRAS, 405, 2579

Padmanabhan, N., Schlegel, D. J., Finkbeiner, D. P., et al. 2008, ApJ, 674, 1217

Pan, Y.-C., Sullivan, M., Maguire, K., et al. 2014, MNRAS, 438, 1391

Pastorello, A., Kasliwal, M. M., Crockett, R. M., et al. 2008, MNRAS, 389, 955

Peng, C. Y., Ho, L. C., Impey, C. D., & Rix, H.-W. 2002, AJ, 124, 266

Perlmutter, S., Aldering, G., Goldhaber, G., et al. 1999, ApJ, 517, 565

Phillips, M. M. 1993, ApJL, 413, L105

Pike, R. W., & Hudson, M. J. 2005, ApJ, 635, 11

Planck Collaboration, Ade, P. A. R., Aghanim, N., et al. 2013, ArXiv e-prints

—. 2014, A&A, 571, A16

—. 2015, ArXiv e-prints

Planck Collaboration, Aghanim, N., Ashdown, M., et al. 2016, A&A, 596, A107

Postman, M., Coe, D., Benítez, N., et al. 2012, ApJS, 199, 25

Poznanski, D., Maoz, D., & Gal-Yam, A. 2007, AJ, 134, 1285

Press, W. H. 1997, in Unsolved Problems in Astrophysics, ed. J. N. Bahcall & J. P. Ostriker, 49–60

Rest, A., Stubbs, C., Becker, A. C., et al. 2005, ApJ, 634, 1103

Rest, A., Scolnic, D., Foley, R. J., et al. 2014, ApJ, 795, 44

Richardson, D., Jenkins, III, R. L., Wright, J., & Maddox, L. 2014, AJ, 147, 118

Richardson, D., Thomas, R. C., Casebeer, D., et al. 2001, in Bulletin of the American Astronomical Society, Vol. 33, American Astronomical Society Meeting Abstracts, 1428

Richmond, M. W., Treffers, R. R., Filippenko, A. V., & Paik, Y. 1996, AJ, 112, 732

Riello, M., & Patat, F. 2005, MNRAS, 362, 671

Riess, A. G., & Livio, M. 2006, ApJ, 648, 884

Riess, A. G., Press, W. H., & Kirshner, R. P. 1996, ApJ, 473, 88

Riess, A. G., Filippenko, A. V., Challis, P., et al. 1998, AJ, 116, 1009

Riess, A. G., Kirshner, R. P., Schmidt, B. P., et al. 1999, AJ, 117, 707

Riess, A. G., Nugent, P. E., Gilliland, R. L., et al. 2001, ApJ, 560, 49

Riess, A. G., Strolger, L.-G., Tonry, J., et al. 2004, ApJ, 607, 665

Riess, A. G., Strolger, L.-G., Casertano, S., et al. 2007, ApJ, 659, 98

Riess, A. G., Macri, L., Casertano, S., et al. 2011, ApJ, 730, 119

Riess, A. G., Macri, L. M., Hoffmann, S. L., et al. 2016, ApJ, 826, 56

Rigault, M., Copin, Y., Aldering, G., et al. 2013, A&A, 560, A66

Rigault, M., Aldering, G., Kowalski, M., et al. 2015, ApJ, 802, 20

Rodney, S. A., & Tonry, J. L. 2009, ApJ, 707, 1064

Rodney, S. A., Riess, A. G., Dahlen, T., et al. 2012, ApJ, 746, 5

Rodney, S. A., Riess, A. G., Strolger, L.-G., et al. 2014, AJ, 148, 13

Rodney, S. A., Riess, A. G., Scolnic, D. M., et al. 2015, AJ, 150, 156

Ross, A. J., Samushia, L., Howlett, C., et al. 2015, MNRAS, 449, 835

Rubin, D., Knop, R. A., Rykoff, E., et al. 2012, arXiv:1205.3494

Rubin, D., Aldering, G., Barbary, K., et al. 2015, ApJ, 813, 137

Saha, A., Wang, Z., & Zaidi, T. 2016, in Proc. SPIE, Vol. 9910, Observatory Operations: Strategies, Processes, and Systems VI, 99100F

Sako, M., Bassett, B., Becker, A., et al. 2008, AJ, 135, 348

Sako, M., Bassett, B., Connolly, B., et al. 2011, ApJ, 738, 162

Sako, M., Bassett, B., Becker, A. C., et al. 2014, ArXiv e-prints

Salim, S., Rich, R. M., Charlot, S., et al. 2007, ApJS, 173, 267

Sanders, N. E., Soderberg, A. M., Gezari, S., et al. 2015, ApJ, 799, 208

Schlafly, E. F., & Finkbeiner, D. P. 2011, ApJ, 737, 103

Schlafly, E. F., Finkbeiner, D. P., Jurić, M., et al. 2012, ApJ, 756, 158

Schlegel, D. J., Finkbeiner, D. P., & Davis, M. 1998, ApJ, 500, 525

Scodeggio, M., Guzzo, L., Garilli, B., et al. 2016, ArXiv e-prints

Scolnic, D., & Kessler, R. 2016, ArXiv e-prints

Scolnic, D., Rest, A., Riess, A., et al. 2014a, ApJ, 795, 45

Scolnic, D., Casertano, S., Riess, A., et al. 2015, ApJ, 815, 117

Scolnic, D. M., Riess, A. G., Foley, R. J., et al. 2014b, ApJ, 780, 37

Shivvers, I., Mazzali, P., Silverman, J. M., et al. 2013, MNRAS, 436, 3614

Shivvers, I., Modjaz, M., Zheng, W., et al. 2017, PASP, 129, 054201

Silverman, J. M., Foley, R. J., Filippenko, A. V., et al. 2012, MNRAS, 425, 1789

Skrutskie, M. F., Cutri, R. M., Stiening, R., et al. 2006, AJ, 131, 1163

Smee, S. A., Gunn, J. E., Uomoto, A., et al. 2013, AJ, 146, 32

Smith, M., Bacon, D. J., Nichol, R. C., et al. 2014, ApJ, 780, 24

Stritzinger, M. D., Phillips, M. M., Boldt, L. N., et al. 2011, AJ, 142, 156

Strolger, L.-G., Dahlen, T., & Riess, A. G. 2010, ApJ, 713, 32

Suh, H., Yoon, S.-c., Jeong, H., & Yi, S. K. 2011, ApJ, 730, 110

Sullivan, M., Le Borgne, D., Pritchet, C. J., et al. 2006, ApJ, 648, 868

Sullivan, M., Conley, A., Howell, D. A., et al. 2010, MNRAS, 406, 782

Sullivan, M., Guy, J., Conley, A., et al. 2011, ApJ, 737, 102

Suzuki, N., Rubin, D., Lidman, C., et al. 2012, ApJ, 746, 85

Taubenberger, S., Hachinger, S., Pignata, G., et al. 2008, MNRAS, 385, 75

Taubenberger, S., Navasardyan, H., Maurer, J. I., et al. 2011, MNRAS, 413, 2140

Tonry, J., & Davis, M. 1979, AJ, 84, 1511

Tripp, R. 1998, A&A, 331, 815

Tsvetkov, D. Y., Volkov, I. M., Baklanov, P., Blinnikov, S., & Tuchin, O. 2009, Peremennye Zvezdy, 29

Tully, R. B., & Fisher, J. R. 1977, A&A, 54, 661

Wang, B., & Han, Z. 2012, NewAR, 56, 122

BIBLIOGRAPHY

Weinberg, D. H., Mortonson, M. J., Eisenstein, D. J., et al. 2013, Physics Reports, 530, 87

Wiklind, T., Dickinson, M., Ferguson, H. C., et al. 2008, ApJ, 676, 781

Wolf, R. C., D'Andrea, C. B., Gupta, R. R., et al. 2016, ApJ, 821, 115

Yang, X., Mo, H. J., van den Bosch, F. C., Zhang, Y., & Han, J. 2012, ApJ, 752, 41

Yaron, O., & Gal-Yam, A. 2012, PASP, 124, 668

Vita

David O. Jones received undergraduate degrees in Astronomy and Music Performance from Boston University in 2010. He received a M.A. degree from Boston University in 2011 with a Master's thesis entitled "Using Stellar Spectra to Constrain the Distribution of Galactic Dust". Beginning in September 2017, he will be a Moore Foundation Postdoctoral Fellow at the University of California at Santa Cruz.